Observational Signatures of Nonlinear Interactions in the Solar Wind

by

Trevor Bowen

A dissertation submitted in partial satisfaction of the
requirements for the degree of

Doctor of Philosophy
in
Physics
in the
Graduate Division
of the
University of California, Berkeley

Committee in charge:
Professor Stuart Bale, Chair
Professor Jonathan Wurtele
Professor Eliot Quataert

Spring 2019

Abstract

Observational Signatures of Nonlinear Interactions in the Solar Wind

by

Trevor Bowen

Doctor of Philosophy in Physics
University of California, Berkeley
Professor Stuart Bale, Chair

Spacecraft observations from the interplanetary medium of our solar system reveal the presence of a magnetized super-sonic flow emanating from the sun, commonly known as the solar wind. Empirically, *in-situ* measurements from spacecraft suggest that the solar wind is in a turbulent state frequently occurring fluid-like systems. Though theories of non-magnetized hydrodynamic turbulence have been successfully adapted to account for plasma dynamics relevant to the solar wind (e.g. strong magnetization, multi-particle composition, non-viscous dissipation, and weak collisionality), there is lacking consensus regarding the physical processes responsible for empirically observed phenomena: e.g. compressible fluctuations, intermittent coherent features, injection of energy at large scales, and particle heating. Interpreting *in-situ* spacecraft measurements is often complicated by limitations associated with single point me which most often consist of a single point (or at best a few points) located near Earth. At the largest physical scales, processes associated with solar wind generation and evolution consist of temporal variation over the 11 year solar cycle, with spatial gradients extending over the large scale heliosphere, ~ 200 AU. At the smallest scales, heating and dissipation process can occur on electron kinetic scales corresponding to ~ kHz frequencies and centimeter length scales in the inner heliosphere. Even in observing fluid-like magnetohydrodynamic (MHD) fluctuations of the solar wind, "easily" measurable by spacecraft at 1 AU, significant ambiguity exists in distinguishing effects associated with plasma transport from the processes related to the generation (heating and acceleration) of the solar wind in the inner-heliosphere.

The source of the solar wind is the corona, a hot magnetized upper-atmosphere of our sun with ambient temperatures ranging from ~ 10^5-10^6 Kelvin: orders of magnitude larger than the solar photospheric surface at 5800 Kelvin. Even the roughest estimation of the coronal energy budgets suggest that the magnetic field must be responsible for heating the corona to these temperatures. However, the specific processes which drive coronal heating, and subsequently accelerate the solar wind, are yet

unknown; though many models of coronal heating exist, little empirical evidence is currently available to distinguish between theories.

The NASA Parker Solar Probe (PSP) mission, launched in August 2018, recently became the closest human-made object to orbit the sun. During its closest perihelion approach, PSP will reach an altitude of 9.8 solar radii (0.045 AU), well within the expected boundary between the solar wind corona, known as the Alfvén point. By measuring the local plasma environment, PSP will provide an empirical understanding of the processes responsible for coronal heating and solar wind acceleration which cannot be observed using remote sensing techniques. In addition, through studying the turbulent environment present in the inner heliosphere, PSP will inevitably make significant contribution to our understanding of magnetized turbulence and the role it plays in shaping astrophysical systems.

This dissertation highlights the development of observational techniques and instrumentation used in studying nonlinear dynamic processes, e.g. turbulence and plasma instabilities, in astrophysical plasmas. Part I consists of a discussion of incompressible magnetohydrodynamic turbulence in the solar wind and the observed coupling with compressible fluctuations. Chapter 1 contains an overview of the historical and mathematical development of MHD turbulence based on both empirical observations from spacecraft and theory of hydrodynamic turbulence. Chapter 2 contains original research on the effect of intermittency on the observational signatures of MHD turbulence. Chapter 3 discusses the the nature of compressible fluctuations in the solar wind based on the mathematical and observational techniques developed in Chapter 2. Chapter 4 describes an observational study which examines the existence of parametric mode coupling in the solar wind which could drive compressible fluctuations as well as initiate non-linear turbulent interactions in the heliosphere.

Part II surveys the calibration and operation of the PSP/FIELDS magnetometer suite. Chapter 5 highlights the operation and calibration of the PSP/FIELDS DC fluxgate magnetometer (MAG). Chapter 6 consists of an overview of the PSP/FIELDS search coil magnetometer (SCM) and an in depth discussion of instrument calibration through the framework of linear time invariant filter design. Chapter 7 describes a merged fluxgate and search coil data product for PSP created using optimal filter design techniques.

ACKNOWLEDGMENTS

I exited "high-school #1" after a single year with an impressively miserable GPA and an algebra teacher convinced that I needed remedial course work. The experiences with teachers in a nontraditional high-school largely inspired me to pursue an education in science. Lisa Luhn ran a class which facilitated student internships with local scientists, providing my first experience with research: Professor Brian Hynek mentored me for two years and deserves immense credit for letting a crusty high-school student map out river valley systems and impact craters on floor-size printouts of the Martian surface.

My experience with nontraditional education led me to liberal arts school. Professor Travis Norsen (who would regularly commute to campus in blizzard conditions to chat about quantum mechanics) was pivotal in pushing me to explore off-campus research opportunities. Professor Sara Salimbeni was key in helping me learn to communicate scientific ideas through various forms and to manage the goals of an open ended research project.

I first worked with Dr. Katharine Reeves and Dr. Paola Testa as a summer intern, both are largely responsible for my continued enthusiasm in doing research. After finishing college, Kathy and Paola hired me to wrap up our project on solar flares. I was simultaneously applying to graduate programs, though it seemed like a reach, Kathy advised me to apply to Berkeley. Their efforts and kind mentorship are definitely what prepared me most for graduate school.

I started at Berkeley jaded by course work and the concept of attending 100+ person early morning lectures. The friendships solidified during these first two years (Robert Kealhofer, Dr. Parker Fagrelius, Halleh Balch, Dr. Alison Saunders, Dr. Carolyn Kierans, Lex Kosieradzki, Taylor Burrows, Marcelo Caceres) provided support which kept me enrolled in graduate school long enough to see it through.

The successful completion of this thesis is due to mentorship provided by Professor Stuart Bale, who has regularly provided intellectually stimulating problems and projects. Though absent from this thesis, a significant portion of my graduate work was done with Professors Jonathan Wurtele and Dmitry Budker who brought me onto a project to study magnetic fields in urban areas, providing an opportunity to hone technical skills with interdisciplinary relevance. I would also like to acknowledge Sam Badman and Dr. Alfred Mallet, who have coauthored work central to this thesis, as well as Professor Thierry Dudok de Wit and Dr. John Bonnell who are invaluable mentors that have helped me learn many fundamental aspects of signal processing. A lot of this work was made possible by everyone in the Silver-260 office (Dr. David Sundkvist, Dr. Marc Pulupa, Dr. Juan Carlos Martinez-Oliveros, Dr. Chadi Salem, Yuguang Tong, Juan Camilo Buitrago-Casas, et al.) who always assist with little questions and provide advice and friendly chatter.

I am truly indebted to friends and family who have always supported these endeavors; there are countless people who have positively contributed to the work in this thesis and who I am dearly thankful for their presence in my life.

CONTENTS

LIST OF FIGURES

PART I

TURBULENCE IN THE SOLAR WIND

1

INTRODUCTION TO TURBULENCE IN THE SOLAR WIND

1.1 EARLY OBSERVATIONS OF SOLAR WIND TURBULENCE

Much of the universe is known to be in an ionized state of matter called plasma. Textbooks commonly introduce plasma dynamics as the exhibition of collective behavior, such that strong binary interactions between constituent particles are subdominant to many-body interactions mediated by electromagnetic forces (Chen, 1974; Nicholson, 1983; Fitzpatrick, 2014). In developing a formal theory to explain the collective behavior of charged particles from kinetic principles, non-linearities quickly emerge in the systems of equation which describes both particle kinetic motion as well as the evolution of electromagnetic fields.

Non-linearities are a common occurrence in both fluid and kinetic descriptions of dynamic particle motion (Kolmogorov, 1941; Batchelor, 1950; Balbus, 2018). Over the last several centuries, observations of non-linear phenomena have been studied observationally, leading to the development of classical theories of turbulence based on hydrodynamics. More recently, the effects of magnetization have been incorporated into these theories (Iroshnikov, 1963; Kraichnan, 1965; Goldreich and Sridhar, 1995; Boldyrev, 2006). Turbulence plays a significant roll in the dynamics of many astrophysical systems, ranging from large scale motions in the interstellar medium, e. g. Higdon (1984); Lithwick and Goldreich (2001); Armstrong and Rickett (1981), to particle heating in stellar winds and coronae (Vasquez et al., 2007; Chandran et al., 2010), as well as the environment in and around planetary magnetospheres (Zimbardo, 2006). Outside of the discipline of astrophysics, magnetized turbulence is known to occur in controlled laboratory devices, such as fusion plasmas generated by tokamaks and lasers (Bickerton, 1997; Rigby et al., 2018).

The development space-borne instrumentation in the 1950s and 1960s led to the first *in-situ* observations of our solar system's inter-planetary medium, revealing a magnetized plasma in a state of turbulence. Since these initial observations, the solar wind has proven to be an excellent environment for testing theories of both kinetic and magnetohydrodynamic plasma turbulence (Coleman, 1968; Belcher and Davis, 1971; Bieber et al., 1996; Tu and Marsch, 1994; Marsch and Tu, 1990b; Tu and Marsch, 1991; Leamon et al., 1998; Horbury et al., 2008; Dudok de Wit et al., 2013; Alexandrova et al., 2013; Bale et al., 2005; Bruno and Carbone, 2013b). The fundamental physical principles which have emerged from the study of space plasma physics has significantly impacted research in disciplines such

as laboratory plasma physics, astronomy, cosmology, nuclear engineering, and fundamental particle searches Higdon (1984); Dorfman and Carter (2016); Lithwick et al. (2007); Brunetti and Lazarian (2007); Connor (1993); Cranmer (2008); Davidson (2010).

Theoretical thermodynamic and electromagnetic considerations of the heliosphere were largely enabled by attempts to couple electromagnetism with hydrodynamics, e.g. by Alfvén (1942) and Elsasser (1950), and complementary efforts to explain physical processes driving the aurora, geomagnetism, and the earth's magnetosphere, e.g. Chapman (1952); Alfvén (1958). The first *in-situ* observations of solar wind plasma were made by NASA's *Mariner II* mission to Venus, which observed steady inter-planetary flows originating from the inner heliosphere (Neugebauer and Snyder, 1962). Though visual observations of bifurcated comet tails led to discourse regarding the nature of "solar corpuscular radiation" in the interplanetary medium, e.g. Alfvén (1957); Biermann (1953, 1957), *in-situ* observations of the solar wind by spacecraft provided the first evidence for a dynamic, super-sonic, flow expanding through the inter-planetary medium consistent with predictions of Parker (1958).

Magnetometers, a fundamental *in-situ* observational tool for observing space plasmas, were flown on spacecraft as early 1958 on the *Sputnik III* and *Pioneer I* missions, though some of the first significant observations of the interplanetary magnetic field were made by $IMP-1$ which first crossed Earth's bow shock, entering the inner planetary medium (Ness et al., 1964; Ness et al., 1971). While these studies defined the first results of magnetospheric physics, the some of the most significant *in-situ* results from the heliosphere were provided by the fluxgate magnetometer on Mariner II, delivering the first evidence of spiraling in IMF spiral magnetic field predicted by Parker (1958).

Observations of magnetic and velocity fluctuations perpendicular to the mean IMF direction led Coleman (1968) and Belcher and Davis (1971) to interpret the fluctuations in the solar wind as transverse Alfvén modes (Alfvén, 1942). The theoretical work from Barnes (1966), which suggested high damping rates of compressive magneto-acoustic modes under typical solar wind conditions, in turn provided the theoretical support for the observed dominance of Alfvénic modes. Simultaneous development of digital signal processing algorithms for spectral estimation, e.g. Blackman and Tukey (1958), provided the necessary observational tools to measure spectral distributions of magnetic fluctuations in the solar wind (Coleman Jr., 1964, 1966; Jokipii, 1968; Belcher and Davis, 1971; Russell, 1972). Coleman (1968), measured distributions of fluctuations consistent with power-law spectral distributions reminiscent of hydrodynamic turbulence, interpreting the results as evidence for magnetized turbulent fluctuations suggested by Iroshnikov (1963) and Kraichnan (1965). While many early studies explored the wave like behavior of fluctuations in the solar wind, identifying observed solar wind fluctuations as consistent with magnetized turbulence has contributed greatly to our understanding of the heliosphere and large scale astrophysical systems (Tu and Marsch, 1994; Goldstein et al., 1995; Marsch, 2006; Bruno and Carbone, 2013b).

1.2 A MATHEMATICAL INTRODUCTION TO TURBULENCE

1.2.1 TURBULENCE IN HYDRODYNAMICS

The fundamental dynamics of plasmas can be theoretically obtained from kinetic theory, which uses distribution function $f_s(\mathbf{r}, \mathbf{v}, t)$, as a statistical description of the respective positions and velocities of a system of N_s particles of species s in configuration (phase) space (Nicholson, 1983). As a statistical distribution, $f_s(\mathbf{r}, \mathbf{v}, t)$ is normalized in phase space such that the integrated probability of a particle being at any point in space, with any velocity is unity:

$$1 = \frac{1}{N_s} \int_{-\infty}^{\infty} f_s(\mathbf{r}, \mathbf{v}, t) d^3\mathbf{v} d^3\mathbf{r}. \tag{1.1}$$

The conservation of phase space volume, known as Liouville's theorem, leads to a continuity equation, known as the Vlasov equation, which governs the time evolution of $f_s(\mathbf{r}, \mathbf{v}, t)$in phase space

$$\frac{df_s(\mathbf{r}, \mathbf{v}, t)}{dt} = \frac{\partial f_s}{\partial t} + \mathbf{v} \cdot \nabla_r f_s + \mathbf{a} \cdot \nabla_v f_s = 0, \tag{1.2}$$

where the effect of collisions, or particle creation and annihilation is omitted. The equations of hydrodynamics are obtained through taking statistical moments of $f_s(\mathbf{r}, \mathbf{v}, t)$ with respect to the phase space coordinate $\mathbf{v}$ and its i-th order tensors:

$$M_s^i(\mathbf{r}, t) = \int \mathbf{v}^i f_s(\mathbf{r}, \mathbf{v}, t) d^3\mathbf{v}; \tag{1.3}$$

These average quantities correspond to the definition of macroscopic average quantities such as density,

$$n_s = \int f_s d^3\mathbf{v} \tag{1.4}$$

and flow velocity

$$n\mathbf{u}_s = \int \mathbf{v} f_s d^3\mathbf{v} \tag{1.5}$$

are defined. Simultaneously, taking statistical moments of the Vlasov equation, leads to a set of conservation equations governing the evolution of these macroscopic quantities: the continuity equation,

$$\frac{\partial n_s}{\partial t} + \nabla \cdot (n_s \mathbf{u}_s) = 0; \tag{1.6}$$

and the conservation of momentum, known as the Euler equation,

$$\frac{\partial \mathbf{u}_s}{\partial t} + \mathbf{u}_s \cdot \nabla \mathbf{u}_s = \frac{1}{m_s n_s} \nabla \cdot \mathbf{P}_s + \mathbf{f}_s, \tag{1.7}$$

where $\mathbf{f}$ contains external and internal forces on the fluid term. In general the distribution $f_s(\mathbf{r}, \mathbf{v}, t)$ is defined for every individual species of particle, e. .g . protons, electrons, neutrals, and heavy ions. For common astrophysical plasmas which are predominately composed of protons and electrons, f_i and f_e are coupled by the electromagnetic force

$$\mathbf{f} = q_s(\mathbf{E} + \mathbf{u}_s \times \mathbf{B}) \tag{1.8}$$

through, for example, the electric field given by Gauss's law

$$\nabla \cdot \mathbf{E} = \frac{q(n_i - n_e)}{\epsilon_0}. \tag{1.9}$$

Subsequent higher order moments of the distribution functions may be defined; however, the conservation equation governing each statistical moment is inherently coupled to the next higher order moment, leading to an infinite hierarchy of equations. Typically, the hierarchy of moments may be truncated by setting all moments $M_s^i = 0$ for some i. Alternatively, defining high order moments in terms of lower order moments allows for closure of the system of moments; for example the polytropic relation $pn^{-\gamma} = Const$ provides closure through defining the thermodynamic equation of state for the internal energy of the system.

Contained within the gradient tensor

$$\mathbf{P} = \int \mathbf{v}\mathbf{v} f(\mathbf{r}, \mathbf{v}, t) d^3\mathbf{v} \tag{1.10}$$

are the average properties of the kinetic distribution $f(\mathbf{r}, \mathbf{v}, t)$ which emerge as the macroscopic effects of shear and pressure due to multi-particle interactions. For an isotropic pressure, decomposition of this tensor is commonly made as

$$\mathbf{P} = -\mathbf{I}p + \tau, \tag{1.11}$$

where τ is the viscosity tensor. In classical (unmagnetized) hydrodynamics, this tensor commonly appears as $\tau = \nu \nabla \mathbf{u}$ such that the viscous term appears as $\nu \nabla^2 \mathbf{u}$.

Making the substitution into the conservation of momentum leads to the Navier-Stokes equation:

$$nm\left(\frac{\partial \mathbf{u}}{\partial t} + \mathbf{u} \cdot \nabla \mathbf{u}\right) = -\nabla p + \nu \nabla^2 \mathbf{u} + \mathbf{f}. \tag{1.12}$$

For an incompressible fluid the condition $\frac{dn}{dt} = 0$ leads to the condition $\nabla \cdot \mathbf{u} = 0$. Incompressible hydrodynamic turbulence emerges from the relative weighting of the non-linear term $\mathbf{u} \cdot \nabla \mathbf{u}$ relative to the viscous term $\nu \nabla^2 \mathbf{u}$:

$$R_H = \frac{\mathbf{u} \cdot \nabla \mathbf{u}}{\nu \nabla^2 \mathbf{u}} = \frac{U^2/L}{\nu U/L^2} = \frac{UL}{\nu}, \tag{1.13}$$

where R_H is known as the Reynolds number, and L, U, and $T = L/U$ are typical length, velocity, and time scales characterizing the system. For low R_H, the Navier-Stokes equation reduces to a simple linear diffusion equation

$$\frac{\partial \mathbf{u}}{\partial t} = \nu \nabla^2 \mathbf{u}, \tag{1.14}$$

which can be solved by e.g. separation of variables .

Physical systems with large R_H are subject to strong non-linear interactions; the study of which has largely been undertaken with statistical analysis. Richardson (1922) was the first to suggest that non-linear interactions would lead to a cascade, where large vortical structures, eddies, could cascade into smaller structures. The largest of these structures, at scale L, commonly called the injection scale, with velocity fluctuations of amplitude U, are able to exchange energy at a rate (per unit mass) which is dimensionally calculated as

$$\epsilon = \frac{U^2}{T} = \frac{U^3}{L} \tag{1.15}$$

For a stationary state, such that energy does not build up in the system, energy must simultaneously be dissipated energy at the rate ϵ. For hydrodynamic systems with large Reynolds numbers, this dissipation occurs due to the viscosity, and must occur at scales much smaller than the injection scale L. Dimensionally, the length, known as the Kolmogorov scale, which corresponds to a viscous dissipation rate of ϵ is

$$l_{KG} = (\nu/\epsilon)^{1/4} = L R_H^{-3/4}, \tag{1.16}$$

The scale l_{KG} sets the smallest scale at which a viscosity of ν can dissipate energy injected at scale L. The range of scales between the injection scale, L and the dissipation scale l_{KG} are commonly called the inertial range. Kolmogorov (1941) argued that in the inertial range, the energy flux is constant, and local between neighboring scales,

$$\epsilon = \frac{U^3}{L} = \frac{v_l^3}{l}, \tag{1.17}$$

leading to the Kolmogorov proportionality:

$$v_l = (\epsilon l)^{1/3}. \tag{1.18}$$

The total energy E_l at any scale l_0 is given as the integral of the fluctuating energy at scales above that scale

$$v_l^2 = \int_{l_0}^{l_{kg}} E(l)dl, \tag{1.19}$$

such that the spectrum scales with $E \sim l^{-1/3}$ or introducing the wavenumber $k = \frac{2\pi}{l}$, then

$$E(k) \sim E(l)\frac{dl}{dk} \sim k^{-5/3}, \tag{1.20}$$

known as the Kolmogorov spectra.

1.3 ENERGY (POWER) SPECTRA

Much scientific discourse of turbulence focuses on the scaling spectral energy density $E(k)$ with wavenumber. With various theories of turbulence (hyrdrodynamic and otherwise) providing predictions for the scaling of energy with scale based on the nature of the dynamic non-linear processes which drive the turbulence (Kolmogorov, 1941; Kraichnan, 1965; Iroshnikov, 1963; Goldreich and Sridhar, 1995; Boldyrev, 2006).

In hydrodynamic theory the difference between the velocity at the position $\mathbf{x}$ from the velocity flow at a displacement $\mathbf{r}$,

$$\Delta\mathbf{u}(\mathbf{r}) = \mathbf{u}(\mathbf{r}+\mathbf{x}) - \mathbf{u}(\mathbf{x}), \tag{1.21}$$

commonly called *increments*, are used to study the structure of a turbulent flow at a given scale $\mathbf{r}$ in position space (Davidson, 2015; Frisch, 1995). By computing increments over a set os scales corresponding to displacements $\mathbf{r}$ the statistical properties of the flow at a given scale can be computed.

In general, m-th order moments of measured increments, referred to as structure functions $S_m(\mathbf{r})$ of the scale $\mathbf{r}$ defined as

$$S_m(\mathbf{r}) = \langle(\Delta\mathbf{u}(\mathbf{r})^m\rangle = \langle(\mathbf{u}(\mathbf{r}+\mathbf{x}) - \mathbf{u}(\mathbf{x}))^m\rangle \tag{1.22}$$

are obtained as a scale dependent statistical measure of turbulence (Frisch, 1995; Schulz-DuBois and Rehberg, 1981; Hnat et al., 2003). The averaging operator $\langle ...\rangle$ can most generally represent time, ensemble, or spatial averaging. Typically, conditions are imposed ensuring the equality between different averages, formally known as ergodicity (Bendat and Piersol, 1990). The second order structure

function allows for the statistical properties of increments to be formulated as correlations over space and time:

$$S_2(\mathbf{r}) = \langle(\Delta\mathbf{u}(\mathbf{r})^2\rangle = \langle\mathbf{u}(\mathbf{x}')\mathbf{u}(\mathbf{x}')\rangle + \langle\mathbf{u}(\mathbf{x})\mathbf{u}(\mathbf{x})\rangle - 2\langle\mathbf{u}(\mathbf{x})\mathbf{u}(\mathbf{x}')\rangle, \tag{1.23}$$

where $\mathbf{x}' = \mathbf{x} + \mathbf{r}$.

For a system with homogenous turbulence, the average energy in the fluctuations is independent of position (time) then $\langle\mathbf{u}(\mathbf{x}')^2\rangle = \langle\mathbf{u}(\mathbf{x})^2\rangle = \langle\mathbf{uu}\rangle$ such that

$$S_2(\mathbf{r}) = \langle(\Delta\mathbf{u}(\mathbf{r})^2\rangle = 2(\langle\mathbf{uu}\rangle - \mathbf{R}(\mathbf{r})) = 2(\mathbf{uu} - \mathbf{R}(\mathbf{r})), \tag{1.24}$$

where $\mathbf{R}(\mathbf{r})$ is the tensor with entries $R_{ij} = \langle u_i(\mathbf{x})u_j(\mathbf{x}')\rangle$, and $\mathbf{uu}$ is the zero-lag covariance matrix $\mathbf{R}(0)$. The tensor $\mathbf{R}(\mathbf{r})$ is a function of the scale $\mathbf{r}$ which, for a zero mean flow, is equivalent to the autocorrelation function computed at the scale $\mathbf{r}$ (Schulz-DuBois and Rehberg, 1981; Bendat and Piersol, 1990). Considering the tensor of the zero lag covariance matrix, evidently the total energy

$$\mathcal{E} = R_{ii}(0) = \langle u^2\rangle \tag{1.25}$$

The autocorrelation and cross correlation functions, and the closely related auto-variance and cross variance, are common tools in time-series analysis with a number of intuitive and analytic properties.

The connection between correlation functions and the spectral density function is well established by the one-dimensional Wiener-Khinchin theorem, stating that for a stationary process, such that mean and covariances are constant with respect to time and position translations, then the energy spectra $E(k)$ and correlation function $R(r)$ are related by

$$E_{ij}(k) = \frac{1}{2\pi}\int_{\infty}^{\infty} R_{ij}e^{-ikr}dr, \tag{1.26}$$

$$R_{ij}(r) = \int_{\infty}^{\infty} E_{ij}e^{ikr}dk, \tag{1.27}$$

identified as Fourier transform pairs between the variables r and k. The proof of which can demonstrated by the use of the convolution theorem 6. Evaluating the trace of the zero-lag correlation function

$$\mathcal{E} = \langle u^2\rangle = \int_{\infty}^{\infty} E_{ii}dk \tag{1.28}$$

such that the energy spectrum is recovered as the derivative of the total energy with respect to wave number

$$E(k) = \frac{\partial\mathcal{E}}{\partial k}. \tag{1.29}$$

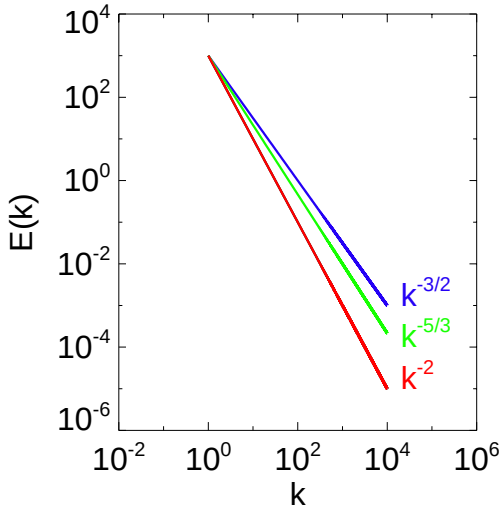

Figure 1.1: An illustration of sample power law distributions common associated with turbulence.

The energy spectra can be interpreted as the amount of energy contained within given wave number between k and $k + \Delta k$. Figure 1.1 shows an illustration of power law spectral distributions in log-log space. Common spectral indices associated with hydrodynamic and MHD turbulence are plotted -5/3, -3/2, -2.

For the second order structure function of velocity increments, which has been defined in terms of the displacement vector $\mathbf{r}$, the three dimensional analog to the Wiener-Khinchin theorem enables direct relation between the correlation tensor with respect to scale $\mathbf{r}$ and the spectral density function as a function of the vector wave number $\mathbf{k} = 2\pi/\lambda$.

$$\Phi_{ij}(\mathbf{k}) = \frac{1}{(2\pi)^3} \int_{\infty}^{\infty} R_{ij} e^{-i\mathbf{k}\cdot\mathbf{r}} d^3\mathbf{r} \tag{1.30}$$

$$R_{ij}(\mathbf{r}) = \int_{\infty}^{\infty} \Phi_{ij} e^{i\mathbf{k}\cdot\mathbf{r}} d^3\mathbf{k} \tag{1.31}$$

Again, by considering the trace of the zero-lag correlation tensor $R_{ii}(0)$

$$R_{ii}(0) = \mathcal{E} = \int_{\infty}^{\infty} \Phi_{ii} e^{i\mathbf{k}\cdot\mathbf{0}} d^3\mathbf{k} \tag{1.32}$$

$$\mathcal{E} = \int_{\infty}^{\infty} \Phi_{ii} k^2 sin(\theta) d\theta d\phi dk \tag{1.33}$$

which leads to an energy spectrum

$$\frac{\partial \mathcal{E}}{\partial k} \propto E(k) \propto \Phi_{ii} k^2. \tag{1.34}$$

For spherically symmetric turbulence the three dimensional spectral density function is simply a function of the modulus $k = |\mathbf{k}|$ and can described by one dimensional transform:

$$E_{ij}(\mathbf{k}) = \frac{1}{(2\pi)^2}\int_0^{r=\infty}\int_0^{\theta=\pi} R_{ij}e^{-ikrcos\theta}r^2 dr d(-cos\theta) \tag{1.35}$$

$$R_{ij}(\mathbf{r}) = 2\pi\int_0^{k=\infty}\int_0^{\theta=\pi} E_{ij}e^{ikrcos\theta}k^2 dk d(-cos\theta) \tag{1.36}$$

$$E_{ij}(\mathbf{k}) = \frac{1}{2(\pi)^2}\int_0^{r=\infty} R_{ij}r^2\frac{sin(kr)}{kr}dr \tag{1.37}$$

$$R_{ij}(\mathbf{r}) = 4\pi\int_0^{k=\infty} E_{ij}k^2\frac{sin(kr)}{kr}dk \tag{1.38}$$

In general, isotropy in magnetohydrodynamic turbulence is broken by the presence of a mean magnetic field.

1.4 MAGNETOHYRDRODYNAMIC TURBULENCE

Elsasser (1950) obtained a set of symmetric MHD equations by defining the variables

$$\mathbf{b} = \frac{\mathbf{B}}{\sqrt{nm\mu_0}} \tag{1.39a}$$

$$\mathbf{z}^+ = \mathbf{u} + \mathbf{b} \tag{1.39b}$$

$$\mathbf{z}^- = \mathbf{u} - \mathbf{b} \tag{1.39c}$$

and noting symmetry between the magnetic induction equation

$$\begin{aligned}\frac{\partial \mathbf{B}}{\partial t} &= \nabla\times\mathbf{u}\times\mathbf{B} + \eta\nabla^2\mathbf{B}\\ &= \mathbf{u}(\nabla\cdot\mathbf{B}) - \mathbf{B}(\nabla\cdot\mathbf{u}) + (\mathbf{B}\cdot\nabla)\mathbf{u} - (\mathbf{u}\cdot\nabla)\mathbf{B} + \eta\nabla^2\mathbf{B}\\ &= (\mathbf{B}\cdot\nabla)\mathbf{u} - (\mathbf{u}\cdot\nabla)\mathbf{B} + \eta\nabla^2\mathbf{B},\end{aligned} \tag{1.40}$$

and the momentum equation 1.7, with the Lorentz force added as $\mathbf{f} = nq(\mathbf{E} + \mathbf{u}\times\mathbf{B})$.

Neglecting the diffusive terms, and considering the total pressure $P_{tot} = p + B^2/\sqrt{2\mu_0}$ leads to two symmetric equations

$$\frac{\partial \mathbf{z}^+}{\partial t} + \mathbf{z}^-\cdot\nabla\mathbf{z}^+ = -\nabla P_{tot} \tag{1.41a}$$

$$\frac{\partial \mathbf{z}^-}{\partial t} + \mathbf{z}^+\cdot\nabla\mathbf{z}^+ = -\nabla P_{tot} \tag{1.41b}$$

Kraichnan (1965) noted that the presence of a time constant, mean magnetic field $b_0 = B_0/\sqrt{nm\mu_0}$ has the effect of breaking the apparent symmetry of the non-linear terms in Equations 1.41a and 1.41b.

$$\mathbf{z}^{+\prime} = \mathbf{z}^{+} + \mathbf{b}_0 = \mathbf{v} + (\mathbf{b} + \mathbf{b_0}) \tag{1.42a}$$
$$\mathbf{z}^{-\prime} = \mathbf{z}^{-} + \mathbf{b}_0 = \mathbf{v} - (\mathbf{b} + \mathbf{b_0}) \tag{1.42b}$$
$$\tag{1.42c}$$

$$\frac{\partial \mathbf{z}^{+}}{\partial t} - (\mathbf{b_0} \cdot \nabla)\mathbf{z}^{+} + \mathbf{z}^{-} \cdot \nabla \mathbf{z}^{+} = -\nabla(P_{tot}) \tag{1.43}$$
$$\frac{\partial \mathbf{z}^{-}}{\partial t} + (\mathbf{b_0} \cdot \nabla \mathbf{z}^{-}) + \mathbf{z}^{+} \cdot \nabla \mathbf{z}^{-} = -\nabla(P_{tot}) \tag{1.44}$$

Neglecting the non-linear and pressure terms gives rise to two wave modes which propagate linearly, and anti-parallel to each other, along the mean field:

$$\frac{\partial \mathbf{z}^{\pm}}{\partial t} = \pm(\mathbf{b_0} \cdot \nabla \mathbf{z}^{\pm}) \tag{1.45}$$

From Equation 1.43, it is evident that if either of the Elsässer fluctuations, $\mathbf{z}^{-}$or $\mathbf{z}^{+}$, are zero, then the non-linear interaction disappears, and the non-zero amplitude $\mathbf{z}^{\pm}$propagates linearly along the mean magnetic field at the Alfvén speed $v_A = b_0$

Linearization of the fluctuations and derivative operators is commonly performed by representing the fluctuations in a Fourier basis

$$\mathbf{u}(\mathbf{x}) = \sum_k \tilde{\mathbf{u}}(\mathbf{k}) e^{-i(\omega t - \mathbf{k}\cdot x)} \tag{1.46}$$

where the orthogonality of the Fourier basis is understood to enable separation of each term such that the linear operators act as

$$\frac{\partial \mathbf{u}}{\partial t} = \sum_k -i\omega \tilde{\mathbf{u}}(\mathbf{k}) e^{-i(\omega t - \mathbf{k}\cdot x)} \tag{1.47a}$$
$$\frac{\partial}{\partial t} \rightarrow -i\omega \tag{1.47b}$$
$$\nabla \rightarrow +i\mathbf{k} \tag{1.47c}$$

Applying the Fourier decomposition to the linear portion of the momentum equation gives

$$-i\omega \mathbf{z}^{\pm} = \pm \mathbf{b_0} \cdot i\mathbf{k} \mathbf{z}^{\pm} \tag{1.48}$$

which are identified as Alfvén waves (Alfvén, 1942).

Kraichnan (1965) argues that because the non-linear term exists only between oppositely propagating waves, their interactions are weakened because the mean field transports the two modes away from each-other in the *linear time* $\tau_l = (kb_0)^{-1}$. Whereas distortions to the $\mathbf{z}^{\pm}$fluctuations occur on the dynamical, or *non-linear time* $\tau_{nl} = (kb_k)^{-1}$, where b_k is the fluctuation amplitude at wave number k. Kraichnan argues that the non linear interactions are weak such that $\tau_l << \tau_{nl}$, and that the resulting energy transfer rate at a given scale ϵ is limited by the linear time and thus $\epsilon \propto \tau_l$.

Using the Kolmogorov (1941) assumptions of a scale independent energy transfer rate ϵ and the existence of scale locality Kraichnan (1965) makes the dimensional argument that

$$\epsilon \left[\frac{m^2}{s^3} \right] = (kb_0)^{-1} {b_k}^4 k^2 \left[s \frac{m^4}{s^4} \frac{1}{m^2} \right] \tag{1.49}$$

At a scale k the fluctuation amplitude

$$b_k^2 = \int E(k) dk \tag{1.50}$$

where for a power-law $E(k)$ then $b_k = \sqrt{E(k)k}$, resulting in the dimensionality

$$E(k) \sim \epsilon^{1/2} k^{-3/2}. \tag{1.51}$$

Iroshnikov (1963) separately came to a -3/2 spectra in the context of weak magnetized turbulence. The framework of Iroshnikov and and Kraichnan (IK) turbulence is simply understood as a weakening of the Alfvénic non-linear interactions relative to the hydrodynamic case, resulting in the increase in time required to transfer energy from one scale to the next (Dobrowolny et al., 1980b; Schekochihin and Cowley, 2007). For a weak interaction, the fluctuations $\mathbf{z}^{\pm}$ are weakly perturbed, such that the turbulent decoherence time can be thought of as a stochastic process where in one linear interaction time, τ_l there deformation to the fluctuation of order $\delta\mathbf{z}^{\pm}$. The statistical number N of stochastic deformations to de-correlate the fluctuation is given by $\sqrt{N}\delta\mathbf{z}^{\pm} = \mathbf{z}^{\pm}$. Such that the time to de-correlate a fluctuation transfer it to another scale is, $\tau_{DC} \sim N\tau_l$.

The ordering of the fluctuation perturbation $\delta\mathbf{z}^{\pm}/\mathbf{z}^{\pm} \sim \mathbf{z}^{\pm}/b_0$ leads to an energy transfer time

$$\tau_{DC} = \frac{b_0}{z^2 k} \tag{1.52}$$

which is longer than the hydrodynamic Kolmogorov dynamic time by

$$\frac{\tau_{DC}}{\tau_{kg}} = \frac{b_0}{z}$$

(Dobrowolny et al., 1980b; Boldyrev, 2006).

The energy transfer rate

$$\epsilon = \frac{z^2}{\tau_{DC}} = \frac{z^4 k}{b_0} \tag{1.53}$$

is again constant and local to the scale k, such that the total energy

$$z^2 = \left(\frac{\epsilon b_0}{k}\right)^{1/2} \sim \int E(k) dk \tag{1.54}$$

leads to an energy density of

$$E(k) \sim \epsilon^{1/2} k^{-3/2}. \tag{1.55}$$

1.5 EARLY OBSERVATIONS OF ANISOTROPIC TURBULENCE

In addition to the identification of power-law spectra in solar wind fluctuations, measurements evidence demonstrating the stationarity of the solar wind, as well as the observed invariance of magnetic and cross helicity consistent with theoretical predictions for incompressible turbulence gradually led to the acceptance of the solar wind as a turbulent medium (Matthaeus and Goldstein, 1982a,b; Schwenn and Marsch, 1991). The *Helios-1* and *Helios-2* satellites launched, respectively in 1974 and 1976, into elliptical orbits between 0.3 and 0.7 AU were outfitted with *in-situ* payloads to continuously survey the solar wind. Observations from *Helios* allowed for in-detailed studies of solar wind turbulence which revealed significant deviations from the relatively simple theory of (Kraichnan, 1965) for isotropic MHD turbulence.

Denskat and Neubauer (1982) and Bavassano et al. (1982) performed a radial surveys of the solar wind turbulent spectra demonstrating the steepening of the turbulent fluctuations to -5/3 spectra at 1AU, with shallower spectra in the inner heliosphere. Additional work demonstrated that the distribution of wave vectors and anisotropy deviated significantly from what would be expected from adiabatic propagation (Barnes, 1992; Bavassano et al., 1982a). Theoretical studies attempting to explain the deviations from from the -3/2 slope were attempted by various authors (Grappin et al., 1982; Tu et al., 1984). Matthaeus and Goldstein (1982a) explored the nature of cross and magnetic helicity in the solar wind turbulence using Voyager data and found that the -5/3 spectra best explained their observations; in their conclusions pointing out that the minimum-variance analysis of the solar wind fluctuations, e.g. Belcher and Davis (1971); Barnes (1981); Dobrowolny et al. (1980a); Bavassano et al. (1982b), suggest anisotropy in the solar wind inconsistent with the assumptions of isotropy made by Kolmogorov (1941) and Kraichnan (1965). Observationally, Higdon (1984) suggested that the interstellar medium exhibits anisotropic density fluctuations. Numerically, Shebalin et al. (1983) demonstrated anisotropic energy transfer which was inhibited along the parallel direction. The argument for inhibited energy

transfer along the mean field is made evident by considering a three wave interaction given by the resonance conditions (i.e. conservation of energy and momentum) as

$$\mathbf{k}_1 + \mathbf{k}_2 = \mathbf{k}_3 \tag{1.56a}$$
$$\omega(\mathbf{k}_1) + \omega(\mathbf{k}_2) = \omega(\mathbf{k}_3). \tag{1.56b}$$

For interacting Alfvén waves with dispersion $\omega = \mathbf{k} \cdot b_0$ and forward (parallel mean field) and backwards (anti parallel) propagation for the respective $\mathbf{k}_1$ and $\mathbf{k}_2$ fluctuations, it is possible to decompose the resonant conditions parallel and perpendicular to the field

$$k_{1\perp} + k_{2\perp} = k_{3\perp} \tag{1.57a}$$
$$k_{1\parallel} + k_{2\parallel} = k_{3\parallel} \tag{1.57b}$$
$$k_{1\parallel} b_0 - k_{2\parallel} b_0 = \pm k_{3\parallel} b_0 \tag{1.57c}$$

which is only met if either $k_{1\parallel}$ or $k_{2\parallel}$ is zero, such that there is no interaction between fluctuations with different parallel wave numbers, inhibiting energy transfer along the mean field (Shebalin et al., 1983). However, no constraint on $k_\perp$ is imposed such that the interaction can lead to higher wave numbers at smaller scales perpendicular to the mean field.

Matthaeus et al. (1990) used two-point correlation functions to show the anisotropy of the wind could be consistent with two different components, slab like parallel fluctuations, with two dimensional non propagating turbulence with large perpendicular wave numbers $k_\perp$ and no $k_\parallel$ existing in superposition (Bieber et al., 1996). The anisotropy implied by these observations is in stark contrast to the assumption of isotropy assumed in both Kolomogorov and Iroshnikov-Kraichnan types of turbulence.

1.6 CRITICAL BALANCE

Goldreich and Sridhar (1995) develop theory of incompressible turbulence with *critically balanced* linear and non-linear time-scales which simultaneously describes the deviation from the -3/2 index predicted by Iroshnikov (1963); Kraichnan (1965) as well as the observed anisotropy of solar wind fluctuations. In both Kolmogorov and Iroshnikov-Kraichnan turbulence, isotropy in the wavenumber k is assumed such that the linear time τ_l=$1/kb_0$ and non linear time τ_{nl}=$1/kb_0$ depend on the same k. Equation 1.43 shows that the gradient in the linear term $\mathbf{b}_0 \cdot \nabla \mathbf{z}^\pm$ is projected parallel to the mean field direction such that the appropriate linearization gives $\mathbf{b}_0 \cdot \nabla \sim b_0 k_\parallel$. For the non linear term $\mathbf{z}^\pm \cdot \nabla \mathbf{z}^\mp$ the gradient is projected along the perpendicular polarized, i. e.Alfvénic, fluctuation $\mathbf{z}^\pm$ such that $\mathbf{z}^\pm \cdot \nabla \sim \mathbf{z}^\pm k_\perp$.

Goldreich and Sridhar (1995) conjecture that the linear and non-linear time scales are equal (critically balanced)

$$z^{\pm}k_{\perp} \sim b_0 k_{\parallel}. \tag{1.58}$$

For a constant energy flux $\epsilon = {z^{\pm}}^2/\tau$ critical balance allows the turbulent cascade time τ is equal to both τ_{nl} and τ_l. At the largest inertial scales L the energy transfer rate is equal to

$$\epsilon = b_0^2/\tau_L = b_0^3/L. \tag{1.59}$$

Following the assumptions of constant energy flux through the inertial scales leads to the equation

$$\epsilon \sim \frac{z^2}{\tau} \sim \frac{b_0 k_{\parallel}/k_{\perp}}{(b_0 k_{\parallel})^{-1}} \tag{1.60}$$

the assumption of critical balance leads to the condition on wavenumber anisotropy

$$k_{\parallel} \sim k_{\perp}^{2/3} L^{-1/3} \tag{1.61}$$

such that the fluctuation amplitude at a given scale is given by

$$z \sim b_0 (k_{\perp} L)^{-1/3}. \tag{1.62}$$

Defining an anisotropic energy spectrum $E(k_{\parallel}, k_{\perp})$ the fluctuation amplitude at a scale is given by

$$z^2 \sim k_{\perp}^{-2/3} \sim k_{\parallel}^{-1} \sim \int_k^{\infty} E(k_{\parallel}, k_{\perp}) k_{\perp} dk_{\perp} dk_{\parallel} \tag{1.63}$$

for which the individual parallel and perpendicular energy spectrum can be individually defined:

$$k_{\parallel}^{-1} = \int_{k_{\parallel}}^{\infty} E(k_{\parallel}) dk_{\parallel} \tag{1.64}$$

$$k_{\perp}^{-2/3} = \int_{k_{\perp}}^{\infty} E(k_{\perp}) dk_{\perp} \tag{1.65}$$

Which lead to the wavenumber anisotropy associated with critical balance

$$E(k_{\parallel}) \sim k_{\parallel}^{-2} \tag{1.66}$$

$$E(k_{\perp}) \sim k_{\perp}^{-5/3} \tag{1.67}$$

1.7 DYNAMIC ALIGNMENT & 3D ANISOTROPY BOLDYREV

Though observations of the solar wind reveal two dimensional anisotropy of the solar wind fluctuation consistent with critical balance, e.g. Horbury et al. (2008); Podesta et al. (2009); Forman et al. (2011), there are a number persistence characteristic differences between spacecraft measurements and the Goldreich and Sridhar (1995) predictions. For instance, while observations of magnetic energy spectra suggest a -5/3 scaling, numerical simulations of the solar wind have suggested that the presence of -3/2 distributions are persistent in the solar wind energy spectra Maron and Goldreich (2001); Müller and Grappin (2005). Additionally, a number of authors have empirically demonstrated that intermittent features, not captured by Goldreich and Sridhar (1995), affect the spectral index associated with solar wind fluctuations (Roberts and Goldstein, 1987; Li et al., 2011; Salem et al., 2009; Bowen et al., 2018b). The specific effects of intermittency on spectral index are discussed in detail in Chapter 2. Additionally, Goldreich and Sridhar (1995) does not attempt to resolve differences between the magnetic and velocity fluctuations in magnetized turbulence; however, it has been shown that a -3/2 scaling is present in the velocity fluctuations, while a -5/3 scaling is common in the magnetic field fluctuations Podesta et al. (2007); Tessein et al. (2009); Salem et al. (2009); Chen et al. (2013); Bowen et al. (2018b).

Previous to Goldreich and Sridhar (1995) theory of critical balance, the relationship between turbulent velocity and magnetic field fluctuations in the solar wind had been studied in detail by Dobrowolny et al. (1980a); Grappin et al. (1982); Matthaeus and Goldstein (1982a). A particular aspect of MHD turbulence arises in the presence of perfectly correlated state where $\mathbf{u} \sim \pm\mathbf{b}$ such that the normalized cross helicity $\sigma_c = \pm 1$:

$$\sigma_c = \frac{2\langle \mathbf{b}\cdot\mathbf{u}\rangle}{\langle \mathbf{u}^2\rangle + \langle \mathbf{b}^2\rangle} = \frac{\langle \mathbf{z}^{+2}\rangle - \langle \mathbf{z}^{-2}\rangle}{\langle \mathbf{z}^{+2}\rangle + \langle \mathbf{z}^{-2}\rangle} = \pm 1. \tag{1.68}$$

In a correlated state, the fluctuations are described entirely by either $\mathbf{z}^+$ or $\mathbf{z}^-$ such that the non-linear interaction between the Elsässer fluctuations must vanish. The existence of turbulence with high cross helicity, occasionally referred to as Alfvénic turbulence, has been reported widely in the solar wind (Belcher and Davis, 1971).

The tendency for initially asymmetric distributions of $\mathbf{z}^\pm$ to relax to an Alfvénic, high cross helicity state was first suggested by Dobrowolny et al. (1980b) with subsequent work by Grappin et al. (1982) exploring the process by dynamic alignment, in which the orientations of $\mathbf{b}$ and $\mathbf{v}$ become preferentially aligned due to turbulent interactions. Both the correlation between $\langle \mathbf{b}\cdot\mathbf{u}\rangle$ and the total energy $\langle \mathbf{v}^2\rangle + \langle \mathbf{b}^2\rangle$ can be shown to be conserved by the non-linear MHD equations (Matthaeus and Goldstein, 1982a). Based on an a statistical dissipative framework, known as eddy-damped quasi normal Markovian (EDQNM) closure, Grappin et al. (1982) suggest that rate of energy dissipation (viscosity and resistivity) removes energy from the $\mathbf{z}^\pm$ fields fluctuations at roughly equal rates, such that an initial imbalance between $\mathbf{z}^\pm$ leads to a relaxed state with only a single species of $\mathbf{z}^\pm$ propagating via linear interactions.

Boldyrev (2005, 2006) suggest that the dynamic alignment between velocity and magnetic field fluctuations weakens the non-linear interaction time relative to Goldreich and Sridhar (1995). Boldyrev (2005) make the heuristic argument that the Alfvénic perpendicular non-linear interactions are of order

$$\mathbf{z}^{\mp} \cdot \nabla \mathbf{z}^{\pm} = (z^2 k_\perp)(z/b_0)^\alpha \tag{1.69}$$

the exponent α effectively parameterizes the strength of the non-linear interaction such that $\alpha = 0$ for strong turbulence, i.e. Goldreich and Sridhar (1995) and $\alpha = 1$ for weak turbulence, i.e. Iroshnikov (1963); Kraichnan (1965).

The perpendicular turbulent non-linear time for dynamic alignment is dimensionally

$$\tau_{DA}^{-1} \sim (z k_\perp)(z/b_0)^\alpha \tag{1.70}$$

and critical balance is again presumed such that the parallel fluctuations de-correlate with time

$$\tau_{DA}^{-1} \sim (k_\parallel b_0). \tag{1.71}$$

Conserving the energy flux through dynamically aligned scales gives

$$\frac{z^2}{\tau_{DA}} \sim \epsilon \tag{1.72}$$

$$z \sim k_\perp^{\frac{-1}{3+\alpha}} \tag{1.73}$$

while the parallel wave numbers scale as

$$k_\parallel \sim k_\perp^{\frac{2}{3+\alpha}} \tag{1.74}$$

The wave number scalings for the energy spectra can be obtained as

$$\langle \mathcal{E} \rangle \sim \langle z^2 \rangle \sim k_\perp^{\frac{-2}{3+\alpha}} \int E(k_\perp) dk_\perp \tag{1.75}$$

$$E(k_\perp) = k_\perp^{\frac{-5-\alpha}{3+\alpha}} \tag{1.76}$$

$$E(k_\parallel) = E(k_\perp) \frac{dk_\perp}{dk_\parallel} \sim k_\parallel^{-2} \tag{1.77}$$

Boldyrev (2006) suggest that the magnetic and velocity fluctuations are aligned to within a small angle, θ, which is just large enough to preserve the non-linear interactions needed to ensure a constant energy flux ϵ. For alignment of fluctuations within small angle θ, the non-linear interaction is smaller than the critical balance dynamic time by

$$\mathbf{z}^{\pm} \cdot \nabla \mathbf{z}^{\mp} \sim z^2 \theta k_\perp. \tag{1.78}$$

The dynamic alignment timescale is then

$$\tau_{DA} \sim \frac{1}{k_\parallel b_0} \sim \frac{1}{k_\perp z\theta} \tag{1.79}$$

with a parallel scale $k_\parallel \sim k_\perp \frac{z\theta}{b_0}$.

The scale independent energy flux $\epsilon \sim z^2 \tau_{DA}$ leads to a scaling

$$z \sim \left(\frac{\epsilon}{k_\perp \theta}\right)^{1/3}. \tag{1.80}$$

The assumption of a preferred alignment between $\mathbf{b}$ and $\mathbf{u}$ creates a three-dimensional anisotropy not-present in the Goldreich and Sridhar (1995) theory. In the linear time

$$\tau_\parallel \sim \tau_{DA} \sim (k_\parallel b_0)^{-1} \tag{1.81}$$

the perpendicular fluctuation displaces the background field by a distance $\xi \sim z\tau_\parallel \sim z\frac{1}{zk_\perp\theta}$ such that the ratio in perpendicular wave numbers

$$k_\xi / k_\perp \sim \theta \tag{1.82}$$

$$k_\xi \ll k_\perp. \tag{1.83}$$

The anisotropy in the plane of the mean field suggests that as fluctuations cascade to smaller scales, the anisotropy grows between the two perpendicular directions. For z and $k_\perp$ to both obey self similar distributions power laws, the constraint $z \sim \left(\frac{\epsilon}{k_\perp\theta}\right)^{1/3}$ demands that θ is either a constant function of scale, or itself a power law. By parameterizing the scaling of $\theta(k_\perp) \sim k_\perp^{\frac{-\alpha}{3+\alpha}}$, Boldyrev (2006) shows that the power law scalings follow as

$$z \sim k_\perp^{\frac{-1}{3+\alpha}} \tag{1.84}$$

$$k_\xi \sim k_\perp^{\frac{-3}{3+\alpha}} \tag{1.85}$$

$$k_\parallel \sim k_\perp^{\frac{-2}{3+\alpha}} \tag{1.86}$$

Boldyrev (2006) argues that due to the conservation of cross helicity, e.g. Matthaeus and Goldstein (1982a), the alignment should be maximized at all scales, which determines α though minimizing the total angular alignment angles between the fluctuations.

$$\theta \sim k_{\xi}/k_{\perp} \sim k_{\perp}^{\frac{-\alpha}{3+\alpha}} \tag{1.87}$$

$$\phi \sim k_{\parallel}/k_{\xi} \sim k_{\perp}^{\frac{-1}{3+\alpha}} \tag{1.88}$$

The small fluctuations in θ and ϕ can be shown to minimize the total alignment when $\theta = \phi$ equivalent to $\alpha = 1$ which, from Boldyrev (2005) leads to a

$$E(k_{\perp}) = k_{\perp}^{-3/2} \tag{1.89}$$

energy spectra.

These theoretic results have helped explain the presence of the -3/2 spectra observed in the numerical models of plasmas, as well as the velocity fluctuations and (non intermittent) magnetic fields of the solar wind. Additionally the development of the 3-dimensional anisotropy has played a key role in explaining the development of current sheets at small scales which correspond to observed dissipation and intermittency (Matthaeus et al., 2015; Mallet et al., 2016, 2017).

1.8 INTERMITTENCY

The theoretical frameworks of turbulence as suggested by Kolmogorov (1941); Iroshnikov (1963); Kraichnan (1965); Goldreich and Sridhar (1995); Boldyrev (2006) are based on the common thread a self similar inertial range with a power law spectral distribution and a conserved energy flux through inertial scales. In reality, a true power law distribution for the energy spectra over all scales is impossible to obtain, as the total energy

$$\mathcal{E} = \int_0^{\infty} Ck^{-\alpha} dk = Ck^{1-\alpha}\Big|_0^{\infty} \tag{1.90}$$

must necessarily diverge at small k for $\alpha > 1$ and large k for $\alpha < 1$ (Frisch, 1995).

By considering the one dimensional Wiener-Khinchin theorem, the relationship between the one dimensional energy spectra and structure function is demonstrated as

$$S_2(r) = 2(\langle \delta z(x)^2 \rangle - \langle \delta z(x+r)\delta z(x) \rangle) = 2\mathcal{E} - 2\int_x \delta z(x)\delta z(x+r)dx = 2\int E(k)(1-e^{ikr})dk \tag{1.91}$$

Assuming a power law energy spectra $E(k) = Ck^{-\alpha}$ and symmetry in positive and negative wavenumber due to homogeneity, a simple integration by parts can be used to demonstrate that the structure function converges for $1 < \alpha < 3$, with the scaling of the structure function $S_2(r) \propto r^{\alpha-1}$.

For increments which scale as $\delta z \sim l^{\beta}$, self similarity implies the scaling relation $\frac{\delta z(\lambda l)}{\delta z(l)} = \lambda^{p}$ where p is known as the scaling exponent. For Kolmogorov like turbulence, the dimensional relationship $\epsilon \sim \delta z^3/l$ with the assumption of constant energy flux immediately gives a scaling exponent as $p = 1/3$.

The scaling of higher order structure functions is seen to be

$$S_m(r) = \langle \delta z(r)^m \rangle \sim \langle l^p (r)^m \rangle \sim l^{pm}. \tag{1.92}$$

The scaling exponents of the structure function, are a linear function of p with respect to the order of the structure function m (Dudok de Wit et al., 2013).

By measuring higher order structure functions, deviations from linear scaling are observed in both hydrodynamic and MHD turbulence (Frisch, 1995; Tu and Marsch, 1995; Veltri and Mangeney, 1999; Hnat et al., 2003; Salem et al., 2009). However, the measurement of high order structure functions becomes difficult as the accurate determination of the higher order moments depends signfiicantly on the presence of outliers (Frisch, 1995; Dudok de Wit, 2004). A common measure of intermittency is the kurtosis, $\kappa(\delta z) = \frac{\langle \delta z^4 \rangle}{\langle \delta z^2 \rangle^2}$ which clearly relates to the 4th order structure function. For a self-similar process the kurtosis is scale dependent (Frisch, 1995; Horbury and Balogh, 1997; Burlaga, 2001; Matthaeus et al., 2015). Observationally, κ is an increasing function of scale, which indicates the presence of processes which break the self-similarity hypothesis.

In MHD turbulence it known that the magnetic field exhibits enhanced intermittency over the velocity fluctuations, e. g. Biskamp (2003); Bruno et al. (2003); Salem et al. (2009); Bruno and Carbone (2013b), which tend to occur in the form of current sheets (Maron and Goldreich, 2001; Mininni and Pouquet, 2009; Li et al., 2011; Chandran et al., 2015; Mallet et al., 2016, 2017). Recent observations and simulations of current sheets suggest that they are likely associated with dissipative processes through heating through magnetic reconnection (Dmitruk et al., 2004; Osman et al., 2010; Matthaeus et al., 2015; Mallet et al., 2017). Whether such magnetically dominated intermittent structures are generated by turbulence itself, or are propagated from within the inner heliosphere is an open question which will be discussed in detail in Chapter 2.

The deviations from self-similar turbulence as highlighted by intermittency serve to highlight that while observed spectral energy distributions are consistent with predictions from theory, a wide range of phenomena are observed which suggest the existence of dynamic non-linear processes outside the theoretical framework of a constant-energy flux cascade of Alfvénic fluctuations. Another such example which complicates these theories of incompressible turbulence is the observation of compressive fluctuations in the solar wind.

1.9 COMPRESSIBLE TURBULENCE AND SCALAR FLUCTUATIONS

Observations of density fluctuations in the interstellar medium by Armstrong and Rickett (1981) provided evidence for large scale turbulence in the interstellar medium, though at the time little theory regarding the nature of compressible turbulence had been developed. Ambiguities regardingthe coupling

between density fluctuations with incompressible hydrodynamic turbulence led Higdon (1984) to develop a theory of the mixing of compressive entropy (non-propagating) fluctuations in the presence of a strong mean magnetic field, arguing that compressible fluctuations should follow the magnetic spectral density, which is anisotropic with respect to the mean field. Montgomery et al. (1987) develop a theory of "pseudosound" again predicting the agreement of the density spectra with the spectral density of the magnetic and velocity energy. Using the observations of anisotropy associated with critical balance, Schekochihin and Cowley (2007) demonstrate the decoupling of the entropy and slow-mode waves from the Alfvénic spectrum in the limit of reduced MHD (RMHD).

The equations of reduced MHD, first derived by Strauss (1976) to simply computations for fusion plasma in tokamaks, amounting to an ordering in the perturbed quantities with a small quantity ϵ (not equal to the energy cascade rate)

$$\frac{\rho_1}{\rho_0} \sim \frac{P_1}{P_0} \sim \frac{b_\perp}{b_0} \sim \frac{b_\parallel}{b_0} \sim \frac{u_\perp}{b_0} \sim \frac{u_\parallel}{b_0} \sim \epsilon \tag{1.93}$$

Additionally, the anisotropy associated with critical balance leads to the ordering in wave number

$$\frac{k_\parallel}{k_\perp} \sim \epsilon \tag{1.94}$$

and frequency $\omega \sim k_\parallel b_0$.

Following e.g. Schekochihin and Cowley (2007); Schekochihin et al. (2009) the decoupling of compressive fluctuations from Alfvénic modes is performed by considering the relative order of the nonlinear interactions between various fluctuations.

For the continuity equation

$$\frac{d\rho}{dt} = -\rho \nabla \cdot \mathbf{u} \tag{1.95}$$

the lowest order term on the left-side ($i\omega\rho_1$) is order ϵ^2, while the perpendicular component of the right side ($\rho_0 \nabla_\perp \cdot \mathbf{u}_\perp$) is of order ϵ such that the divergence of the perpendicular velocity fluctuations is to first order

$$\nabla_\perp \cdot \mathbf{u}_\perp = 0 \tag{1.96}$$

$$\nabla_\perp \cdot \mathbf{b}_\perp = 0 \tag{1.97}$$

Accordingly, to first order the RMHD equations are similar to incompressible turbulence. As the perpendicular magnetic and velocity fluctuations are divergenceless, the stream functions can be defined as

$$\mathbf{u}_\perp = \nabla_\perp \times \Phi \tag{1.98}$$
$$\mathbf{b}_\perp = \nabla_\perp \times \Psi \tag{1.99}$$

with $\Psi = [0, 0, \psi]$.

Taking the perpendicular portion of the induction equation and keeping only terms with order ϵ^2 gives,

$$\frac{\partial \mathbf{B}}{\partial t} = -\mathbf{B}(\nabla \cdot \mathbf{u}) + (\mathbf{B} \cdot \nabla)\mathbf{u} - (\mathbf{u} \cdot \nabla)\mathbf{B} \tag{1.100}$$
$$\frac{\partial \mathbf{b}_\perp}{\partial t} = (\mathbf{b}_\perp \cdot \nabla_\perp)\mathbf{u}_\perp + (\mathbf{b_0} \cdot \nabla_\parallel)\mathbf{u}_\perp - (\mathbf{u}_\perp \cdot \nabla_\perp)\mathbf{b}_\perp \tag{1.101}$$
$$\frac{\partial \mathbf{b}_\perp}{\partial t} = \nabla_\perp \times (\mathbf{v}_\perp \times \mathbf{b}_\perp) + (\mathbf{b_0} \cdot \nabla_\parallel)\mathbf{u}_\perp \tag{1.102}$$
$$\frac{\partial (\nabla \times \mathbf{\Psi})}{\partial t} = \nabla_\perp \times ((\nabla \times \mathbf{\Phi}) \times (\nabla \times \mathbf{\Psi})) + (\mathbf{b_0} \cdot \nabla_\parallel)(\nabla \times \mathbf{\Phi}) \tag{1.103}$$

Commuting the derivatives, and considering only the parallel component of the stream functions gives:

$$\frac{\partial \psi}{\partial t} = (\nabla \times \Phi) \times (\nabla \times \mathbf{\Psi}) + (\mathbf{b_0} \cdot \nabla_\parallel)\phi \tag{1.104}$$

using the perpendicular portion of the momentum equation, a similar evolution function can be solved for the stream function ϕ. Together the equations for ψ and ϕ lead to a description of Alfvénic fluctuations and turbulence.

By considering the parallel component of the induction, momentum, and continuity equations, the compressive modes are shown to be decoupled, with non-linear interactions only occurring with the perpendicular Alfvénic fluctuations.

To first order in ϵ, the momentum equation

$$\frac{\partial \mathbf{u}}{\partial t} + (\mathbf{u} \cdot \nabla)\mathbf{u} = -\nabla(p + \frac{B^2}{2\mu_0}) + \mathbf{b} \cdot \nabla \mathbf{b} \tag{1.105}$$
$$0 = -\nabla_\perp (p_1 + \frac{1}{\mu_0} b_0 b_\parallel) \tag{1.106}$$

gives pressure balance such that

$$\frac{b_\parallel}{b_0} + \beta \frac{\rho_1}{\rho_0} = 0, \tag{1.107}$$

with

$$\beta = \frac{\gamma p_0}{\rho_0 b_0} \tag{1.108}$$

The continuity and parallel portion of the induction equation, along with the first order pressure balance term can be solved for the parallel field fluctuation amplitude an order ϵ^2 quantity.

$$\frac{\partial}{\partial t}\rho_1 = -(u_\perp \nabla_\perp)\rho_1 + -\rho_0(\nabla_\parallel u_\parallel) \tag{1.109}$$

$$\frac{\partial}{\partial t}b_\parallel = -(u_\perp \nabla_\perp)\, b_\parallel + (b_\perp \nabla_\perp)u_\parallel - b_0(\nabla_\parallel u_\parallel) + (b_0 \nabla_\parallel)u_\parallel \tag{1.110}$$

$$\tag{1.111}$$

which can be solved to give

$$\left[\frac{\partial}{\partial t} + (u_\perp \nabla_\perp)\right]\rho_1 = -\frac{\rho_0}{b_0}\frac{1}{1+\beta}[(b_0 \nabla_\parallel)u_\parallel + (b_\perp \nabla_\perp)u_\parallel] \tag{1.112}$$

$$\left[\frac{\partial}{\partial t} + (u_\perp \nabla_\perp)\right]b_\parallel = \frac{\beta}{1+\beta}[(b_0 \nabla_\parallel)u_\parallel + (b_\perp \nabla_\perp)u_\parallel]. \tag{1.113}$$

The second order expansion from the he parallel portion of of the velocity fluctuations can be solved for from the momentum equation (Equation 1.105):

$$\frac{\partial u_\parallel}{\partial t} + (\mathbf{u}_\perp \cdot \nabla_\perp)u_\parallel = -\nabla_\parallel(p + \frac{B^2}{2\mu_0}) + b_0 \nabla_\parallel b_\parallel + b_\perp \nabla_\perp b_\parallel \tag{1.114}$$

$$\left[\frac{\partial}{\partial t} + (u_\perp \nabla_\perp)\right]u_\parallel = b_0 \nabla_\parallel b_\parallel + b_\perp \nabla_\perp b_\parallel. \tag{1.115}$$

where the pressure term can be neglected due to the 1st-order pressure balance.

defining $\alpha = \frac{\beta}{\beta+1}$and using the notation for the convective derivative and propagation terms as

$$D = \frac{\partial u_\parallel}{\partial t} + (\mathbf{u}_\perp \cdot \nabla_\perp) \tag{1.116}$$

$$P = b_0 \nabla_\parallel + b_\perp \nabla_\perp \tag{1.117}$$

The compressible analog to the Elsässer variables can be defined through determining the solutions to the equations

$$\begin{pmatrix} D & -P \\ -\alpha P & D \end{pmatrix}\begin{pmatrix} u_\parallel \\ b_\parallel \end{pmatrix} = \mathbf{0} \tag{1.118}$$

It is evident that $D = \pm\sqrt{\alpha}P$, giving solutions $u_\parallel = \pm b_\parallel/\sqrt{\alpha}$ such that the equation of motion for the compressive fluctuations,

$$w^\pm = u_\parallel \pm b_\parallel/\sqrt{\alpha} = u_\parallel \pm b_\parallel(1+1/\beta)^{1/2}, \tag{1.119}$$

follows as

$$\frac{\partial w^\pm}{\partial t} + (\mathbf{u}_\perp \cdot \nabla_\perp) w^\pm = \pm\alpha^{1/2}(b_0\nabla_\parallel + \mathbf{b}_\perp \cdot \nabla_\perp) w^\pm \tag{1.120}$$

$$\frac{\partial w^\pm}{\partial t} + (\mathbf{z}^+ + \mathbf{z}^-)\cdot\nabla_\perp w^\pm = \pm\left(\frac{1}{1+b_0^2/c_s^2}\right)^{1/2}\left[b_0\nabla_\parallel w^\pm + (\mathbf{z}^- - \mathbf{z}^-)\nabla_\perp w^\pm\right] \tag{1.121}$$

Equations 1.112, 1.114 and 1.121 show that the lowest order non-linear terms for compressive fluctuations are due to interactions with the perpendicular fluctuations; non-linear interactions between parallel fluctuations requires retaining higher order ϵ interactions (Chen, 2016). Accordingly, the turbulence associated with compressible fluctuations is driven by interactions with the non-compressive fluctuations. Simultaneously, it's evident that the lowest order non-linear interactions for the perpendicular fluctuations do not involve compressive modes such that the incompressible turbulence is unaffected by the compressible component. Additionally, Equation 1.121 shows that the incompressible fluctuations are decoupled from each other, such that scattering by perpendicular gradients does not exchange energy between incompressible modes. Because, to lowest order, non-linear interactions are coupled to the incompressible turbulence, the spectra of compressible fluctuations is expected to be identical to that of the incompressible fluctuations. In Chapter 3 the observational signatures of compressible fluctuations will be explored in detail.

Additionally, the source of compressive fluctuations in the solar wind has not yet been determined. Whether such fluctuations are generated in the inner-heliosphere and are propagated out or are continuously injected into the solar wind through instabilities or stream interface regions is not yet clear. Additionally, the strong collisionless damping of such fluctuations, as predicted by Barnes (1966) proves to be another puzzle. In Chapter 4 the possibility of parametric instabilities associated with finite amplitude effects is explored as a source of the compressions in the solar wind.

1.10 OBSERVING TURBULENCE IN THE SOLAR WIND

By considering the Vlasov (and the derived MHD) equation, the *in-situ* instrumentation needed to observe dynamic turbulent processes in the solar wind becomes quite evident. A complete specification of kinetic phase space dynamics is given by the specification of the distribution function $f(\mathbf{r}, \mathbf{v}, t)$ as well as the local electromagnetic forces acting on the distribution. Measurements of particle distributions (electrons, protons, alphas) on spacecraft are typically made with electrostatic analyzers (ESAs), and Faraday cups, Lin et al. (1995); Ogilvie et al. (1995); Kasper et al. (2016); Wüest et al. (2007); Kasper

et al. (2016). Low frequency magnetic fields are measured by flux-gate or atomic magnetometers (Ness et al., 1971; Acuña, 2002; Primdahl, 1979). While higher frequency magnetic fields are measured using inductive search coils (MacIntyre, 1980; Prance et al., 2003; Robert et al., 2014; Roux et al., 2008). Electric field experiments can measure both radio frequencies and low frequency electric fields associated with MHD and kinetic waves as well as the local convected field of ideal MHD, $\mathbf{E} = -\mathbf{u} \times \mathbf{B}$ (Bougeret et al., 1995; Bonnell et al., 2009; Ergun et al., 2016; Bale et al., 2016a). Additionally, the electric field experiments can provide information regarding macroscopic plasma properties (density and temperature) through observations of signatures of electron plasma frequency as well as the random thermal variations of the local electron population (Meyer-Vernet and Perche, 1989; Issautier et al., 2001).

1.10.1 SINGLE POINT MEASUREMENTS & TAYLOR HYPOTHESIS

Observations of the solar wind via *in-situ* satellite instrumentation are typically limited to single point measurements. Recently, multiple spacecraft missions such as, Cluster, THEMIS, and Magnetospheric Multiscale Mission have expanded outside the single point paradigm, focusing on Earth's magnetospheric structure, and have provided three dimensional measurements of structure and time evolution on millisecond scales (Escoubet et al., 1997; Angelopoulos, 2008; Burch et al., 2016). Though multi-point measurements greatly improve observations spatiotemporal variability in the solar wind, in principle the development of multiple spacecraft is often cost prohibitive.

There is an inherent ambiguity associated with single point *in-situ* measurements from spacecraft associated with distinguishing the time evolution in the local plasma from spatial gradients. It is instructive to consider, from an order of magnitude perspective, typical parameters of the solar wind observed at 1 AU, the proton temperature T_p, density n_p, magnetic field strength B, and wind speed v_{sw}:

$$T_p \sim T_e \sim 10 \text{ eV} \tag{1.122}$$

$$n_p \sim n_e \sim 10 \text{ cm}^{-3} \tag{1.123}$$

$$B \sim 10 \text{ nT}^{-3} \tag{1.124}$$

$$v_{sw} \sim 300 \text{ km/s}(\text{ slow wind}) - 650 \text{ km/s (fast wind)} \tag{1.125}$$

(Wilson et al., 2018; Bruno and Carbone, 2013b).

The proton gyro-frequency ω_i and radius ρ_i, corresponding to the rotation of protons around the mean field,

$$\omega_i = \frac{qB}{m_p} \sim 1 \text{ rad / s} = \frac{m_p}{m_e}\omega_e \tag{1.126}$$

$$\rho_i = \frac{m_p v_{th\perp}}{qB} \sim 35 \text{ km} = \sqrt{\frac{m_p}{m_e}}\rho_e. \tag{1.127}$$

The Debye length, which corresponds to the length scale at which collective effects of the plasma dominate over single particle (electrostatic) interactions:

$$\lambda_D = \sqrt{\frac{\epsilon_0 k_B T}{nq^2}} \sim 10 \text{ m}. \tag{1.128}$$

Typical speeds in the solar wind are given as the Alfvén speed v_A, the propagation speed for transverse magnetic fluctuations, and the thermal speed v_{th} of the protons

$$v_A = \frac{B_0}{\sqrt{\mu_0 \rho_0}} \sim 50 \text{ km/s} \tag{1.129}$$

$$v_{th} = \sqrt{\frac{k_B T}{m_p}} \sim 30 \text{ km/s} \tag{1.130}$$

$$\tag{1.131}$$

The ratio between the squared Alfvén speed and the thermal speed, is the parameter known as plasma β with

$$\beta \sim \mathcal{O}(1), \tag{1.132}$$

at 1 AU, with $\beta < 1$ typically expected in the inner heliosphere. A key observation is that the solar wind speed is significantly larger than either the thermal or Alfvén speeds, i.e. the solar wind flow is super sonic and super Alfvénic.

In the reference frame associated with spacecraft observations, the time scale associated with advection the proton gyro-scale by the solar wind is a small fraction ($\tau \sim \rho/v_{sw} \sim 0.1$ s) a small fraction of the actual gyro-period. In this respect, the time variation of protons as they advect over a spacecraft is quite small. While the gyroscale is known to limit the MHD cascade as a dissipative scale Leamon et al. (1998); Hollweg and Isenberg (2002); Alexandrova et al. (2013); Chen et al. (2014), at larger spatial scales, with time variations significantly slower than the gyroperiod, the dynamic time evolution of the fluctuations is further reduced relative to the advection time over the spacecraft.

The limit of slow variation of fluctuations in the spacecraft frame is formalized by the Taylor hypothesis (Taylor, 1938). The spectrum of waves measured in a medium with a fast bulk flow by a stationary observer consists of a set of Doppler shifted fluctuations

$$\omega_{sc} = \omega + \mathbf{k} \cdot \mathbf{v}_{sw} \tag{1.133}$$

such that the observed time dependence in the spacecraft frame consists of both the evolution of the fluctuating wave modes in the plasma rest frame, as well as the evolution associated with their advection past the spacecraft. In the limit of slow dynamic variation relative to the advection time, the Taylor hypothesis states that the time variation can be interpreted as sampling of spatial structure of the flow:

$$\omega_{sc} = \omega(1 + \mathbf{k} \cdot \mathbf{v_s w}/\omega) \tag{1.134}$$

$$\omega_{sc} \sim \mathbf{k} \cdot \mathbf{v}_{sw}. \tag{1.135}$$

The observed time-series from spacecraft measurements can be interpreted as spatial measurements with the transform in time as $t \rightarrow (\mathbf{v}_{sw} \cdot \mathbf{k})^{-1}$. Accordingly, under the Taylor hypothesis, temporal variation in the plasma frame are observed as a Doppler shifted spatial scales in the spacecraft frame, e.g. the plasma frame ion gyrofrequency $\omega_c = qB/m$ corresponds to the doppler shifted spacecraft frame scale $f_{sc} = v_{sw}/(2\pi\rho) = (v_{sw}/2\pi)(qB)/(mv_{th})$ (Bale et al., 2005; Chen et al., 2014).

Taylor's hypothesis is, in principle, valid for low frequency fluctuations at 1 AU. However, for high frequency waves $\omega >> \mathbf{k} \cdot \mathbf{v}_{sw}$ or when the spacecraft velocity is approximately equal to the solar wind speed, the Taylor hypothesis is likely an inadequate approximation. For PSP, the transverse orbital velocity of the spacecraft around the sun will reach maximum values larger than 200 km/s, on order the solar wind speed. Recent work by has explored techniques for disentangling spatial and temporal structure in the presence in large transverse velocities as well as limitations in interpreting PSP observations with the Taylor hypothesis Klein et al. (2015); Bourouaine and Perez (2018) .

1.10.2 REDUCED SPECTRA

The Taylor hypothesis has a strong effect on observations of turbulent energy spectra in the solar wind. Because of the ambiguity associated with spatiotemporal evolution associated with single point measurements, the observed energy associated with the spacecraft frequency f includes spectral components from multiple wave numbers

$$\mathcal{E} = \int E(f)df = \int d^3\mathbf{k} E(\mathbf{k}) \delta(2\pi f - \mathbf{k} \cdot \mathbf{v}_{sw}) \tag{1.136}$$

(Fredricks and Coroniti, 1976; Horbury et al., 2008; Forman et al., 2011). For a uniform flow, and assuming a two dimensionally anisotropic wave vector $\mathbf{k} = k_\perp \hat{\perp} + k_\parallel \hat{B}_0$

$$\mathcal{E} = \int E(f)df = \int d^3\mathbf{k} E(\mathbf{k}) \delta(2\pi f - k_\parallel v_{sw} cos\theta_{Bv} - k_\perp v_{sw} sin\theta_{Bv}) \tag{1.137}$$

where θ_{Bv} is the angle between the mean field direction and the flow direction. In the case of $\theta_{Bv} \rightarrow 90$, the perpendicular wavenumber spectra becomes the dominant contribution to $E(f)$, while at $\theta_{Bv} \sim 0$,

the parallel wave number spectra becomes the dominant contribution to the observed spectra. Horbury et al. (2008) used this consideration to show that high speed solar wind from *Ulyssses* demonstrate a -2 spectral index when $\theta_{Bv} \sim 0$ and a -5/3 spectral index when $\theta_{Bv} \sim \pi/2$, consistent with the scalings of anisotropic turbulence predicted by (Goldreich and Sridhar, 1995). The extension of this analysis to all θ_{Bv} was made by Forman et al. (2011), demonstrating good agreement with critical balance over all angles.

In general several types of anisotropy are present in the solar wind (Horbury et al., 2012). The early observations of Belcher and Davis (1971) revealed larger fluctuations in directions perpendicular to the mean field, the angular distribution of power, known variance anisotropy; extending variance anisotropy to measurements of anisotropic distributions of wave power leads to power anisotropy. Bieber et al. (1996) demonstrate the enhancement of power perpendicular to the mean field, interpreted as 2-D fluctuations with $k_{\parallel} \sim 0$. While power anisotropy is perhaps the easiest form of anisotropy to measure in the solar wind, e. g. using energy spectra or correlation functions, Matthaeus et al. (1990); Bieber et al. (1996); Horbury et al. (2008) it does not directly measure the anisotropy related to distribution of wave vectors: the spatial anisotropy associated with the elongation of turbulent structures in the parallel direction $k_{\parallel} << k_{\perp}$ is an important signature of anisotropic energy flux between parallel and perpendicular wave-numbers (Goldstein et al., 1995; Boldyrev, 2006). Chen et al. (2010c) use scaling relations to derive the relationship between power and wave-vector anisotropies. In principle, the determination of anisotropic characteristics of solar wind from single spacecraft point measurements requires the use of statistical studies which compile results from a conditioned set of observations in order to determine, e. g.power at scale k as a function of θ_{Bv} (Horbury et al., 2008; Podesta et al., 2009; Wicks et al., 2010; Chen et al., 2012; Wicks et al., 2013a,b).

The theoretical formulation of turbulence using statistical measurements of correlation functions naturally lends itself to observational studies implementing statistical methods. However, measuring dynamic processes which are not easily formulated with correlation functions, such as collisional relaxation and the growth of instabilities, proves more difficult. Regardless, the limitations imposed by single point *in-situ* spacecraft measurements largely demand that observational surveys are undertaken using statistical methods.

1.10.3 STATISTICAL STUDIES OF PLASMA INSTABILITIES

While single point measurements in the presence of a fast bulk flow preclude the observation of local time dynamics of a single parcel of plasma in its frame. Statistical techniques have emerged to study time dynamics not associated with turbulence and correlation functions. A primary example is the study of plasma instabilities in the solar wind. Plasmas are known to support number of instabilities at both fluid (MHD) as well as kinetic scales. In general, the concept of instability can be thought of as the redistribution of free energy in a plasma which evolves the system towards a stable equilibrium condition (Treumann and Baumjohann, 1997). At fluid and MHD macroscopic instabilities, may relate

to spatial inhomogeneity or anisotropy (Kelvin-Helmholtz instability, firehose instability, mirror Instability, parametric instabilities) in the thermodynamic and electromagnetic conditions of the plasma (Derby, 1978; Hellinger et al., 2006; Hellinger, 2007; Bale et al., 2009; Matteini et al., 2010a; Squire et al., 2016; Tenerani et al., 2017; Bowen et al., 2018a). Kinetic micro-instabilties (e.g. Landau resonance, cyclotron resonance, particle drift instabilities) which relate to perturbations, or structure in the particle distribution function and resonance with electrostatic or electromagnetic waves (Gary and Lee, 1994; Hollweg and Isenberg, 2002; Marsch, 2006; Matteini et al., 2010b; Verscharen et al., 2013; Tong et al., 2019; Vasko et al., 2019; Chen et al., 2019).

The concept of instability can be understood as generalization of the Fourier expansion

$$\mathbf{u}(\mathbf{x}) = \sum_k \tilde{\mathbf{u}}(\mathbf{k}) e^{-i(\omega t - \mathbf{k}\cdot x)} \tag{1.138}$$

to allow for complex frequency solutions of the form $\omega = \omega_r + i\gamma$. An unstable mode with wavenumber k then grows in amplitude as

$$u_k(t) = e^{\gamma t}. \tag{1.139}$$

Simply, the concept of stability analysis is simply thought of as determining the complex portion of the dispersion relation relating ω and k. The strength of an instability can be measured by the ratio between γ/ω_r, with weak slowly growing instabilities satisfying $\gamma/\omega_r << 1$ and strong instabilities which deviate quickly from an equilibrium state satisfying $\gamma/\omega_r \gtrsim 1$.

A common observational technique for identifying the presence of instabilities in the solar wind to compare the distribution of single spacecraft measurements with theoretical instability growth rate thresholds. Dynamically relevant instabilities, with significant growth rates, should constrain spacecraft observations of the solar wind. Intervals which are subject to some instability will grow and evolve to an equilibrium state, such that unstable intervals should not be easily observable in single point measurements. In this way, the observational signatures of instabilities can be measured without observing the time evolution of the instability in the plasma.

As an example, consider the oblique fire hose and mirror instabilities, which arise due to large, unstable, anisotropy between the parallel and perpendicular temperatures of the two dimensional distribution function $f(v_\parallel, v_\perp, \mathbf{x})$ (Treumann and Baumjohann, 1997). The stability threshold is approximated by

$$T_\perp/T_\parallel = 1 + \frac{a}{(\beta_\parallel - \beta_0)^b}, \tag{1.140}$$

where a, b, and β_0 are fit parameters Hellinger et al. (2006). Figure 1.2 shows the distribution of 10 years of observations of solar wind temperature anisotropy $T_\perp/T_\parallel$ and plasma β at a 5 minute scale from the *Wind* 3DP and MFI Lin et al. (1995); Lepping et al. (1995a) instruments; data are from Bowen et al. (2018a), Chapter 4. The contours show numerical predictions made by Hellinger et al. (2006)

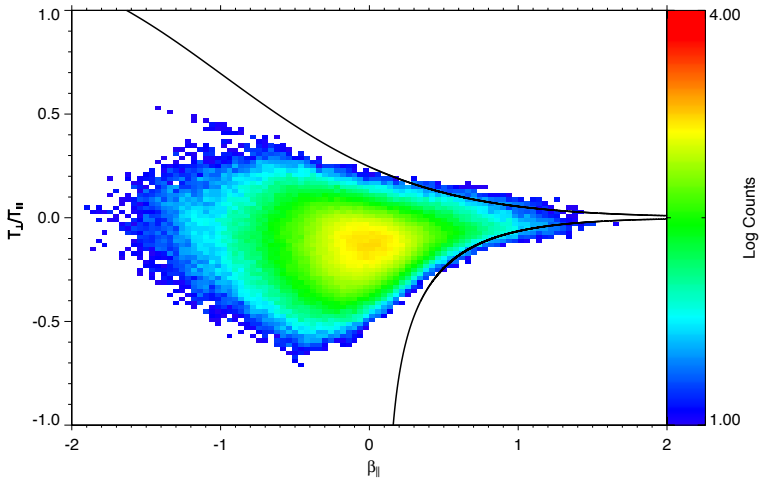

Figure 1.2: 10 years of *Wind* 3DP data. The distribution of data is bounded by the temperature anisotropies which are associated with the oblique fire hose and mirror instabilities.

for oblique fire hose (approximated with fit parameters $a = -1.4$, $b = 1$, $\beta = -0.11$) and mirror instabilities (approximated with $a = 0.77$, $b = 0.76$, $\beta_0 = -0.016$), for growth rate of $\gamma = 10^{-3}\omega_{ic}$. The thresholding of the data distribution by the contours has been interpreted as evidence for occurrence of mirror and fire hose-instabilities in the solar wind (Hellinger and Matsumoto, 2001; Kasper et al., 2002; Bale et al., 2009).

Instabilities can play an important role in solar wind turbulence. While the firehose and mirror instabilities act to disrupt the incompressible non-linear turbulence, early theories of solar wind turbulence proposed that shears related to Kelvin-Helmholtz instabilities could seed the non-linear Alfvénic interactions (Dobrowolny, 1972; Korzhov et al., 1984). Recent efforts have been made to understand how macroscopic instabilities can affect Alfvénic turbulence in the solar wind. Squire et al. (2016, 2017) use analytical and numerical methods to demonstrate that at high β, linear polarized Alfvén waves with amplitude $\delta B/B_0 > \beta^{-1/2}$ are unstable to the firehose instability due to the non-linear magnetic pressure associated with the fluctuation amplitude δB; such large amplitude waves should inherently interrupt the Alfvénic turbulent cascade. Tenerani et al. (2017) have explored the presence of parametric instability, Chapter 4 in the presence of pressure anisotropy. Parametric coupling between Alfvén and compressive fluctuations provides energy transfer between the wave modes such that they no longer passive to the Alfvén cascade waves as in the framework of RMHD.

1.10.4 KINETIC AND DISSIPATION SCALE TURBULENCE

While he majority of the research contained in this thesis is specific to the inertial scale of MHD turbulence, a brief discussion of kinetic scales of turbulence complements this discussion. In the solar wind, a collisionless plasma with strong magnetic fields, the kinetic scales associated with the ion-gyroscale and ion inertial length provide a high frequency limit to the quasi self-similarity of the MHD inertial range of turbulence at which kinetic effects become relevant (Leamon et al., 1998; Schekochihin et al., 2009; Chen et al., 2014). At 1 AU, this scale corresponds to a spacecraft frequency of ~1 Hz, above which spectral steepening is observed in the turbulence, the change in power law scaling is referred to as a spectral break point (Alexandrova et al., 2013). Many authors have attempted to distinguish between the ion-gyroscale, ρ_i, and ion-inertial length

$$d_i = v_A/\omega_i = \rho_i/\sqrt{\beta} \tag{1.141}$$

as the high-frequency limit to the inertial range. Bruno and Trenchi (2014) found scaling in heliospheric distance which corresponds to the cyclotron frequency, leading them to interpret the gyroscale as the dissipation scale. Leamon et al. (1998) suggest that the cyclotron resonance as a dissipative mechanism for the Alfvénic cascade. Chen et al. (2014) compare the dissipative breakpoint to the ion inertial length and gyro scale at low and high β and find the spectral break corresponds to lower frequency of the two scales. Vech et al. (2018) provided measurements consistent with the disruption of the turbulent cascade by current sheet reconnection associated with the 3D anisotropy introduced by dynamic alignment (Mallet et al., 2017).

Above the spectral break, it's thought that kinetic turbulence can exist (Galtier, 2006; Schekochihin et al., 2009; Boldyrev and Perez, 2012). While a consensus regarding the specifics of the kinetic scale has yet to be obtained, observational studies suggest they correspond to a cascade of turbulent kinetic Alfvénwaves (Bale et al., 2005; Salem et al., 2012). Understanding the kinetic scale turbulent dynamics is one of the primary science objectives of the PSP mission. Recent work by Chen et al. (2019) has demonstrated observationally the presence of wave-particle interactions in kinetic range turbulence via Landau damping in Earth's magnetosphere. Whether such wave-particle interactions significantly contribute to heating in the inner-heliosphere, or whether other turbulent heating process dominate is one of the fundamental questions for PSP (Chandran et al., 2010; Mallet et al., 2018).

1.10.5 OUTER SCALE TURBULENCE

The existence of an inertial cascade requires the injection of energy at large scales, known as the outer or injection scale range. Observations of the injection scale suggest that it is consistent with a $1/f$ spectral index (Matthaeus and Goldstein, 1986). Matthaeus et al. (2007) observe $1/f$ injection scaling in both the interplanetary magnetic field and density fluctuations, similar to observations of the fluctuating solar photospheric magnetic field, suggesting a solar origin. Alternatively Velli et al. (1989) suggest

that the WKB propagation of a single Elsässer modes through gradients in the interplanetary medium can generate a $1/f$ spectrum. Verdini et al. (2012) suggest that the $1/f$ spectrum originates due to interactions within the solar atmosphere between outward propagating waves and reflected waves due to density and magnetic field gradients in the inner heliosphere. Chandran (2018) suggest that the photospheric motions, which have a peak frequency at timescales of $\sim$ 300 s may induce an inverse cascade (energy cascade to lower frequencies) through parametric coupling between Alfvén and slow mode waves.

Observationally the $1/f$ spectrum has been studied at a range of heliospheric radii. Several authors have observed the frequency $1/f$ break scale decrease with heliospheric distance, suggesting that the inertial cascade consumes more of the wave-number frequency distribution Bavassano et al. (1982b); Bavassano and Bruno (1992); Bruno et al. (2009). At 1 AU the $1/f$ scales correspond to $f \lesssim 10^{-4}$ Hz, while observations from *Helios* at 0.3 AU have measured the break as high as $f \sim 10^{-2}$ Hz. Nicol et al. (2009) observe the parallel and perpendicular components of both magnetic and velocity fluctuations, concluding that the perpendicular components have similar distributions, while the parallel components of the low frequency magnetic and velocity fluctuations show characteristically different scalings indicative of propagation effects.

Matteini et al. (2018) recently explored the $1/f$ scale, arguing that the observations suggest that the injection range fluctuations are constant amplitude Alfvén waves confined to the surface of a sphere. Consideration of the structure function for low k and an energy spectra with scaling $\alpha = -1$ gives a constant value of the structure function corresponding to a constant amplitude fluctuations. In addition to being of constant amplitude, the results of Matteini et al. (2018) suggest that the fluctuations in the $1/f$ are of finite amplitude $B_1/B_0 \sim 1$. The finite amplitude associated with these flucutations suggests that instabilities associated with finite amplitude effects could play a part in the transition from the $1/f$ injection scales to the inertial range. The parametric decay instability is, in the limit of low β, known to have a growth rate of

$$\frac{\gamma}{\omega_0} \sim \frac{B_1}{B_0}\beta^{-1/4} \tag{1.142}$$

(Galeev and Oraevskii, 1963; Sagdeev and Galeev, 1969; Derby, 1978; Goldstein, 1978). The finite amplitude effects associated with $B_1/B_0 \sim 1$ suggest that such finite amplitude instabilities may be active in the $1/f$ range. Specifically, for the $1/f$ range with constant amplitude $\frac{B_1}{B_0}$, and weak dependence of $\beta^{-1/4}$ for $\beta < 1$, relevant to the inner heliosphere, the parametric growth rate is an approximately constant quantity on order $\gamma/\omega_0 \simeq 0.1$ or larger. With large growth rates, it is possible that parametric instabilities could couple outward propagating Alfvén waves to the generation of slow modes and inwards propagating Alfvén waves, thereby seeding non-linear interactions which lead to inertial range turbulence.

Wicks et al. (2013a) study the alignment of the Elsässer fluctuations near the $1/f$ break, demonstrating that the fluctuations are dominated by outward propagating fluctuations with a subdominant

population of anti-aligned inward fluctuations which are anti-aligned below the break and thus do not interact non-linearly until the $1/f$-inertial break is reached. Wicks et al. (2013b) demonstrate that the size of the $1/f$ range is strongly related to the cross helicity of the magnetic and velocity fluctuations, with higher correlation corresponding to a $1/f$ spectra spanning a larger frequency rage. Similarly the de-correlation of the magnetic and velocity fluctuations is observed with an increase in magnetically dominated structures and spectral steepening to the Kolmogorov type -5/3 spectra; Wicks et al. (2013b) show this evolution in the outer scales, Chapter 2 subsequently highlights the occurrence of the residual energy in the inertial scales and its connection with intermittency.

2

IMPACT OF RESIDUAL ENERGY ON SOLAR WIND TURBULENT SPECTRA

T. A. Bowen, A. Mallet, J. W. Bonnell, and Stuart D. Bale.
Impact of Residual Energy on Solar Wind Turbulent Spectra
ApJ, 865:45, Sep 2018b. doi: 10.3847/1538-4357/aad95b.

ABSTRACT It is widely reported that the power spectra of magnetic field and velocity fluctuations in the solar wind have power law scalings with inertial-range spectral indices of -5/3 and -3/2 respectively. Studies of solar wind turbulence have repeatedly demonstrated the impact of discontinuities and coherent structures on the measured spectral index. Whether or not such discontinuities are self-generated by the turbulence or simply observations of advected structures from the inner heliosphere has been a matter of considerable debate. This work presents a statistical study of magnetic field and velocity spectral indices over 10 years of solar-wind observations; we find that anomalously steep magnetic spectra occur in magnetically dominated intervals with negative residual energy. However, this increase in negative residual energy has no noticeable impact on the spectral index of the velocity fluctuations, suggesting that these intervals with negative residual energy correspond to intermittent magnetic structures. We show statistically that the difference between magnetic and velocity spectral indices is a monotonic function of residual energy, consistent with previous work which suggests that intermittency in fluctuations causes spectral steepening. Additionally, a statistical analysis of cross helicity demonstrates that when the turbulence is balanced (low cross-helicity), the magnetic and velocity spectral indices are not equal, which suggests that our observations of negative residual energy and intermittent structures are related to non-linear turbulent interactions rather than the presence of advected pre-existing flux-tube structures.

2.1 INTRODUCTION

Observations of power law spectral distributions of magnetic and kinetic energy in the solar wind, i.e. $E_\alpha \propto k^\alpha$, have led to the development of various theories of magnetohydrodynamic (MHD) turbulence.

It is widely reported that magnetic energy in the inertial range follows a power law spectrum with $E_b \propto k_\perp^{-5/3}$, while kinetic energy follows a shallower power law spectrum of $E_v \propto k_\perp^{-3/2}$ (Mangeney, 2001; Salem et al., 2009; Podesta et al., 2007; Borovsky, 2012). These spectral indices respectively support the theories of critically balanced turbulence and subsequent modifications accounting for the alignment between velocity and magnetic fluctuations (Goldreich and Sridhar, 1995; Boldyrev, 2006). The presence of $E \propto k_\perp^{-3/2}$ spectral distributions has been recovered in many subsequent numerical simulations (Perez and Boldyrev, 2009; Chandran et al., 2015; Mallet et al., 2017).

It is known that discontinuities and intermittency in observations of turbulence affect measured spectral indices. Roberts and Goldstein (1987) identified large amplitude coherent and discontinuous structures resulting in steep k^{-2} spectra. Li et al. (2011) showed that excluding intermittent current sheets from *Ulysses* magnetometer data led to the measurement of a $E_b \propto k^{-3/2}$ scaling, rather than the typically reported $E_b \propto k^{-5/3}$ scaling. Borovsky (2010) reconstructed the spectral distribution of magnetic field discontinuities of Advanced Composition Explorer (ACE) observations using a synthetic time-series, finding a $E_b \propto k_\perp^{-5/3}$ scaling. There are two dominant explanations for discontinuities and intermittency in the solar wind. The first suggests that discontinuities arise dynamically from the turbulent evolution of the plasma into current sheets (Salem et al., 2009; Mininni and Pouquet, 2009; Matthaeus et al., 2015; Boldyrev et al., 2011; Chang et al., 2004). The second suggests that observations of discontinuities correspond to advected flux tube structures from the inner-heliosphere (Tu and Marsch, 1993; Borovsky, 2008; Mariani et al., 1973; Bruno et al., 2001, 2007).

It is also known that the solar wind contains statistically more magnetic than kinetic energy (Bavassano et al., 1998; Salem et al., 2009; Bruno et al., 1985; Roberts et al., 1987b). Various models of MHD turbulence under a range of physical conditions show the growth of negative residual energy, defined as $E_r = E_v - E_b$ (Müller and Grappin, 2005; Gogoberidze et al., 2012a; Perez and Boldyrev, 2009; Boldyrev et al., 2011). The normalized residual energy,

$$\sigma_r = \frac{\langle v^2 \rangle - \langle b^2 \rangle}{\langle v^2 \rangle + \langle b^2 \rangle} = \frac{2\langle \mathbf{z}_+ \cdot \mathbf{z}_- \rangle}{\langle z_-^2 \rangle + \langle z_+^2 \rangle}, \tag{2.1}$$

is understood to quantify the relative dominance of magnetic or kinetic energy, or equivalently, the alignment between the Elsässer variables defined as $\mathbf{z}_\pm = \mathbf{v} \pm \mathbf{b}/\sqrt{\mu_0 \rho_0}$, where $\mathbf{v}$ and $\mathbf{b}$ are the fluctuating velocity and magnetic fields and ρ_0 is the mean mass density.

A power law spectrum for E_r was derived by Grappin et al. (1983), with $E_r \propto k^{-2}$ under the assumption of weak turbulence. Müller and Grappin (2005) have subsequently suggested $E_r \propto k^{-7/3}$ spectra for decaying isotropic turbulence and $E_r \propto k^{-2}$ scaling for forced anisotropic turbulence. Chen et al. (2013) used a statistical study of *Wind* observations to explore connections between spectral index and residual energy, reporting a mean value of α_r=-1.91 and a significant correlation between α_r and α_b. In a study demonstrating scale invariance of normalized cross helicity

$$\sigma_c = \frac{2\langle \delta\mathbf{b} \cdot \delta\mathbf{v} \rangle}{\langle v^2 \rangle + \langle b^2 \rangle} = \frac{\langle z_+^2 \rangle - \langle z_-^2 \rangle}{\langle z_-^2 \rangle + \langle z_+^2 \rangle}, \tag{2.2}$$

Podesta and Borovsky (2010) reported $\alpha_r = -1.75$. Both studies demonstrate correlations between cross helicity and spectral indices for magnetic fields, velocity, as well as total energy.

The connection between cross helicity and residual energy is well established. Bruno et al. (2007) show that as fast solar wind evolves from 0.3 -1AU the distribution of *Helios* measurements moves from a highly cross helical (imbalanced) state to a state with low cross helicity (balanced) and high negative residual energy. Wicks et al. (2013a) studied the evolution of cross helicity and residual energy over injection and inertial scales, arguing that the mean angle between the Elsässer variables is scale dependent and maximized at the outer scale. Wicks et al. (2013b) show that observations of turbulence tend to be either strongly cross helical, or have strong residual energy. In this Letter, we use 10 years of *Wind* observations to study statistical connections between intermittency, magnetic discontinuities, residual energy, and spectral index. We demonstrate that discontinuous events are associated with magnetically dominated intervals with large negative residual energies. Intermittent discontinuities steepen the magnetic spectral index, but have little effect on the measured velocity spectra. Our observations are consistent with the generation of residual energy and intermittency through turbulence, and suggest a close link between residual energy and intermittency.

2.2 DATA

We use observations from several instruments on the *Wind* mission ranging 1996 January 1 through 2005 December 31: Magnetic Field Investigation (MFI) Lepping et al. (1995a), Solar Wind Experiment (SWE) Ogilvie et al. (1995), and Three Dimensional Plasma (3DP) experiment Lin et al. (1995). Data are separated into non-overlapping 1 hr intervals. Intervals are excluded if any of several conditions are met: *Wind's* geocentric distance is less than $35R_E$, the average solar wind speed is < 250 km/s, or if more than 5% of of observations are missing from any one instrument. Linear interpolation is implemented across small data gaps when < 5% of an interval is missing. The resulting data consists of 39415 intervals of 1 hour.

The 3 s cadence 3DP "on board" proton moment measurements are interpolated to the MFI time base. We separate velocity, and magnetic field measurements ($\mathbf{v}$, and $\mathbf{B}$) into mean and fluctuation quantities using time-averaged values, denoted as $\langle ... \rangle$. For example, the mean magnetic field, $\mathbf{B_0}$, is determined by $\langle \mathbf{B} \rangle = \mathbf{B_0}$ with the fluctuation quantities as $\delta\mathbf{B} = \mathbf{B} - \mathbf{B_0}$. We normalize the magnetic field to Alfvén units using $\delta\mathbf{b} = \delta\mathbf{B}/\sqrt{\mu_0\rho_0}$ where ρ_0 is the mean mass density.

Each interval is characterized by energies associated with the velocity and magnetic field fluctuations $E_b = \frac{1}{2}\langle \delta b^2 \rangle$ and $E_v = \frac{1}{2}\langle \delta v^2 \rangle$, normalized cross helicity,

$$\sigma_c = \frac{2\langle \delta\mathbf{b} \cdot \delta\mathbf{v} \rangle}{\langle \delta b^2 \rangle + \langle \delta v^2 \rangle}, \tag{2.3}$$

and normalized residual energy

$$\sigma_r = \frac{E_v - E_b}{E_v + E_b}. \tag{2.4}$$

A minimum variance analysis (MVA) is performed on $\delta\mathbf{v}$ and $\delta\mathbf{b}$ to decompose each interval into eigenvectors corresponding to directions of minimum, maximum, and intermediate variance (Sonnerup and Cahill, 1967). Intervals with maximum energy is largely distributed along a single direction, i.e. if $\lambda_b^{max} \approx E_b$, may indicate the presence of strong discontinuities or a linear polarization to the fluctuations (Bruno et al., 2001).

Intermittency in the magnetic field is often associated with current sheets Matthaeus et al. (2015); Veltri and Mangeney (1999); Mininni and Pouquet (2009); Mallet et al. (2016). Using Ampere's law

$$\nabla \times \mathbf{B} = \mu_0 \mathbf{J} \tag{2.5}$$

and invoking the Taylor hypothesis, $\frac{\partial}{\partial t} \sim \mathbf{V} \cdot \nabla$ allows the time derivative of magnetic field observations in the spacecraft frame to be used as a proxy for current (Podesta and Roytershteyn, 2017). Because single spacecraft observations constrain spatial derivatives to the bulk solar wind flow direction, the full curl cannot be computed. To estimate the magnitude of currents we implement the reduced curl

$$\nabla_x \times \mathbf{B} = -\frac{\partial}{\partial x} B_z \hat{y} + \frac{\partial}{\partial x} B_y \hat{z}, \tag{2.6}$$

where the solar wind flow is along $\hat{x}$. Applying the Taylor hypothesis gives an estimate of the current magnitude,

$$J = \frac{1}{\mu_0 V_{sw}} \sqrt{\left(\frac{\partial B_y}{\partial t}\right)^2 + \left(\frac{\partial B_z}{\partial t}\right)^2}. \tag{2.7}$$

A reduced estimate for the vorticity magnitude $\omega = \nabla \times \mathbf{v}$ is similarly computed.

Intermittency is frequently quantified using the kurtosis,

$$\kappa_x = \frac{\langle x^4 \rangle}{\langle x^2 \rangle^2} \tag{2.8}$$

(Bruno et al., 2001, 2003; Salem et al., 2009; Mangeney, 2001; Veltri and Mangeney, 1999; Frisch, 1995; Matthaeus et al., 2015). Gaussian distribution have $\kappa = 3$, with $\kappa > 3$ indicating heavy tailed, non-Gaussian statistics. As a simple statistic to quantify intermittency in the magnetic and velocity fluctuations we measure the kurtosis of the reduced curl estimations of the current and vorticity, κ_J and κ_ω for each interval, subtracting 3 to compare with Gaussian statistics.

2.3 SPECTRAL FITTING

Trace spectral indices for the magnetic and velocity fluctuations in the inertial turbulent range are estimated by performing a linear least squares fit of the power spectra to a line in logarithmic space. Power spectra for $\mathbf{b}(t)$ and $\mathbf{v}(t)$ are estimated with a fast-Fourier transform. The trace power spectra, $\tilde{E}_b$ and $\tilde{E}_v$ are calculated as the sum power spectra from each direction axis.

To prevent overlapping with injection scales, our fits only consider frequencies above ~ 0.277 Hz (6 minutes). To avoid spectral steepening associated with the dissipative scales at high frequencies, we only consider the subsequent 190 frequency bins (up to 0.0555 Hz, or 18 seconds). The trace spectra are linearly interpolated to an abscissa of 50 logarithmically spaced frequencies (linearly spaced in the logarithmic domain) between 0.277-0.0555 Hz. The power spectra is estimated using a linear least square fit of the interpolated spectra and frequencies in log-log space, with the slope of the best fit line giving the spectral index (Podesta, 2016; Chen et al., 2013). The spectral index of the trace residual energy is calculated from fitting $|\tilde{E}_r| = |\tilde{E}_v - \tilde{E}_b|$ with the same interpolation and least square fitting scheme. Additionally, the high frequency limit helps to minimize flattening effects due Gaussian noise in low amplitude 3DP velocity measurements; though the range of our spectral fits extends to slightly higher frequencies than what previous authors have used, we find good agreement with their estimates for mean values of α_v and α_b (Chen et al., 2013; Wicks et al., 2013a; Podesta and Borovsky, 2010).

Uncertainty of our estimated spectral indices is found through propagation of error (Press et al., 1992a). The variance associated with single FFT estimation of spectral density is equal to the power spectral density itself. Typically, variance is reduced through averaging over an ensemble of spectra, or windowing the autocorrelation function of a time-series. Here we derive the uncertainty in spectral index associated with least squares fitting of a single FFT estimation of spectral density. For spectral density S_i where index i refers to a given frequency bin, f_i, Stoica and Moses (2005) give the variance of the spectral density as

$$\mathrm{Var}[S_i] = \sigma_i^2 \approx S_i^2. \tag{2.9}$$

Propagating the variance σ_i^2 to the logarithm of the spectral density $\log_{10}(S_i)$ gives

$$\mathrm{Var}[\log_{10} S_i] = \sigma_L^2 = \left(\frac{1}{\ln 10}\right)^2 \frac{\sigma_i^2}{S_i^2} \approx 0.19. \tag{2.10}$$

The scaling of $\mathrm{Var}[\tilde{S}_i] = S_i$ leads to constant variance in the estimation of the logarithm of spectral density.

For a power law spectra $S_i = \beta f_i^{\alpha}$ minimizing

$$\chi^2 = \sum_{i=0}^{N-1} \left(\frac{y_i - \beta - \alpha x_i}{\sigma_L}\right)^2, \tag{2.11}$$

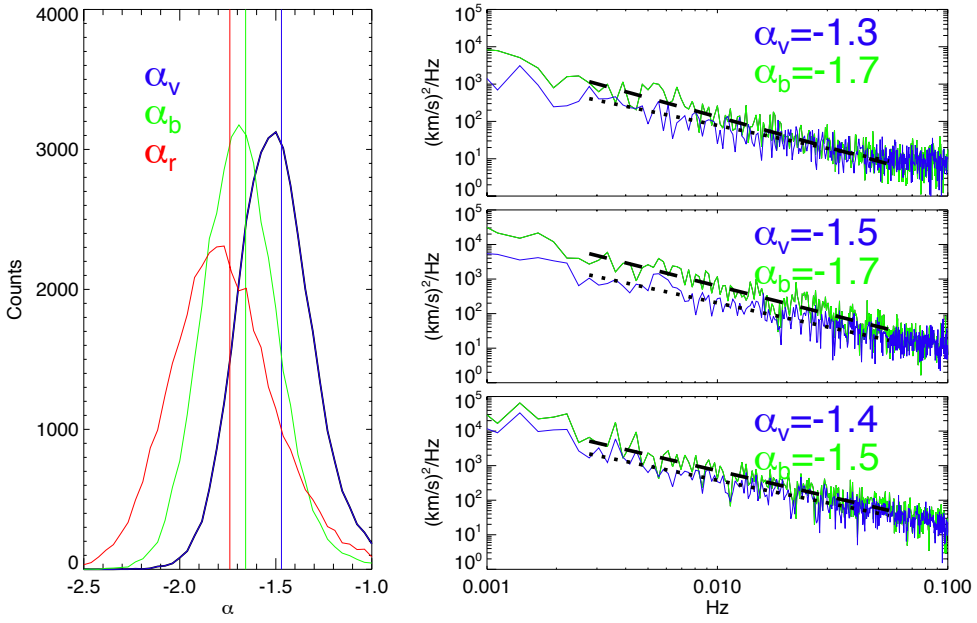

Figure 2.1: (Left) Distribution of fits power-law indices for magnetic field (green), velocity (blue), and residual energy (red) spectra, mean values are shown with vertical lines. (Right) Examples of measured magnetic field (in Alfvén units) and velocity fluctuation spectra. Fits for the magnetic and velocity spectra are shown respectively as black dashed and dotted lines.

where $y_i = \log_{10} S_i$ and $x_i = \log_{10} f_i$, with respect to α and β gives the least square best fits for the spectral index and scaling amplitude. Following Press et al. (1992a) for propagation of errors gives the uncertainty in α as

$$\sigma_\alpha^2 = \sum_i \left(\frac{\partial \alpha}{\partial y_i} \right)^2 \sigma_L^2 = \sigma_L^2 \frac{\sum x_i^2}{N \sum x_i^2 - (\sum x_i)^2}. \tag{2.12}$$

The uncertainty in the estimated spectral index, a function of σ_L^2 and the uniformly used frequency abscissa, is constant for each interval with $\sigma_\alpha = \pm 0.16$.

2.4 RESULTS

Figure 2.4 shows the probability distributions of α_b, α_v, and α_r, with respective means of -1.66,-1.47, and -1.73. Our fits for the the velocity and magnetic energy spectra agree with spectral indices given in previous studies (Mangeney, 2001; Salem et al., 2009; Podesta et al., 2007; Borovsky, 2012). The mean value of α_r slightly shallower than observations in Chen et al. (2013) but is consistent with Podesta and

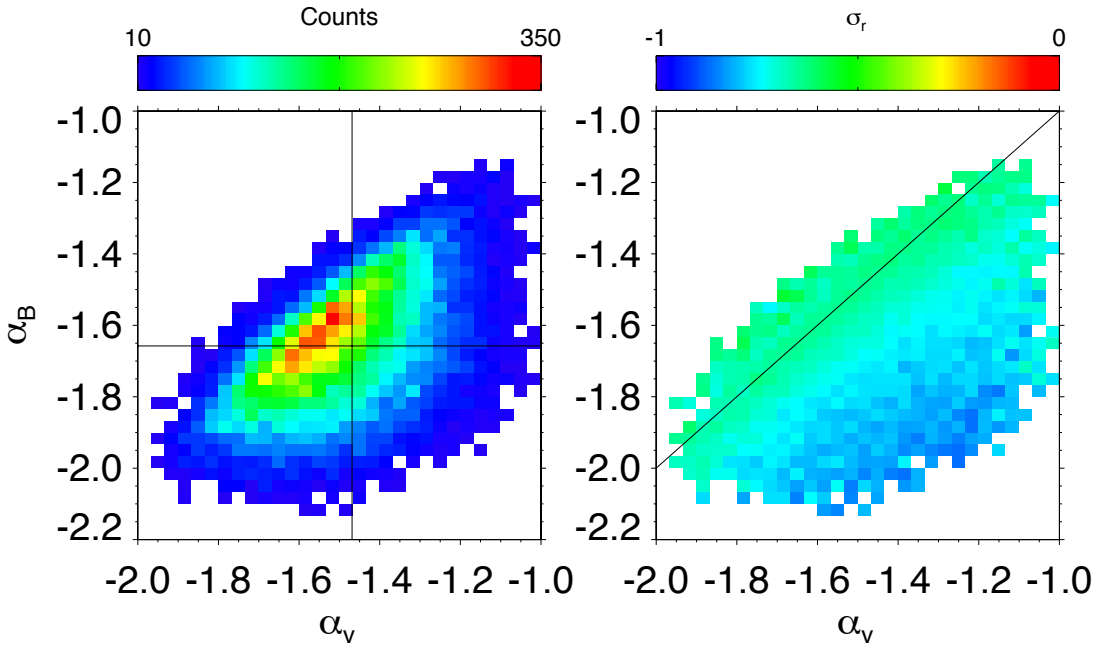

Figure 2.2: (Left) Joint distribution of the fitted spectral indices for magnetic field, α_b, and velocity, α_v, fluctuations in the inertial range. The black lines show the mean values of $\alpha_v \sim -3/2$ and $\alpha_b \sim -5/3$. (Right) The distribution of α_v and α_b colored by the mean residual energy in each bin. The black line shows $\alpha_v = \alpha_b$. Deviations from $\alpha_v \approx \alpha_b$ lead to an increase in negative residual energy ($E_b > E_v$).

Borovsky (2010). Our observations of α_r are also shallower than predictions of various models of MHD turbulence (Grappin et al., 1983; Müller and Grappin, 2005; Gogoberidze et al., 2012a); however, these models are conducted using assumptions which are not satisfied by solar wind turbulence, e.g. weak turbulence, isotropy, and quasi-normal closure. Deviation in our measurements of α_r from Chen et al. (2013) likely occur due to differences in the fitting technique and normalization of the magnetic field. Our work directly fits $\tilde{E}_r$ as the difference in observed velocity and magnetic spectra, and implements MHD normalization of the magnetic field. Chen et al. (2013) use fitted spectra to calculate α_r and implement a kinetic normalization of the magnetic field. The right panels of Figure show examples of $\tilde{E}_b$, $\tilde{E}_v$, and $\tilde{E}_r$ with our fits.

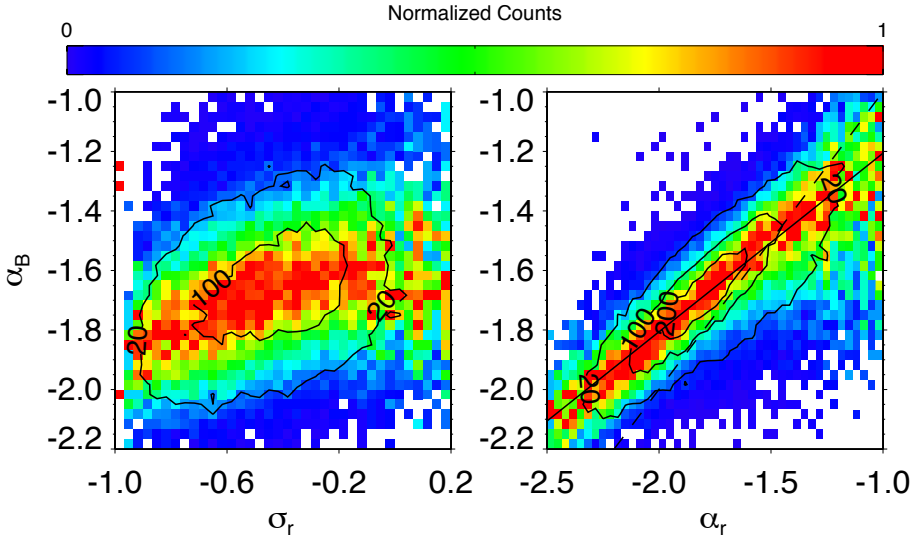

Figure 2.3: (Left) Joint distribution of normalized residual energy σ_r and spectral index of the inertial range magnetic fluctuations α_b. Data is column normalized to the maximum number of counts in each σ_r bin. (Right) Joint distributions of fitted power law spectral indices of residual energy spectra α_r and inertial range magnetic field fluctuations α_b. The solid black line shows the least square linear fit to the data with correlation 0.77 and slope of 0.56. The dashed line shows $\alpha_r = \alpha_b$. Contours in either panel show 20, 100, and 200 level counts of the joint distributions.

The left panel of Figure shows the joint distribution of α_b and α_v. The mean value of the velocity spectral index is $\alpha_v = -3/2$. A tendency for $\alpha_b < \alpha_v$ is evident in the distribution. The right panel of Figure shows the joint distribution of magnetic and velocity indices colored by the mean value of σ_r. The statistical preference for negative residual energy is clearly evident in our observations. The residual energy becomes more negative as the spectral indices α_v and α_b diverge, i.e. as the magnetic spectral index steepens. Particularly interesting is the consistent level of residual energy along the line $\alpha_v = \alpha_b$ throughout the range of observations.

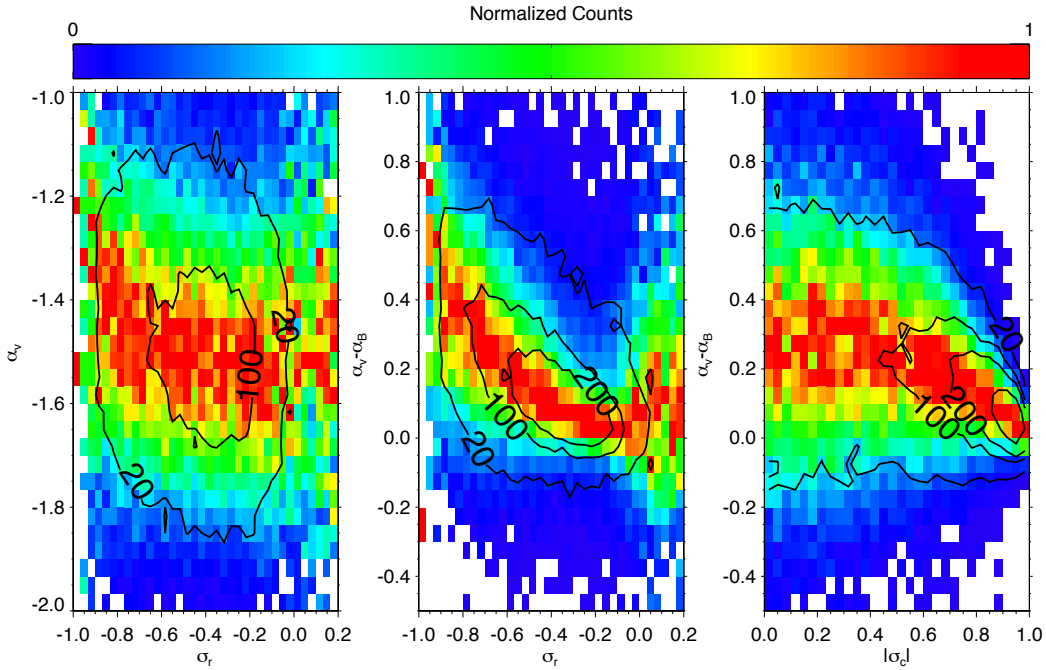

Figure 2.4: (Left) Joint distribution of fit velocity spectral index α_v with root-mean-square residual energy σ_r. The distribution is column normalized to the maximum occurrence of α_v for each value of σ_r. (Center) Joint distribution of the difference in velocity and magnetic field spectral indices, $\alpha_v - \alpha_b$, with σ_r. (Right) Joint distribution of the difference in velocity and magnetic field spectral indices, $\alpha_v - \alpha_b$, with σ_c. Data is column normalized to the maximum number of counts of $\alpha_v - \alpha_b$ in each bin of σ_c. Contours in all three plots show 20, 100, and 200 count levels of the distributions.

The left panel of Figure shows the joint distribution of σ_r and α_b. The secular trend suggests that the residual energy plays a significant role in setting the spectral index of the magnetic field. Specifically, it is evident that magnetically dominated intervals, with $\sigma_r \approx -1$, exhibit steeper magnetic spectra. The right panel of Figure shows the joint distribution of α_r and α_b, these variables are highly correlated with a Pearson correlation value of 0.78. A linear best fit gives $\alpha_b \propto 0.56\alpha_r$. These results imply that spectral indices of the magnetic fluctuations and residual energy are largely determined by the average residual energy over each interval.

The left panel of Figure shows the joint distribution of σ_r and α_v. Unlike the spectral index of the magnetic fluctuations, α_v exhibits little dependence on σ_r, suggesting that residual energy is mostly determined by magnetic fluctuations. The middle panel of Figure shows the difference between the magnetic and velocity spectral indices as a function of residual energy. As the residual energy increases, i.e. the plasma becomes less magnetically dominated, the spectral index of the magnetic field approaches that of the velocity spectra.

The right panel of Figure shows the joint distribution of the difference between magnetic and velocity spectral indices, $\alpha_v - \alpha_b$, and cross helicity, σ_c, suggesting that high cross helicity measurements occur only when $\alpha_v = \alpha_b$. A geometrical consideration of cross helicity and residual energy gives the constraint of $\sigma_c^2 + \sigma_r^2 < 1$ (Wicks et al., 2013b). Clearly, the decrease of $|\sigma_c|$ with large negative σ_r and $|\alpha_b| > |\alpha_v|$ is inevitable. However, there is no such geometric argument which demands balanced turbulence (i.e. $|\sigma_c| < 1$) to coincide with unequal spectral indices such that $\alpha_b \neq \alpha_v$. The observations in Figure (Right), in which the joint distribution of $\alpha_v - \alpha_b$ is conditioned on σ_c suggests that balanced turbulence (i.e. $|\sigma_c| < 1$) coincides with $|\alpha_b| > |\alpha_v|$. There is no *a priori* reason that we expect balanced turbulence (i.e. $|\sigma_c| < 1$) to have different spectral indices, $\alpha_b \neq \alpha_v$. This result is consistent with the generation of negative residual energy through turbulence, i.e. that non-linear interactions between the Elsässer variables lead to the growth of intermittent structures with negative residual energy, since at fixed total energy the nonlinear interaction term $\mathbf{z}_\pm \cdot \nabla \mathbf{z}_\mp$ are stronger when $\sigma_c = 0$.

Using the MVA analysis, the value λ^{max} corresponding the fraction of energy associated with the maximum variance direction, is calculated for both the magnetic and velocity fluctuations. The top panels of Figure show the joint distributions of λ_b^{max} (Left) and λ_v^{max} (Right) with the residual energy. There is a strong dependence of λ_b^{max} on the residual energy which is not observed for λ_v^{max}. The suggests that large negative residual energy occurs as the result of discontinuous/coherent structures in the magnetic field. In fact, the most negative values of residual energy seem to demonstrate the smallest values of λ_v^{max}, which suggest more isotropic velocity fluctuations; however, this could be due to sampling bias towards very low amplitude velocity fluctuations subject to noise.

To further connect the negative residual energy with magnetic intermittency, we examine the kurtosis of the reduced curl estimates for current and vorticity, κ_J and κ_ω, as proxies for intermittent features. The bottom panels of Figure show the joint distribution of the residual energy and κ_J. A decrease in κ_J is observed with increasing residual energy, suggesting that the negative residual energy is caused by magnetic discontinuities with associated bursty currents. At low residual energy the velocity fluctuations appear more Gaussian, which may indicate very low amplitude velocity fluctuations possibly subject to noise. Regardless, we uniformly observe $\kappa_\omega < \kappa_J$, suggesting less intermittency in the velocity fluctuations.

2.5 DISCUSSION

Many authors recover $k^{-3/2}$ spectra in simulations (Maron and Goldreich, 2001; Müller and Grappin, 2005; Perez and Boldyrev, 2009; Mallet et al., 2016). This scaling is in agreement with analytic predictions of strong, three dimensional, anisotropic, turbulence appropriate for the solar wind (Boldyrev, 2006; Chandran et al., 2015; Mallet et al., 2017; Bruno and Carbone, 2013a). Our observations here suggest that the observed difference between the spectral indices of velocity and magnetic field turbulent fluctuations occurs due to the presence of negative residual energy in the form of intermittent current sheets. When the magnetic and velocity energies are in equipartition, the spectral slope of the

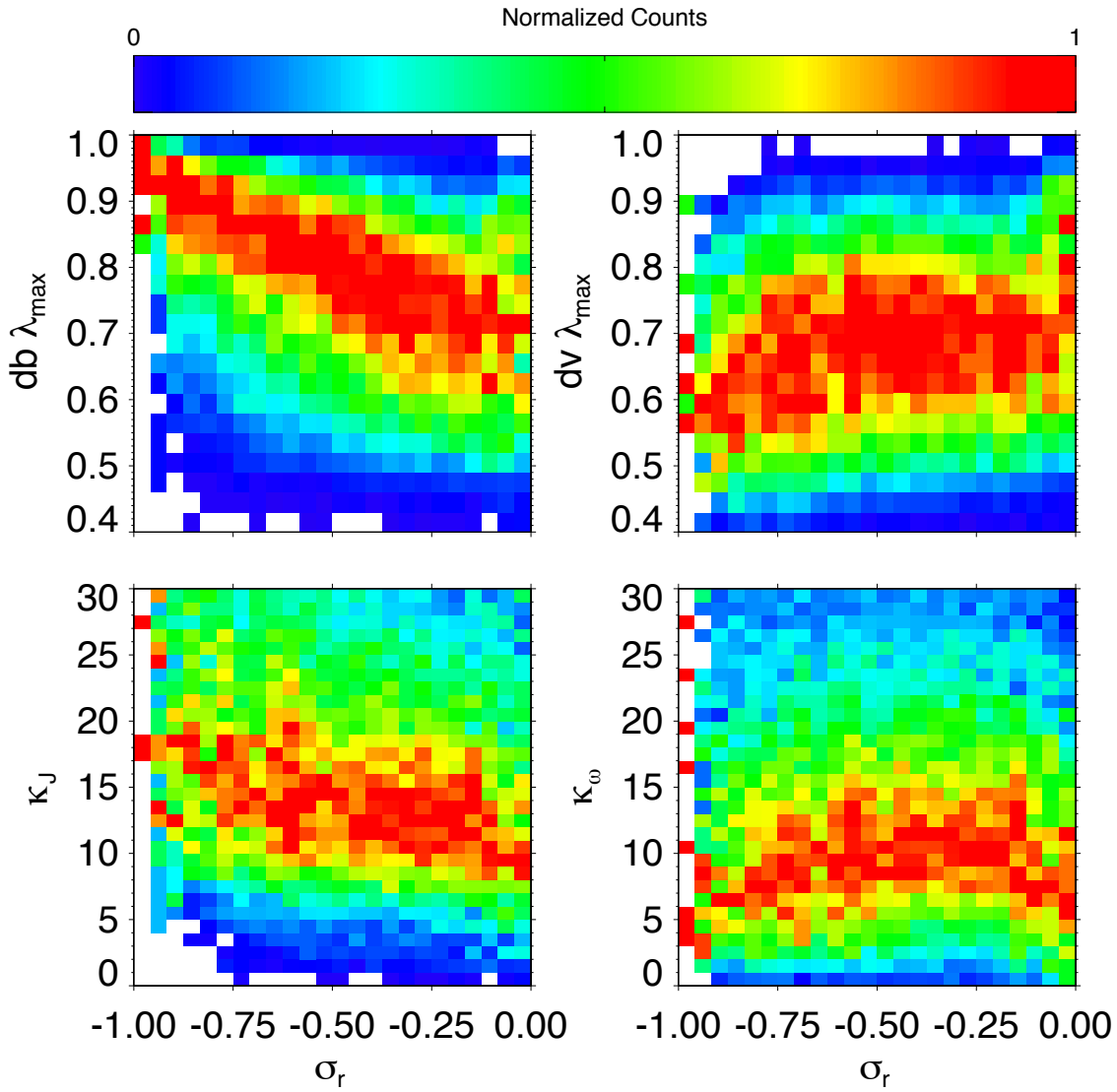

Figure 2.5: (Top Left) Joint distribution of maximum normalized eigenvalue of magnetic field fluctuations, λ_b^{max}, with σ_r. Large negative residual energy corresponds with large $\lambda_b^m ax$. The joint distribution of λ_v^{max} with the residual energy (Top Right) does not show a dependence on the residual energy. Joint distributions of the kurtosis of reduced current (Bottom Left) and vorticity (Bottom Right) with residual energy show that negative residual energy corresponds to intermittent currents with no associated signature in the velocity fluctuations.

magnetic fluctuations approaches the velocity spectral index. The velocity spectral index is insensitive to the residual energy with a mean value of $\alpha_v = -3/2$. This picture is consistent with the numerical model of Mininni and Pouquet (2009), which demonstrates the formation of thin current sheets in the magnetic field through decaying turbulence leading to enhanced intermittency and steepening of magnetic spectral index of $\alpha_b = -5/3$. In this interpretation, the magnetic fluctuations form thinner structures than the velocity fluctuations, which then dissipate energy more quickly. This picture does not address the collisionless and kinetic nature of dissipation in the solar wind; a full explanation requires a more complex account of the physical mechanisms of dissipation.

Our results are congruent with Li et al. (2011) who interpreted their results as indicative of flux-tube crossings. However, for several reasons, we believe our results support the idea of intermittency through turbulence rather than observations of advected flux tubes. First, we have identified the presence of intermittent events in the magnetic field contributing to negative residual energy which have no accompanying signature in the velocity fluctuations. Observed intervals with intermittent signatures present in both velocity and magnetic fluctuations are likely contained along the $\alpha_v = \alpha_b$ line, where steepening may occur in both the magnetic and velocity spectra. If observations of flux tube crossings are present in the dataset, they likely exist in this region. Additionally, our results agree with Salem et al. (2009) who note that the high kurtosis distributions which affect measurements of spectral indices occur at lower fluctuation amplitudes in the magnetic field than in the velocity measurements. This again suggests the presence of intermittent magnetic fluctuations with no velocity component.

The joint distribution of the difference of spectral slopes, $\alpha_v - \alpha_b$, and the cross helicity σ_c, suggests that intervals of balanced turbulence preferentially occur with $\alpha_v \neq \alpha_b$. Though unequal spectral slopes, associated with non-equipartitioned E_v and E_b, geometrically preclude the observation of imbalanced fluctuations with $|\sigma_c| \sim 1$, the observations in Figure (Right) suggest the stronger statement that balanced turbulence occurs only with unequal spectral indices. We interpret the lack of balanced turbulence with $\alpha_v = \alpha_b$ as evidence for the generation of residual energy through non-linear turbulent interactions (Boldyrev et al., 2011). The observation that solar wind turbulence is either highly imbalanced, $|\sigma_c| = 1$ or highly anti-aligned $\sigma_r = -1$ has been noted by previous authors (Wicks et al., 2013b; Bruno et al., 2007); however, observations of low cross helicity directly corresponding directly to deviations in turbulent spectral indices suggests that the residual energy is closely connected with non-linear turbulent interactions.

The quantification of the variance in spectral density estimates demonstrates that our fit spectral indices are accurate to 10%. The implementation of this variance estimate will help constrain observations made of the inner heliosphere by the FIELDS instrument on the Parker Solar Probe (Bale et al., 2016b). Additionally, a quantitative characterization of spectral index variance may prove useful in further studies of *Wind* observations, e.g. determining the nature compressive fluctuations in the solar wind (Bowen et al., 2018a).

3

SPECTRAL AND INTERMITTENT SIGNATURES OF COMPRESSIVE FLUCTUATIONS

ABSTRACT Theories of inertial range solar wind turbulence primarily focus on the dominant incompressible Alfvénic fluctuations; however, the presence of a significant compressible component to solar wind turbulence is well known. Compressions in the solar wind are likely composed of either non-propagating pressure balanced structures or slow mode waves with highly oblique wave vectors nearly in pressure balance. Modern theories of magnetohydrodynamic turbulence suggest that the compressible components are actively mixed by the Alfvénic perpendicularly polarized component of the turbulence, but are energetically decoupled, such that no energy transfer occurs between the modes in the dynamic turbulent timescales. Accordingly, it is commonly thought that compressions are passive to the Alfvénmodes, inheriting the spectral scaling and intermittent properties of the perpendicular cascade; ample numerical, analytic, and observational evidence exists to support this hypothesis. However, due to instrumental noise associated with *in-situ* density measurements, characterization of the spectral signatures of the compressible solar wind in the inertial range can be quite difficult. This work explores the spectral scaling and intermittent properties of the compressive component of solar wind turbulence in comparison with the Alfvénic turbulence using an empirical determination of instrumental noise characteristics to retain only observations with good signal to noise ratios. It is demonstrated that the compressible fluctuations, consisting of both parallel magnetic field and density fluctuations, have different spectral scaling and intermittent properties. In intervals with large cross helicity, with low amplitude density fluctuations, deviations from the observed scaling of Alfvénic turbulence are observed. Additionally, the intermittency of the density fluctuations is observed to exhibit characteristically different signatures from the compressive magnetic field. The connection to pressure balance is additionally explored which suggests that finite amplitude effects may cause deviations from first-order pressure balance common in MHD approximations.

3.1 COMPRESSIBLE FLUCTUATIONS

Early observations of the solar wind revealed correlated magnetic and velocity fluctuations characteristic of incompressible, transverse Alvén waves (Belcher and Davis, 1971; Roberts et al., 1987c,a).

Measurements of the spectral composition of magnetohydrodynamic fluctuations in solar wind revealed spectral distributions with power law scaling, $E \propto k^{\alpha}$, reminiscent of hydrodynamic turbulence (Russell, 1972; Matthaeus and Goldstein, 1982a; Bavassano et al., 1982b; Tu and Marsch, 1995). The resulting observations have led to the development of magnetized turbulence theories for incompressible MHD turbulence (Kraichnan, 1965; Goldreich and Sridhar, 1995; Boldyrev, 2006; Schekochihin et al., 2009).

Despite the common use of incompressible theories of MHD turbulence in describing the solar wind, e. g. Marsch and Tu (1990a); Goldstein et al. (1995), observations reveal that the solar wind contains a compressible component (Roberts et al., 1987c; Roberts, 1990; Marsch and Tu, 1990b; Tu and Marsch, 1994). Early research into the compressible solar wind could not uniquely determine whether compressions corresponded to wave mode fluctuations or non-propagating structures (Roberts, 1990; Tu and Marsch, 1994). However, Barnes (1966) argued that fast and slow magnetosonic modes should undergo significant damping in the solar wind; accordingly, many subsequent studies suggested that compressible fluctuations are likely non-propagating pressure balanced structures (PBS) with equal and opposite magnetic and thermal perturbed pressures (Burlaga and Ogilvie, 1970; Roberts, 1990; Tu and Marsch, 1994).

More recently, Klein et al. (2012) suggest that approximately 10% of the energy in solar wind fluctuations at 1 AU is contained in compressive fluctuations. Using the characteristic anti-correlation between compressive magnetic and density fluctuations, Yao et al. (2011) demonstrate the presence of PBS through the inertial range; subsequent work showing that such pressure balance structures were driven by the slow magnetosonic and mirror modes (Yao et al., 2013a,b). Kellogg and Horbury (2005) have pointed out that the pressure balance structure, often also referred to as the entropy mode, is the same as the slow-mode in the limit of perpendicular propagation (Krauss-Varban et al., 1994). Using a quasi-linear mix of Alfvén fluctuations with kinetic slow and fast modes Klein et al. (2012) and Howes et al. (2012) argue that the vast majority of compressive energy is contained in oblique slow magnetosonic modes.

In many magnetohydrodynamic theories the compressions are decoupled from the Alfvénic fluctuations and behave as passive scalar fluctuations (Higdon, 1984; Montgomery et al., 1987; Matthaeus et al., 1991; Zank and Matthaeus, 1993; Goldreich and Sridhar, 1997; Schekochihin et al., 2009). Though scalar compressive fluctuations are advected and scattered by the Alfvénic fluctuations, no energy exchange between the compressive and Alfvénic modes exists (Chen, 2016). The collisionless damping outlined by Barnes (1966) is a parallel process, such that the perpendicular components of compressive modes are free to interact with the Alfvénic turbulence, while only the component parallel to the mean field is removed through collisionless damping. At sufficiently small parallel wave-numbers, $k_{\parallel}$, the collisionless damping of slow-mode waves becomes negligible and only the compressive modes with $k_{\perp}$ exist (Klein et al., 2012; Howes et al., 2012). The preceding heuristic argument has been supported observationally by Chen et al. (2013), demonstrating that compressive magnetic fluctuations are elongated parallel to the mean magnetic field, indicating fluctuations with $k_{\parallel} << k_{\perp}$ consistent

with the description of a quasi-perpendicular cascade with parallel damping. Further evidence for scalar-advected compressive fluctuations has been provided in the numerical experiments of Maron and Goldreich (2001), which demonstrate that scalar fluctuations advected by turbulence cascade retain the power-law of the active cascade. Observations by Chen et al. (2011) suggest that the spectral density of the magnetic field agrees with that of the density fluctuations, consistent with the model of passive scalar advection.

While MHD theories suggest scalar advection of the density fluctuations, kinetic and non-linear processes outside of the MHD approximation can cause deviations from the compressive-scalar framework. Verscharen et al. (2017) attempt to distinguish the MHD slow magnetosonic, kinetic compressive (ion-acoustic) slow, and PBS, in the solar-wind by comparing numerical results from a non-linear dispersion solver with observations from the *Wind* mission, determining that observations are most consistent with the MHD slow-mode. Accordingly, the authors propose that some process with an effective collisionality could counteract the expected kinetic damping. Recent work by Schekochihin et al. (2016) suggests that non-linear turbulent phase mixing may act to collisionialize the solar wind. Additionally, the numerical results of Meyrand et al. (2019) suggest that non-linear turbulent processes work to cancel out collisionless damping due to phase mixing, and additionally demonstrate that the density fluctuations cascade with the velocity portion of the Alfvénic spectrum. Bowen et al. (2018a) explored the signatures of compressible fluctuations in comparison with parametric decay instability (PDI), which has been suggested as the source of backwards propagating Alfvén waves and density fluctuations (Derby, 1978; Goldstein, 1978; Tu et al., 1989; Marsch and Tu, 1990b). Stochastic phase mixing and PDI are both physical dynamic process existing outside of MHD approximations which predict passive scalar density (slow-mode) fluctuations (Schekochihin et al., 2009). Accordingly, the presence of such dynamic processes in the solar wind may introduce empirically observable deviations from scalar-compression hypothesis.

A number of previous authors have recovered a -5/3 scaling of the inertial range density fluctuations (Marsch and Tu, 1990b; Bellamy et al., 2005; Chen et al., 2011). Marsch and Tu (1990b) argued that turbulence is typically more developed for slow solar wind, driving higher density and magnitude fluctuations from which a -5/3 spectra is recovered. Their results show that high speed streams tend to have flatter spectra, a result consistent with the Issautier et al. (2010) observations from Ulysses. Chen et al. (2011) measure a -5/3 scaling for the density spectra coinciding with their measurement of magnetic field fluctuations. Previously, Bershadskii and Sreenivasan (2004) showed that the magnitude of the magnetic field in the solar wind, a signature of compressibility, attains the same high order structure function statistics as passive scalar fluctuations, suggesting that the field magnitude, indicative of compressions, obtains the same scaling and intermittent structure as the Alfvénic cascade. Hnat et al. (2003) suggest that the magnetic field magnitude show non-self-similar scaling characteristic of the Alfvénic perpendicular fluctuations, while the density fluctuations largely exhibit self-similar scalings.

Of particular interest is whether or not the density fluctuations behave as a true scalar fluctuation. Recent observations from Bowen et al. (2018b) demonstrate that the difference in spectral indices of in-

ertial range magnetic and velocity fluctuation is determined by presence of residual energy associated with intermittency; a result consistent with previous studies which identify the presence of non-zero residual energy with intermittency in the form of coherent structures such as current sheets (Salem et al., 2009; Li et al., 2011). In light of observed deviations between the spectral scalings of magnetic and velocity fluctuations associated with intermittency, it is important to consider the effects of intermittency and deviations from self-similarity on the compressible component of the solar wind. In this work the spectral fitting methodology from Bowen et al. (2018b) is used to measure the observational signatures of compressive fluctuations in comparison with the measured magnetic and velocity fluctuations. Through comparing the observed signatures of these turbulent quantities, we hope to explore the connection between the Alfvénic cascade, the coherent intermittent structures which produce it, and the supposedly scalar cascade of density fluctuations.

3.2 DATA SELECTION AND PROCESSING

Data processing follows procedures similar to previous work in Bowen et al. (2018b). Observations ranging from 1996 January 1 through 2005 December 31 are taken from instrumentation on NASA's *Wind* mission: Magnetic Field Investigation (MFI) and the Three Dimensional Plasma (3DP) experiment, (Lepping et al., 1995a; Lin et al., 1995). Data are separated into non-overlapping 1 hr intervals. Intervals are excluded if *Wind's* geocentric distance is less than $35R_E$, the bulk solar wind flow is < 250 km/s over the interval, or if more than 5% of of observations are missing from any one instrument. When data gaps totaling < 5% of an interval are present, linear interpolation is used. The resulting data consists of 39415 one hour intervals.

The 3 s cadence proton moment measurements are interpolated onto the MFI time base and separated into mean and fluctuation quantities, e. g. $n = n_0 + n_1$, where n_0 is determined using the interval time average $\langle n \rangle$. The magnetic field is normalized to Alfvén (i.e. velocity units) as $\mathbf{b}_1 = \mathbf{B}_1/\sqrt{\mu_0 \rho_0}$ where ρ_0 is the average interval proton mass density. Vector fluctuations $\mathbf{v}_1$ and $\mathbf{b}_1$ are rotated into a field aligned coordinate (FAC) system, $\mathbf{b}_{FAC} = (b_{\perp 1}, b_{\perp 2}, b_{\parallel})$, with parallel fluctuations, $b_{\parallel}$, defined along the mean field direction $\mathbf{b}_0/|b_0|$ and perpendicular fluctuations along two perpendicular $(\perp_1, \perp_2)$ directions. Additionally, parallel compressive magnetic fluctuations are obtained through the magnitude of the fluctuating magnetic field $|\mathbf{b}|$.

Several other quantities are computed for each interval including the root-mean-square (r-m-s) amplitudes of the fluctuating magnetic field, velocity, and densities:

$$\delta b_\perp = \sqrt{\langle b_{\perp 1}^2 + b_{\perp 2}^2 \rangle} \tag{3.1}$$

$$\delta b_\parallel = \sqrt{\langle b_\parallel^2 \rangle} \tag{3.2}$$

$$\delta v = \sqrt{\langle v_{\perp 1}^2 + v_{\perp 2}^2 \rangle} \tag{3.3}$$

$$\delta n = \sqrt{\langle n_1^2 \rangle}, \tag{3.4}$$

as well as the normalized cross helicity

$$\sigma_c = \frac{2\langle \mathbf{b}_1 \cdot \mathbf{v}_1 \rangle}{\langle {b_1}^2 \rangle + \langle {v_1}^2 \rangle}. \tag{3.5}$$

Intermittency for the magnetic and velocity fluctuations is typically associated with current sheets and vortices (Frisch, 1995; Matthaeus et al., 2015). Invoking the Taylor hypothesis, $\frac{\partial}{\partial t} \sim \mathbf{V_{sw}} \cdot \nabla$ allows the time derivative of magnetic field observations in the spacecraft frame to be used as a proxy for the spatial derivatives along the solar wind flow, taken as the radial Geocentric solar-ecliptic x-axis,

$$\nabla_x \times \mathbf{B} = -\frac{\partial}{\partial x} B_z \hat{y} + \frac{\partial}{\partial x} B_y \hat{z} = \frac{1}{V_{sw}} \frac{\partial}{\partial t} \left(B_z \hat{y} + B_y \hat{z} \right) \tag{3.6}$$

$$\nabla_x \times \mathbf{v} = -\frac{\partial}{\partial x} v_z \hat{y} + \frac{\partial}{\partial x} v_y \hat{z} = \frac{1}{V_{sw}} \frac{\partial}{\partial t} \left(v_z \hat{y} + v_y \hat{z} \right) \tag{3.7}$$

(Podesta and Roytershteyn, 2017).

To quantify the intermittency of the magnetic and velocity fluctuations, we use the kurtosis

$$\kappa_x = \frac{\langle x^4 \rangle}{\langle x^2 \rangle^2} \tag{3.8}$$

of the magnitudes of the measured reduced current $J = |\nabla_x \times \mathbf{B}|$ and vorticity $\omega = |\nabla_x \times \mathbf{v}|$ (Frisch, 1995; Salem et al., 2009; Matthaeus et al., 2015). Likewise, the intermittency of the compressive quantities, i.e. density and magnetic field magnitude, is obtained through the kurtosis of the time derivatives in order to compare intermittent fluctuations on consistent–i.e. the 3 s sampling–scales.

$$\kappa_n = \kappa \left(\frac{dn}{dt} \right) \tag{3.9}$$

$$\kappa_{|b|} = \kappa \left(\frac{d|b|}{dt} \right) \tag{3.10}$$

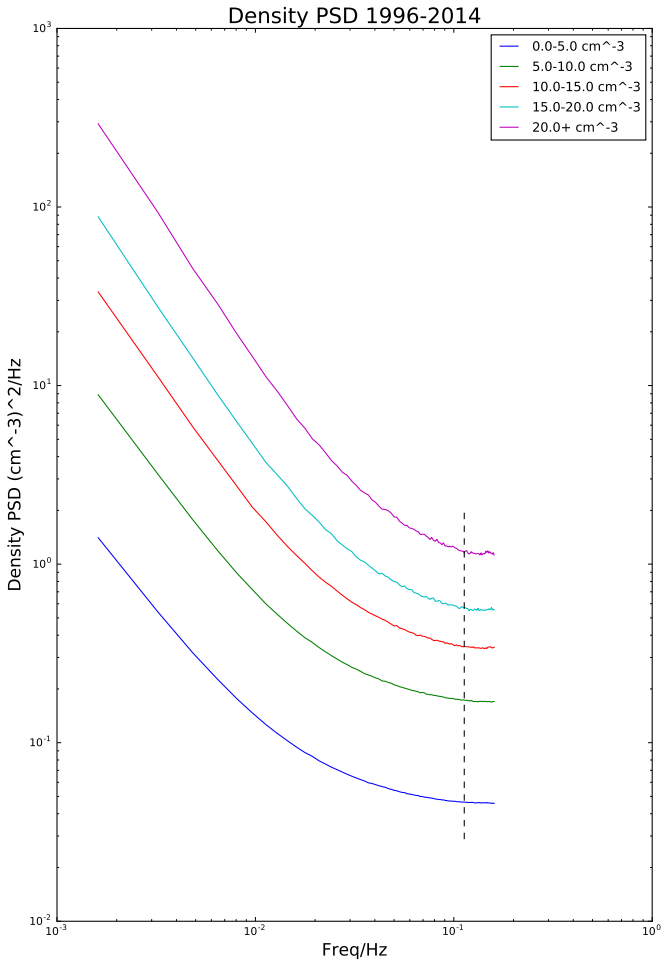

Figure 3.1: (a) Median density spectra for *Wind* 3DP proton moments binned by n_0 in intervals of 5.0 cm^{-3}. Dashed black line shows frequencies greater than 0.113 Hz (0.67 of the Nyquist frequency) used to quantify flattening). (b) Median values of quantization noise as function of n_0. For each spectra, the average spectral density higher than 0.113 Hz is recorded as n_f; with the quantization noise estimated as the median value n_f of all spectra with similar n_0, binned by 0.2 cm^{-3}.

3.2.1 QUANTIFICATION OF 3DP NOISE FLOOR

Inspection of spectral composition of 3DP density moments reveals a typical flattening at high frequencies indicative of the noise floor. On-board calculated moments from 3DP are known to be subject to instrumental noise, the spectral characteristics of which may impact measured spectra (Podesta et al., 2006, 2009; Chen et al., 2013). Through perturbing the auto-correlation function of the magnetic field to reproduce observed velocity fluctuation autocorrelations, Gogoberidze et al. (2012b) estimate the noise floor of the Wind 3DP velocity fluctuations to ≈3 km/s. Chen et al. (2013) extend this analysis through experimenting with contributions to spectral flattening from several sources of noise (Poisson, quantization, and spectral aliasing), determining that each contributes to flattening of the spectral estimate at high frequencies, while low frequencies (10^{-3} – 10^{-2} Hz) are largely unaffected. Additionally, Wicks et al. (2013b) additionally demonstrate an error on order 2 km/s through determining the statistical mode of differenced 3DP velocity moments.The perturbation approach to estimating the 3DP noise floor taken by Chen et al. (2013) and Gogoberidze et al. (2012b) require the assumption of Alfvénicity, i.e. $\delta b = \pm\delta v$; however, no analogous equality or proportionality exists enabling such a perturbation approach to determining the noise in the 3DP proton density onboard moment.

Measurements in the 3DP proton moment density noise floor are thought to limited by the log compression algorithm of the density moments Larson (2018-2019). Each density moment is compressed and telemetered as an 8-bit floating point exponential number; the first bits represent the significand coefficent and the last bits represent the order of magnitude of the exponent. For large densities, more bits are required to represent the floating point exponential such that the precision of the significand is reduced, leading to effective noise in the quantization of the density fluctuations associated with the least significant bit used in the significand of the compressed moment. Accordingly at high densities, the noise-floor in the 3DP moments is expected to be larger.

To determine the noise floor scaling with mean density, intervals of *Wind* 3DP density moments from 1996-2014 were separated into 10 minute intervals. For each 10 minute interval the power spectra was computed, and the median value of the highest frequency bins ($f > 0.113$ Hz) is measured and recorded as a noise floor. A distribution of noise floors level with mean density is computed and fit to a polynomial. The fits give an expected level of the noise in the 3DP proton density measurements as a function of mean density. Figure 3.1 shows the ensemble averaged ten minute spectra binned by mean density. The flattening observed at high frequencies suggests that even in the densest solar wind plasmas there is contribution from quantization noise. Additionally, it is evident the instrument can make best absolute measurements of the fluctuating field during intervals with low solar wind density, though flattening occurs at lower frequencies.

Figure 3.2 shows the median of the measure noise floor (measured spectral density $f > 0.113$ Hz) as a function of mean solar wind density. The measured noise floor in units $[\mathrm{cm}^{-6}/\mathrm{Hz}]$ is fit to a quadratic

$$f(n_0)[\mathrm{cm}^{-6}/\mathrm{Hz}] = An_0^2 + Bn_0 + C$$

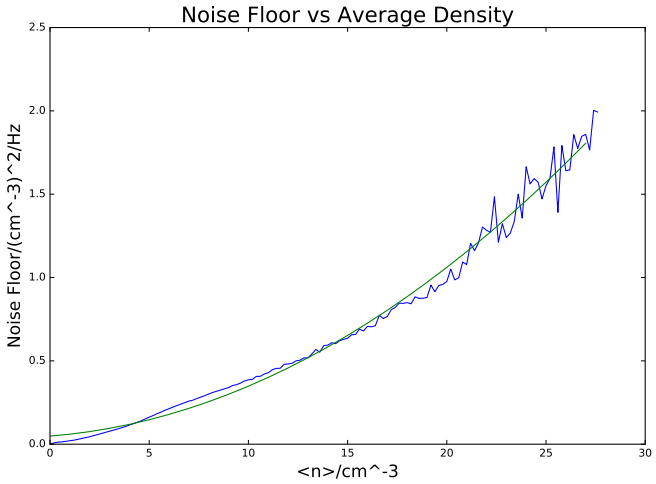

Figure 3.2: Median values of quantization noise as function of n_0. For each spectra, the average spectral density higher than 0.113 Hz is recorded as n_f; with the quantization noise estimated as the median value n_f of all spectra with similar n_0, binned by 0.2 cm^{-3}. Green curve shows the quadratic fit with coefficients A = 0.002 B = 0.009 and C = 0.049.

with the coefficients determined as A = 0.002 B = 0.009 and C = 0.049. By rejecting intervals with measured fluctuations at the level associated with the estimated quantization noise, it is possible to perform a systematic study of the spectrum of solar wind density fluctuations.

3.2.2 MEASURING SPECTRAL INDICES

Power spectra for each axis of $\mathbf{b}(t)$ and $\mathbf{v}(t)$ are obtained using fast Fourier transform (FFT) methods, with trace spectra $\tilde{E}_b(f)$ and $\tilde{E}_v(f)$ taken as the sum over each vector axis. The magnitude of the field is computed as $|\mathbf{b}|(t)$ and the power spectra taken $\tilde{E}_{|b|}(f)$. The spectrum of density fluctuations $\tilde{E}_\rho(f)$ is similarly computed.

To prevent possible contamination from outer-scale fluctuations at low frequencies as well as the 3DP noise floor at high frequencies, we fit only scales between 45 seconds to 12 minutes (~ 0.0013 – 0.0223 Hz). Each interval is interpolated to 25 logarithmically spaced frequency bins; a linear least square fit is performed in log space. Bowen et al. (2018b) show that the uncertainty spectral index estimated through FFT methods is independent of frequency in logarithmic space. For any individual interval, uncertainty in the estimated spectral index for this fit range and frequency spacing corresponds to σ_α = 0.24. This uncertainty can be reduced by fitting over a larger range of frequencies, however the relatively large amplitude of the quantization noise then requires rejecting more intervals.

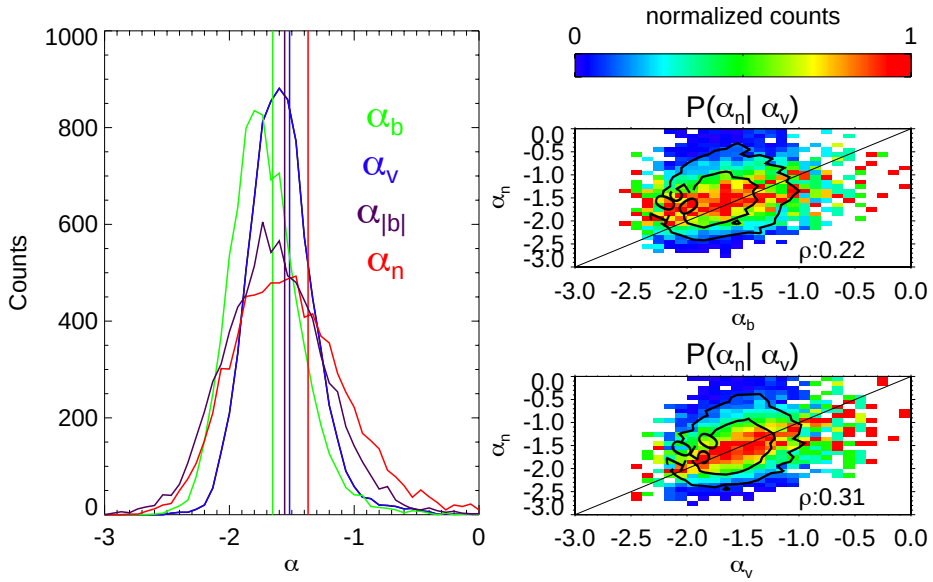

Figure 3.3: (a) Distributions of measured α_b (green), α_v (blue), $\alpha_{|b|}$ (purple), α_n (red). (b) Joint distribution of α_n and α_b normalized to the maximum number of counts for each bin of α_b a Pearson coefficient of $\rho = 0.22$ is calculated. (c) Joint distribution of α_n and α_v normalized to the maximum number of counts for each bin of α_v a Pearson coefficient of $\rho = 0.31$ is calculated. Contours show the count levels of each joint distribution.

For each interval the power law fit is then evaluated at the highest fit frequency (0.0223 Hz) and compared to the estimated noise floor for that interval. If the fit value is less than two times the level of the estimate noise floor, shown in Figure 3.2, then the interval is discounted such that we only retain fits to intervals with densities significantly above the noise floor. The resulting ensemble, after rejecting intervals with significant noise, has 7122 individual intervals (out of 39145).

3.3 RESULTS

Figure 3.3 shows the 1-D probability distribution functions of the measured spectral indices. The mean values of the measured magnetic and velocity spectral index are α_b=-1.65 and α_v=-1.51. The magnitude of the magnetic field has a mean index of $\alpha_{|b|} = -1.56$, while the density fluctuations have a mean spectral index of $\alpha_n = -1.36$. The right panels of Figure 3.3 show the joint distributions of α_n and α_b conditioned on α_b, i.e. $P(\alpha_n, \alpha_b|\alpha_b)$; as well as $P(\alpha_n, \alpha_v|\alpha_v)$ relatively small Pearson correlations of $\rho(\alpha_n, \alpha_b) = 0.22$ and $\rho(\alpha_n, \alpha_v) = 0.31$ are obtained. The relatively small variance in the distribution of observed spectra coupled with the large measurement uncertainty ($\sigma_\alpha \sim 0.24$) significantly limits the maximum expected correlation.

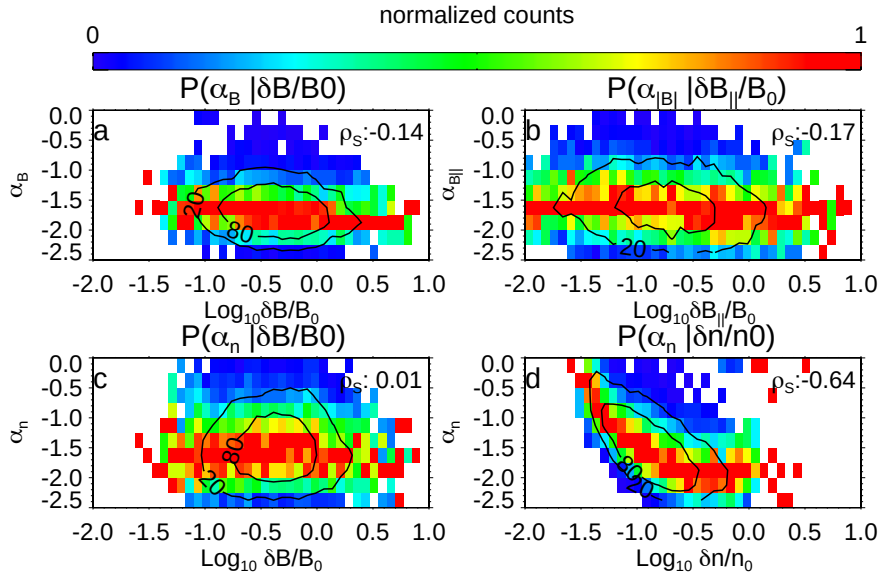

Figure 3.4: Column normalized joint distributions of spectral indices and r-m-s fluctuation amplitudes. (a) The joint distribution of the r-m-s magnetic field fluctuations $\delta b/b_0$ with α_b has relatively weak Spearman correlation of $\rho_S = -0.14$. (b) The joint distribution of the r-m-s magnitude magnetic field fluctuations $\delta|b|/b_0$ with $\alpha_{|b|}$ has a weak Spearman correlation of $\rho_S = -0.17$. (c) The joint distribution of the r-m-s fluctuations $\delta b/b_0$ with α_n has Spearman correlation of$\rho_S = -0.01$. (d) The joint distribution of the r-m-s fluctuations $\delta b/b_0$ with α_n is significantly stronger than the other distributions with Spearman correlation of $\rho_S = -0.6$

Consider a perfectly correlated ensemble, of measurements e. g. $\rho(\alpha, \alpha) = 1$, by introducing an associated zero mean Gaussian process random error with variance σ^2, the expected Pearson correlation deviates from unity:

$$\rho(\alpha + \sigma_1, \alpha + \sigma_2) = \frac{E[(\alpha + \sigma_1 - \bar{\alpha})(\alpha + \sigma_1 - \bar{\alpha})]}{(E[(\alpha + \sigma_1 - \bar{\alpha})^2]E[(\alpha + \sigma_1 - \bar{\alpha})^2])^{1/2}} = \frac{1}{1 + \frac{\sigma^2}{\sigma_\alpha^2}}, \tag{3.11}$$

where σ_α^2 is the variance of the distribution of α. For our measurements of the trace magnetic spectral index with uncertainty $\sigma_\alpha = 0.24$ and a measured dispersion $\sigma_\alpha = 0.28$, the expected Pearson correlation for perfectly correlated variables is approximately $\rho(\alpha_b + \sigma_\alpha, \alpha_b + \sigma_\alpha) \approx 0.6$. Evidently, the inherent small dynamic range of measured spectral indices in comparison with the measurement uncertainty significantly decreases the accuracy to which linear regression can establish a linear correlation between two measured spectral indices.

The top two panels of Figure 3.4 show the joint distribution of spectral index of the trace magnetic field α_b and $\alpha_{|b|}$ with the r-m-s fluctuations amplitudes $\delta b/b_0$ and $\delta|b|/b_0$; logarithmic axes are used to

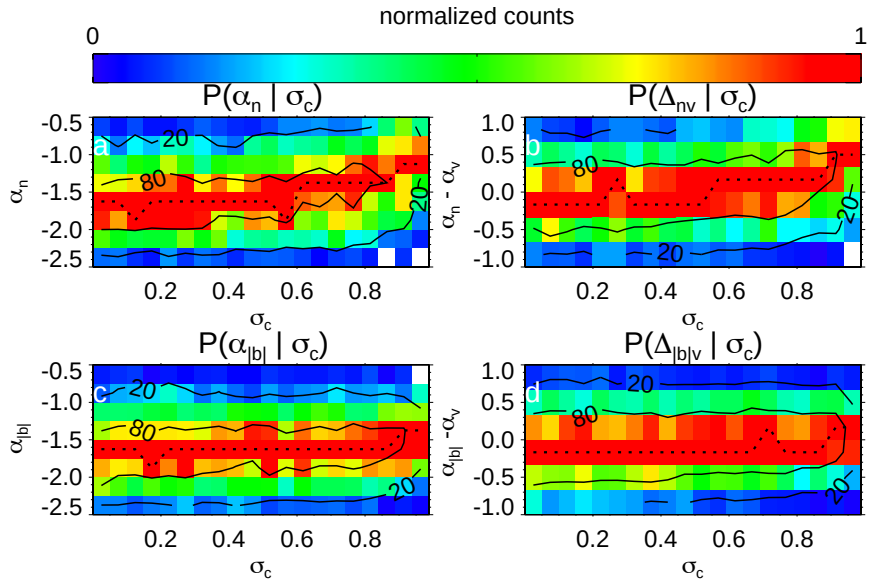

Figure 3.5: (a) The column normalized joint distribution of the density fluctuation spectral index α_n with σ_c. (b) The column joint distribution of the difference in spectral index $\Delta_{nv} = \alpha_n - \alpha_v$ with σ_c. (c) The column joint distribution of the density fluctuation spectral index $\alpha_{|b|}$ with σ_c. (d) The column joint distribution of the difference in spectral index $\alpha_{|b|} - \alpha_v$ with σ_c.

display the dynamic range of fluctuation amplitudes. Each panel is column normalized to maximum of the distribution in e. g. α_n at fluctuation amplitude $\delta n/n_0$, the notation $P(\alpha_n|\delta n/n_0)$ is introduced to represent this distribution. The Pearson correlation is inherently a test of linear relation between two sample populations, and is a poor measure of any non-linear correlation between spectral index and fluctuation amplitude. In the case of a non-linear correlation, the Spearman ranked correlation, ρ_S, provides a determination of whether a monotonic relationship exists between two sample populations.

The Spearman coefficients for the joint distributions in Figure 3.4(a,b) are $\rho_S(\alpha_b, \delta b/b_0) = -0.13$ and $\rho_S(\alpha_{|b|}, \delta|b|/b_0) = -0.17$ respectively, indicating relatively weak correlations between spectral index and r-m-s fluctuation amplitude. The bottom panels, Figure 3.4(c-d) show the joint distributions of α_n with the perpendicular magnetic fluctuations $\delta b/b_0$ and density fluctuation amplitude $\delta n/n_0$ respectively. The Spearman ranked correlation coefficients of $\rho_S(\alpha_n, \delta b/b_0) = 0.01$ indicates a very weak dependence of the density spectral index on the lamplitude of magnetic field fluctuations. However, the coefficient $\rho_S(\alpha_n, \delta n/n_0) = -0.64$ suggests a strong dependence of α_n on the amplitude of the density fluctuations. Though not pictured, the Spearman correlation between the r-m-s density fluctuation amplitudes with the trace magnetic fluctuation amplitudes is $\rho_S(\delta n/n_0, \delta b/b_0) = 0.05$ indicating the lack of a monotonic relationship between magnetic turbulent amplitude and the density fluctuations.

Figure 3.5(a) shows the joint distribution of the measured spectral index of density fluctuations α_n with the absolute value of the normalized cross helicity $|\sigma_c|$; the absolute value is chosen to improve statistics and highlights the dependence on α_n on the relative alignment of v and b. The distribution is conditioned on cross helicity, depicting the maximum of the distribution of α_n for each bin of σ_c, effectively showing the conditional probability $P(\alpha_n|\sigma_c)$. The bin resolution of α_n is equal to our measurement uncertainty σ_α to help ensure the statistical independence of each point in the plotted distribution. At large values of normalized cross helicity e. g. $\sigma_c > 0.8$, corresponding to aligned (Alfvénic velocity and magnetic fluctuations, a systematic flattening of the density spectra is observed. A similar analysis Bowen et al. (2018b) show that at high σ_c the velocity and magnetic fluctuations both attain a -3/2 spectra. Accordingly, the flattening below -3/2 suggests deviation from observation of scalar density fluctuations for high cross helicity intervals. Indeed, Figure 3.5(b) which shows the joint distribution of difference between density and velocity spectral indices $\Delta_{nv} = \alpha_n - \alpha_v$, with $|\sigma_c|$ shows a deviation of equal spectral indices in high cross helicity intervals. To ensure statistical independence, the bin resolution of the difference in spectral indices Δ is chosen as one standard deviation: $\sigma_\Delta = \sqrt{2\sigma_\alpha^2} \approx 0.33$

Figure 3.5(c) shows the joint distribution spectral index of the magnitude of the magnetic field $\alpha_{|b|}$ with the absolute value of the normalized cross helicity $|\sigma_c|$. Figure 3.5(d) shows the difference between the spectral index of the magnitude fluctuations from the trace magnetic fluctuations $\Delta_{|b|v} = \alpha_{|b|} - \alpha_v$. Unlike the density fluctuations the fluctuations in the magnetic field magnitude do not seem to deviate at high cross helicity.

3.3.1 PRESSURE BALANCE

The MHD momentum equation is given by

$$\frac{\partial \mathbf{u}}{\partial t} + (\mathbf{u}\cdot\nabla)\mathbf{u} = -\frac{1}{\rho_0}\nabla(P_{th} + P_{mag}) + \mathbf{b}\cdot\nabla\mathbf{b} \tag{3.12}$$

where pressure balance in them magnetic and thermal fluctuations leads to

$$-P_{th} = P_{mag} \tag{3.13}$$

$$-\beta\frac{n_1}{n_0} = \frac{b_\parallel}{b_0} + \frac{1}{2}\left(\frac{b_\perp}{b_0}\right)^2 + \frac{1}{2}\left(\frac{b_\parallel}{b_0}\right)^2 \tag{3.14}$$

$$\beta = \frac{c_s^2}{b_0^2} \tag{3.15}$$

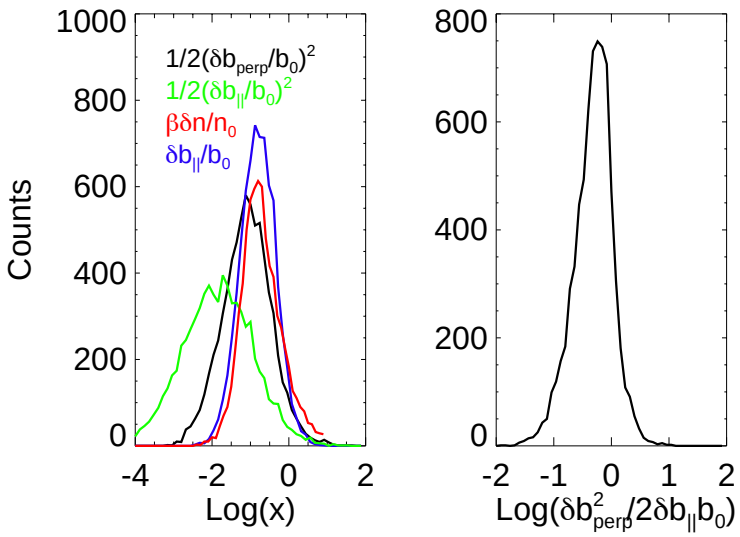

Figure 3.6: (a) Distribution of measured thermal and magnetic pressure corresponding to both first and second order quantities. The first order parallel magnetic field and thermal pressure have similar magnitudes to the contribution from the second order perpendicular magnetic field pressure. (b) Distribution of ratio of contribution to total magnetic pressure from parallel magnetic field and second order perpendicular field.

Theoretical orderings for reduced magnetohydrodynamics (RMHD) assume equal orderings between the perpendicular and parallel fluctuations commonly reduce pressure balance to the expression

$$\frac{b_\parallel}{b_0} + \beta\frac{\rho}{\rho_0} = 0, \tag{3.16}$$

with $\beta = \frac{\gamma p_0}{\rho_0 b_0}$(Strauss, 1976; Schekochihin et al., 2009). Where second order contributions to the magnetic pressure (e. g. ${b_\perp}^2 \sim {b_\parallel}^2$) are assumed to be small relative to the first order terms ($b_\parallel \sim \rho_1$).

Figure 3.6(a) shows distributions of measurements of the first and second order terms in Equation 3.14 for hour long intervals with density measurements above the measured quantization noise (note that the distributions of magnetic pressure do not change when allowing the entire set of measurements); while the first order parallel pressure term is the largest contribution to the magnetic pressure, the second order contribution from $(b_\perp/b_0)^2$ only slightly smaller than the first order parallel component ($b_\parallel/b_0$). The quantity

$$\gamma_\beta = \frac{\delta b_\perp^2}{2\delta b_\parallel b_0} \tag{3.17}$$

may be used to measure the ratio from the perpendicular to parallel contribution to magnetic pressure. Figure 3.6(b) shows the distribution of γ_β; on average, $\gamma_\beta = 0.7$, suggesting that the perpendicular Alfvénic perturbations are significantly large to contribute an equal amount to the magnetic pressure as the small amplitude parallel fluctuations. In essence, the ordering $\delta b_\parallel b_0 \sim {\delta b_\perp}^2$ suggests slightly different distribution of energy in perpendicular and parallel fluctuations than what is traditionally assumed in the RMHD ordering $\delta b_\parallel \sim \delta b_\perp$.

Defining

$$\xi_\beta = \frac{\delta b_\parallel/b_0}{\beta\delta n/n_0} \tag{3.18}$$

allows for an investigation into the effect on spectral indices from deviation in RMHD first order pressure balance. When $\xi_\beta = 1$ the measurements suggest that the parallel field and density fluctuations are in (first order) pressure balance

Figure 3.7(a,b) shows joint distributions of α_b and α_n with the pressure balance ξ_β. Intervals with magnetically dominated pressure $\xi_\beta > 1$ ($\log \xi_\beta > 0$) demonstrate a flattening of the density spectra $\alpha_n < \alpha_b$ which suggests a deviation from scalar advection by Alfvénic turbulence. No significant trend in the measured magnetic field (or velocity) spectra is observed with deviation from pressure balance.

Similarly, investigating γ_β with deviation from RMHD first order pressure balance shows that for magnetically dominated pressure intervals with $\xi_\beta > 1$, the contribution to the magnetic pressure from the perpendicular magnetic field becomes larger. Figure 3.8 shows that for $\xi_\beta > 1$ the perpendicular

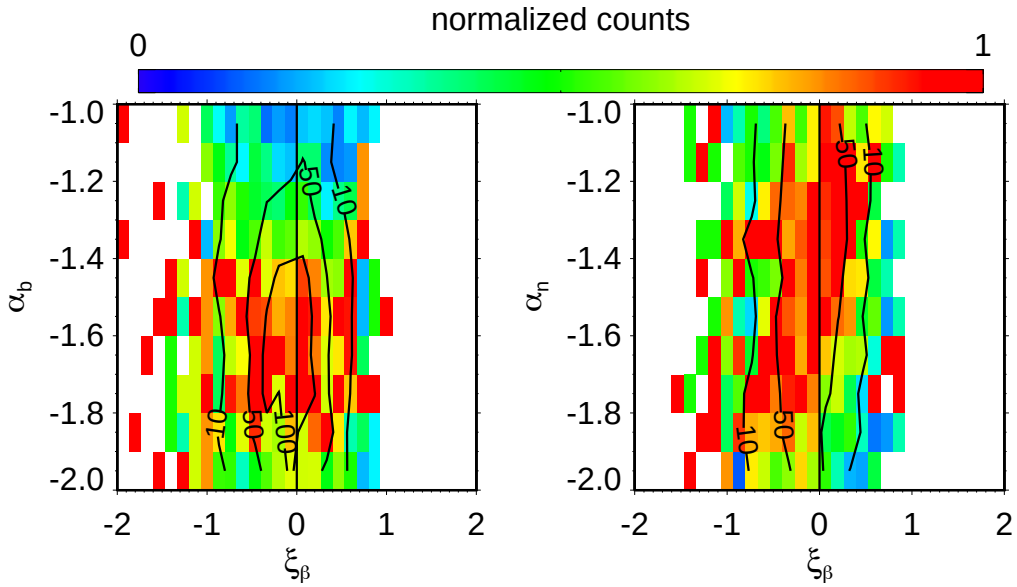

Figure 3.7: (a) Joint distribution of trace magnetic spectral index and first order magnetic-thermal pressure balance log ξ_β. (b) Joint distribution of density fluctuation spectral index and log ξ_β. Contours for data counts are shown in either plot with a line centered at log $\xi_\beta = 0$ indicating the point of pressure balance in first order quantities. Distributions are conditioned on the maximum value of spectral index in each bin of log ξ_β.

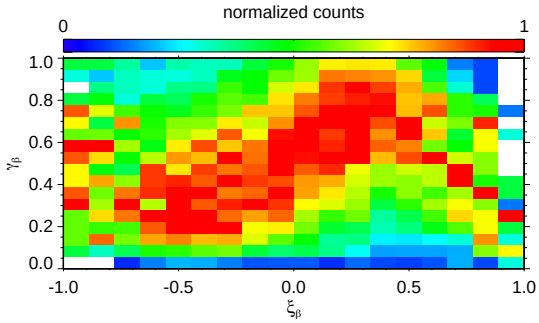

Figure 3.8: Joint distribution of pressure ratios γ_β and log ξ_β. Distributions are conditioned on the maximum value each bin of log ξ_β. When the first order fluctuations are dominated by magnetic pressure, the contribution from the second order perpendicular field becomes more significant

and parallel field pressures are equal, $\gamma_\beta \sim 1$. This result suggest that finite amplitude effects associated with the higher order pressure from perpendicular magnetic fluctuations may play a significant role in shaping pressure balance, and the compressive fluctuations.

Deviations from pressure balance with $\xi_\beta > 0$ indicative of large magnetic fluctuations may be in force free configuration such that

$$\nabla \times \mathbf{B} \times \mathbf{B} = 0 \tag{3.19}$$

where the solar wind is in an equilibrium state. This may explain the lack of large amplitude density fluctuations, and the flattening of density spectra for intervals with $\xi_\beta > 1$, as an equilibrium state can be maintained by the pressure balance of the force free magnetic field terms.

Additionally, finite amplitude effects are associated with instabilities such as the modulational instability and parametric decay Derby (1978); Goldstein (1978); Shivamoggi (1984); Jayanti and Hollweg (1993); Hollweg (1994); Bowen et al. (2018a). Further work is needed to discern whether the finite amplitude effects associated with perpendicular pressure are consistent with an instability which could drive compressive fluctuations.

3.4 INTERMITTENCY

Intermittency, understood as the deviation from self similarity in the turbulent cascade, provides another measure by which to compare the turbulent compressive fluctuations with the incompressible cascade Horbury and Balogh (1997); Hnat et al. (2003, 2005). Magnetohydrodynamic simulations of the solar wind show that passive scalars exhibit intermittent behavior similar to the actively turbulent fluctuations (Maron and Goldreich, 2001; Meyrand et al., 2019). Figure 3.9 shows the kurtosis of the reduced curl estimates (subtracted by 3 for direct comparison with Gaussian statistics) for the current density and vorticity, as well as the kurtosis of the density gradient and magnetic field magnitude gra-

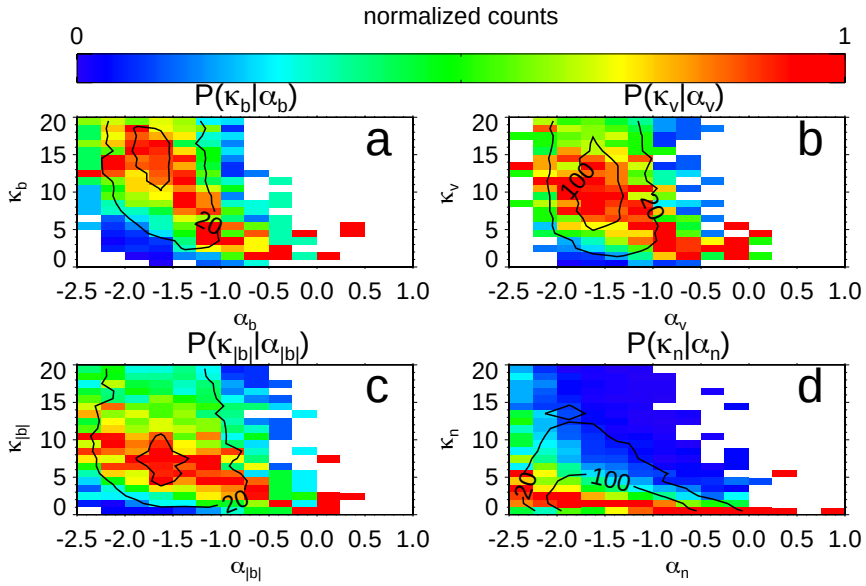

Figure 3.9: (a) The column joint distribution of the kurtosis κ_b and spectral index α_b. (b) The column joint distribution of the kurtosis κ_v and spectral index α_v. (c) The column joint distribution of the kurtosis $\kappa_{|b|}$ and spectral index $\alpha_{|b|}$. (d) The column joint distribution of κ_n with spectral index α_n.

dient. For each quantity, strong correlations are generally observed between the spectral index and and kurtosis. Consistent with the results of Bowen et al. (2018b) the trace magnetic field and velocity fluctuations both show significant intermittency, with lower levels of intermittency corresponding to flatter spectral indices. Figure 3.9(d) shows that the kurtosis of the density fluctuations is systematically lower than the other fluctuating quantities and typically obey roughly Gaussian statistics. This result can be implicitly inferred from Salem et al. (2009), demonstrating that the structure function scaling of the density fluctuations are insensitive to the removal of high-σ outliers (i.e. intermittent events). This result is similarly in agreement with Hnat et al. (2003) who obtain self-similar scalings in the density, but non-self-similar scalings of magnetic field magnitude indicative of intermittency. In contrast, the parallel compressive fluctuations taken from $|b|$ show significant intermittency, with kurtosis less than the trace magnetic field but similar to the velocity fluctuations; consistent with the work of Bershadskii and Sreenivasan (2004) demonstrating that the fluctuations of the magnetic field magnitude retain the properties of higher order structure functions moments.

Hnat et al. (2005) performed structure function analysis on solar wind density and magnetic field magnitude fluctuations, again recovering the passive scalar behavior of the magnitude fluctuations, but with observed different behavior in the density fluctuations. Figure 3.10 shows directly kurtosis of the magnitude field fluctuations $\kappa_{|b|}$ and κ_n with the kurtosis and and spectral index of the trace magnetic fluctuations κ_b, α_b, a strong correlation exists between $\kappa_{|b|}$ and κ_b, which is not observed betweenκ_n and κ_b.

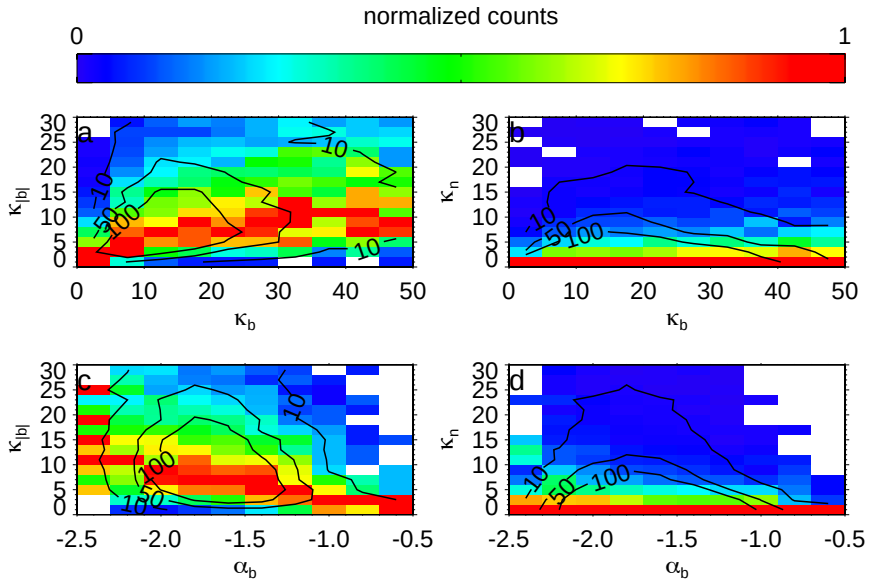

Figure 3.10: (a) The column joint distribution of the kurtosis $\kappa_{|}b|$ and k_b. (b) The column joint distribution of the kurtosis κ_n and spectral index κ_b. (c) The column joint distribution of the kurtosis $\kappa_{|b|}$ and spectral index α_b. (d) The column joint distribution of κ_n with spectral index α_b.

Given the significant correlation observed between compressive fluctuations in the magnetic field the density fluctuations reported by Yao et al. (2011); Howes et al. (2012); Bowen et al. (2018a) differences in spectral scalings and intermittency between the field magnitude and density quantities are quite striking. Indeed the known anti-correlation between parallel field and density fluctuations for the MHD slow-mode should give $\delta n = \xi \delta B$, where ξ is a negative number depending on the wave number, frequency, plasma β, and B_0. Furthermore, our results show, that it seems that the magnetic field magnitude behaves like a passive scalar, while the spectral scaling of the density fluctuations is driven primarily by the r-m-s amplitude of the fluctuations.

Additionally, Figure 3.11 shows the occurrence of of high kurtosis intervals relative to the joint distributions of $P(\alpha_n|\delta n/n_0)$ and $P(\alpha_{|}b|\delta b/b_0)$. In the magnetic field fluctuations, large kurtosis intervals occur uniformly over the $\delta b/b_0$ but coincide with steeper spectral indices–suggesting that the turbulence has innate intermittent properties irrespective of the fluctuation amplitude. However, high kurtosis in the density fluctuations occur primarily where large δ_n/n fluctuations occur, suggesting that these are associated predominantly with large amplitude fluctuations and perhaps discontinuities.

3.5 DISCUSSION

Both analytical predictions and numerical simulations suggest that compressible fluctuations in astrophysical plasmas are typically scalar quantities advected by the incompressible turbulent fluctuations

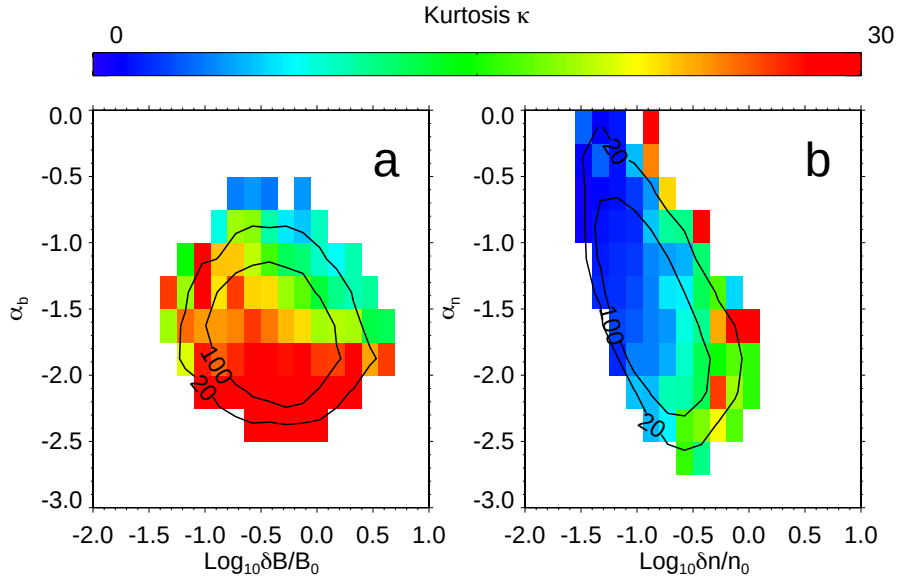

Figure 3.11: (a) The column joint distribution of the spectral index α_b with the logarithm of the fluctuation amplitude $\delta b/b_0$; the distribution is colored by the mean κ_b in each bin. (b) The column joint distribution of the density fluctuation spectral index α_n with the logarithm of the fluctuation amplitude $\delta n/n_0$; the distribution is colored by the mean κ_n in each bin.

(Higdon, 1984; Maron and Goldreich, 2001; Schekochihin et al., 2009; Chen, 2016). This hypothesis has been supported by solar windo bservations which show spectral scaling of density and field magnitude fluctuations consistent with the trace magnetic field fluctuations (Bershadskii and Sreenivasan, 2004; Chen et al., 2011). However deviations from scalar advection have been suggested by Hnat et al. (2005), who demonstrate self similarity in the density fluctuations not-characterized by the intermittency characteristic of incompressible turbulence.

Measuring the spectral scaling of compressive fluctuations with *Wind* 3DP is complicated by the presence of quantization noise which flattens observed density spectra at high frequencies. Similar spectral flattening effects have been previously noted in the 3DP velocity moments (Podesta et al., 2006, 2009; Gogoberidze et al., 2012b; Chen et al., 2013). To account for spectral flattening in density moments, the level of quantization noise is empirically determined using average characteristics of the observed flattening as a function of mean density. Though this characterization, intervals with poor signal to noise are rejected from analysis of spectral scaling.

A characteristic flattening of the density spectra associated with high cross helicity intervals is observed, suggesting deviation from the scalar advection (Figure 3.5); these intervals are associated with low mean densities. Previously Marsch and Tu (1990b) and Issautier et al. (2010) have observed the same flattening of density spectra in high cross helicity intervals. Additionally, Figure3.4 shows that strong correlation is present between the scaling of density spectra in the solar wind and the r-m-s

amplitude of the fluctuations; similar correlations between the spectral index and amplitude of incompressible turbulence are not present, which suggests a deviation from the scalar turbulent advection of the density fluctuations. However, the magnitude of the magnetic field, also a signature of the compressive fluctuations, tends to show the same spectral index and intermittent features as the incompressible turbulence even at high cross helicity. These results are consistent with those reported respectively by Bershadskii and Sreenivasan (2004) and Hnat et al. (2005).

Whether the difference between the magnitude of the magnetic field and density fluctuations can be attributed to physical processes other than scalar advection is an interesting question which warrants further study. Recent work by Verscharen et al. (2017) suggests that the MHD slow mode, in oblique propagation, is likely the source of the observed compressions; however the solar wind is typically thought to be collisionless, and it is not clear how exactly the kinetic solar wind exhibits collective and fluid-like properties well approximated by MHD. Recent observations by Bowen et al. (2018a) suggest that parametric instability could be dynamically relevant in the solar wind, while Meyrand et al. (2019) has suggested that non-linear stochastic statistical turbulent properties may counteract collisionless damping. Whether processes which counteract kinetic collisionless damping, through either injection of compressive fluctuations or a reducing the kinetic damping rates, cause deviations from scalar advection of compressible fluctuations are not well known. The observations presented here provide testable observations to test theoretical predictions of deviations from scalar advection.

The theoretical basis of the scalar advection of compressible fluctuations is understood as an effect of the ordering of RMHD which leads to first order pressure balance between the thermal pressure and the parallel portion of the magnetic field Schekochihin et al. (2009); Chen (2016). By comparing the relative sizes of the magnetic pressure terms, it is determined that the second order contribution from the perpendicular field fluctuations (incompressible Alfvénic turbulence) is frequently of similar order to the first order parallel field (Figure 3.6), violating the typical ordering assumptions. It is shown that the flattening of the density spectra again occurs during deviations from pressure balance (Figure 3.7); however it is clear that during these intervals the magnetic pressure associated with second order perpendicular fluctuations becomes a significant fraction of the first order contribution from the parallel field (Figure 3.8). The contribution of perpendicular fluctuations to the magnetic pressure suggests that either force free structures may be present in which an equilibrium state is attained; alternatively, finite amplitude effects may be present which could lead to the presence of dynamically active finite-amplitude instabilities Derby (1978); Jayanti and Hollweg (1993); Hollweg (1994).

4

DENSITY FLUCTUATIONS IN THE SOLAR WIND DRIVEN BY ALFVÉN WAVE PARAMETRIC DECAY

T. A. Bowen, S. Badman, P. Hellinger, and S. D. Bale.
Density Fluctuations in the Solar Wind Driven by Alfvén Wave Parametric Decay.
ApJ, 854:L33, February 2018a. doi: 10.3847/2041-8213/aaabbe.

ABSTRACT Measurements and simulations of inertial compressive turbulence in the solar wind are characterized by anti-correlated magnetic fluctuations parallel to the mean field and density structures. This signature has been interpreted as observational evidence for non-propagating pressure balanced structures (PBS), kinetic ion acoustic waves, as well as the MHD slow-mode. Given the high damping rates of parallel propagating compressive fluctuations, their ubiquity in satellite observations is surprising, and suggestive of a local driving process. One possible candidate for the generation of compressive fluctuations in the solar wind is Alfvén wave parametric instability. Here we test the parametric decay process as a source of compressive waves in the solar wind by comparing the collisionless damping rates of compressive fluctuations with growth rates of the parametric decay instability daughter waves. Our results suggest that generation of compressive waves through parametric decay is overdamped at 1 AU, but that the presence of slow-mode like density fluctuations is correlated with the parametric decay of Alfvén waves.

4.1 INTRODUCTION

Observations of the solar wind contain a characteristic anti-correlation between density fluctuations and magnetic perturbations parallel to the mean field. Tu and Marsch (1994) interpreted observed correlations on hourly timescales between magnetic pressure, thermal pressure, and density fluctuations from *Helios* as non-propagating pressure balance structures (PBS). Using spacecraft potential measurements as a proxy for density fluctuations, Kellogg and Horbury (2005) reported the same anti-correlation in *Cluster* data, noting that PBS are consistent with the perpendicular limit of the ion-acoustic wave. Yao et al. (2011), using wavelet coherence analysis, demonstrated this anti-correlation

through the range of inertial scales; subsequent work interpreted these observations as PBS driven by either slow-modes or mirror modes arising from temperature anisotropies (Yao et al., 2013a,b). Through statistical analysis of a decade of *Wind* observations, Howes et al. (2012) attributed the compressible component of magnetic fluctuations entirely to the kinetic slow-mode. However, comparisons between a decade of *Wind* observations and numerical predictions made in both kinetic and MHD simulations by Verscharen et al. (2017) suggest that the MHD slow-mode best explains the compressible component of the solar wind.

Strong collisionless Landau damping of kinetic slow-mode waves propagating parallel to the magnetic field is expected for solar wind parameters at 1 AU (Barnes, 1966). For this reason, the generation, presence, and damping of kinetic slow-mode fluctuations in the solar wind remains an open question in space physics. Klein et al. (2012) argued that the distribution of slow-mode waves in the solar wind is consistent with critically balanced turbulence, in which non-linear interactions between Alfvénic and slow-mode fluctuations cascade weakly damped perpendicular compressible fluctuations at large scales to smaller parallel scales. The damping of these waves could provide a source of heating in the solar wind (Narita and Marsch, 2015).

In this letter, we explore the parametric decay instability (PDI) as a process for generating compressive fluctuations in the solar wind. In MHD, the PDI is recognized as the instability of circularly polarized Alfvén eigenmodes at high fluctuation amplitudes (Derby, 1978; Goldstein, 1978). For low β plasmas, the large amplitude Alfvénic fluctuation (mother wave) couples to two daughter waves: a parallel propagating compressive fluctuation, and a backwards propagating Alfvén wave. A class of parametric instabilities exist outside the low β PDI decay: e.g. at $\beta \geq 1$ the instability is dominated by the growth of forward propagating Alfvénic daughter waves at twice the mother wave frequency (Jayanti and Hollweg, 1993; Hollweg, 1994).

Simulations of high amplitude circularly polarized Alfvén waves have verified the PDI process in the MHD regime, and have suggested that PDI daughter waves can seed turbulent cascades Del Zanna et al. (2001); Tenerani and Velli (2013); Malara et al. (2001). Simulations have extended the PDI to large amplitude Alfvén waves with arc and linear polarizations, non-monochromatic wave distributions, and oblique propagation Del Zanna (2001); Matteini et al. (2010a); Del Zanna et al. (2015). Furthermore, kinetic simulations recover PDI in multi-species models, including effects such as, the preferential heating of α particles, proton core heating, and beam formation Araneda et al. (2008); Araneda et al. (2009); Kauffmann and Araneda (2008). Numerical simulations of PDI in a turbulent solar wind demonstrate the generation of slow-mode fluctuations from the decay of Alfvénic fluctuations in a relatively robust theoretical scenario Shi et al. (2017).

4.2 DATA

We use 10 years of solar wind measurements at 1AU from the NASA *Wind* mission ranging from 1996 January 1 through 2005 December 31. Data from the Magnetic Field Investigation (MFI) Lepping

et al. (1995a), Solar Wind Experiment (SWE) Ogilvie et al. (1995), and Three Dimensional Plasma (3DP) experiment Lin et al. (1995) are separated into non-overlapping 300 second intervals. Intervals are excluded when *Wind's* geocentric distance is less than $35R_E$, the average solar wind speed is < 250 km/s, or if an interval is missing $> 15\%$ of coverage from any instrument. Data gaps are interpolated when $< 15\%$ of measurements are missing. Additionally, intervals are excluded if there is significant discrepancy between 3DP and SWE measurements of mean proton density such that $|(n_{SWE} - n_{3DP})|/n_{SWE} > 0.1$. The resulting data set consists of 533222 individual 300 second intervals. Techniques from Pulupa et al. (2014) were used to obtain electron densities and temperatures for 282286 of these intervals.

The 3 s cadence 3DP "on board" proton moment measurements are interpolated to the MFI time base. For each interval, measurements of density, velocity, and magnetic field (represented as n, $\mathbf{v}$, and $\mathbf{B}$) are separated into mean and fluctuation quantities using time averaged quantities, denoted as $\langle ... \rangle$. For example, the mean magnetic field, $\mathbf{B_0}$, is determined through $\langle \mathbf{B} \rangle = \mathbf{B_0}$ while the fluctuation field is determined through $\mathbf{B} = \mathbf{B_0} + \delta\mathbf{B}$. Vector fluctuations are rotated into a field aligned coordinate (FAC) system, $\delta\mathbf{B}_{FAC} = (\delta B_{\perp 1}, \delta B_{\perp 2}, \delta B_{\parallel})$, with the parallel fluctuations, $\delta B_{\parallel}$, defined along the mean field direction $\mathbf{B_0}/|B_0|$.

Each interval is characterized through root-mean-square (RMS) quantities normalized to the mean value

$$\bar{\delta n} = \sqrt{\langle \delta n^2 \rangle}/n_0.$$

Vector fluctuations characterizing each interval separated into parallel and perpendicular RMS values of the form

$$\delta \bar{B}_{\perp} = \frac{\sqrt{\langle \delta B_{\perp}^2 \rangle}}{B_0} = \frac{\sqrt{\langle \delta B_{\perp 1}^2 + \delta B_{\perp 2}^2 \rangle}}{B_0}$$

and

$$\delta \bar{B}_{\parallel} = \frac{\sqrt{\langle \delta B_{\parallel}^2 \rangle}}{B_0}.$$

The FAC fluctuation quantities are used in deriving Elsässer variables,

$$\mathbf{z}^{\pm} = \delta\mathbf{v}_{FAC} \pm \delta\mathbf{b}_{FAC};$$

normalized cross helicity,

$$H_c = \frac{\langle \delta\mathbf{b}_{FAC} \cdot \delta\mathbf{v}_{FAC} \rangle}{\langle \delta b^2 \rangle + \langle \delta v^2 \rangle};$$

and the zero lag cross correlation between parallel field fluctuations and density,

$$C(\delta n, \delta B_{\parallel}) = \frac{\sum_{i=0}^{N-1} \delta n_i \delta B_{\parallel i}}{\sqrt{\sum_{i=0}^{N-1} \delta {n_i}^2} \sqrt{\sum_{i=0}^{N-1} \delta {B_{\parallel}}_i^2}}.$$

The magnetic field has been normalized as $\delta\mathbf{b} = \delta\mathbf{B}/\sqrt{\mu_0 n_p m_p}$.

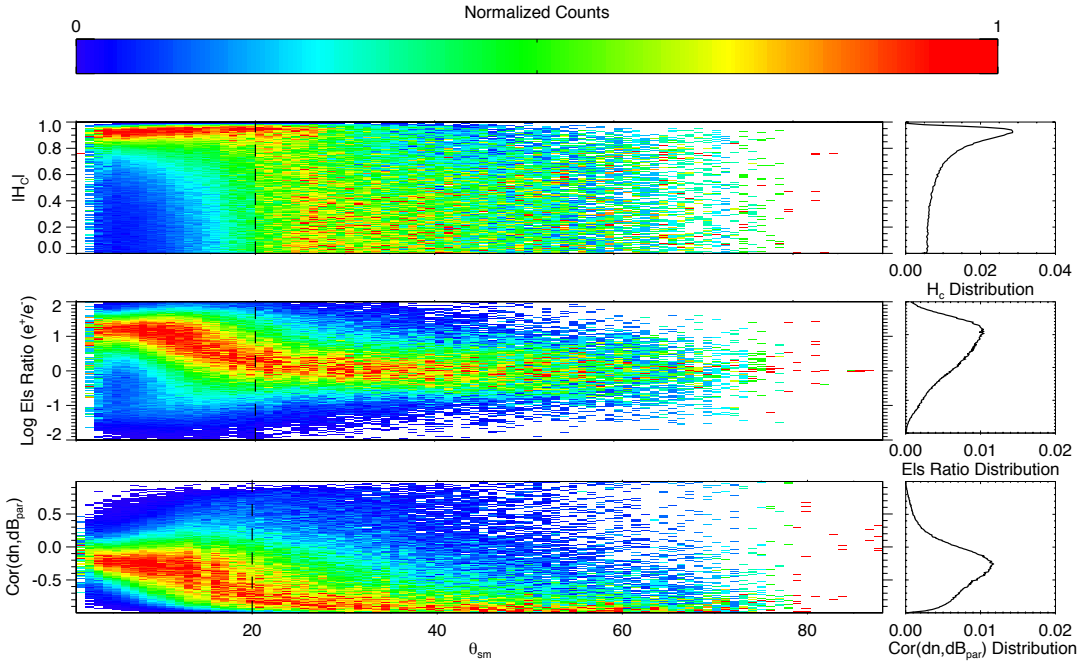

Figure 4.1: (Top) Joint distribution of normalized cross helicity, H_c and slow-mode propagation angle θ_{sm}. Data are column normalized within each angle bin. The distribution of H_c observations shown on the right. (Middle) Column normalized distribution of the Elsässer ratio and θ_{sm}. The distribution of Elsässer ratios is plotted to the right. (Bottom) Joint distribution of $C(\delta n, \delta B_{\parallel})$, and the slow-mode propagation angle, θ_{sm}. The data are column normalized and the distribution of $C(\delta n, \delta B_{\parallel})$ observations plotted to the right. A dashed line identifies a transition observed in all three panels at $\theta_{sm} \sim 20^{o}$.

4.3 MODEL PROPAGATION DIRECTION

For slow-mode waves with propagation vector, $\mathbf{k}$, such that $\mathbf{k} = (k_{\perp 1}, 0, k_{\parallel})$ it follows that $\delta\mathbf{v} = (\delta v_{\perp 1}, 0, \delta v_{\parallel})$. From the MHD induction equation $\omega\delta\mathbf{B} = (\mathbf{k}\cdot\delta\mathbf{v})\mathbf{B_0} - (\mathbf{k}\cdot\mathbf{B_0})\delta\mathbf{v}$, it is derived that

$$\tan\theta_{sm} = \left|\frac{k_{\perp}}{k_{\parallel}}\right| = \left|\frac{\delta B_{\parallel}}{\delta B_{\perp}}\right|,$$

where θ_{sm} gives the slow-mode propagation angle relative to the mean magnetic field.

The limit of small $\delta B_{\parallel}$, corresponds to quasi-parallel propagation of the slow-mode. For exact parallel propagation, $\delta B_{\parallel} = 0$, the compressive component of the slow-mode becomes purely acoustic, while the perpendicular fluctuations obey the dispersion for parallel propagating shear Alfvén waves.

In this quasi-parallel limit, our model for slow-mode propagation angle resembles parallel Alfvénic fluctuations.

Figure (top) shows joint probability distributions of $|H_c|$ and θ_{sm} normalized to the maximum counts in each column. For a shear Alfvén wave $H_c = \pm 1$; our observations show that, for small propagation angles, the majority of intervals have a cross-helicity similar to shear Alfvén waves.

Figure (middle) shows the column normalized joint distribution of θ_{sm} and the ratio of Elsässer energies: e^+/e^-, where $e^\pm = \langle (z^\pm)^2 \rangle$. Intervals consisting of pure outward propagating Alfvén waves have large Elsässer ratios: i.e. intervals with $z^+ \gg z^-$ correspond to $e^+ \gg e^-$. Intervals containing balanced compositions of z^- and z^+ fluctuations have Elsässer ratios ~ 1. We find that intervals with small propagation angles are dominated by z^+ fluctuations. Intervals with larger θ_{sm} show balanced z^+ and z^- energies, suggesting that these intervals are not easily represented as single wave fluctuations, but must be modeled by either counter-propagating Alfénic fluctuations or a quasi-linear superposition of wave-modes (Klein et al., 2012).

Figure (bottom) shows the the column normalized joint distribution of $C(\delta n, \delta B_\parallel)$ and θ_{sm}. The transition to highly anti-correlated density δn and parallel magnetic fluctuations $\delta B_\parallel$ occurs at approximately the same propagation angle, $\theta_{sm} \sim 20^\circ$, as cross helicity decreases and the Elsässer energies balance.

Two regimes are apparent: the first consists of intervals characterized by large cross helicity and 'outward' propagating energies. The second regime consists of highly compressible intervals with mixed cross helicity, balanced Elsässer energies, and strong density-field correlations consistent with slow-mode fluctuations. Howes et al. (2012) restricted analysis to intervals with $\delta n > 0.5$ cm^{-3}, arguing that lower density intervals may be subject to instrumental noise; the uniform and simultaneous transitions in H_c, e^+/e^-, and $C(\delta n, \delta B_\parallel)$ with θ_{sm} without restricting density amplitudes suggests that our analysis is insensitive to noise due to low amplitude densities.

4.4 DAMPING

Historically, the presence of kinetic slow-mode fluctuations in the solar wind has been questioned due to the heavy collisionless damping expected for solar wind parameters at 1 AU. (Barnes, 1966). However, Figure (bottom) reveals the presence of compressive fluctuations with relatively parallel propagation (e.g. $\theta_{sm} \sim 20^o$). Verscharen et al. (2017) previously argued that observations of the compressive solar wind plasma are best represented as oblique, weakly damped, MHD slow-mode waves which propagate more freely through the heliosphere; we adopt their expression for ion acoustic (IA) damping rates:

$$\gamma_{IA}/\omega_s \simeq -\sqrt{\pi}\frac{c_s^3}{w_{\parallel p}^3}\frac{e^{-c_s^2/w_{\parallel p}^2}}{1+3w_{\parallel p}^2/c_s^2}, \tag{4.1}$$

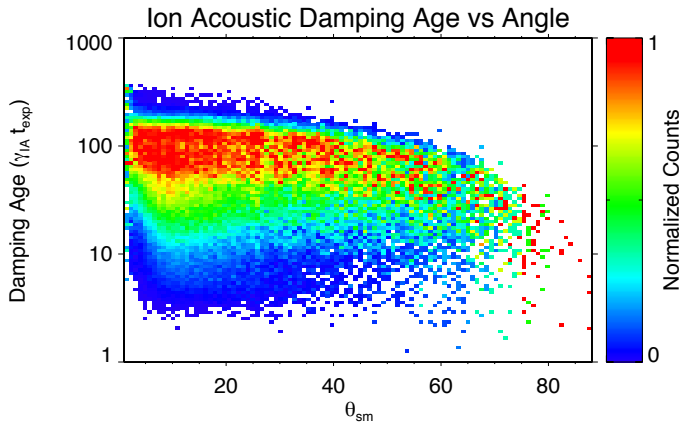

Figure 4.2: Joint distribution of expansion normalized ion-acoustic damping rates, $\gamma_{IA}t_{exp}$, (t_{exp} = 1AU/V_{sw}) and slow-mode propagation angle θ_{sm}. Data are restricted to intervals with fitted electron temperatures. The distribution is column normalized in each angle bin. Damping ages, $\gamma_{IA}t_{exp}$, are uniformly greater than unity.

where the ion acoustic frequency is $\omega_s = k_{\|}c_s$, the parallel thermal proton speed is $w_{\|p} = \sqrt{2k_BT_{\|p}/m_p}$, the sound speed is

$$c_s = \sqrt{\frac{3k_BT_{\|p} + k_BT_{\|e}}{m_p}},$$

$k_{\|} = k\cos\theta_{sm}$, m_p is the proton mass, and $T_{\|j}$ is the parallel temperature for species j.

Figure 4.2 shows IA damping rates normalized to the solar wind expansion time t_{exp} = 1AU/V_{sw} as a function of θ_{sm}. Data are restricted to intervals with fits of electron distributions (Pulupa et al., 2014). The majority of expansion normalized damping ages are above 10, and uniformly above unity, suggesting that even highly oblique propagating kinetic slow-mode like fluctuations undergo significant damping over 1 AU propagation.

Figure 4.3 (top) shows the column normalized joint distribution of $\delta\bar{n}$ and $C(\delta n, \delta B_{\|})$ while Figure 4.3 (bottom) shows that the slow-mode correlation emerges even for quasi-parallel propagation ($\theta_{sm} < 20^o$). If these fluctuations are associated with a strongly damped kinetic slow-mode, then their presence at 1 AU demands a local driving process.

4.5 PARAMETRIC DECAY

To test whether parametric coupling between wave modes generate compressive fluctuations from the decay of large amplitude Alfvénic fluctuations we compare our observations with analytically derived parametric growth rates. Following Derby (1978) and Goldstein (1978), a dispersion relation for the evolution of a compressive wave coupled to an MHD mother wave is given by:

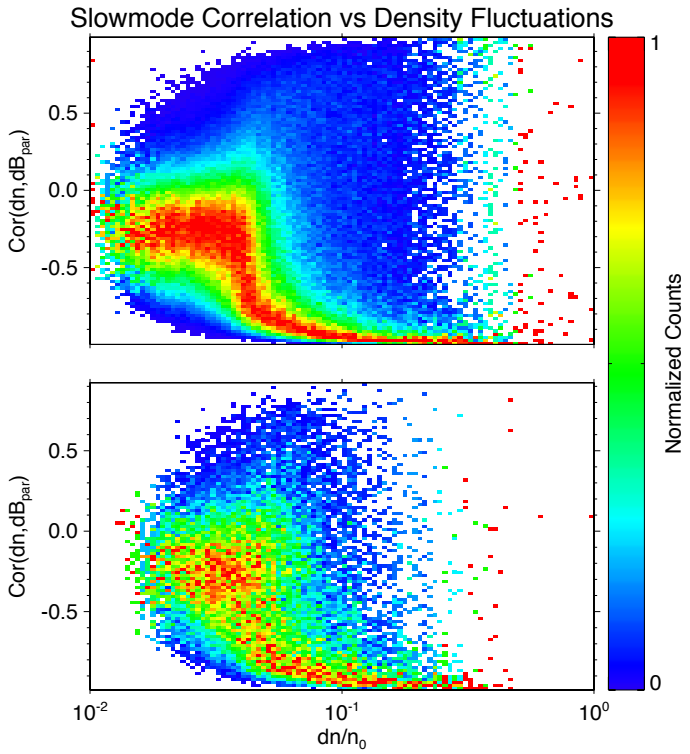

Figure 4.3: (Top) Joint probability distribution of density-parallel magnetic fluctuation cross-correlation, $C(\delta n, \delta B_{\parallel})$, and density fluctuation amplitude, $\bar{\delta n}$. (Bottom) Restricting data to intervals with $\beta < 0.5$ and $\theta_{sm} < 20^{o}$ reveals the presence of fluctuations with slow-mode like density-field correlations propagating quasi-parallel to the mean magnetic field. Data are column normalized to the maximum counts of $C(\delta n, \delta B_{\parallel})$ in each $\bar{\delta n}$ bin.

$$(\omega + k + 2)(\omega + k - 2)(\omega - k)(\omega^2 - \beta k^2) - \left(\frac{\delta B_{\perp}}{B_0}\right)^2 k^2(\omega^3 + k\omega^2 - 3\omega + k) = 0. \quad (4.2)$$

This 5$^{\text{th}}$ order polynomial, with k and ω corresponding to wave number and frequency of the compressive daughter wave normalized to mother wave quantities, depends only on β and $\delta B_{\perp}/B_0$. There is a small range of $k_L < k < k_U$ for which a single conjugate pair of complex solutions exist. The imaginary part of the solution, i.e. the parametric decay rate γ_{pd}, corresponding to the fastest growing decay product is determined numerically given observed values of β and $\delta \bar{B}_{\perp}$.

Figure 4.4 (left) shows the joint distribution of $\delta \bar{B}_{\perp}$ and β. Contours of numerically determined γ_{pd}/ω_0, plotted as solid black lines, bound the data at $\gamma_{pd}/\omega_0 \sim 0.05 - 0.1$, suggesting that the solar

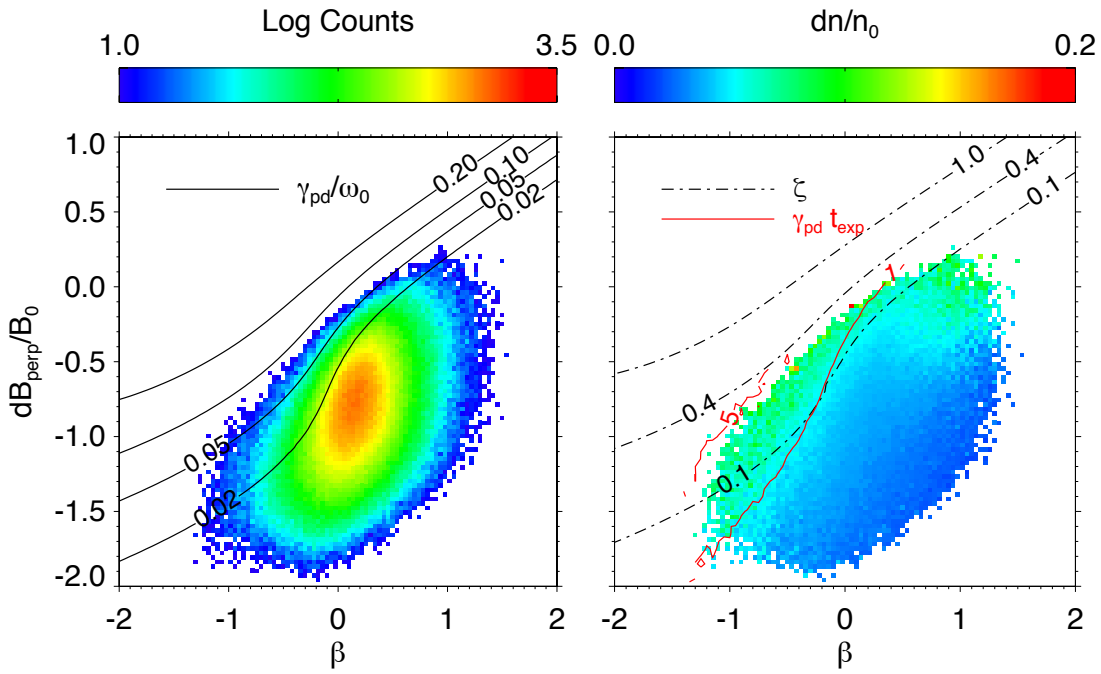

Figure 4.4: (Left) Joint distribution of $\delta\bar{B}_\perp$ and β. Contours of the parametric growth rate normalized to the linear wave frequency are shown in solid black. Data are bounded by high PDI growth rates. (Right) Joint distribution of $\delta\bar{B}_\perp$ and β with color scale given by mean values of $\bar{\delta n}$. Contours of the expansion normalized parametric decay rate, $\gamma_{pd}t_{exp}$ shown in red, suggest that several iterations of the decay may occur over 1 AU propagation. Contours of $\zeta = \frac{\gamma_{pd}/\omega_0}{\gamma_{IA}/\omega_s}$ are shown in dashed black lines. Though large density fluctuations correspond to the largest values of ζ, generation of density fluctuations through PDI is overdamped.

wind at 1 AU is bounded by PDI growth. Figure 4.4 (right) shows the same distribution of $\delta\bar{B}_\perp$ and β with the average value of $\bar{\delta n}$ projected onto the plane. The median $\bar{\delta n}$ is 0.034, ranging between [0.01, 1.10]. Our results show that intervals with the largest density fluctuations correspond to intervals of high parametric growth rates.

Two sets of contours are overlaid in Figure 4.4 (right). The first set, $\gamma_{pd}t_{exp}$ plotted in red, correspond to PDI growth rates normalized to solar wind expansion time. Normalizing by expansion timescale requires estimating γ_{pd}, with physical units of s^{-1}, from contours of γ_{pd}/ω_0. Using

$$\omega_0 = k_\parallel V_{alf},$$

where k is given by the Taylor hypotheses, $k = 1/(\tau V_{sw})$, where τ is the interval duration (300 s), and $k_{\parallel} = k\cos\theta$, it follows that,

$$\gamma_{pd} t_{exp} = \frac{\gamma_{pd}}{\omega_0} \frac{1\text{AU}}{\tau} \frac{V_{alf}}{V_{sw}^2} \cos\theta. \tag{4.3}$$

Contours of γ_{pd}/ω_0, are normalized using mean values of V_{sw} and V_{alf} in each bin of the joint $\delta\bar{B}_{\perp}$ and β distribution. We choose an oblique propagation angle of $\theta = 80°$ in accordance with observations of anisotropy in the solar wind (Horbury et al., 2008). At oblique propagation angles $\cos\theta$ varies weakly with θ, implying that our results are robust to specific oblique angle chosen. Previous work by Matteini et al. (2010a) and Del Zanna et al. (2001) has shown that the decay of oblique waves is analogous to parallel decay, scaling as $\cos\theta$; furthermore, Chandran (2017) demonstrate that non-linear PDI interactions for oblique waves occur between parallel components, generating an inverse parallel cascade of Alfvén waves.

Figure 4.4 (right) shows that intervals undergoing a single iteration of parametric decay demonstrate enhanced density fluctuations, suggesting that density fluctuations are correlated with growing compressive PDI daughter waves. Though parametric decay rates measured at *Wind* are fairly small, propagation over 1AU allows for growth of the instability. Additionally, contours of $\gamma_{pd} t_{exp}$ show that PDI growth could be smaller than our theoretical rates for circularly polarized, parallel propagating waves, and still generate compressive fluctuations at 1AU.

Uncertainty in contours of $\gamma_{pd} t_{exp}$ are determined through the fractional error of Equation 4.3, derived as

$$\frac{\Delta(\gamma_{pd} t_{exp})}{\gamma_{pd} t_{exp}} = \sqrt{\left(4\frac{\Delta V_{sw}}{< V_{sw} >}\right)^2 + \left(\frac{\Delta V_{alf}}{< V_{alf} >}\right)^2 - 4\frac{\Delta V_{sw}\Delta V_{alf}}{V_{sw} V_{alf}}} \tag{4.4}$$

The ensemble mean values follow as $< V_{sw} >= 453$ km s^{-1} and $< V_{alf} >= 60$ km s^{-1}, with standard deviations of $\Delta V_{sw} = 108$ km s^{-1} and $\Delta V_{alf} = 34$ km s^{-1} respectively. Measurements of V_{alf} and V_{sw} are correlated with a value of $\rho = 0.38$. Evaluating $\Delta(\gamma_{pd} t_{exp})/\gamma_{pd} t_{exp}$ gives fractional uncertainty on the contours of 60%. For a single instance of the parametric decay, $\gamma_{pd} t_{exp} = 1$, uncertainty of 60% does not significantly impact the contour location.

The second set of contours in Figure 4.4 (right), $\zeta = \frac{\gamma_{pd}/\omega_0}{\gamma_{IA}/\omega_s}$, represent the ratio of PDI growth rates to IA damping rates. High values of ζ presumably indicate the presence of driven compressive daughter waves. Intervals with low values of ζ should dissipate compressive fluctuations faster than the PDI can drive them. Contours of ζ are constructed by normalizing the contours of γ_{pd}/ω_0 to the observed median dimensionless damping rates, median(γ_{IA}/ω_s). For intervals with available electron fit data and $\beta < 0.5$ the median value of γ_{IA}/ω_s is 0.26, with a standard deviation of ~ 0.05. This leads to a fractional error to the contours of $\Delta\zeta/\zeta \sim 15\%$. Figure 4.4 (right) shows that though intervals with

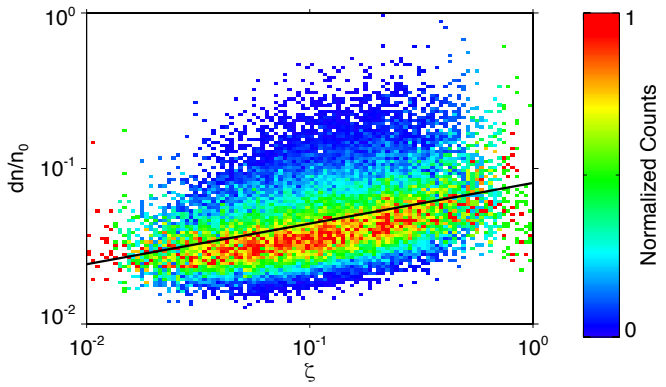

Figure 4.5: Distribution of $\delta\bar{n}$ and ζ. Data are column normalized to each ζ bin. A least squares fit to the data, shown as a black line, gives a power law of 0.25 and a Pearson correlation of 0.36.

large density fluctuations occur with greater values of ζ, compressive fluctuations driven by parametric decay are overdamped, i.e. have PDI growth rates less than IA damping rates.

Figure 4.5 shows the scaling of $\delta\bar{n}$ with ζ computed for each interval. Data are restricted to $\beta < 0.5$, where PDI generates compressive daughter waves. A positive correlation is observed between the density fluctuations and ζ. A least squares fit in logarithmic space suggests a power law relationship of $\delta\bar{n} \sim (\zeta)^{0.26}$ with a Pearson cross correlation of $\rho = 0.36$; again we note that approximately 99% of the data are overdamped. When a least square fit is performed between $\delta\bar{n}$ and the dimensionless parametric growth rate, γ_{pd}/ω_0 we recover a power law relation of $\delta\bar{n} \sim (\gamma_{pd}/\omega_0)^{0.26}$ and a Pearson correlation of $\rho = 0.37$. Suggesting that density fluctuations $\delta\bar{n}$ are weekly dependent on the IA damping rate. Additionally, the positive correlation between parametric instability growth rate and density fluctuations in the solar wind suggests that compressive fluctuations may be related to PDI. Both of these correlations are stronger than the correlation between amplitudes of $\delta\bar{B}_\perp$ and $\delta\bar{n}$, for which we find $\rho = 0.24$.

4.6 DISCUSSION

Our results show that the compressive component of solar wind plasma is not restricted to fluctuations propagating perpendicular to the magnetic field. If these compressive fluctuations correspond to a kinetic slow-mode, their presence likely requires a driving process. Previous work has invoked a scalar turbulent cascade to explain the replenishing of slow-mode like fluctuations (Klein et al., 2012; Chen et al., 2012).

In this letter, we suggest that parametric coupling of large amplitude Alfvén waves to compressional modes may exist in the solar wind. We consider parametric decay as a low β parallel process; however,

the decay of oblique shear Alfvén waves generates a spectrum of fluctuations over a range of angles relative to the mean magnetic field (Matteini et al., 2010a). One complication is that the parametric growth rates adopted from Derby (1978) are relevant for low β plasmas; however, we note that Tenerani et al. (2017) demonstrate that pressure anisotropies allow PDI growth at higher β.

Parametric decay has been verified in analytic and computational studies but it has yet to be observed in the solar wind. Parametric coupling is an attractive physical mechanism for explaining compressive fluctuations in the solar wind for two reasons. First, backwards propagating Alfvénic fluctuations, a product of PDI, are required for non-linear interactions leading to critically balanced turbulence (Tenerani and Velli, 2013; Malara et al., 2001). Second, parametric coupling preferentially excites slow-mode fluctuations; which may explain the distribution of fluctuations observed at 1 AU: Alfvénic ~ 90%, slow-mode ~ 10%, and very little fast-mode contribution (Klein et al., 2012).

The results presented in Figure 4.4 in which slow-mode fluctuations are observed simultaneously with balanced (i.e. equally distributed backwards and forwards propagating Alfvénic fluctuations) intervals provide compelling observational evidence for parametric decay. Furthermore, observations from *Wind* show that high PDI growth rates bound the distribution of data, suggesting that parametric coupling may limit the amplitude of Alfvénic fluctuations. The results in Figure 4.4 show that intervals of solar wind which undergo a single growth of parametric decay have enhanced density fluctuations.

We note that the IA damping term given in Equation 4.1 is greater than PDI growth rates. However, we also highlight the results of Verscharen et al. (2017), which suggest that slow-mode fluctuations in the solar wind are fluid like with low damping rates. Reducing IA damping by approximately a factor of 5 would provide underdamped growth of compressive fluctuations through PDI. Additionally, scaling arguments give much higher PDI rates in the inner heliosphere, increasing generation of compressive waves through PDI near the sun (Tenerani and Velli, 2013). The launch of the NASA Parker Solar Probe mission in July 2018 will reveal whether parametric coupling between fluctuations play an increased role in the inner heliosphere.

In considering the growth rate of the PDI relative to the linear wave time, ω_0, we do not take into account the effect of turbulence solar wind. The non-linear interaction time between Alfvénic fluctuations likely plays an important role in parametric coupling. Specifically, it is likely that a critically balanced cascade with non-linear interactions occurring on order the wave propagation time could disrupt parametric coupling between Alfvénic and slow-mode like fluctuations Schekochihin et al. (2009). This idea has been touched upon in Shi et al. (2017), in which reduced PDI growth rates were found in a turbulent plasma. Our future work looks to address the physics of parametric coupling in a turbulent plasma and to compare the growth of compressive modes through PDI versus their recycling through a turbulent cascade.

CONCLUDING PART I

Part I of this dissertation has introduced the historical and mathematical background of magnetohydrodynamic turbulence (Chapter 1) in the solar wind as well as common observational techniques used in studying non-linear interactions in the solar wind (Chapters 2 3,4). The observational difficulties associated with studying non-linear processes with single point *in-situ* measurements are quite evident, as highlighted both with measurement uncertainties, as well as ambiguities in spatiotemporal evolution of the solar wind. To better understand the non-linear evolution of the solar wind, e.g. to discriminate between propagation effects from different sources of the solar wind in the corona as it propagates through the heliosphere, it is imperative to understand the conditions of the solar wind at the point of its generation. The low densities of the interplanetary medium and upper boundary corona preclude study through remote sensing. Additionally, small scale structures, where heating in dissipation can occur, can not be resolved with optical techniques. As a result of, there is little empirical knowledge regarding the dynamics of the solar wind, and the nature of non-linear processes, in the inner-heliosphere.

NASA's Parker Solar Probe attempts to address the lack of empirical knowledge of the inner heliosphere through making direct *in-situ* measurements of the solar wind and corona. Using *in-situ* instrumentation with heritage from missions such as *Wind, STEREO, MAVEN, and CLUSTER, Ulysses,* and others, PSP will study the electromagnetic and plasma environments of the inner heliosphere, becoming the first mission to transverse the Alfvén point which separates the solar corona from the super sonic solar wind.

Part II of this dissertation highlights the calibration of the PSP magnetometer suite, consisting of a set of three magnetometers, in order to develop an optimally merged magnetic field data product for PSP usable by the scientific community. Chapter 5 discusses the PSP fluxgate magnetometer calibration. Chapter 6 provides an introduction and review of linear time invariant filter theory and their use in time series calibration of the PSP/FIELDS SCM. Chapter 7 describes the development of a merged data product which consists of both SCM and MAG measurements, observing the magnetic fields in both the inertial range of MHD turbulence as well as the dissipation range.

Through developing state of the art merging algorithms for the PSP/FIELDS magnetometers, enabling simultaneous observations of small and large dynamic scales, the magnetic component of the turbulent environment of the inner heliosphere can be thoroughly measured and quantified. Though observational difficulties associated with single point measurements will likely be compounded due to the large transverse velocity of PSP, these measurements will revolutionize the understanding of dynamic non-linear processes in magnetized plasmas.

PART II

MEASURING THE MAGNETIC FIELD OF THE INNER-HELIOSPHERE

5

REMOVING OFFSETS OF FLUXGATE MAGNETOMETERS

The Parker Solar Probe FIELDS instrument includes a suite of three magnetometers located on a boom mounted behind the spacecraft chassis in the umbra provided by the thermal protection system (TPS) (Bale et al., 2016a). Two fluxgate magnetometers (MAGs), developed at NASA Goddard Spaceflight Center (GSFC), are situated at 1.9 m and 2.7 m from the spacecraft, respectively referred to as the inboard (MAGi) and outboard (MAGo) sensors, measure DC and low frequency magnetic fields. The GSFC MAGS are heritage instruments similar to sensors flown on many previous missions, e.g. Juno, MAVEN, Van Allen Probes, STEREO, (Acuña et al., 2008; Kletzing et al., 2013; Connerney et al., 2015, 2017). These low frequency instruments are accompanied by an inductive search coil magnetometer (SCM) located at the end of the boom, providing vector measurements of fluctuating magnetic fields up to 1 MHz, Chapter 6. The primary objectives of the FIELDS magnetometer suite are to determine the magnetic signatures of structures and dynamical processes which contribute to the heating of the solar corona and acceleration of the solar wind: shocks, reconnection, turbulence, wave-particle interactions (Bale et al., 2016a).

Both the MAGs and SCM have continuous survey mode acquisition rates with a maximum waveform sampling cadence of ~ 293 Sa/s. Onboard anti-aliasing for downsampling of the DC MAGs is implemented using Bartlett, (triangle window) filters in order to meet telemetry limitations of the spacecraft. At lowest cadence, the MAGs may operate at an approximate 1 Sa/S rate during cruise phase. In general, due to its increased distance from the spacecraft, the outboard MAG is the primary science instrument and is run at faster sampling rates.

Accurate calibrations for the three magnetometers are imperative in understanding magnetic signatures associated with dynamical processes which heat and accelerate the solar wind and corona. Due to fundamental differences in instrument design and operation between fluxgates and inductive coils, the calibration procedures for the MAG and SCM sensors differ significantly. In order to compare measurements from the different instruments, care must be taken to calibrate the measurements to physical units and rotate the measurements into a shared coordinate system. Additionally, to improve the quality of observations of survey rate frequencies a composite magnetic field data product from merged SCM and MAG measurements is produced to generate a single continuous magnetic field dataset over the survey mode bandwidth with optimized signal to noise ratio, Chaper 7 of this manuscript. Similar merging routines have been explored on a number of recent spacecraft missions

including CLUSTER and MMS (Alexandrova et al., 2004; Chen et al., 2010a; Torbert et al., 2016; Fischer et al., 2016). However, the procedure of merging time series from multiple sources, also known as linear diversity combining, first requires accurate calibrations of the individual MAGs and SCM sensors (Kahn, 1954; Brennan, 1959).

5.1 INFLIGHT CALIBRATION OF DC FLUXGATE MAGNETOMETERS

The MAG frequency response has a characteristics of a single pole, low pass Butterworth filter, e.g. see Section 6.3.3 (Connerney et al., 2015, 2017). Accordingly, fluxgate magnetometers are inherently sensitive to DC fields associated with the spacecraft. Since the development of space-borne magnetometry in the 1950's and 1960's, the identification and removal of DC magnetic fields inherent to the sensor and spacecraft, also known as zero offsets has been a primary concern in calibration procedures (Ness, 1970). Accounting for spacecraft fields is typically undertaken using magnetic cleanliness programs and design techniques as well as ground based measurements of the spacecraft magnetic field as well as in-flight calibration routines (Ness, 1970; Ness et al., 1971; Acuña, 2002; Connerney et al., 2015, 2017). Davis and Smith (1968) developed a system of equations based on the covariance matrix to remove DC spacecraft fields using in-flight observations of the interplanetary magnetic field (IMF); overtime, many iterations of the equations have developed leading to well understood and robust estimation techniques for removing spacecraft offsets (Belcher, 1973; Acuña, 2002; Leinweber et al., 2008). The technique developed by Davis and Smith (1968), and subsequent iterations, depends on the assumption of a constant magnitude IMF, with Alfvénic (perpendicular) fluctuations that do not change the field magnitude. Leinweber et al. (2008) provide a comprehensive derivation and review of these techniques relying on constant magnitude fluctuations of the IMF with slowly varying field levels. For PSP/FIELDS, Acuña (2002) outline the DC offset calibration routine typically performed on GSFC designed magnetometers used on Juno, Van Allen Probes, MAVEN etc, which is currently used to determine DC offsets on PSP/FIELDS (Kletzing et al., 2013; Connerney et al., 2015, 2017).

Typically, the process of magnetometer calibration is accomplished through a least square error minimization of a linear system of equations which convert between raw fluxgate output and the physical field. (Davis and Smith, 1968; Belcher, 1973; Acuña, 2002; Leinweber et al., 2008). The calibration process is accomplished through either matrix inversion or least square error minimization of the model linear equations, e.g. Belcher (1973); Acuña (2002); Leinweber et al. (2008). A common formulation of the matrix equation converting from the MAG output to a physical signal is given by

$$\mathbf{B} = \mathbf{A}[\mathbf{s}(\mathbf{V} - \mathbf{Z})], \tag{5.1}$$

where $\mathbf{V}$ is the measured raw magnetometer output, $\mathbf{Z}$ is a vector containing the effective zero offset values associated with observations of a static internal and external fields, $\mathbf{s}$ is a vector containing instrumental scale factors between the raw magnetometer output and physical units, and $\mathbf{A}$ is a matrix

associated with inherent non-orthogonality between sensor axes, the sensors alignment relative to the spacecraft and boom, and a possible rotation to a desired coordinate system (Acuña, 2002; Connerney et al., 2015, 2017) . While scale factors and orthogonalization of the MAG sensors may performed on the ground before flight, values for sensor zero offsets are typically not determined until post launch (Acuña, M., 1981; Olsen et al., 2003; Risbo et al., 2003; Connerney et al., 2015, 2017).

For a three axes stabilized spacecraft, such as PSP, performing controlled maneuvers to roll the spacecraft allows for measurements of the superposed of the spacecraft field and the external ambient IMF at various orientations, from which various system of equations can be constructed to determine the DC offsets associated with the spacecraft field. Such rolls typically consist of controlled maneuvers occurring periodically through the mission to determine and monitor the DC offsets Connerney et al. (2015). For PSP, spacecraft rolls are performed during the aphelion phase of the orbit to determine the best values for magnetometer offsets during the perihelion encounters. Several techniques can be used to determine the DC offsets from such spacecraft rolls.

5.1.1 DAVIS & SMITH EQUATION

Following Leinweber et al. (2008) the Davis-Smith equation can be constructed as a correlation matrix which is solved for the magnetometer offsets. The measured magnetic field $\mathbf{B}_m$ is taken to be a superposition of the actual IMF, $\mathbf{B}_a$ with the set of offsets $\mathbf{Z}$. Taking the covariance

$$\begin{aligned} S_{ij} &= \frac{1}{N-1}\sum_{k=0}^{N-1}(B_{ik}-\langle B_i\rangle)(B_{jk}-\langle B_j\rangle) \\ &= \frac{1}{N-1}\left(\sum_{k=0}^{N-1}B_{ik}B_{jk}-\langle B_j\rangle\sum_{k=0}^{N-1}B_{ik}-\langle B_i\rangle\sum_{k=0}^{N-1}B_{jk}+(N-1)\langle B_i\rangle\langle B_j\rangle\right) = \\ &\qquad \langle B_iB_j\rangle-\langle B_i\rangle\langle B_j\rangle \end{aligned} \tag{5.2}$$

The addition of a DC zero offset to the measured magnetic field will not affect the covariance, e.g. by letting $\tilde{B}_i = B_i + Z_i$ and $\tilde{B}_j = B_j + Z_j$, it is easily shown that

$$\begin{aligned} \tilde{S}_{ij} &= \frac{1}{N-1}\sum_{k=0}^{N-1}(\tilde{B}_{ik}-\langle\tilde{B}_i\rangle)(\tilde{B}_{jk}-\langle\tilde{B}_j\rangle) \\ &= \frac{1}{N-1}\sum_{k=0}^{N-1}(B_{ik}+Z_i-\langle B_i\rangle-\langle Z_i\rangle)(B_{jk}+Z_j-\langle B_j\rangle-\langle Z_j\rangle) \\ &\qquad = S_{ij} \end{aligned} \tag{5.3}$$

The key assumption of the Davis-Smith equation is that variations in the magnetic field are perpendicular fluctuations which do not change the field magnitude. During controlled spacecraft rolls, this

assumption is satisfied as long as the IMF is relatively constant over the spacecraft roll period. Additionally, the Davis-Smith method can be used for intervals when the solar wind is particularly Alfvénic such that rotations are transverse and have no parallel compressive component (Belcher and Davis, 1971; Belcher, 1973).

Mathematically, this assumption enters as a statement that the covariance between variations in the IMF magnitude and the measured fluctuations along each axis is zero, which is only possible if for each component i of the magnetic field

$$\langle B_i|B_a|^2\rangle = \langle B_i\rangle\langle|B_a|^2\rangle. \tag{5.4}$$

With the condition $\mathbf{B}_m = \mathbf{B}_a + \mathbf{Z}$ the measured field magnitude can be written as

$$|B_m|^2 = (\mathbf{B_a} + \mathbf{Z})\cdot(\mathbf{B_a} + \mathbf{Z}) = |B_a^2| + 2Z_xB_x + 2Z_yB_y + 2Z_zB_z + \mathbf{Z}\cdot\mathbf{Z} \tag{5.5}$$

The covariance of the components of the magnetic field with the fluctuation magnitude 5.4 can then be written as

$$\begin{aligned}
&\langle B_i(|B_m|^2 - 2Z_xB_x - 2Z_yB_y - 2Z_zB_z - \mathbf{Z}\cdot\mathbf{Z})\rangle \\
&= \langle B_i\rangle\langle|B_m|^2 - 2Z_xB_x - 2Z_yB_y - 2Z_zB_z - \mathbf{Z}\cdot\mathbf{Z}\rangle \\
&= \langle B_i|B_m|^2\rangle - 2\langle B_iZ_xB_x\rangle - 2\langle B_iZ_yB_y\rangle - 2\langle B_iZ_zB_z\rangle - \langle B_i\mathbf{Z}\cdot\mathbf{Z})\rangle \\
&= \langle B_i\rangle\langle|B_m|^2\rangle - \langle B_i\rangle\langle 2Z_xB_x\rangle - \langle B_i\rangle\langle 2Z_yB_y\rangle - \langle B_i\rangle\langle 2Z_zB_z\rangle - \langle B_i\rangle\langle\mathbf{Z}\cdot\mathbf{Z}\rangle
\end{aligned} \tag{5.6}$$

Using the covariance matrix $\mathbf{S}$, this equation can be compactly written as

$$\frac{1}{2}\begin{pmatrix}(\langle B_x|B_m|^2\rangle - \langle B_x\rangle\langle|B_m|^2\rangle)\\(\langle B_y|B_m|^2\rangle - \langle B_y\rangle\langle|B_m|^2\rangle)\\(\langle B_z|B_m|^2\rangle - \langle B_z\rangle\langle|B_m|^2\rangle)\end{pmatrix} = \mathbf{SZ}. \tag{5.7}$$

The covariance matrix $\mathbf{S}$ is a square symmetric matrix with real values and is therefore diagonalizable Lang (1987). For a non-singular matrix, the diagonalizability of the symmetric matrix allows for inversion of the covariance matrix calculation of the zero offsets. However, frequently, such as in spacecraft rolls, and Alfvénic rotations of the IMF, fluctuations are polarized in a plane such that significant variance in the magnetic field is only observed in two directions; in this case the 3x3 covariance matrix is singular and not invertible. In which case, the covariance matrix is of insufficient rank and cannot uniquely determine all three offsets via matrix inversion. However, a 2x2 covariance matrix may be defined and offsets obtained in the plane of the rotation. Typically, either controlled rolls around multiple axes or the observation of many perpendicular Alfvénic fluctuations around non-parallel axes are required to fully constrain the magnetic field offsets.

5.1.2 ACUÑA 2002 SSR METHOD FOR ZERO DETERMINATIONS

Following Acuña (2002), measurements of the magnetic field are made at two times $\mathbf{B}_{m1}$ and $\mathbf{B}_{m2}$. The actual interplanetary magnetic field at the corresponding times is given as $\mathbf{B}_{a1}$ and $\mathbf{B}_{a2}$ with the measured fields are offset by spacecraft and instrumental DC values $\mathbf{B}^{sc}$ such that $\mathbf{B}_{m1}$=$\mathbf{B}_{a1}$ + $\mathbf{B}^{sc}$ and $\mathbf{B}_{m2}$=$\mathbf{B}_{a2}$ + $\mathbf{B}^{sc}$. It is known that the solar wind predominantly consists of transverse Alfvénic fluctuations corresponding to a change in field direction, with little to no compressible component or change in field strength. For a transverse magnetic fluctuation $\Delta\mathbf{B}_a$, it follows that $\Delta\mathbf{B}_a \cdot \mathbf{B}_{a1} = 0$ and $\Delta\mathbf{B}_a \cdot \mathbf{B}_{a2} = 0$. It follows that $\Delta\mathbf{B}_a \cdot (\mathbf{B}_{a1} + \mathbf{B}_{a2}) = 0$. For the measured field with constant offset $\mathbf{B}^{sc}$ the difference between two measurements is equal to the difference in the IMF at the two times $\Delta\mathbf{B}_m = \Delta\mathbf{B}_a$. The offsets $\mathbf{B}^{sc}$ add an additional component to the measured magnetic field such that

$$\Delta\mathbf{B}_m \cdot (\mathbf{B}_{m1} + \mathbf{B}_{m2}) = \Delta\mathbf{B}_a \cdot (\mathbf{B}_{a1} + \mathbf{B}_{a2} - 2\mathbf{B}^{sc}),$$

$$\begin{aligned} \Delta\mathbf{B}_m \cdot \mathbf{B}^{sc} &= \frac{1}{2}[\Delta\mathbf{B}_m \cdot (\mathbf{B}_{m1} + \mathbf{B}_{m2})] \\ \mathbf{B}^{sc} &= \frac{1}{2}[\Delta\mathbf{B}_m^{-1}][\Delta\mathbf{B}_m \cdot (\mathbf{B}_{m1} + \mathbf{B}_{m2})] \end{aligned} \tag{5.8}$$

The right hand side of Equation 5.8 is composed entirely of measured quantities. The matrix $[\Delta\mathbf{B}_m^{-1}]$ can be solved for using least square numerical methods known as the singular value decomposition (SVD), Appendix A (Connerney et al., 2015). The assumption of transverse, rotational, fluctuations, i.e. $\Delta\mathbf{B}_a \cdot \mathbf{B}_{a2} = 0$ is key to solving this particular set of equations. In general, this method can be used through either fitting offsets to intervals of strongly Alfvénic solar wind (IMF) fluctuations or by rotating the spacecraft coordinates over a relatively quiescent period over which the IMF vector is roughly constant. Unique determination of all three components of $\mathbf{B}^{sc}$ requires that the set of observations $[\Delta\mathbf{B}_m]$ and its corresponding inverse be a matrix with rank three, i.e. three non zero eignvalues are required to obtain offsets in all three sensor directions.

In addition to static DC fields, the low pass filter nature of the fluxgate is inherently sensitive to low frequency variable spacecraft signatures e.g. reaction wheels, power supplies, or spacecraft solar panel arrays (Connerney et al., 2015). Though all magnetic sensors are likely to observe such contamination, signatures related to the spacecraft are strongest close to the spacecraft; the development magnetometer booms was originally made for this purpose (Ness, 1970). For PSP/FIELDS, signatures of spacecraft noise will be largest in the inboard fluxgate magnetometer (MAGi), due to the close proximity to the spacecraft and solar panel array. Accordingly, the outboard fluxgate magnetometer (MAGo) is expected to make the primary measurement for low frequency environmental magnetic fields and for this reason is typically sampled at higher cadences than the inboard sensor. Ness et al. (1971) originally proposed the use of two magnetometers for identifying the presence of spacecraft fields using a

multipole expansion of the spacecraft field. Though Davis et al. (1973) discuss some weaknesses and limitations inherent in the two sensor approach, in general modern missions have implement several DC sensors, for scientific robustness, redundancy, as well as cross calibration purposes. Ness (1973) additionally demonstrate a two sensor approach to identification of spacecraft noise.

5.1.3 SUN-POINTED ROLLS FIT TO CIRCLE

Determining DC offsets can also be used by directly fitting Sun-pointed rolls to a circular surface. The method is similar to the David-Smith method, but uses a direct least square fitting using an SVD, see Appendix A, rather than a determination of 2x2 covariance matrix. Sun pointed rolls consist of a rotation of the spacecraft about the sun pointing ($\mathbf{z}_{sc}$) axis such that projection angle between the ambient magnetic field and the spacecraft $\hat{\mathbf{x}}_{sc}$ and $\hat{\mathbf{y}}_{sc}$ axes is cycled at the rotation frequency ω_{sc}. The projection of the ambient magnetic field in the spacecraft xy_{sc} plane is a two dimensional vector $\mathbf{B}_{xy}$. If the solar wind magnetic field is slowly varying such that the field magnitude and direction are approximately constant, then, as the spacecraft rotates, the projection angle between the normal direction $\hat{\mathbf{B}}_{xy}$ and spacecraft $\hat{\mathbf{x}}_{sc}$ and $\hat{\mathbf{y}}_{sc}$ axes varies as $\hat{\mathbf{B}}_{xy} \cdot \hat{\mathbf{x}}_{sc} = \cos(\omega_{sc}t + \phi_0)$ and $\hat{\mathbf{B}}_{xy} \cdot \hat{\mathbf{y}}_{sc} = \sin(\omega_{sc}t + \phi_0)$. The observed field in the rotating sensor is then

$$B_y = |\mathbf{B}_{xy}| sin(\omega_{sc}t + \phi_0) + B_y^{sc}$$

and

$$B_x = |\mathbf{B}_{xy}| \cos(\omega_{sc}t + \phi_0) + B_x^{sc},$$

corresponding to a circle with radius equal to the magnitude of $|\mathbf{B}_{xy}|$, with the center of the circle offset from zero by spacecraft field vector $\mathbf{B}_{xy}^{sc}$.

Least squares fitting through using the SVD (Appendix A) can be used to determine the spacecraft offsets in the $\hat{\mathbf{x}}_{sc}$ and $\hat{\mathbf{y}}_{sc}$ directions. Because the spacecraft rotates around $\hat{\mathbf{z}}_{sc}$ the sensors cannot distinguish the superposition of B_z^{sc} spacecraft field and the component of the environmental field orthogonal to the rotational plane(Acuña, 2002; Connerney et al., 2015). Such is the case for two dimensional rolls around any spacecraft axis, only by performing rolls around two unique perpendicular axes can the DC offsets be uniquely determined from a spacecraft roll routine.

For the set of N measurements $\{B_{xj}, B_{yj}\}$, with $0 \leq j \leq N$, a least square fit to a circle is constructed through minimizing

$$\frac{\partial}{\partial \alpha_k} \left[(B_{xj} - B_{scx})^2 + (B_{yj} - B_{scy})^2 - {B_{xy}}^2 \right]^2 = 0,$$

where α_k corresponds to the fit parameters ${B_{xy}}^2$, B_x^{xsc}, and B_y^{sc}. The least squares solution can be obtained through constructing the matrix equation

$$\begin{pmatrix} B_{x0}^2 + B_{y0}^2 \\ \vdots \\ B_{xj}^2 + B_{yj}^2 \end{pmatrix} = \begin{pmatrix} B_{x0} & B_{y0} & 1 \\ \vdots & \vdots & \vdots \\ B_{xj} & B_{yj} & 1 \end{pmatrix} \begin{pmatrix} 2B_{scx} \\ 2B_{scy} \\ \Delta \end{pmatrix} \tag{5.9}$$

using the constraint of constant $\Delta = {B_{xy}}^2 - B_{scx}^2 - B_{scy}^2$ and solving for the pseudo-inverse to give the least square estimates for B_{xy}^2, B_{scx}, and B_{scy}.

The first sun-pointed rolls on PSP were performed on 10/03/2018 shortly after the spacecraft's first encounter with Venus. During the approximately three hour maneuver, MAGo and MAGi were operating at a 36.67 Sa /s rate, accumulating ~ 380000 vector samples from each sensor. To enable a computationally feasible inversion, the 36.67 Sa/S rate time series were low pass filtered and downsampled by a factor of 128 to a ~ 0.28 Sa/s rate. This low pass filtering additionally removes high frequency variation to the ambient mean magnetic field.

Figure 5.1 shows the time series of the magnetic field during sun-pointed rolls taken by PSP on 10/03/2018. Signatures of low frequency spacecraft rotations of ~ 0.7 mHz (~ 1400 s) are observed in the xy plane of both MAGi and MAGo sensors. Offsets from the spacecraft field are easily observed in the two sensors. The bottom panel shows the hodogram of filtered and downsampled (~ 0.28 Sa/s rate) B_y and B_x for both sensors, highlighting the circular rotation of the spacecraft relative to the mean ambient magnetic field.

Figure 5.2 shows the same data subtracting the DC offset fields. For the MAGo sensor, least square fits give offsets from the spacecraft field as B_{scx}^o = 6.9 nT and B_{scy}^o = 11.2 nT. For the MAGi sensor B_{scx}^i = 11.0 nT and B_{scy}^i = 27.2 nT. The bottom panels of Figure 5.2 show the DC removed hodograms of B_y and B_x in both sensors. Inspection of the upper panel and lower panels shows that the traces of inboard and outboard magnetic fields are in agreement with root mean square differences between the inboard and outboard sensors after DC removal of 0.25 nT in B_x and 0.11 nT in B_y; section 5.2 will address these residuals in detail. Additionally, when calculating the residuals from the least square fit

$$\lambda_j = (B_{xj} - B_{scx})^2 + (B_{yj} - B_{scy})^2 - {B_{xy}}^2,$$

a root mean square of λ is obtained as 8.4 nT^2 and 8.5 nT^2 respectively for the inboard and outboard sensor. A strong correlation, R=0.985 is computed between residuals of the inboard and outboard sensors (Figure 5.3), implying that the residual errors are not random fluctuations local to each sensor, but are driven by variation in the total mean field; i.e. violations of the assumption of a constant external field. Consideration of the root-mean-square fluctuations of the observed magnetic field magnitude gives a result of 2 nT. Accordingly, the size of the residuals is simply driven by the fluctuations in the ambient magnetic field; the accuracy of the least square fit is thus constrained by the typical root-mean-square fluctuation in the magnitude of the ambient magnetic field.

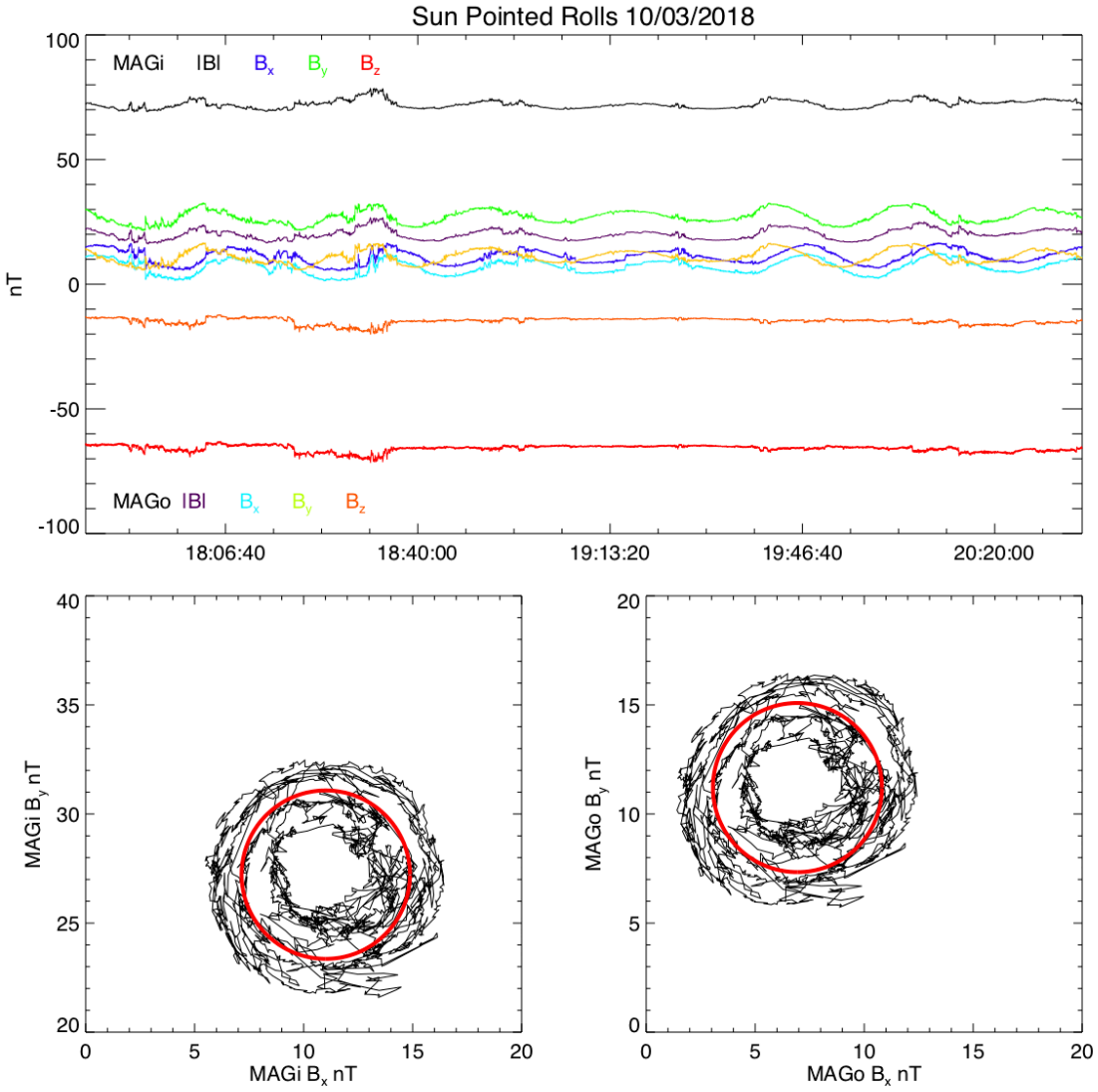

Figure 5.1: Top Waveforms for inboard and outboard MAG measurements during October 3rd,2018 sun-pointed MAG rolls. (Bottom) Hodograms of MAGi and MAGo xy_{sc} plane measurements from sun-pointed MAG rolls; best fit to the data assuming constant background magnetic field is shown in red.

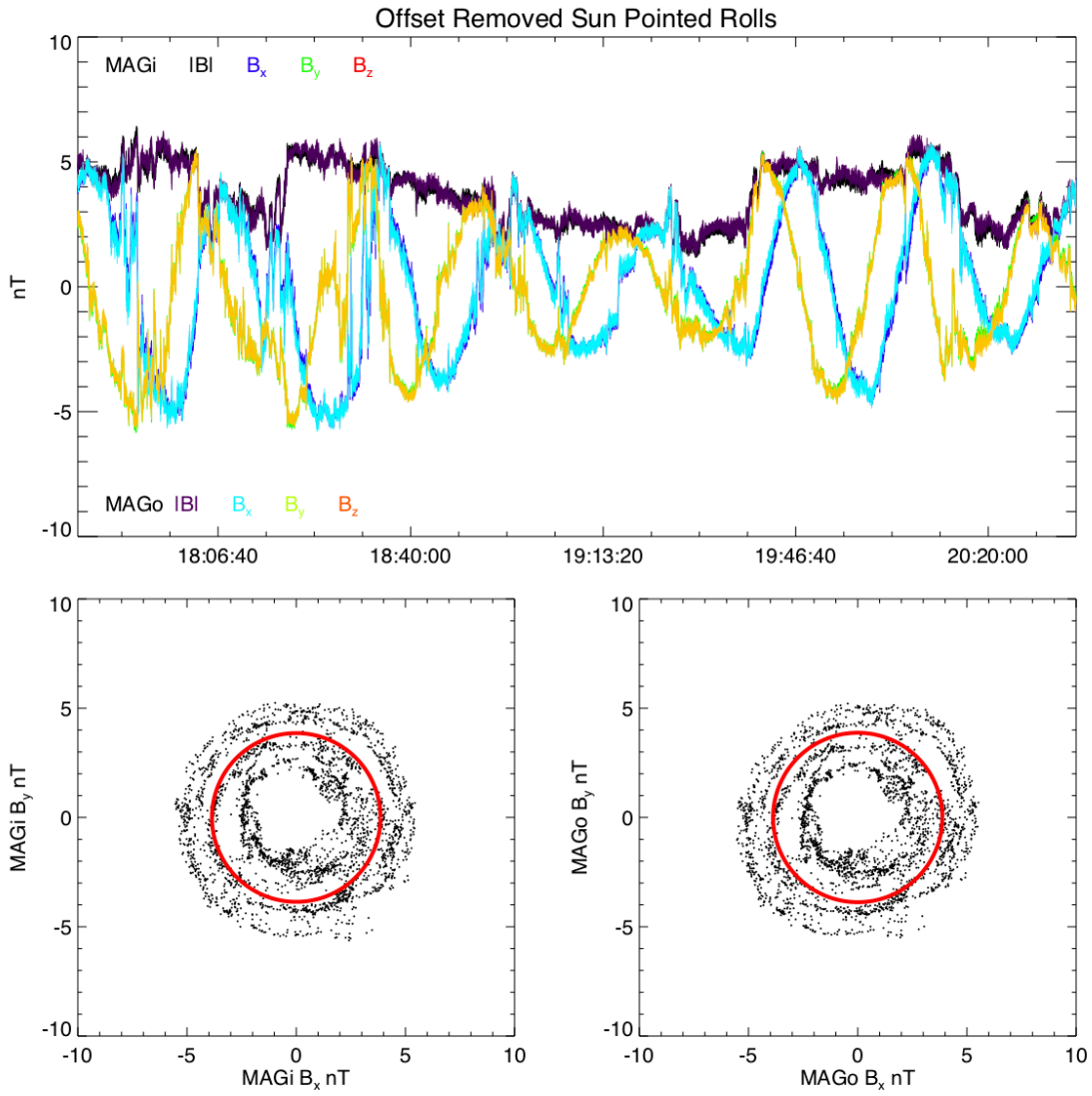

Figure 5.2: Top Spacecraft DC offset removed waveforms for inboard and outboard MAG measurements in $\hat{\mathbf{x}}_{SC}$ and $\hat{\mathbf{y}}_{SC}$ during October 3rd,2018 sun-pointed MAG rolls. (Bottom) Hodograms of spacecraft DC offset MAGi and MAGo xy_{SC} plane measurements from sun-pointed MAG rolls; best fit to the data assuming constant background magnetic field is shown in red.

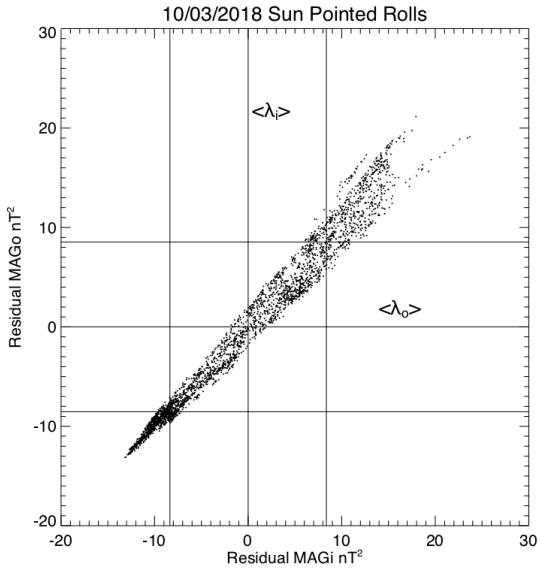

Figure 5.3: Residuals from least square fit of MAGi and MAGo observations to an offset circle

In addition to its dependence on the assumption of a constant magnetic field constraint; it is evident that the two dimensional sun-pointed roll does not uniquely determine the spacecraft field in the $\hat{\mathbf{z}}$ direction. However, the sun pointed roll does give a constraint on $\Delta B_z^{sc} = B_z^o - B_z^i$ such that the specification of B_z^{sc} for either the inboard or outboard field will determine the offset present in the other sensor. In order to determine the $\hat{\mathbf{z}}$ component of the fluctuations, either spacecraft rolls with measurements which span the 3-axes or an alternative method of offset determination are required.

5.2 CROSS CALIBRATION AND ALIGNMENT OF INBOARD AND OUTBOARD SENSORS

The previously outlined routine removes DC offsets from each individual magnetometer assuming a constant ambient magnetic field in the presence of a rotating coordinate system with a constant spacecraft field. A system of equations is constructed from which the least square fit of the inboard and outboard offsets for each sensor are constructed. In both the sun-pointed and conical rolls, the resulting ambient field is implicitly taken as the measured field from each sensor with DC offsets removed. The algorithm, which is applied individually to each sensor, then gives two different estimates for the ambient magnetic field, with as Figure 5.3 show, highly correlated residuals between the inner and outer sensors. Analysis of the residuals sensor observations and the residuals provides an important

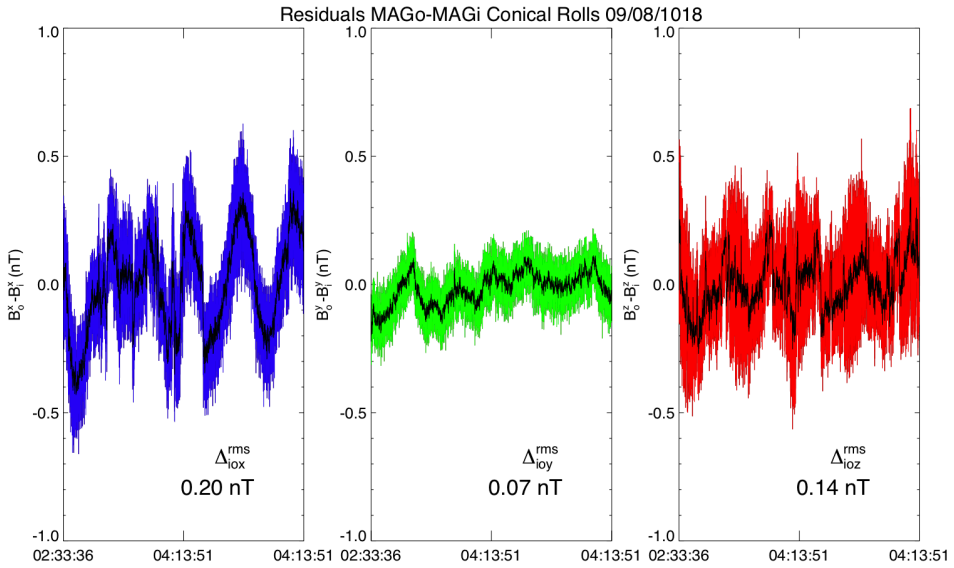

Figure 5.4: Difference between MAGi and MAGo observations for each sensor axis during conic rolls

quantification of the performance of the algorithm as well as an absolute uncertainty on the observations of the ambient magnetic field.

Figure 5.4 shows the residuals between the inner and outer sensors for each axis, rms values for each axis are obtained as $\Delta_{io}^{rms} = [0.19, 0.074, 0.14]$ nT with a total rms difference of 0.15 nT. Evident in the residuals is a sinusoidal variance at the frequency of the spacecraft roll. Computing the cross correlation matrix of the residuals Δ_{io} with measurements of either the outer or inner time-series reveals strong cross correlations between the sensor axes, suggesting slight deviations of the sensor coordinates from the spacecraft coordinate system. The sensor coordinates system relative to the inboard and outboard can be computed using the SVD of the covariance matrix of $\mathbf{B^o}$ and $\mathbf{B^i}$. The measured correlation matrix (covariance matrix normalized to cross) between the inner and outer sensors is found to be

$$Cor(\mathbf{B^i}, \mathbf{B^o}) = \begin{pmatrix} 0.996 & 0.191 & -0.278 \\ 0.125 & 0.999 & -0.017 \\ -0.25 & 0.0414 & 0.997 \end{pmatrix} \tag{5.10}$$

an approximately symmetric matrix with diagonal entries near unity. Singular values for the covariance matrix are given as Diag(W)$5.70, 2.90, 3.87$

$$\mathrm{cov}(\mathbf{B^i}, \mathbf{B^o}) = \mathbf{UWV}^\dagger$$

$$\mathbf{W} = \mathbf{U}^\dagger \mathrm{cov}(\mathbf{B^i}, \mathbf{B^o})\mathbf{V} = \mathbf{U}^\dagger(\frac{\mathbf{B^i B^{o\dagger}}}{N})\mathbf{V}$$

The coordinate system in which the covariance matrix of the inner and outer observations is diagonal is given by the rotations of $\mathbf{U}^\dagger\mathbf{B^i}$ and $\mathbf{V}^\dagger\mathbf{B^o}$. In the MAGo coordinate system, this appropriate rotation of the inner sensor is $\mathbf{VU}^\dagger\mathbf{B^i}$. The matrix $\mathbf{VU}^\dagger$ is interpreted as the difference in alignment between the inboard and outboard sensors:

$$\mathbf{VU}^\dagger \simeq \begin{pmatrix} 0.999 & 0.039 & -0.016 \\ -0.039 & 0.998 & -0.033 \\ 0.016 & 0.034 & 0.999 \end{pmatrix} \tag{5.11}$$

The axis of rotation is determined by the vector $\hat{\mathbf{r}}$ for which the rotation matrix maps $\hat{\mathbf{r}}$ to itself

$$\mathbf{VU}^\dagger\hat{\mathbf{r}} = \alpha\hat{\mathbf{r}}$$

, which is easily found through the eigenvalue decomposition of the $\mathbf{VU}^\dagger$ rotation.The angular magnitude of the rotation about the rotation axis may be found by $\cos^{-1}(\mathbf{VU}^\dagger\hat{\mathbf{q}}\cdot\hat{\mathbf{q}})$ where $\hat{\mathbf{q}}$ is perpendicular to the rotation axis $\hat{\mathbf{r}}$. (For the rotation matrix $\mathbf{VU}^\dagger$ determined from the SVD covariance matrix of the sensors which rotates the inner mag such that the covariance of MAGi and MAGo is maximally orthogonal, a rotation axis of $\hat{\mathbf{r}} = [-0.623, 0.295, 0.724]$ is calculated with an angle of 3.1^o degrees.

Figure 5.5 shows the residuals after processing by the orthogonalization routine. The rms difference between the MAGi and MAGo observations is reduced by the orthogonalization, with a trace rms variation of 0.12nT and with $\Delta^{rms}_{r[i]_o} = [0.13, 0.10, 0.12]$ nT on each axis. However, it is evident that the low frequency cross axes correlations are still present. The reduction in measurements by .03 nT with an orthogonal rotation is fairly weak, and suggests that it is not simply an alignment error in the sensor axes which leads to the discrepant measurements between the inner and outer sensor.

Generalizing the sensor alignment rotation ($\mathbf{VU}^\dagger$) to allow non orthogonal matrices allows for construction of a linear matrix $\mathbf{A}$ such that $\mathbf{B^o} = \mathbf{AB^i}$ In which case, the least square solution to $\mathbf{A}$ may be obtained again through a SVD least squares pseudo-inversion.

$$\mathbf{B^o} = \mathbf{AB^i}$$

Accordingly,

$$\mathbf{A} = \mathbf{B^o}\mathbf{B^i}^{-1},$$

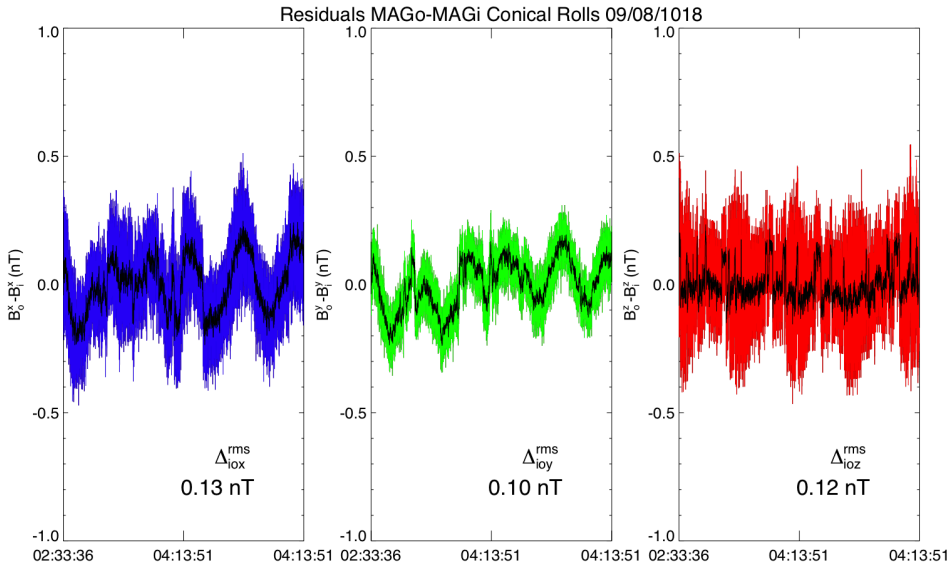

Figure 5.5: Difference between MAGi and MAGo observations for each sensor axis during conic rolls after rotating MAGi to MAGo coordinates

where $\mathbf{B^i}^{-1}$ is found subject to the SVD composition and $\mathbf{B^i} = \mathbf{U_i W_i V_i^\dagger}$ such that $\mathbf{B^i}^{-1} = \mathbf{V_i W_i^{-1} U_i}\dagger$.

The least square solution is found to be

$$\mathbf{A} = \begin{pmatrix} 1.008 & 0.090 & -0.016 \\ 0.005 & 1.001 & -0.023 \\ 0.015 & 0.033 & 0.997 \end{pmatrix} \tag{5.12}$$

Figure 5.6 shows the residuals between MAGo and MAGi after application of the matrix $\mathbf{A}$. A trace rms value of 0.09 nT is obtained with $\Delta^{rms}_{A[i]o} = [0.08, 0.05, 0.12]$.

Figure 5.7 shows the spectral density of MAGo and the residuals $\mathbf{B^o} - \mathbf{AB^i}$. The spectrum of residuals is observed to be significantly below the outer MAG,

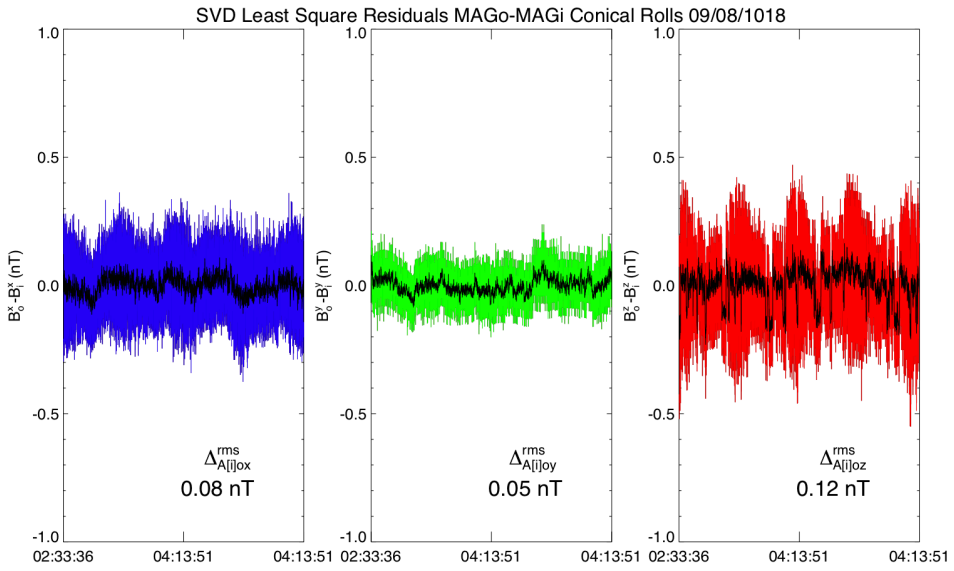

Figure 5.6: Difference between MAGi and MAGo observations for each sensor axis during conic rolls after processing time series with SVD to find maximally orthogonal axes.

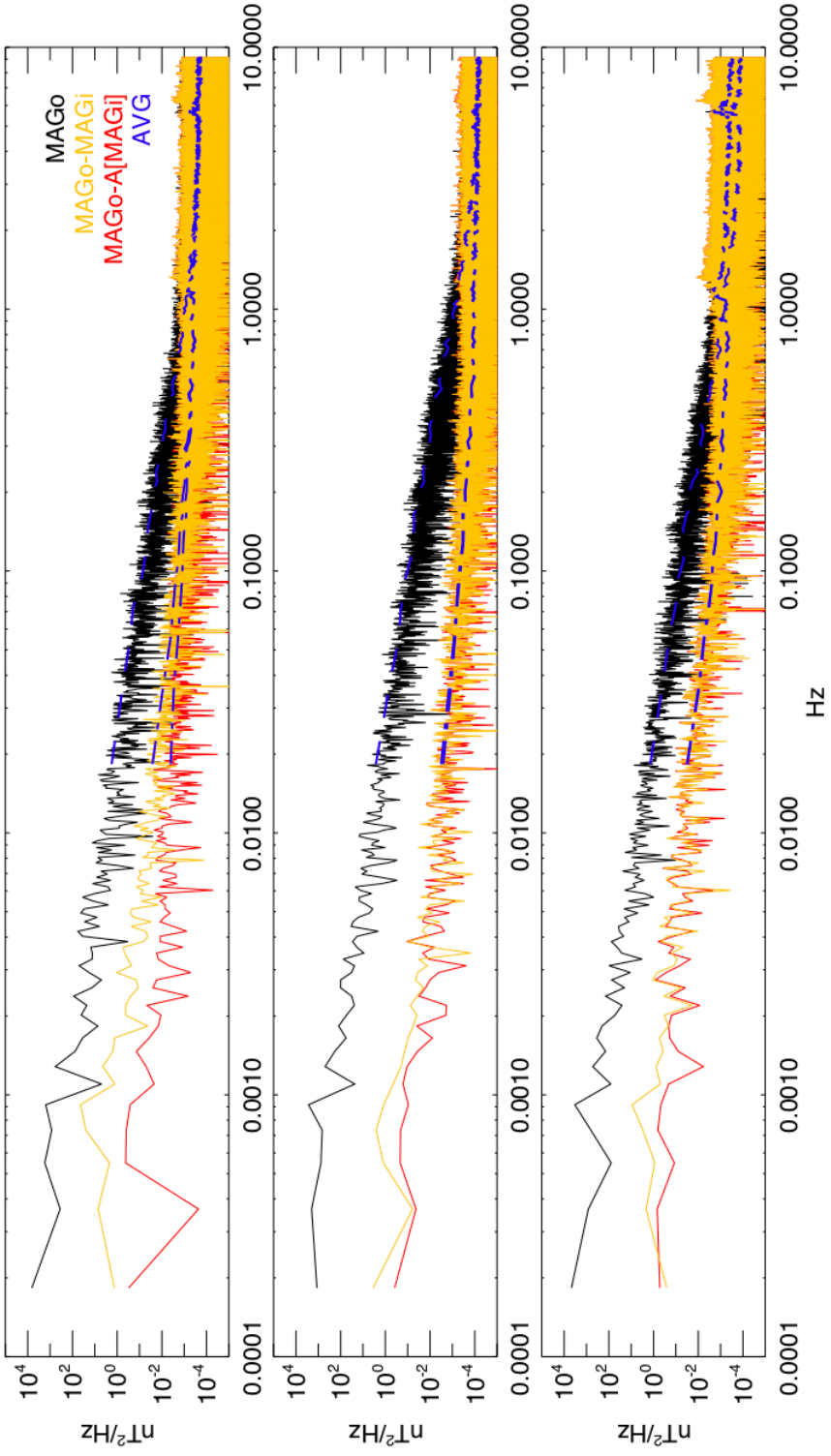

Figure 5.7: Spectral Densities of MAGo (black), residuals of calibrated data (orange) and SVD processed data (red). Spectral density of MAGo approaches that of residuals at noise floor (1 Hz)

6

DIGITAL FILTERING AND CALIBRATION OF SCM MAGNETOMETERS

6.1 INTRODUCTION TO SEARCH COIL MAGNETOMETER

Magnetometer calibration is the process of inverting the raw measurements of an instrument to create an estimate of the observed environmental field. For the case of a fluxgate magnetometer (Chapter 5), the inversion from raw instrumental output to an estimate of the environmental field is obtained through the inversion of a time invariant linear model relating the external environmental field to an output time series signal. A similar process is performed in order to calibrate the FIELDS/SCM magnetometer; however, because of operational principles, calibrating SCM measurements requires substantial technical tools digital signal processing to extract an estimate of the measured field.

Search coil magnetometers operate on the principle of Faraday's law of induction

$$\nabla \times \mathbf{E} = -\frac{\partial \mathbf{B}}{\partial t}, \tag{6.1}$$

written in integral form as

$$\oint_S \mathbf{E} \cdot d\mathbf{l} = -\frac{\partial}{\partial t} \iint_S \mathbf{B} \cdot d\mathbf{A} \tag{6.2}$$

which relates the induced electromotive force, $\mathcal{E}$ measured in volts, to the time variation of the magnetic flux through a closed loop. For a conductive coil of N turns and cross sectional area $\mathbf{A}$, the induced voltage over the coil is given by

$$\mathcal{E} = N\mathbf{A} \cdot \frac{\partial \mathbf{B}}{\partial t}, \tag{6.3}$$

relating the potential induced in the coil system to time varying magnetic fields normal to the coil axis. Early search coil instruments implemented simple windings of wire, the modern introduction of magnetic cores within the inductive loop winding has significantly improved instrumental performance by allowing greater control over noise and frequency characteristics through controlling the inductance through the magnetic permeability of the core (MacIntyre, 1980; Prance et al., 2003; Le Contel et al., 2016). For a inductive coil wrapped around a magnetic core, the induced voltage is given by

$$V(t) = -\mu_{eff} NAt \tag{6.4}$$

where the field is assumed parallel to the core normal (Séran and Fergeau, 2005).

Equation 6.4 highlights the fundamental inductive principle of search coil measurments ; in the Fourier domain

$$V(\omega) = \int V(t)e^{-i\omega t}dt = -\int \mu_{eff}NAte^{-i\omega t}dt \tag{6.5}$$

$$= -\mu_{eff}NA\left(B(t)e^{-i\omega t}\Big|_{-\infty}^{\infty} + \int i\omega B(t)e^{-i\omega t}dt\right) \tag{6.6}$$

$$= -\mu_{eff}NAi\omega B(\omega) \tag{6.7}$$

This simple model, neglecting effects from the magnetic core, coil resistance, and pre-amplifier response, highlights the phase shift between the ambient magnetic field and the measured voltage time-series associated with the inductive nature of the measurement.

The PSP/FIELDS SCM was designed at Laboratoire de Physique et Chimie de l'Environnement et de l'Espace (LPC2E) in Orl*é*ans, Fr and is nearly identical to instrumentation currently in development for the Solar Orbiter and Taranis missions (Jannet, G., and Martin, P. and Dudok de Wit, T., 2013). The SCM consists of three mutually orthogonal inductive coils mounted on the end of the spacecraft magnetometers boom has been tailored to study the magnetic fields of the inner heliosphere Bale et al. (2016a) from 10-50 kHz. Additionally, one of the coils serves as a double band-width sensor with an additional winding sensitive to 10kHz-1MHz. In contrast to the FIELDS fluxgate magnetometers, the SCM has significant gain and phase shifts in the survey mode range such that significant effort is required to convert from the DFB counts to the measured ambient fields. However, the AC sensitivity of the SCM precludes observations of DC spacecraft fields, however contamination from AC spacecraft fields in the SCM time-series is still possible.

6.2 LINEAR TIME INVARIANT (LTI) FILTER THEORY

The voltage induced in the SCM by the time variation in the external magnetic field is an analog signal which is fed to a preamplifier and sampled by the FIELDS main electronics package(Malaspina et al., 2016; Pulupa et al., 2017; Bale et al., 2016a). Digitization of the analog SCM voltage allows for the tools of digital signal processing become available in inverting the observed raw SCM signal to estimate the external magnetic field. Hayes (1996) describes a discrete time system as a "mathematical operator or mapping that transforms one signal (the input) by means of a fixed set of rules or functions." Modeling SCM sampling and operation in the context of discrete time systems provides a simple framework for magnetometer calibration through the theoretical formalism of linear time invariant and finite impulse response filters.

In the context of signal processing, the digitization of the analog signal $V(t)$ is accomplished through multiplying the signal by a sampling function $s(t)$, given by an infinite train of continuous impulse (δ_C) functions separated by the sampling time Δt. The δ_C function is defined according to

$$\delta_C(t) = \begin{cases} \infty & t = 0 \\ 0 & t \neq 0 \end{cases} \tag{6.8a}$$

$$\int_{-\infty}^{\infty} \delta_C(t)dt = 1 \tag{6.8b}$$

accordingly, the sampling function defined as

$$s(t) = \sum_{m=-\infty}^{\infty} \delta_C(t - m\Delta T) \tag{6.9}$$

Formally, for each sample, the discretized time series

$$V[m] = \lim_{\epsilon \to 0} = \int_{m\Delta t - \epsilon}^{m\Delta t + \epsilon} V(t)s(t)dt \tag{6.10}$$

such that

$$V[m] = V(m\Delta t) \tag{6.11}$$

where square brackets are used to imply a discrete quantized time series versus the continuous variable (Crochiere and Rabiner, 1983).

The ideal properties of *linearity and* time-shift-invariance allow for instrument calibration to be generally captured in a relatively simple framework of filter design. The function $T(x[n])$, which maps an discrete input series, $x[n]$, to an output $y[n] = T(x[n])$, is linear if it obeys properties of linear scaling and superposition such that

$$T(\alpha x[m]) = \alpha T(x[m]) \tag{6.12a}$$

$$T(x_1[m] + x_2[m]) = T(x_1[m]) + T(x_2[m]) \tag{6.12b}$$

Time-shift-invariance implies that the search coil response to the external environmental field should remain approximately constant: given the same environmental stimulus at two different times, the SCM provides the same output. Formally time-shift invariance states that:

$$\text{if } y[m] = T(x[n]) \text{ then } y[m - n] = T(x[m - n]).$$

Linearity and time-invariance provide for a simple model for which the function $T(x[m])$ can be represented as mathematical convolution in the time domain.

Representing the input series as a set of scaled unit samples shifted in time as

$$x[m] = \sum_{n=-\infty}^{\infty} x(n)\delta[n-m] \tag{6.13}$$

where the discrete δ function is defined as

$$\delta[i-j] = \begin{cases} 1 & i = j \\ 0 & i \neq j, \end{cases} \tag{6.14}$$

If T is linear then $y[m] = T(x[m])$ can be written as

$$T(x[m]) = T(\sum_{n=-\infty}^{\infty} x(n)\delta[m-n]) = \sum_{n=-\infty}^{\infty} x[n]T(\delta[m-n]). \tag{6.15}$$

Defining the response to an impulse function (impulse response) of $h[m] = T(\delta[m])$ then time shift invariance allows for the $h(m-n) = T(\delta[m-n])$ such that

$$y[m] = T(x[m]) = \sum_{n=-\infty}^{\infty} x[n]h[m-n], \tag{6.16}$$

which is identical to mathematical convolution and commonly represented as the operator $y[m] = (x * h)[m]$.

Assuming linearity and time invariance for the SCM response function, allows for the raw output sampled by the FIELDS MEP to be interpreted as a simple mathematical model in which a linear time invariant (LTI) filter is applied to the environmental field. Acquiring an estimate of the environmental magnetic field measured by the SCM from the digitized output is accomplished through determining and inverting the impulse response function $h[m]$ associated with the FIELDS SCM and MEP response.

6.2.1 SPECTRAL DECOMPOSITION

In addition to the time domain representation of the digitized signal, its spectral representation can be obtained using the z-transform and discrete time Fourier transform (DTFT). The z-transform is defined as the infinite sum

$$X(z) = \sum_{n=-\infty}^{\infty} x[n]z^{-n}, \tag{6.17}$$

where z is a general complex number given by $Ae^{i\phi}$. The z-transform is the discrete time analog of the Laplace transform which serves as a linear map between a, possibly complex valued, time-series

and a power-series in the complex-frequency domain Oppenheim and Schafer (1975). In general, the z-transform is only defined in a region of convergence where the sum in Equation 6.17 is finite. Truncating the z-transform to a finite number of terms creates a polynomial which may be evaluated explicitly; for an infinite number of terms care must be taken to ensure the finiteness and convergence of the z-transform.

The properties of the z-transform, under simple mathematical operations, contain several identities which facilitate the transform's use as an analytical tool of digital signals. For example for a delay by m samples the z-transform is shown to be

$$X'(z) = \sum_{n=-\infty}^{\infty} x[n-m]z^{-n} \tag{6.18}$$

$$p = n - m \tag{6.19}$$

$$X'(z) = \sum_{p=-\infty}^{\infty} x[p]z^{-(p+m)} \tag{6.20}$$

$$= \left(\sum_{p=-\infty}^{\infty} x[p]z^{p} \right) z^{-m} \tag{6.21}$$

$$= z^{-m}X(z). \tag{6.22}$$

By substituting $z = e^{-i\omega}$, equivalent to evaluating the z-transform on the complex unit circle, the frequency response of the impulse response $h[n]$ can be derived. Letting $x[m] = e^{i\omega m}$ and using the commutation property of the discrete convolution, equation 6.16 may be written as

$$y[m] = \sum_{n=-\infty}^{\infty} x[m-n]h[n] \tag{6.23}$$

$$= \sum_{n=-\infty}^{\infty} e^{i\omega(m-n)}h[n] \tag{6.24}$$

$$= e^{i\omega m} \sum_{n=-\infty}^{\infty} e^{-i\omega n}h[n] \tag{6.25}$$

The final sum in Equation is identified as both the z-transform of $h[n]$ on the complex unit circle $z = e^{-i\omega}$ as well as the DTFT of $h[n]$. The complex frequency response function is defined as

$$H(\omega) = \sum_{n=-\infty}^{\infty} e^{-i\omega n}h[n]. \tag{6.26}$$

The complex frequency response function is a powerful tool for LTI filters, given the input of complex exponential functions at a given frequency, $x[m] = e^{-im\omega}$, the LTI filter returns a complex exponential of the same frequency but multiplied by a complex, frequency dependent, number $H(\omega)$ which

introduces both gain and phase shifts to the output signal, but does not modulate the input frequency (Frerking, 1994; Hayes, 1996).

6.2.2 DTFT

The DTFT of a complex valued function of the continuous variable ω is the z-transform evaluated on the unit circle $z = e^{-i\omega}$

$$X(\omega) = \sum_{n=-\infty}^{\infty} x[n]e^{-in\omega}. \tag{6.27}$$

The inverse of the DTFT follows as

$$x[n] = \frac{1}{2\pi}\int_{-\pi}^{\pi} X(\omega)e^{in\omega}d\omega. \tag{6.28}$$

The DTFT is linear transform which decomposes the energy contained in a time series into an orthogonal basis of complex exponentials. Because these exponentials are eigenvalues of an LTI filter (Equation 6.2.1), the DTFT is typically sufficient to determine the frequency response characteristics of an LTI filter, enabling inversion of the output time series of a discrete system without significant considering the z-transform over the entire complex plane Stoica and Moses (2005). The condition for existence of the DTFT is finite energy or convergence such that

$$\sum_{t=-\infty}^{\infty} |x(t)|^2 < \infty. \tag{6.29}$$

Defining the energy spectral density as the modulus of signal energy at each frequency

$$P(\omega) = |X(\omega)|^2, \tag{6.30}$$

Parseval's theorem states that the total signal energy contained in either the frequency or time domain equal is conserved

$$\int_{\pi}^{\pi} P(\omega)d\omega = \int_{-\pi}^{\pi} \sum_{\tau=-\infty}^{\infty} x[\tau]e^{-i\omega\tau} \sum_{t=-\infty}^{\infty} x^*[t]e^{i\omega t}d\omega \tag{6.31}$$

$$= \sum_{\tau=-\infty}^{\infty} x[\tau] \sum_{n=-\infty}^{\infty} x[t]^* \int_{-\pi}^{\pi} e^{i\omega(t-\tau)} \tag{6.32}$$

$$= \sum_{\tau=-\infty}^{\infty} \sum_{t=-\infty}^{\infty} x[\tau]x^*[t]\delta[t-\tau] \tag{6.33}$$

$$= \sum_{t=-\infty}^{\infty} |x(t)|^2 \tag{6.34}$$

$$\tag{6.35}$$

The convolution theorem is a key principle in relating the DTFT to the linear filter response in both the time and frequency domains. Consider the convolution operation defined in Equation 6.16, then the DTFT representation of the convolution is given by

$$Y(\omega) = \sum_{m=-\infty}^{\infty} \sum_{n=-\infty}^{\infty} x[n]h[m-n]e^{-im\omega} \tag{6.36}$$

$$= \sum_{m=-\infty}^{\infty} \sum_{n=-\infty}^{\infty} x[n]h[m-n]e^{-i(m+n-n)\omega} \tag{6.37}$$

$$\sum_{m=-\infty}^{\infty} h[m-n]e^{-i(m-n)\omega} \sum_{n=-\infty}^{\infty} x[n]e^{-in\omega} \tag{6.38}$$

$$= H(\omega)X(\omega) \tag{6.39}$$

Equation 6.39 demonstrates that the Fourier transform of a convolution in the time domain is equal to a direct product in the frequency domain.

Likewise, convolution in the frequency domain amounts to a direct product of terms in the time domain. Incidentally, time domain convolution may be calculated in the frequency domain taking the direct product of the DTFT of two signals in the frequency domain with a subsequent inverse DTFT applied to recover the time domain convolutions; such a procedure is commonly performed when fast fourier transform algorithms may efficiently expedite the calculation e.g. wavelet analysis of time series (Torrence and Compo, 1998; Farge, 1992).

6.2.3 DIGITIZATION EFFECTS

6.2.3.1 ALIASING

A discussion of the effects associated with digital sampling have thus far been omitted; however there are many effects associated with signal digitization which affect the processing of time-series. The fundamental determination of the sampling function defined in Equation 6.9 is the choice of a sampling interval Δt, with sampling rate defined as $f_s = 1/\Delta t$. The choice of sampling rate determines many of the properties of the spectral composition of the sampled signal x(t). Consider Equation 6.10 as the multiplication of the continuous signal $x(t) by the continuous sampling function $s(t)$. Application of the convolution theorem indicates that in the frequency domain, the digital sampling operation is equivalent to the convolution $X(\omega) * S(\omega)$ where the spectral representation of the sampling function is given as

$$S(\omega) = \int_{-\infty}^{\infty} s(t)e^{-i\omega t}dt = \sum_{m=-\infty}^{\infty} \int_{-\infty}^{\infty} \delta_C(t - m\Delta t)e^{-i\omega t}dt. \tag{6.40}$$

For each element in the sum, the delta function is only defined for some small time, ϵ around each $t = m\Delta t$

$$S(\omega) = \sum_{m=-\infty}^{\infty} \int_{t=m\Delta t-\epsilon/2}^{m\Delta t+\epsilon/2} e^{-i\omega t} dt. \tag{6.41}$$

Defining $\tau_m = t - m\Delta t$, with $dt = d\tau$, allows for the integral to broken into an infinite sum of identical integrals centered on each $t = m\Delta t$:

$$S(\omega) = \sum_{m=-\infty}^{\infty} \int_{-\epsilon/2}^{\epsilon/2} e^{-i\omega t} d\tau_m. \tag{6.42}$$

Taking the integral gives

$$S(\omega) = \sum_{m=-\infty}^{\infty} \frac{ie^{-i\omega\tau_m}}{\omega}\Bigg|_{-\epsilon/2}^{\epsilon/2} = \sum_{m=-\infty}^{\infty} \frac{2sin(\omega\epsilon/2)}{\omega} = \epsilon \text{sinc}(\omega\epsilon/2); \tag{6.43}$$

letting ϵ tend to zero gives a comb of delta functions spaced in the frequency domain at intervals of the $m\Delta t = m/f_s$

$$S(\omega) = \lim_{\epsilon\to 0} \sum_{m=-\infty}^{\infty} \frac{2sin(\omega\epsilon/2)}{\omega} = \sum_{m=-\infty}^{\infty} \delta[\omega - m2\pi f_s] \tag{6.44}$$

Evidently, discretization of a signal $x(t)$ through multiplication with the sampling function $s(t)$ is equivalent the spectral composition of the signal $X(\omega)$ convolved with a train of evenly spaced continuous δ_C functions at the sampling frequency f_s. The spectrum $X(\omega)$ is thus periodic with the sampling frequency f_s. Clearly, the periodic information contained in repeated frequencies exceeds a full description of the spectral composition of the signal.

The periodicity of the sampled spectrum $X(\omega)$ implies that the information contained in the signal is a bandwidth limited. Consider a bandwidth limited frequency $x(t)$ which has spectral composition on the interval $[-B, B]$.

$$x(t) = \int_{-B}^{B} X(\omega) e^{i\omega t} d\omega$$

The spectral composition $X(\omega)$ has been shown to be periodic in f_s. If $B > f_s/2$ it is evident that the spectral composition of the signal for $f < f_s/2$ is a superposition of the bandwidth limited spectral composition $X(\omega)$ and the aliased periodic spectrum $X(\omega + 2\pi f_s)$ centered at f_s. For $B < f_s/2$ the spectral composition centered at $X(\omega + 2\pi f_s)$ does not affect the he spectrum where $f < f_s/2$. This statement is a form of the Nyquist-Shannon sampling theorem, which states that a bandwidth limited signal $x(t)$ must be sampled a frequency $f_s > 2B$ in order to completely determine the signal without aliasing.

The periodicity of the continuous spectrum can is additionally present in the aliasing of the discretized spectrum taken over a finite interval. Consider the DTFT and its inverse defined, in Equation 6.27, as functions of the continuous quantities t and ω. For a finite digitized signal, the DTFT is ill defined and the Discrete Fourier Transform (DFT) representation is alternatively used. The DFT of the discretely sampled time series $x[n]$ of N samples is given by

$$X[k] = \sum_{n=0}^{N-1} x[n] e^{-i2\pi kn/N}. \tag{6.45}$$

The DFT is then equal to the DTFT sampled at discrete frequencies

$$\omega = 2\pi k/N\Delta t.$$

The inverse discrete Fourier transform (IDFT) is given by

$$X[n] = \frac{1}{N} \sum_{k=0}^{N-1} X[k] e^{i2\pi kn/N}. \tag{6.46}$$

Consider frequencies f greater than N, e.g.

$$f = N + k \tag{6.47}$$

$$X[N+k] = \sum_{n=0}^{N-1} x[n] e^{-i2\pi(N+k)n/N} \tag{6.48}$$

$$= \sum_{n=0}^{N-1} x[n] e^{-i2\pi Nn/N} e^{-i2\pi kn/N} \tag{6.49}$$

$$= \sum_{n=0}^{N-1} x[n] e^{-i2\pi n} e^{-i2\pi kn/N} \tag{6.50}$$

$$\tag{6.51}$$

For integer n, the term $e^{-i2\pi n} = 1$ for all n such that $X[N+k] = X[k]$. Again illustrating that the spectrum is periodic in N. It is instructive to let k run negative, specifically such that $X[N-k]$

$$X[N-k] = \sum_{n=0}^{N-1} x[n] e^{-i2\pi(N-k)n/N} \tag{6.52}$$

$$= \sum_{n=0}^{N-1} x[n] e^{i2\pi kn/N} \tag{6.53}$$

$$= X[-k]. \tag{6.54}$$

For the real signal $x[n]^* = x[n]$ the spectrum

$$X[f]^* = \left(\sum_{n=0}^{N-1} x[n]e^{-i2\pi kn/N}\right)^* = \left(\sum_{n=0}^{N-1} x[n]e^{i2\pi kn/N}\right) = X[-k]. \tag{6.55}$$

Equations 6.48- 6.55 demonstrate that the components of the spectra $X[k]$ are periodic in N with spectral coefficients $N/2 \leq f \leq N$ equal to the coefficients for $-N/2 \leq k \leq 0$. Additionally, for a real signal the negative frequency components are the complex conjugate of the positive frequencies such that the specification of coefficients of $X[k]$ for $0 \leq k \leq N/2$ is sufficient to fully determine all other coefficients of the DFT. The frequency $f_c = N/2$ corresponding to $\omega_c = \pi/\Delta t = 2\pi f$ such that $f_c = \frac{1}{2\Delta T} = \frac{f_s}{2}$, known as the Nyquist frequency, is the highest frequency resolvable by the DFT. For a continuous spectrum $X(\omega)$ with bandwidth $[-B, B]$, frequency coefficients for $|B| > f_s/2$ cannot be resolved and are aliased into frequencies below the Nyquist frequency. Typically, low pass filtering is used to ensure that the bandwidth of the spectrum falls within the range allowed by the Nyquist, i.e. to prevent aliasing. The periodicity of the DFT and associated aliasing properties as outlined in both the convolution of a spectrum with a sampling function, as well as an analysis of the term-by-term periodicity in coefficients are both formulations of the Nyquist-Shannon sampling theorem.

6.2.3.2 DECIMATION AND ANTIALIASING

The appropriate treatment of aliasing is particularly important in the decimation, or downsampling, of digital time-series. In decreasing the sample rate of a signal, frequencies above the downsampled Nyqvist must be removed before the signal can be decimated (Crochiere and Rabiner, 1983). Low pass filters used to remove high frequency composition of signals are typically called anti-aliasing filters. As an example of antialiasing On PSP, the Radio Frequency Spectrometer (RFS) samples the FIELDS antennas at a high frequency sample rate of 38.4 MHz, providing spectra consisting of 2048 frequency bins with a resolution of $\Delta f = 9375$ Hz (Pulupa et al., 2017). The frequency resolutionassciatied with the HFR sampling rate mode is larger than the bandwidth associated with some desired observations, i.e. the plasma frequency peak, a low frequency resolution (LFR) mode is provided with an improved frequency resolution. In order to both decimate the HFR mode, and additionally provide anti-aliasing, a cascade-integrator-comb (CIC) filter is implemented (Frerking, 1994).

PULUPA ET AL. 2017 JGR. RFS can decimate the HFR sample rate by a factor of eight, providing an LFR mode with increased frequency resolution ($\Delta f_{\mathrm{LFR}} = 1171.875$ Hz). Antialiasing for the RFS LFR mode is accomplished with a cascaded integrator comb (CIC) filter. Hogenauer (1981) provides a comprehensive overview of the CIC filter, including a thorough discussion of its merits and implementation. The CIC filter consists of a set of N integrators operating at the HFR sample rate followed by N comb filters operating at the decimated LFR rate. The integrator stages operate as

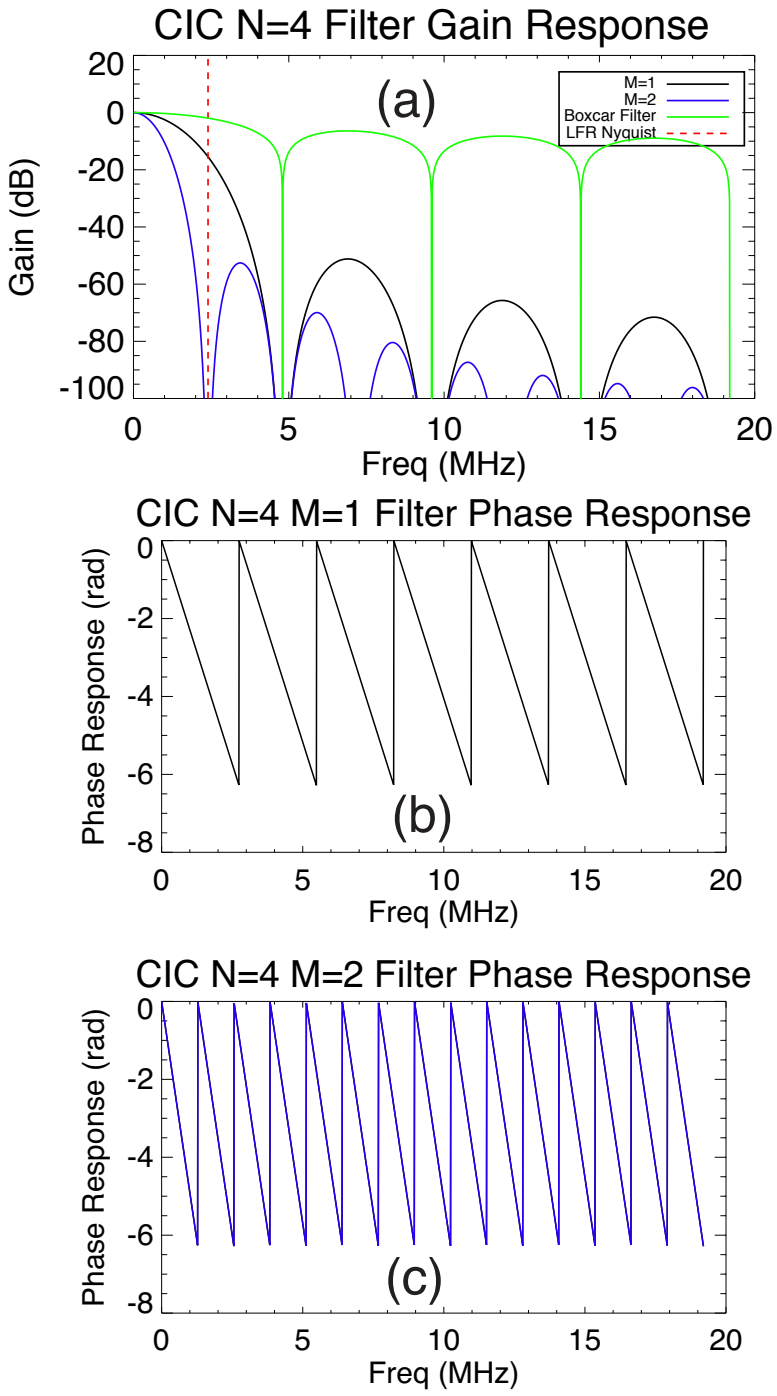

Figure 6.1: (a) Gain response of CIC Filter.(b-c) Linear phase response for CIC filters.

$y[n] = y[n-1] + x[n]$ where the output of each integrator is cascaded into the input of the succeeding stage. Each integrator stage has a a transfer function given by

$$H_I = \frac{1}{1 - z^{-1}}. \tag{6.56}$$

The comb stages are described by $y[n] = x[n] - x[n - RM]$ where R is the decimation factor and M is a parameter known as the differential delay. The comb transfer function is given by

$$H_C = 1 - z^{-RM}. \tag{6.57}$$

Downsampling before the comb cascade increases the CIC filter's efficiency (Donadio, M. P., 2000). After the rate change, the comb operates at a decimated rate described by $y[n] = x[n] - x[n - M]$, effectively decreasing the number of delay elements required in calculating the comb output.

The transfer function of the filter cascade is

$$H_{CIC}(z) = H_I^N(z) H_C^N(z) = \frac{(1 - z^{-RM})^N}{(1 - z^{-1})^N} \tag{6.58}$$

Evaluating on the complex unit circle $z = e^{i(2\pi f/R)}$ gives the frequency response of the CIC filter as

$$P(f) = \left[\frac{\sin \pi M f}{\sin \frac{\pi f}{R}} \right]^{2N}. \tag{6.59}$$

Figure 6.1a shows the gain characteristics of the $N = 4$ stage CIC filter in comparison with a moving average boxcar filter. The CIC filter performs significantly better than a moving average filter as an antialiasing filter. Additionally, the CIC filter provides several economic benefits over FIR filters for implementation in the FIELDS FPGA: no multiplicative steps are required, and storage is reduced by downsampling before passing the integrator stage output to the comb filters.

The RFS uses a four stage integrator-comb filter which can operate with a differential delay set to either one or two. The first null in the $M = 1$ filter occurs at the LFR sample rate. For $M = 2$ the first null occurs at the LFR Nyquist; providing better antialiasing effects, but introducing significant attenuation in the LFR passband. The RFS CIC will typically operate with $M = 1$.

For the LFR receiver with $M = 1$, frequencies just below the Nyquist of 2.4 MHz will have relatively poor anti-aliasing performance. However, these frequencies are not included in the telemetered LFR spectra, which only includes frequencies up to 1.7 MHz. In the frequency range from 1.3 to 1.7 MHz, the telemetered LFR and HFR data will overlap, and the selected LFR and HFR frequencies have been

chosen to match in order to allow accurate inter-calibration. In this overlap range, it will be possible to identify any aliased signals (aliased down from 3.1-3.5 MHz) in the LFR by comparing to the HFR spectrum. Below 1.3 MHz, where there will be no overlap between LFR and HFR, the CIC algorithm should be sufficient to remove aliased signals (aliased down from 3.5 MHz and above), as shown in Figure 6.1a. Should it be determined on orbit that further antialiasing is required, the $M = 2$ mode can be commanded via flight software.

The CIC phase response is linear in frequency, as shown in Figure 6.1b and 6.1c for the $M = 1$ and $M = 2$ modes. For on-board cross-correlations, the same value of M will always be set for the two LFR input channels, so there will be no relative phase difference generated by the CIC.

6.2.4 FINITE TIME EFFECTS

The Nyquist frequency is independent of the length of the sample and dependent only on the sampling rate f_s. Considering the expression for the DFT in equation 6.45, it is evident that as the length of the sample, $T = N\Delta t$ increases, the frequency resolution f/N is decreased such that as as $N \to \infty$ then the DFT asymptotes to the continuous DTFT $X[2\pi f] \to X(\omega)$.

In practice, infinite length signals are not obtainable, and the introduction of the finite length interval effects the signal composition. Two important complementary ideas are related to the finite truncation of a discrete time series: the time-frequency uncertainty principle and the associated spectral leakage.

First consider a signal with a DTFT spectral composition

$$X(\omega) = A\delta(\omega - \omega_0), \tag{6.60}$$

the time-domain representation is, by the IDTFT in equation 6.28,

$$x[n] = \frac{A}{2\pi} e^{in\omega_0}, \tag{6.61}$$

a complex exponential extending for all time. Truncating the time series such that $x[n] = 0$ for $n > |m|$ is conveniently written as the multiplication of the infinite time-series with two Heaviside step functions $H[n]$:

$$(\omega) = \sum_{n=-m}^{m} x[n]e^{-in\omega} = \sum_{n=-\infty}^{\infty} x[n]e^{-in\omega}(H[n+m] - H[n-m]). \tag{6.62}$$

$$H[n] = \begin{cases} 0 & n < 0 \\ 1 & n \geq 0 \end{cases}. \tag{6.63}$$

The convolution theorem is then used to determine the finite length truncation spectrum $X_f(\omega)$ created by multiplication of the rectangular window created by the Heaviside functions. The spectral representation of the Heaviside function can be calculated using the derivative of the continuous Heaviside function

$$\frac{dH}{dt} = \delta(t) \tag{6.64}$$

and integration by parts:

$$\int \frac{dH}{dt} e^{-i\omega t} dt = He^{-i\omega t}\Big|_{-\infty}^{\infty} + i\omega \int He^{-i\omega t} dt \tag{6.65}$$

when neglecting the principal value associated with the integral, which vanishes with the difference of two Heaviside steps, it's evident that

$$\frac{d\tilde{H}}{dt} = i\omega\tilde{H}. \tag{6.66}$$

The DTFT of the truncation function, consisting of two Heaviside functions, is rewritten as a DTFT of its derivative,

$$\tilde{H} = \sum_{n=-\infty}^{\infty} e^{-in\omega}(H[n+m] - H[n-m]) = \sum_{n=-\infty}^{\infty} e^{-in\omega} \frac{\delta[-m] - \delta[m]}{i\omega} = \frac{\sin(m\omega t)}{m\omega t} = \mathrm{sinc}(m\omega t) \tag{6.67}$$

Accordingly, the resulting sampled spectral composition is given by

$$X_f(\omega) = \tilde{H} * X(\omega) = \mathrm{sinc}(m\omega t) * A\delta(\omega - \omega_0) = A\mathrm{sinc}(m\omega_0 t). \tag{6.68}$$

The spectra of the truncated time series no longer has energy confined to a single frequency coefficient: spectral energy is distributed among frequencies in accordance with the Fourier transform of the truncation window. This effect is commonly called spectral leakage and will occur for any finite-length time series. The rectangular window chosen here results in the convolution of a sinc function; typically window, or taper, functions are chosen to minimize spectral leakage, or to direct it towards specific bands in frequency space (Stoica and Moses, 2005; Bendat and Piersol, 1990; Frerking, 1994; Hayes, 1996). Similarly, a truncation in the spectra will generate leakage in the time domain though convolution with the spectral truncation window.

Generally, spectral leakage limits precision in which a signal can be precisely defined in both frequency and time, commonly known as the time-frequency uncertainty principle. For infinitely precise definition in either time of frequency through a δ function, the conjugate transform variable is required to have an infinite extent; the truncation to a finite support of the conjugate variable domain results in the dispersion in the δ distribution.

Defining the time-duration and the bandwidth of a signal respectively as

$$\mathcal{T} = \frac{\sum_{n=-\infty}^{\infty} |x[n]|^2}{x^2[n_0]} \tag{6.69}$$

$$B = \frac{\int_{-\pi}^{\pi} |X(\omega)|^2 d\omega}{|X^2(\omega_0)|} \tag{6.70}$$

where n_0 and ω_0 are the time and frequency of maximum signal strength, Parseval's theorem demands the inequalities

$$|x[n_0]|^2 \leq \sum_{n=-\infty}^{\infty} |x[n]|^2 \tag{6.71}$$

$$|X(\omega_0)|^2 \leq \int_{-\pi}^{\pi} |X(\omega)|^2 d\omega \tag{6.72}$$

such that B and $\mathcal{T}$ are greater or equal to unity. Following e.g. Stoica and Moses (2005) and Bendat and Piersol (1990), it is possible to show that $B\mathcal{T} > \frac{1}{4\pi}$. For the case of the DFT, the uncertainty relation is evident in the minimum frequency resolution (bandwidth) is given by $\Delta_f = f_s/N$ such that the minimum resolvable bandwidth decreases with increasing sample length; likewise the minimum resolvable time duration is improved by increasing the sampling frequency.

6.3 CALIBRATION THROUGH INVERSION OF FREQUENCY RESPONSE

The framework of LTI filters allows for the formulation of a very general equation relating an input signal to it's output through linear transformations in both the time and frequency domains

$$y[m] = (h * x)[m] \tag{6.73}$$

$$Y(\omega) = H(\omega)X(\omega). \tag{6.74}$$

For an LTI filter, the complex frequency response function $H(\omega)$ uniquely determines the filter properties. Using an LTI model for a time-series calibration thus requires the definition of the frequency response function, which may be determined analytically, experimentally, or parametrically.

Most generally $H(\omega)$ is a complex value, which effects both the gain and phase of the spectral components of an input signal. The gain of $H(\omega)$ is defined at each frequency as the ratio between the

output and input signal amplitude $|H(\omega)| = \left|\frac{Y(\omega)}{X(\omega)}\right|$. Frequently, the gain is taken in units of dB (decibels) such that

$$G[\text{dB}] = 20\log_{10}\frac{Y(\omega)}{X(\omega)} = 10\log_{10}\left(\frac{Y(\omega)^2}{X(\omega)^2}\right). \tag{6.75}$$

The phase shift associated with the filter $H(\omega)$ is taken as the angle between the input and output signal in the complex plane

$$\Delta\phi = \tan^{-1}\left(\frac{Y(\omega)}{X(\omega)}\right). \tag{6.76}$$

Experimentally, it is possible to determine the gain and phase of $H(\omega)$using injected stimulus signals, such as white noise, delta functions, sinc functions, or a series of sine waves, with well known spectral energy distributions. Deviations from the expected may be quantified and associated with the the instrumental transfer function $H(\omega)$. For example let $x[n]$ be a controlled signal injected into the LTI filter with a known ideal energy distribution $|X(\omega)|$ and phase $\phi_x(\omega)$. The resulting output signal $y[n]$ with measured spectral distribution $|Y(\omega)|$ and phase $\phi_y(\omega)$ can be inverted using the inverse LTI filter $H^{-1}(\omega)$ to obtain the known ideal spectral distribution $|X(\omega)|$ and phase $\phi_x(\omega)$.

$$H^{-1}(\omega)Y(\omega) = H^{-1}(\omega)H(\omega)X(\omega). \tag{6.77}$$

Where $H^{-1}(\omega)H(\omega)$ is defined to have unity gain and zero phase shift. In this sense, the output signal has been calibrated to estimate the input signal as: $H^{-1}(\omega)Y(\omega) = X(\omega)$. An inversion can also be performed as a convolution in the time domain as

$$x[m] = h^{-1}[m] * y[m] \tag{6.78}$$

where $h^{-1}[m]$ is called the calibration kernel.

Formally, the equation $Y(\omega) = H(\omega)X(\omega)$ is invertible only if $H(\omega)$ is defined for all ω such that the input reconstructed as $X(\omega) = Y(\omega)/H(\omega)$ is not singular (Hayes, 1996). In the context of instrument calibration, inverting the instrumental response function, modeled as an LTI filter with a complex frequency response, provides an estimation of the input stimulus and thus a calibration of the instrument.

6.3.1 FIR AND IIR FILTERS

In the study of LTI systems, two commonly used broad types of filters exist. The first class of filters has a response function to an impulse δ function which has finite support in the time domain, specifically

$$y[m] = (h * \delta[0])[m] = 0 \text{ for } |m| > k, \tag{6.79}$$

where k is an integer which determines the filter order, is accordingly called a finite impulse response filter (FIR). In addition, the concept of causality can be introduced, which imposes that the signal $y[m]$ at any given m can not be a function of input steps $x[n]$ where $n > m$. Equivalently the impulse response function is defined such that $h[n]$ =0 for $n < 0$. A filer with impulse response defined with support on $n < 0$ is called non-causal.

In the convolution described by Equation 6.39, the limits of the sum for a k-tap FIR filter are made finite according to

$$y[m] = \sum_{n=0}^{k-1} h(n)x[m-n]. \tag{6.80}$$

Filters which do not have a finite support to the response function are called infinite impulse response (IIR) filters. A general representation of an IIR in the time domain is given by the difference equation

$$y[m] = \sum_{n=0}^{k-1} a_n x[m-n] + \sum_{n=1}^{l} b_n y[m-n] \tag{6.81}$$

The causal difference equation represents each output $y[m]$ as a weighted sum of all previous input and output values, where the weights a_n and b_n are commonly called the filter coefficients (Hayes, 1996; Crochiere and Rabiner, 1983).

The frequency responses for FIR and IIR filters in form of Equation 6.81 are determined through evaluating the z-transform on the complex unit circle. Rewriting Equation 6.81 and taking the z-transform as

$$\sum_{m=-\infty}^{\infty} \left(y[m] - \sum_{n=1}^{l} b_n y[m-n] \right) z^{-m} = \sum_{m=-\infty}^{\infty} \left(\sum_{n=0}^{k-1} a_n x[m-n] \right) z^{-m}. \tag{6.82}$$

Using Equation 6.18 for the z-transform under translation in time:

$$\left(1 - \sum_{n=1}^{l} b_n z^{-n} \right) Y(z) = \left(\sum_{n=0}^{k-1} a_n z^{-n} \right) X(z) \tag{6.83}$$

$$H(z) = \frac{Y(z)}{X(z)} = \frac{\left(\sum_{n=0}^{k-1} a_n z^{-n} \right)}{\left(1 - \sum_{n=1}^{l} b_n z^{-n} \right)}. \tag{6.84}$$

The numerator and denominator of equation 6.83 can be separately factored as complex polynomials in z^{-1}

$$H(Z) = a_0 \frac{\prod_{n=1}^{k} (1 - z_n z^{-1})}{\prod_{n=1}^{l} (1 - p_n z^{-1})} \tag{6.85}$$

The ratio between two polynomials functions is called a rational function: for equation 6.85, the numerator is a complex polynomial of z^{-1} of order l with roots z_n referred to as zeros of the filter; the denominator is a complex polynomial of order p with roots p_n referred to as poles of the filter. The filter order is referred to as the order of the largest polynomial, i.e. the larger value of k or l.

For an FIR filter, the denominator polynomial is of order zero such that no poles are present, and the filter output at any time is only a function of previous input steps; accordingly the FIR filter is also referred to as an all-pole filter (Hayes, 1996; Smith, accessed 2019).

6.3.2 CALIBRATION AS INVERSION OF FREQUENCY RESPONSE

A physical sensor sampling an external field can be understood as a linear time invariant filter such that the properties of the instrument do not change over time. Sufficiently good design and engineering practices allow for a characterization of the complex instrumental frequency response such that the appropriate inversion gives an estimate of the measured external field. Typically, the analog physical instrumental responses are low order IIR filters which may contain several poles and zeros. In this paradigm, the calibration of an instrument is understood as the application of an inverse filter such that characteristic instrumental response is corrected for.

For real valued signals, such as a measurements made by physical instruments such as an SCM or fluxgate magnetometer, certain constraints on the frequency response are imposed. The complex conjugate of a real signal is given by $x[m] = x^*[m]$

Accordingly the z-transform of a conjugate real signal can be written as

$$X^*(z) = \left(\sum_{n=-\infty}^{\infty} x[n] z^{-n} \right)^* \tag{6.86}$$

$$X^*(z) = \left(\sum_{n=-\infty}^{\infty} x[n] z^{n} \right) = X(z^*) \tag{6.87}$$

evaluating on the unit circle to determine the frequency response gives

$$X^*(\omega) = X(-\omega). \tag{6.88}$$

Equation 6.88 demonstrates that the he z-transform and DTFT of a real signal are Hermitian functions. For the complex frequency response of filter to produce a real signal output from a real signal output, it's time domain coefficients must be real, and thus the instrumental complex frequency response is itself Hermitian.

In order to calibrate a measurement through inversion of the instrumental frequency response, the gain and phase characteristics associated must first be determined. For the FIELDS SCM, analysis of the frequency response was performed with a controlled power supply, signal generator, and stimulus

coils placed directly on each end of the SCM coils (Jannet, G., and Martin, P. and Dudok de Wit, T., 2013). The SCM was placed in a $\mu - metal$ shielding box to provide shielding from ambient environmental fields. Additionally, during flight, the DFB may inject analog signals into SCM preamplifier exciting the secondary coil windings, providing for a control signal by which the SCM response can be measured against known input signal, and variations in the transfer function over time can be monitored (Malaspina et al., 2016; Jannet, G., and Martin, P. and Dudok de Wit, T., 2013). Because of the Hermitian condition of the complex frequency response, specification of the $H_{SCM}(\omega)$ can be completed through injecting a series of sequential sine waves with known amplitude and phase. Additionally, temperature dependent coefficients associated with the DFB and SCM are monitored to provide for higher order modifications to the frequency response (Bale et al., 2016a; Malaspina et al., 2016). These characterization procedures are commonly used in flight hardware search coils, e.g. MMS and THEMIS (Roux et al., 2008; Le Contel et al., 2016)

Figure 6.2 shows the Bode plot (gain and phase curves) measured for the PSP flight model SCM.

6.3.3 MAG TRANSFER FUNCTION

While calibration of the MAG is discussed in Chapter 5, a discussion of the complex transfer function is largely omitted due to the fact that the MAG has unity gain and zero phase shift below ~ $1Hz$. Because the MAG is used to study DC fields, consideration of the complex frequency characteristics are secondary to removing the MAG zero offsets. The MAG complex frequency response is dominated by one pole low pass Butterworth filter corresponding to the analog anti-aliasing filter turned to a -3dB reduction in gain at the survey sample Nyquist ($f_{NY} \approx 147$ Sa/s) (Sheppard, D., 2017; Connerney et al., 2015). The single pole Butterworth filter is a common low pass filter given by the frequency response

$$H(\omega) = \frac{H_0}{1 + i(\omega/\omega_c)} \tag{6.89}$$

where H_0 is the DC gain such that

$$H|(\omega)|^2 = \frac{H_0}{1 + i(\omega/\omega_c)} \frac{H_0}{1 - i(\omega/\omega_c)} = \frac{H_0^2}{1 + (\omega/\omega_c)^2} \tag{6.90}$$

corresponding to a -3 dB gain at the corner frequency ω_c. For low frequencies, $\omega \ll \omega_c$ the gain is approximately that of the DC gain, i.e. unity (Frerking, 1994).

By rewriting the frequency response of the single pole Butterworth filter as

$$H(\omega) = \frac{H_0}{1 + i\omega/\omega_c} \frac{1 - i\omega/\omega_c}{1 - i\omega/\omega_c} = \frac{H_0 - iH_0\omega/\omega_c}{1 + (\omega/\omega_c)^2}, \tag{6.91}$$

the phase response of the single pole Butterworth filter is

$$arg(H_\omega) = -\tan^{-1}(\omega/\omega_c), \tag{6.92}$$

corresponding to no phase shift near DC frequencies, and a phase shift of $\pi/4$ at the Nyquist frequency.

Evidently the antialiasing filters for the MAG sensors provide for little effect on the signal gain and phase shift for low frequencies, in considering frequencies such that $f \ll f_{ny}$ it is possible to neglect the response of the MAG anti-aliasing filter; however, the simplistic analytical form of the Butterworth filter provides for easy inversion of the MAG instrumental frequency response. However, for the case of the SCM, which has significant gain and phase shifts associated with it's operation, a detailed calibration through inversion of the complex frequency response is necessary.

6.3.4 FIR CALIBRATION

Performing calibration through LTI filter response inversion on data which has been obtained on the ground inherently requires the use of FIR filters, e.g. the inversion is performed such that

$$\hat{H}(\omega)^{-1}Y(\omega) = \hat{X}(\omega) \tag{6.93}$$

where $\hat{X}(\omega)$ notation is used to denote an estimate quantity. The values $Y(\omega)$ are taken as the recorded values made by an analog-to-digital sampling converter, e.g. the FIELDS MEP.

Calibration kernels which are used to invert the instrumental response in the time domain e.g. $h^{-1}(t)$ are necessarily digital filters with a finite support. Though the true instrumental response function may be an IIR filter with both poles and zeros, the inversion must correspond to an FIR filter, i.e. all zero, approximation. With the understanding of the system equation as a rational function, i.e. Equations 6.83 and 6.85, it's evident that the inverse of a filter, such that $H^{-1}(\omega)H(\omega) = 1$, amounts to inverting the poles and zeros of a response $H(\omega)$. In essence, a pole in $H(\omega)$ corresponds to a zero in the inverse transfer function $H^{-1}(\omega)$; likewise, the inverse of a filter pole filter is a filter zero. Consider the single pole Butterworth response in Equation 6.89, clearly the inverse of the response consists of a filter with a single zero

$$H^{-1}(\omega) = \frac{1}{H_0}(1 + i\omega/\omega_c). \tag{6.94}$$

Calibration using frequency response inversion with FIR filters, consisting of system functions with all-zeros, is easily performed to invert the frequency responses consisting of poles; however zeros in the filter response, corresponding to poles in the inverse filter, can not be strictly inverted by all zero FIR inverse filters. Accordingly, a high order FIR filter may be required in order to approximate the poles in the inverse frequency response. In another formulation, the transfer function $H(z)$ is most generally a complex rational function, in contrast the response of an FIR filter is only a polynomial function. In order to approximate an IIR filter which has zeros and poles, the FIR filter corresponding to the inverse response may need many terms in order to approximate the true rational function inverse. While for a frequency response with a low order number of poles, such as the Butterworth filter, a low order zero FIR filter polynomial function is sufficient for inversion-calibration. The system equation (Equation

6.83) shows that a low order filter corresponds to a few number of filter coefficients, commonly called taps such that the support of the inversion FIR filter is relatively small.

6.3.5 DETERMINATION OF INVERSE TRANSFER FUNCTION

The time domain kernel $h^{-1}(t)$ which inverts the frequency response $H(\omega)$, is simply the impulse response function associated with $H^{-1}(\omega)$. Accordingly, inversion of the SCM response with an FIR approximation, $\hat{h}^{-1}[n]$ with N equally spaced elements, can be estimated using the inverse DFT of $H(\omega)$, (Frerking, 1994; Hayes, 1996). However such an inversion requires determination of the response function on an equally spaced grid of frequencies with a resolution $\Delta_f \leq f_s/N$. Additionally, in order to preserve gain and phase characteristics, a representation of $H(\omega)$ is desired such that the gain and group delay are constant across each frequency bin $f_0 + \delta f$ associated with the FIR frequency resolution:

$$\frac{d|H|}{df}\delta f = Const \tag{6.95}$$

$$\frac{d\phi}{df}\delta f = Const \tag{6.96}$$

Such an (approximate) condition s necessary to ensure that frequencies within the FIR frequency resolution Δf have phase and gain characteristics invertible by the same $H^{-1}f_0$.

Because of the smooth variations associated with low-order zero-pole filters, empirical characterization of frequency response functions, e.g. with a spectrum analyzer, are not typically not performed over equally spaced intervals at high resolution: as long as the resolution is sufficient and measured to significantly the gain and group delay over the range of desired frequencies, it is typically possible to estimate the true response function with sufficient resolution for inversion. Two approaches are outlined here, the first uses an interpolative method to determine $\hat{H}(\omega)$ from the measured $H(\omega)$ at the set of frequencies ω_i. The second uses a complex least square fitting routine to fit an analytical rational function to $H(\omega)$ (Levy, 1959).

INTERPOLATION Figure 6.2 shows the frequency response of the PSP FIELDS SCM determined through ground testing on an approximately logarithmically distributed frequency grid. Using linear interpolation, the non-linearly distribution of frequencies for which measure gain response can be interpolated onto a linearly distributed set of frequencies between DC and the Nyquist frequency (Jannet, G., and Martin, P. and Dudok de Wit, T., 2013).

In order to perform a linear interpolation, it is required that the frequency response of the instrument has been measured with sufficient resolution such that linear interpolation between frequency bins may accurately represent the instrument transfer function. Figure 6.3(a) shows the measured

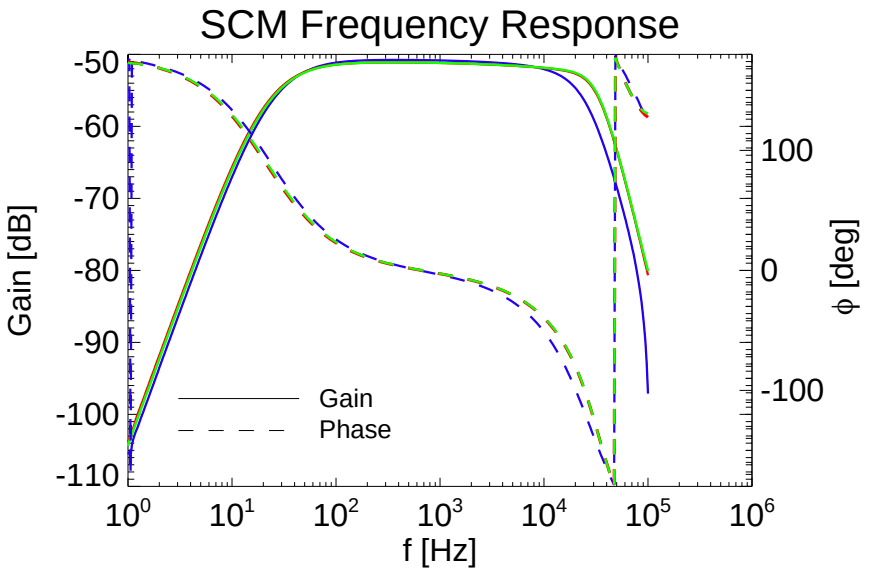

Figure 6.2: Empirically determined gain and phase characteristics of FIELDS SCM

curves of $\Delta|H|/H = \frac{d|H|}{df}\frac{\Delta f}{H}$ and $\Delta\phi/\phi = \frac{d\phi}{df}\frac{\Delta f}{\phi}$ demonstrating that the transfer function is sufficiently smooth such that changes in gain and phase across any single of the logarithmically spaced frequency bins are negligible: e.g. the fractional difference in gain and phase across any single frequency bin is significantly less than 0.10. Given that the measured frequency response has sufficient resolution, it is then possible to redistribute the logarithmically distributed measured $\hat{H}(\omega)$ onto a linear set of frequencies $\hat{H}[k]$ using either spline or linear interpolation (Press et al., 1992b).

Figure (b) shows the SCM LF gain and phase curves in the survey sample mode as measured by the spectral analyzer, in addition with curves interpolated onto 2048 linearly spaced frequencies. Figure (c) shows the full transfer function, negative frequencies constructed as a Hermitian quantity. The inverse transfer function $\hat{H}^{-1}[k]$ is defined such that

$$|\hat{H}|^{-1}[k] = \frac{1}{|\hat{H}|[k]} \tag{6.97}$$

$$\hat{\phi}^{-1}[k] = -\phi[k] \tag{6.98}$$

ANALYTIC APPROXIMATION A continuous analytical approximation for transfer function $\hat{H}(\omega)$ can alternatively be obtained through least squares fitting to the empirically measured transfer function. Several different algorithms exist to approximate $H(\omega)$ based on optimization, (Smith, accessed 2019; Hayes, 1996; Schepker and Doclo, 2016). Levy (1959) presents a method to approximate the poles and zeros of a transfer function by linear least squares fit to a complex rational function. Equations 6.83 and 6.85 show that the complex transfer function of an IIR filter can be represented by a rational

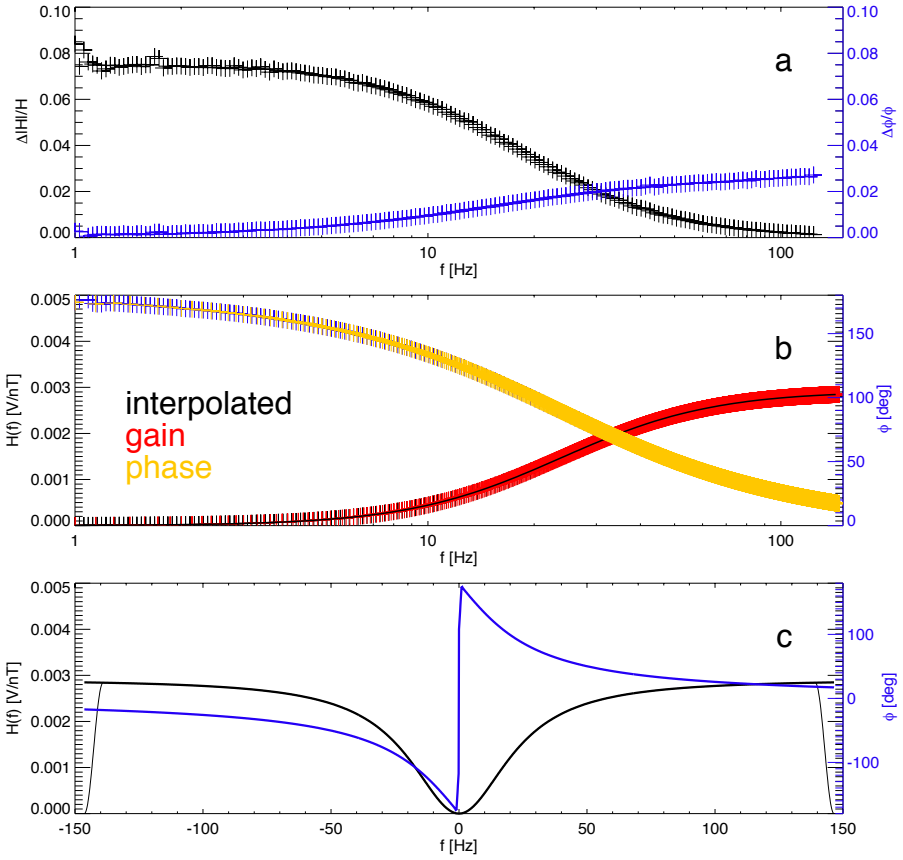

Figure 6.3: (a) Fractional change in gain and phase across each measured frequency of the SCM transfer function. (b) Re-sampled and interpolated linear array of frequencies. (c) Hermitian gain and phase response of the SCM in the survey range.

function of polynomials consisting of complex poles and zeros, given an empirically measured transfer function, the best fit analytical solution to a complex rational function can be obtained through minimization of

$$\epsilon^2 = |H(\omega) - \frac{\hat{A}(\omega)}{\hat{B}(\omega)}|^2 \tag{6.99a}$$

$$\hat{A}(\omega) = \sum A_j (i\omega)^j = \sum_{j=even} (i\omega)^j A_j + i\omega \sum_{k=odd} (i\omega)^{k-1} A_k = \alpha + i\omega\beta \tag{6.99b}$$

$$\hat{B}(\omega) = \sum B_j (i\omega)^j = \sum_{j=even} (i\omega)^j B_j + i\omega \sum_{k=odd} (i\omega)^{k-1} B_k = \sigma + i\omega\tau \tag{6.99c}$$

Instead of minimizing the least square error in Equation 6.99a the method by Levy (1959) allows for a linear least square analytical solution through minimizing

$$|\hat{B}\epsilon|^2 = |\hat{B}H(\omega) - \hat{A}(\omega)|^2 \tag{6.100}$$

which has become known as the equation error (Equation 6.99a) is referred to as the output error (Smith, accessed 2019; Schepker and Doclo, 2016).

Introducing the empirically measured real and imaginary parts of $H(\omega)$

$$H(\omega) = \mathcal{R} + i\mathcal{I} \tag{6.101}$$

The square error solution for $\epsilon_e = \hat{B}\epsilon$, summed each measured point k of transfer function is given by

$$\begin{aligned} &\sum_{k=0}^{m} \epsilon_e^2 \\ &= \sum_{k}^{m} |(\mathcal{R}_k + i\mathcal{I})(\sigma + i\omega\tau) - \alpha + i\omega\beta|^2 \\ &= \sum_{k}^{m} (\mathcal{R}_k\sigma_k - \omega_k\mathcal{I}_k\tau_k - \alpha_k)^2 + (\omega_k\mathcal{R}_k\tau_k + \sigma_k + \mathcal{I}_k - \omega_k\beta_k)^2 \end{aligned} \tag{6.102}$$

The set of measured quantities $\mathcal{R}_k, \mathcal{I}_k, \omega_k$ are all known while $\alpha_k, \beta_k\sigma_k, \tau_k$ are each a sum of terms linear in the fit parameters A_k B_k. Accordingly, differentiation with respect to each fit parameter leads to a system of equations in the other parameters for which a matrix can be computed and inverted. In order to perform the least squares fit, the number of poles and zeros, corresponding to the order of the FIR filter, must be chosen, i.e. an analytical form for the filter must be presumed.

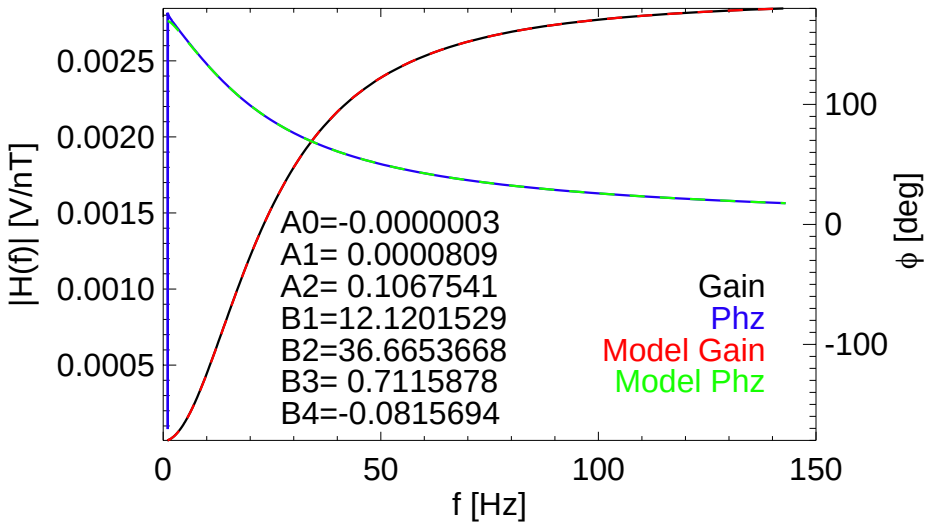

Figure 6.4: SCM transfer function gain (black) and phase (blue) determined from spectral analyzer. A 4-pole 2-zero fit analytical fit (green and red) is performed to the empirical function.

Minimizing equation error amounts to filtering the errors by the function $\hat{B}$ effectively giving smaller error weight near the location of the filter poles (Levy, 1959; Smith, accessed 2019; Schepker and Doclo, 2016) . Reduced error weighting near the poles can be undesirable for filters which use many poles to generate the desired spectral gain and phase characteristics. In essence, fitting the location of a pole to capture desired response behavior can be made difficult, in the least squares fitting sense, if the error is reduced near the filter poles.

Figure 6.4 shows the least square fit to equation error for a 4-pole 2 zero filter to the SCM transfer function using the Levy (1959) method implemented in IDL. Am abscissae of linearly spaced frequencies ranging from $-f_n/2 < f < f_n/2$ is then constructed over which the analytic function $\hat{H}(\omega)$ can be explicitly evaluated without uncertainty associated with interpolation. The inverse transfer function is subsequently obtained with Equation 6.97. The analytic method allows for quick construction kernels of different sizes, i.e. frequency resolutions, without re-interpolating the empirically measured transfer function. Once again, the constraint that the group delay and gain of frequencies within the frequency bin $\Delta f = f_s/N$ be approximately constant in order for the FIR approximation to the analytic $\hat{H}(\omega)$ to be able to correctly invert the gain and phase of the SCM response.

WINDOW METHOD FOR KERNEL CREATION Once the inverse transfer function $H^{-1}(\omega)$ has been determined in the frequency domain, e.g. either through interpolation or analytic approximation, a kernel $h^{-1}[n]$ is constructed to perform the calibration of the time series in the time-domain. The following method is a common numerical routine occasionally referred to as the window method (Smith,

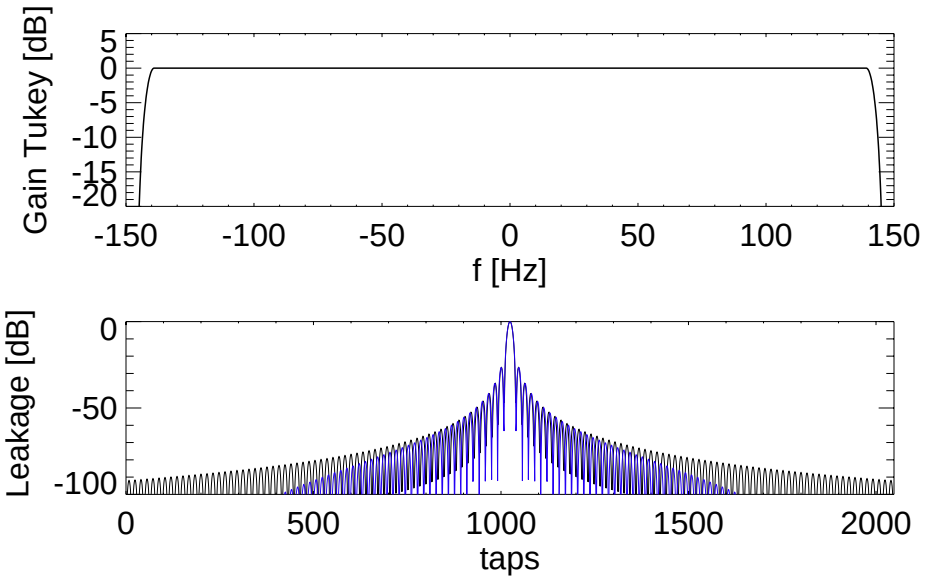

Figure 6.5: (a) Gain associated with Tukey window with α=0.05. (b) Spectral leakage associated with rectangle filter (black) and Tukey window (blue).

accessed 2019; Frerking, 1994; Oppenheim and Schafer, 1975). The DTFT of the impulse response is simply equal to the complex transfer function, accordingly the IDFT of the estimated inverse transfer function $\hat{H}^{-1}[m]$ is taken as the calibration kernel $h^{-1}[m]$ where the number of taps in the kernel is equal to the number of frequency bins N in the associated discretized transfer function. Section 6.2.4 demonstrates, the truncation of the $H^{-1}(\omega)$ by a rectangular window will introduce leakage in the time domain kernel. Accordingly it is desirable to first multiply $H^{-1}(\omega)$ by a window function in order to prevent spectral leakage in the kernel. The use of a real valued window, with symmetric positive and negative frequencies, ensures that no phase shift is associated with the window tapering.

Figure 6.5(a) shows the gain corresponding Tukey (tapered cosine window) consisting of a rectangular window of width $(1-\alpha/2)N$ convolved with a cosine lobe, $w_{\cos} = \cos(\pi n/N)$, with $\alpha = 0.05$ (Harris, 1978). For a 2048 tap FIR filter sampled at the FIELDS survey rate the -3dB gain point of the Tukey window occurs approximately 141 Hz, with 0 dB gain up to 138 Hz. Figure 6.5(b) shows the improvement in performance with respect to spectral leakage using the Tukey tapering window.

Once the inverse transfer function has been tapered, the IDFT is applied to $\hat{H}^{-1}[m]$ to obtain the convolution kernel $h^{-1}[n]$. Figure 6.6 shows the calibration kernel for the x axis of the FIELDS search coil. After the inverse gain and phase effects for the transfer function are corrected for, a scale factor is used to convert from the measured discrete time series signal in, e.g. counts or Volts, to a value of nT. The result is a calibrated time series with physical units representing magnetic field.

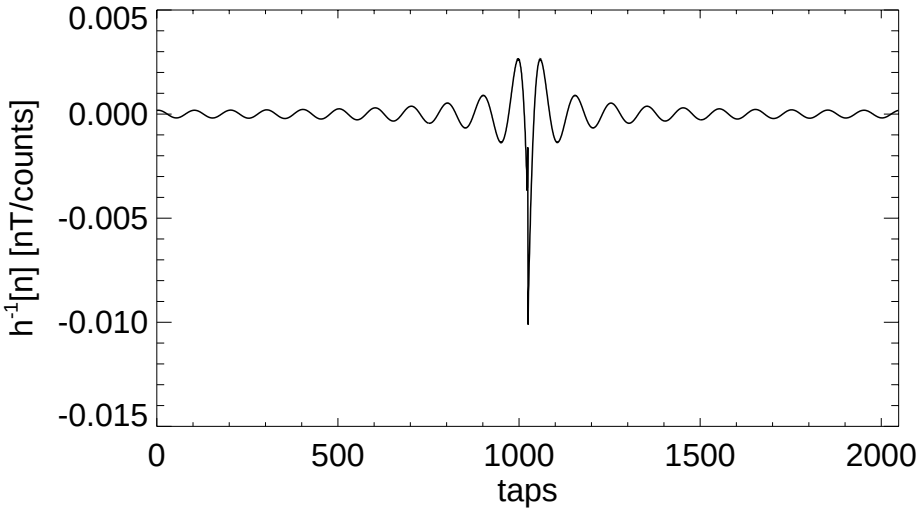

Figure 6.6: Calibration kernel (2048 taps) for PSP SCM x-axis in DFB high-gain state for count to nT conversion.

ADVANCED METHODS FOR FIR FILTER DESIGN The FIR filter approach to calibration consists of an all-zero polynomial fit to a complex transfer function. The window method uses the estimated frequency response at a regularized linear set of frequencies and a DTFT to transform the inverse frequency response into a time domain kernel. In general more advanced methods exist to fit a transfer function to a polynomial, e.g. Remez exchange or Parks-McClellan algorithms for polynomial fitting, relying on Chebyshev transforms (McClellan and Parks, 2005; Frerking, 1994; Smith, accessed 2019). Such algorithms are useful in determining the best fit for a polynomials to a transfer function and may allow for relatively good approximation to an instrumental response using low order FIR filters (few taps). These algorithms can be used when computing resources are limited, or when rapid processing of data is necessary.

6.3.6 COMPARISON BETWEEN MAG AND SCM TIME SERIES

Once a time series which has been recorded by the DFB has been downlinked from the spacecraft it can be convolved with the calibration kernel, the time series is in physical units and represents the estimate of the magnetic field during the recorded interval. For missions such as PSP which have multiple instruments sensitive in similar frequency ranges, the cross calibration between instruments allows for verification of the inversion of the transfer function. Because of the simplicity of the single pole Butterworth filter transfer function associated with the MAG, even a direct comparison between the calibrated SCM time series and the uncorrected MAG data is quite illuminating. Figure 6.7 shows the power spectral densities for the SCM and outer MAG for the interval 11-05-2018T00:00-11-05-

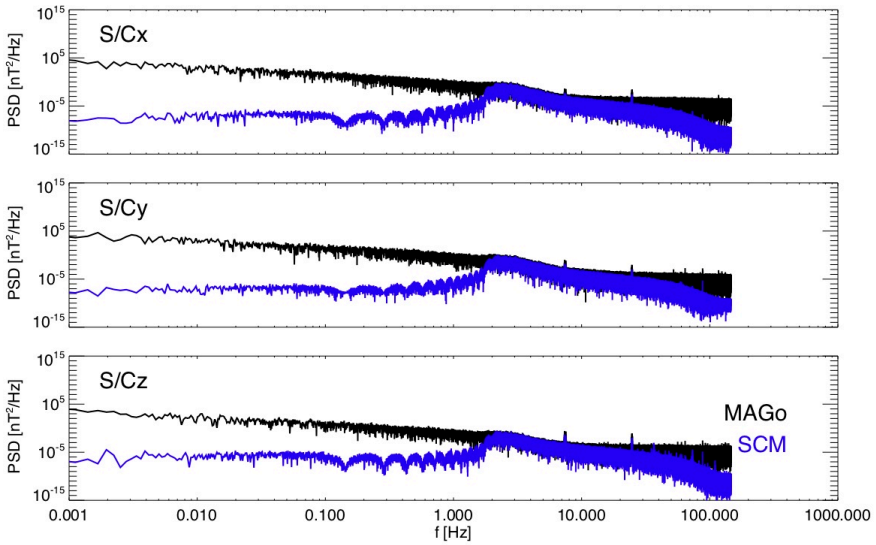

Figure 6.7: Spectral densities for PSP FIELDS magnetic field observations (MAGo, black; SCM, blue) from 11-05-2018T00:00-11-05-2018T01:00 during first solar encounter. The DFB response at high frequencies has not been corrected in the SCM.

2018T01:00. Data were taken from both instruments at the FIELDS survey rate 292.969 Sa/s. A low cut is applied to the SCM inverse transfer function in order to reject the amplification of low frequency noise. The flattening of the MAG power spectra at frequencies greater than 10 Hz is due to the instrumental noise floor, highlighting the need for both AC and DC coupled instruments. Additionally Figure 6.7 highlights the benefits of a merged time series: time series from two instruments are required in order to fully capture the survey mode bandwidth, a single time series which contains the spectral composition of the magnetic field at both low and high frequencies is clearly improvement over the two individual data sets.

Figure 6.8 shows an eight second interval of data with large transverse fluctuations with frequency of several Hz coinciding near the ion-gyroscale on 11-05-2018. The presence of the waves in the co-observation band between the MAG and SCM provides for a test of the performance of the phase of the inverse transfer function. Because the the DC nature of the MAG, a bandpass filter is applied between 3 and 30 Hz in order to isolate the co-observation band ,e.g. Section 7.3.Figure 6.8 demonstrating an extremely good agreement between the MAG and SCM observations.

Figure 6.9 shows the distribution of residual field differences between the outer MAG and SCM in the bandpassed set of frequencies which can be co-observed by both instruments. The root mean squared difference between the two sensors is less than 0.1 nT for each axis, consistent with known levels of spacecraft noise, e.g. reaction wheels observed in the magnetic field time series. The residuals

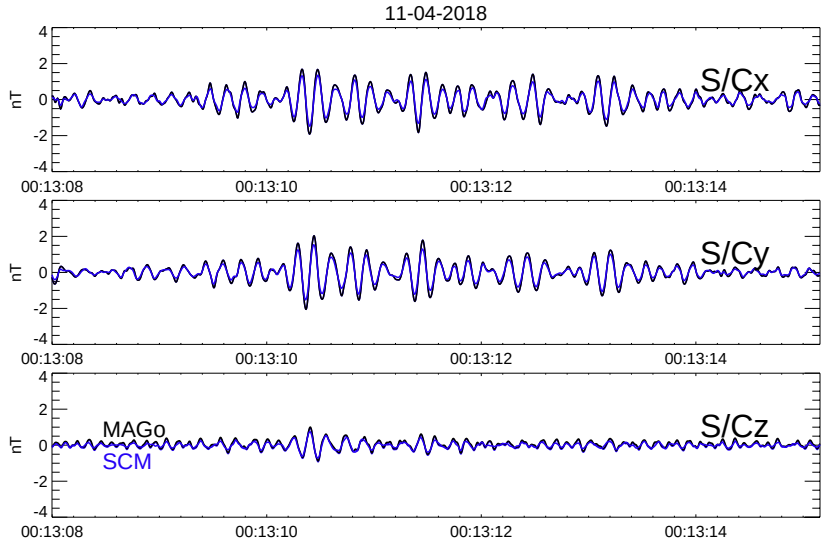

Figure 6.8: Observations of coherent waves of frequency 3 Hz on 11-05-2018T00:13:08-00:13:15. Waves are observed at the cross over between MAG and SCM noise floors, enabling analysis of relative calibration

between the MAG and SCM are dominated by lower frequencies which have more spectral power, at higher frequencies the residual level is set by the spectral density associated with the MAG noise floor.

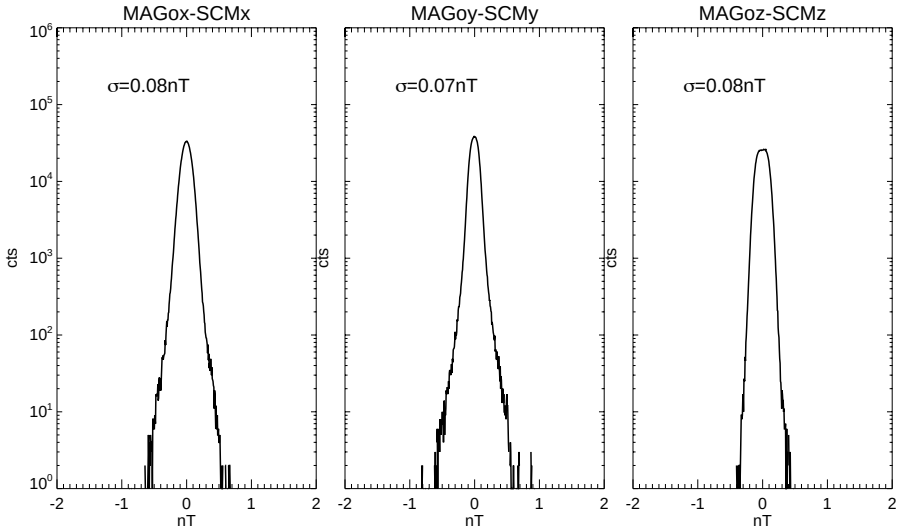

Figure 6.9: Distribution of residuals for bandpassed (3-30 hz) SCM and MAGo observations in spacecraft x (left) ,y (center), z (right) directions. The rms residuals are less than 0.1nT consistent with known sources of spacecraft noise..

7

MERGING SEARCH COIL AND FLUXGATE MAGNETIC FIELD DATA FOR PARKER SOLAR PROBE FIELDS

The FIELDS instrument on Parker Solar Probe (PSP) provides the in-situ measurements of the electric and magnetic fields of the solar wind and corona required to achieve the three principal science objectives of PSP: tracing the flow of energy that heats the solar corona and accelerates the solar wind; determining the structure and dynamics of the plasma and magnetic fields at the sources of the solar wind; and exploring the mechanisms that accelerate and transport energetic particles (Bale et al., 2016a; Fox et al., 2016). The measurements made by FIELDS are complemented by in-situ measurements of the solar wind and coronal plasma through the Solar Wind Electrons Alphas and Protons (SWEAP) Investigation; energetic particles through the Integrated Science Investigation of the Sun (IS⊙IS); as well as white light images from the Wide-Field Imager for Solar Probe (WISPR) instrument (Kasper et al., 2016; McComas et al., 2016; Vourlidas et al., 2016).

Accomplishing the scientific objectives of PSP requires in-situ observations of magnetic and electric fields over wide ranging bandwidths with large dynamic ranges. The electric field measurements made by the FIELDS Radio Frequency Spectrometer (RFS), Digital Fields Board (DFB), and Time Domain Sampler (TDS) instruments will measure electric fields of the inner heliosphere from DC-19.2 MHz through a diverse combination of survey mode waveform, burst mode waveform, and spectral observations (Bale et al., 2016a; Malaspina et al., 2016; Pulupa et al., 2017). Additionally, the FIELDS instrument suite consists for a set of three magnetometers, two low frequency vector fluxgate magnetometers (MAGs) and a single vector search coil magnetometer (SCM) located on boom extending behind the spacecraft and within the umbra of the PSP thermal protection system (TPS).

The two fluxgate magnetometers, built at Goddard Space Flight Center (GSFC) provide waveform observations of the vector DC and low frequency magnetic fields with a maximum survey sample rate of $f_{svy}^{max} = 293.969$ Sa/sec. These low frequency measurements are accompanied by measurements from the FIELDS SCM low frequency (LF) windings sensitive from ≈3 Hz-50 kHz. The SCM sensor x-axis additionally contains a second mid-frequency (MF) winding sensitive from ≈10 kHz-1MHz. During the perihelion encounters and aphelion cruise phases, the SCM is continuously sampled by the DFB with a maximum rate of f_{svy}^{max}(Malaspina et al., 2016). Burst mode waveforms for the LF or MF are sampled up to a maximum rate of 150 kSa/sec by the DFB and 1.92 MSa/sec by the TDS (Malaspina

et al., 2016; Bale et al., 2016a). Additionally, the RFS and DFB are configurable to generate both cross and auto-spectral matrix data products at various cadences (Bale et al., 2016a; Pulupa et al., 2017).

Dynamical processes occurring in astrophysical plasmas, which underly the physics occurring in the solar wind and corona, are typically sensitive to the direction of the mean magnetic field: e.g. determinations of variance anisotropy Chen et al. (2010a); Leamon et al. (1998); wave vector polarizations, He et al. (2012); magnetic compressibility, Bale et al. (2009); wave vector distributions, Horbury et al. (2008); and magnetic reconnection, Phan et al. (2018). Furthermore, such processes may occur on fast time scales with small amplitude magnetic signatures. Accomplishing the scientific objectives of PSP thus inherently requires in-situ observations of magnetic fields over large bandwidths and dynamic ranges. Through using both fluxgate and search coil instrumentation, FIELDS is capable of observing the in-situ magnetic field of the inner heliosphere with a bandwidth from DC-MHz and 150 dB of dynamic range (Bale et al., 2016a).

Recently, missions with multi-sensor magnetic observational suites have moved towards merged data products composed of measurements simultaneously taken from multiple instruments, which are combined to employ the optimal qualities of the separate sensors. Alexandrova et al. (2004) successfully used a discrete wavelet transform to merge CLUSTER fluxgate and search coil data to study waves downstream of a shock (Balogh et al., 2001; Cornilleau-Wehrlin et al., 2003). Chen et al. (2010a) use a similar method to study the variance anisotropy of kinetic turbulence in the sub-proton range with CLUSTER. Through the MAG-SCM merging efforts of Alexandrova et al. (2004) and Chen et al. (2010a) were made in-flight, without specific optimization towards the instrument design and operation, the results have been positive and serve as a proof of concept of merged magnetic datasets. More recently, programmatic efforts to perform quantitative end-to-end testing on the Multiscale Magnetospheric Mission (MMS) search coil and digital and analog fluxgate magnetometer have enabled the development of an optimized merged data set (Le Contel et al., 2016; Russell et al., 2016; Torbert et al., 2016; Fischer et al., 2016).

Because of the shared bandwidth associated with the MAG and SCM survey ranges, as well as their shared master clock, the FIELDS magnetic field data is highly suited for merging. The FIELDS instrument team will produce a single continuous survey mode data product using an optimally combined measurements from the SCM and MAG (SCaM). Here the process by which the FIELDS survey data has been merged is outlined, including an overview of preflight ground testing and instrument characterization, simulations of the merging performance, as well as the results from merging time series from the first encounter. Additionally, we outline the yet to be performed merger of MAG with burst mode SCM data from the DFB above the survey rate.

7.1 FIELDS MAG CALIBRATION

The two fluxgate magnetometers, built at Goddard Space Flight Center provide waveform observations of low frequency magnetic fields. They are placed 1.9 and 2.7 m from the spacecraft and are

respectively referred to as the inboard (MAGi) and outboard (MAGo) sensors. The heritage of the PSP/FIELDS MAGs dates to the 1970's NASA Pioneer missions (Ness et al., 1971; Acuna, 1974; Acuña, 2002). Many iterations of the instrument are currently flying on both NASA heliophysics and planetary science missions (Lepping et al., 1995b; Acuña, 2002; Acuña et al., 2008; Connerney et al., 2015, 2017). The sensors may be run at a maximum survey mode rate of f_{svy}^{max} = 293.969 Sa/Sec, which may be downsampled by factors of two with anti-aliasing performed with a Bartlett window (triangle filter). In general, MAGi is run at a lower sample rate in order to meet telemetry constraints imposed by the spacecraft; the lower cadence measurements allow for diagnosis of magnetic noise associated with spacecraft generated magnetic fields. The primary science instrument for the DC magnetic fields is MAGo, which, due to its position further away from the spacecraft, has systematically better signal to noise ratios.

The complex transfer functions associated with the MAGs, shown in 7.1(a), are dominated by a single low-pass Butterworth filter used for anti-aliasing purposes tuned to -3 dB at the max sample rate Nyquist frequency (f_{svy}^{Ny} ≈146.5Hz) (Acuña et al., 2008; Connerney et al., 2015, 2017). Accordingly, the low-pass nature of the MAG transfer function indicates inherent sensitivity to low frequency fields associated with the spacecraft (Ness, 1970; Ness et al., 1971; Belcher, 1973). Typically, the minimization of such fields is performed through magnetic control programs (Ness, 1970; Musmann, 1988). Generally, for three-axis stabilized spacecraft, driven spacecraft maneuvers are used to establish the magnetometer zero offsets relative to the ambient field e.g. Acuña (2002); Connerney et al. (2015), though it has been demonstrated that similar results can be accomplished without controlled maneuvers through statistical analysis of non-compressive Alfvénic rotations in the solar wind (Belcher, 1973; Leinweber et al., 2008). Several multi-sensor techniques to determine sensor zeros have been developed using gradiometric principles, e.g. Ness et al. (1971) and comparison with scalar magnitude instruments, e.g. (Olsen et al., 2003; Primdahl et al., 2006). Additionally, it's been shown that the using solar wind electron beams, sensitive to the mean field direction, can be used in calibrating fluxgate offsets (Plaschke et al., 2014).

For PSP, the attitude and pointing requirements of the spacecraft preclude the use of controlled maneuvers during perihelion, spacecraft offsets are thus performed before an after each perihelion encounter to establish zero levels of the spacecraft magnetic field. Additional gradiometric techniques are in development to determine offset drifts during each perihelion encounter. In addition to the removal of spacecraft offsets, the vector axes of each MAG are orthogonalized using an alignment matrix determined during pre-flight testing. The alignment matrix, is determined through the process documented in Acuña, M. (1981) and Sheppard, D. (2017) and verified by methods outlined in (Risbo et al., 2003).

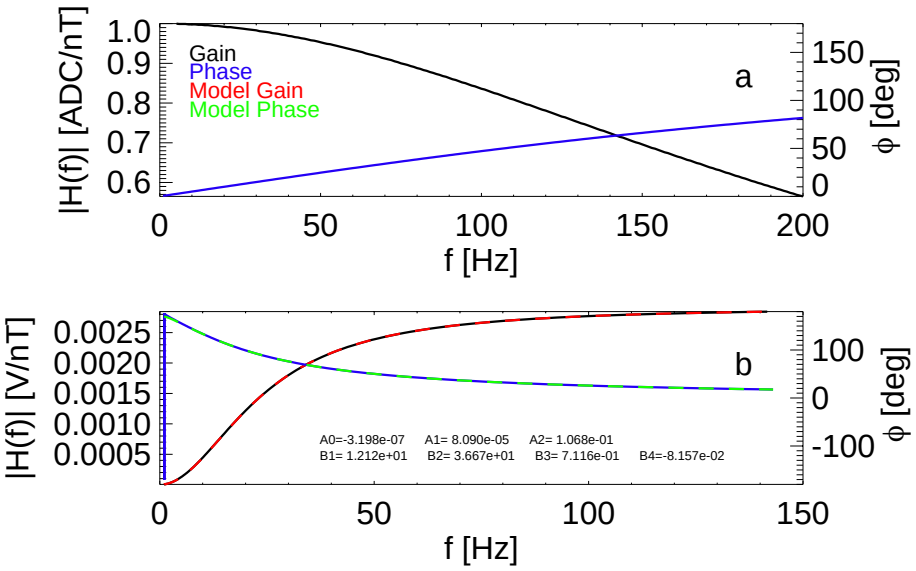

Figure 7.1: (a) MAGo frequency response is dominated by single pole Butterworth filter response tuned to -3 dB at the survey mode Nyquist frequency ($f_{svy}^{max}/2$). (b) SCM frequency response determined from spectral analyzer. A 4-pole 2-zero fit analytical fit is performed to the empirical function.

7.2 FIELDS SCM CALIBRATION

The FIELDS SCM, designed and built at LPC2E, uses the inductive principle to measure the time derivative of the magnetic field. The survey mode waveform data, captured at a maximum rate of f_{svy}^{max} = 293.969 Sa/Sec is sampled and processed by the FIELDS DFB (Malaspina et al., 2016). In addition to continuous survey mode waveform data, the DFB provides a set of highly configurable set of operational modes which can be set in flight to generate a diverse set of burst waveform and spectral data products. In addition to sampling the SCM output, the DFB is designed to inject a programmable calibration signal into the SCM. The response of the SCM to the injected stimulus is captured by the DFB as well as the TDS and the instrumental transfer function can accordingly be determined in-flight.

Figure 7.1(b) shows the gain and phase characteristics of the FIELDS SCM x-axis. determined empirically on ground using a spectral analyzer. A complex rational function with 4-poles and 2-zeros is fit to the the response using the least square estimation techniques outlined in (Levy, 1959).

Because of the large gain and phase shifts associated with the SCM in survey mode range, inversion of the instrumental response function is required in order to obtain an estimate of the observed magnetic field in physical units. During pre-launch integration and testing, several different methods to invert the SCM frequency response were explored, convolution kernel method and a windowed fast Fourier transform (FFT) algorithm similar to methods outlined in Le Contel et al. (2008) and Robert et al. (2014). Preflight Monte-Carlo simulations testing on synthetic data suggested that convolution

in the time domain generated fewer spectral artifacts in the calibrated time series than a windowed FFT algorithm. Compensation filters are developed using the inverse FFT of the response function on an abscissae of 2048 frequencies, corresponding to a 2048 tap (all zero) FIR filter (Oppenheim and Schafer, 1975).

7.3 MERGING

Merging data from multiple sensors, occasionally referred to as data fusion, was initially developed in the context of radio system engineering as a method to optimize signal to noise ratios and correct for signal loss due to random fluctuations, (Kahn, 1954; Brennan, 1959). Recent work has demonstrated the applicability of merging data from multiple sensors onboard a single spacecraft to study magnetic fluctuations in the solar wind: Alexandrova et al. (2004) use a discrete wavelet transform to merge data from the CLUSTER fluxgate and search coil. Subsequently, Chen et al. (2010a) use a similar wavelet merging technique to explore variance anisotropy of turbulence in the kinetic ranges. These studies illustrate an effective use of merged data products, however their methodology does not account for the specific instrumental properties allowing for optimized signal to noise measurements.

On MMS, significant effort was made to design sensors with synchronized timing with pre-launch end-to-end characterization of sensor performance intended to enable optimal merging of the in-flight magnetic field data (Torbert et al., 2016). Fischer et al. (2016) outline a merged magnetic field data product operating at 1024 Sa/S which is derived from 128 Hz fluxgate and 8192 Hz search coil data with good signal to noise characteristics constructed from compensation filters.

The shared clock on between the FIELDS SCM and MAGs, as well as their simultaneous continuous survey mode operation, likewise facilitates a merged data product. In order to produce the merged data product, accurate representations for the complex frequency responses for the MAG and the SCM are required. In addition to the individual characterization of the sensors, multiple end-to-end verifications of the sensor responses were performed. Original ground testing was performed at the Acuña Test facility using FIELDS engineering models. With subsequent testing performed on the flight model hardware during final stages of integration onto the PSP spacecraft. In addition to the characterization of frequency response, the merged data product ideally attains minimal noise characteristics. Accordingly, an accurate description of the individual sensor noise floors is obtained.

To provide an optimal signal to noise merging coefficients, the noise floors of each instrument are assumed to be in-coherent, mean zero gaussian processes, with a spectral composition determined during ground testing. For the SCM the sensitivity of the instrument has been determined at the magnetic test facility in Chambon La Foret. The noise floor of the MAGs were determined in laboratory using measurements taken over several hours inside of a μ-metal container. Additionally some amount of noise is present due to the DFB, as well as the SCM quantization.

The FIELDS merging procedure is designed to maintain an optimized signal to noise ratio. Each sensor observes the environmental field, which is a coherent signal between two sensors, in superposition with incoherent, zero mean noise.

$$B_1 = B(t) + n_1(t) \tag{7.1a}$$
$$B_2 = B(t) + n_2(t) \tag{7.1b}$$

The merged signal B_m is given as a linear combination of the individual sensors, weighted by the coefficients α which maintain an optimal signal to noise ratio.

As instrumental noise from each sensor has different spectral characteristics, it's instructive to consider the spectral representation of the merging coefficients:

$$\tilde{B}_m(\omega) = \alpha_1 \tilde{B}(\omega) + \alpha_2 \tilde{B}(\omega) \tag{7.2}$$
$$\tilde{N}_m = \sqrt{(\alpha_1^2 \tilde{n_1}^2(\omega) + \alpha_2^2 \tilde{n_2}^2(\omega))} \tag{7.3}$$

where the merged noise $\tilde{N}_m$ corresponds to the error of each signal, weighted and added in quadrature, (Kahn, 1954; Brennan, 1959). The condition $\alpha_1 + \alpha_2 = 1$ is required such that the merged signal is equal to the coherent environmental field observed by each sensor.

Because the amplitude of the signal is ideally equal in either sensor, optimizing the ratio B_m/N_m leads to frequency dependent solutions for $\alpha_1(\omega)$ and $\alpha_2(\omega)$ which are independent of the environmental signal, and determined by the spectral composition of the noise floors:

$$\alpha_1(\omega) = \frac{\tilde{n_2}^2}{\tilde{n_1}^2 + \tilde{n_2}^2} \tag{7.4a}$$
$$\alpha_2(\omega) = \frac{\tilde{n_1}^2}{\tilde{n_1}^2 + \tilde{n_2}^2} \tag{7.4b}$$

where $\tilde{n_1}^2$ and $\tilde{n_2}^2$ are computed as the spectral densities of the instrument noise. The coefficients α_1 correspond to an effective weighting in instrumental gain which preserves an optimized signal to noise ratio for the merged SCaM data product. The SCM sensor coordinate system is not initially aligned with the MAG sensor axes, accordingly a rotation matrix $\mathbf{R}$ is applied to bring the SCM measurements, $\mathbf{B}'_{SCM}$, into alignment with the MAG coordinate system,

$$\mathbf{B}_{SCM} = \mathbf{R} \cdot \mathbf{B}'_{SCM}. \tag{7.5}$$

Adhering to an optimal signal to noise merger, spectral composition of the noise of the rotated SCM vector time series in MAG sensor coordinates is then taken as the quadrature weighted error of the SCM sensor axis noise, e.g.

$$n^2_{SCMx}(\omega) = R^2_{xx'} n^2_{SCMx'} + R^2_{xy'} n^2_{SCMy'} + R^2_{xz'} n^2_{SCMz'}. \tag{7.6}$$

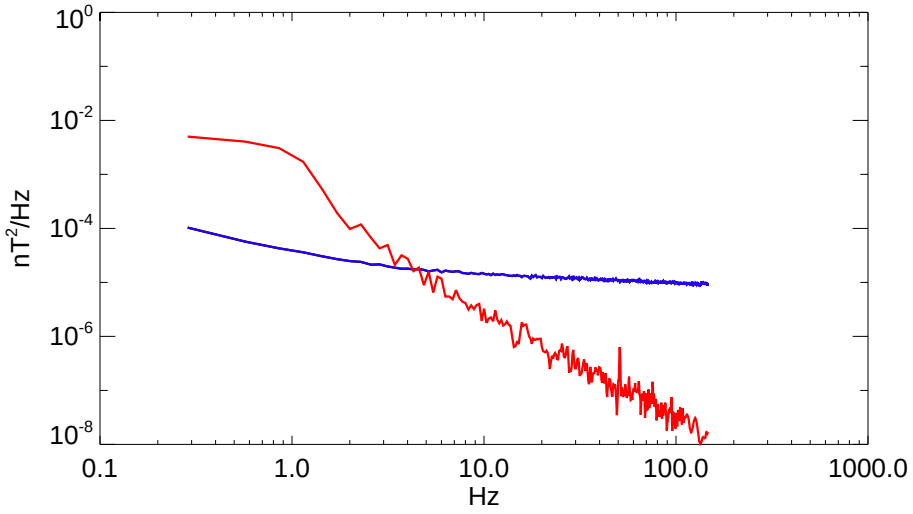

Figure 7.2: Empirically determined noise floors of the x axis of MAGo (blue) and the SCM (red) rotated into the MAGo sensor x-axis coordinates.

Because the MAG orthogonalization matrix is approximately the identity matrix, the measured noise floor for each sensor axis is used without contribution from the other axes.

Figure 7.2 show the noise-floors for both the SCM and MAGs. The optimal merging coefficients α_{MAG} and α_{SCM} are shown in Figure 7.3a. The the weighted instrumental noise floors, and the optimal noise floors are shown in Figure 7.3b.

Figure 7.2a show that the empirically determined noise floors are due to stochastic fluctuations, not particularly smooth functions, due to random fluctuations. A smooth weighting of the merged signals, is obtained by approximating the MAG merging coefficient using a real-valued rational function of the form

$$\hat{\alpha}_{MAG} = R(f) = \frac{N(f)}{D(f)} = \frac{\sum_0^n A_n f^n}{1 + \sum_1^m B_m f^m}.$$

Where the coefficients and order of the fit rational function is determined using non-linear least squares fitting Markwardt (2009). Below the SCM response is cutoff, the full MAG signal is used, i.e. $\alpha_{MAG} = 1$ for $f < 2$ Hz. Constraints are imposed on the fit function $R(f)$ to ensure continuity such that $R(2\text{ Hz}) = 1$ and $R'(2\text{Hz}) = 0$. Figure 7.4 shows the $n = 1, m = 3$ (one zero, three pole) fit to the $\hat{\alpha}_{MAG}$. The SCM coefficients are determined from $\alpha_{SCM} = \hat{\alpha}_{MAG} - 1$.

Fitting $R(f)$ with boundary conditions decreases the degrees of freedom over which the least square fit is performed. The inclusion of boundary conditions requires the use of a higher order rational functions to fit $R(f)$. Determination on the constraints on coefficients which ensure continuity of the function $R(f)$ and $R'(f)$ can be performed similar to the method implemented in to the Padé approx-

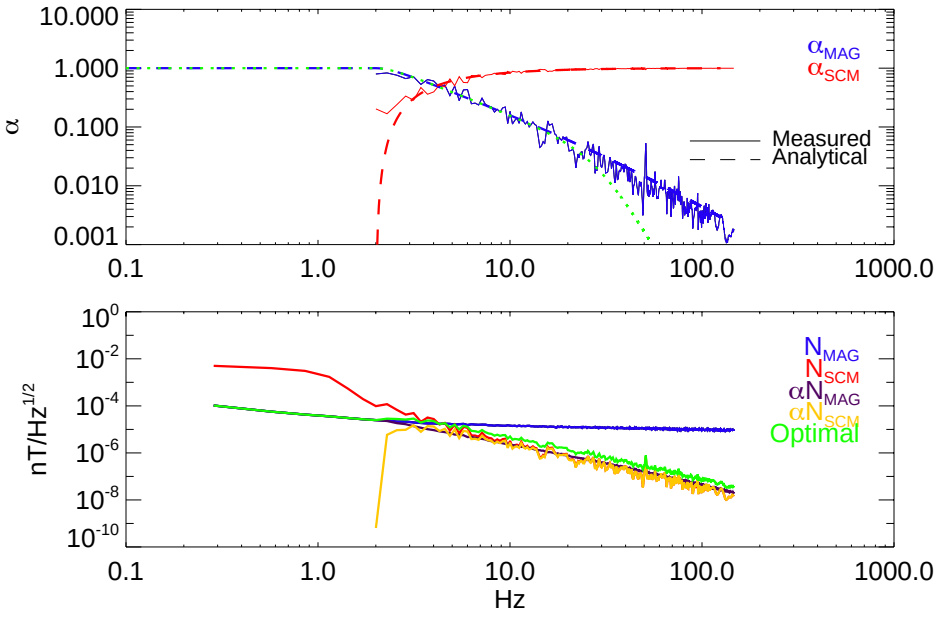

Figure 7.3: Empirically determined noise floors of the x axis of MAGo (blue) and the SCM (red) rotated into the MAGo sensor x-axis coordinates.

imation for rational functions (Hayes, 1996). To ensure continuity of the piecewise merging coefficent, a linear equation in terms of A_n and B_m is constructed from $R(f_0)D(f_0) = N(f_0)$, removing one free parameter from the rational polynomial $R(f)$ is removed. Ensuring continuity of the first derivative is similarly obtained from the product rule

$$R'(f) = \frac{N'(f)D(f) - N(f)D'(f)}{D^2}$$

such that

$$R'(f_0) = \frac{N'(f_0)D(f_0) - N(f_0)D'(f_0)}{D^2(f_0)} = \frac{N'(f_0)N(f_0)/R(f_0) - N(f_0)D'(f_0)}{N^2(f_0)/R^2(f_0)} = \frac{N'(f_0)R(f_0) - R^2(f_0)D'(f_0)}{N(f_0)}. \quad (7.7)$$

Representing the polynomials $N(f)$ and $D(f)$ as matrices

$$N = \begin{pmatrix} A_0 & A_1 & \cdots & A_n \end{pmatrix} \begin{pmatrix} 1 \\ x \\ \vdots \\ x^n \end{pmatrix} \tag{7.8}$$

The derivative operator can be written as a matrix

$$\Delta = \begin{pmatrix} 0 & 1 & 0 & \cdots & 0 \\ 0 & 0 & 2 & \cdots & 0 \\ 0 & 0 & 0 & \cdots & 0 \end{pmatrix} \tag{7.9}$$

such that

$$N' = \left(\Delta \begin{pmatrix} A_0 & A_1 & \cdots & A_n \end{pmatrix}^{\dagger} \right)^{\dagger} \begin{pmatrix} 1 \\ x \\ \vdots \\ x^n \end{pmatrix} \tag{7.10}$$

Analogously writing D'(f) using the Δ provides an efficient method to determine solutions to the two linear equations

$$R(f_0)D(f_0) = N(f_0) \tag{7.11}$$

$$R'(f_0)N(f_0) = \Delta N(f_0)R(f_0) - R^2(f_0)\Delta D(f_0). \tag{7.12}$$

Figure 7.4 shows the rational function, with three poles and one zero, fit to the MAG merging coefficient, α_{MAG}. Ensuring a piecewise continuous merging coefficient requires constraining the function at 2 Hz to unity gain and a local extremum. Below 2 Hz ,the coefficient α_{MAG} is set to unity, e.g. Figure 7.3.

7.4 CALIBRATION AND MERGER OF IN-FLIGHT DATA

During the first PSP perihelion encounter survey mode data were acquired at different cadences in order to meet telemetry constraints. For future encounters the FIELDS team intends to operate the instruments in single data rates over the entire perihelion encounter period. The SCaM merging algorithm is applied directly to the level 1 (l1) FIELDS data after orthogonalization and removal of spacecraft offsets from MAGo. The calibration kernel corresponding to the inverse of the MAG single pole

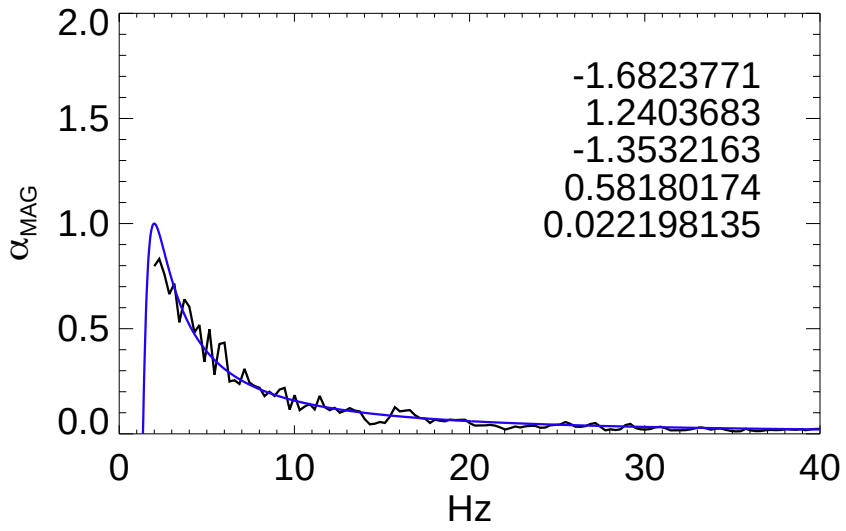

Figure 7.4: Non-linear least square fit of three pole, one zero rational function to α_{MAG}.

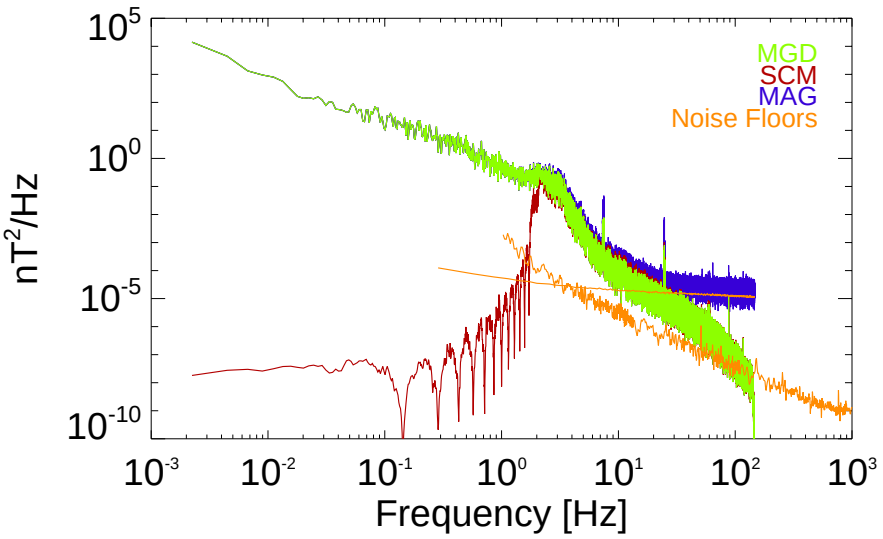

Figure 7.5: Power spectra densities of observed magnetic field in the spacecraft coordinate y direction from ≈ 1 hour interval (2018-11-05/00:00:-01:00) calculated with MAG (blue), SCM (red), and merged SCM and MAG (SCaM, green), time series. Sensor noise floors are shown in orange.

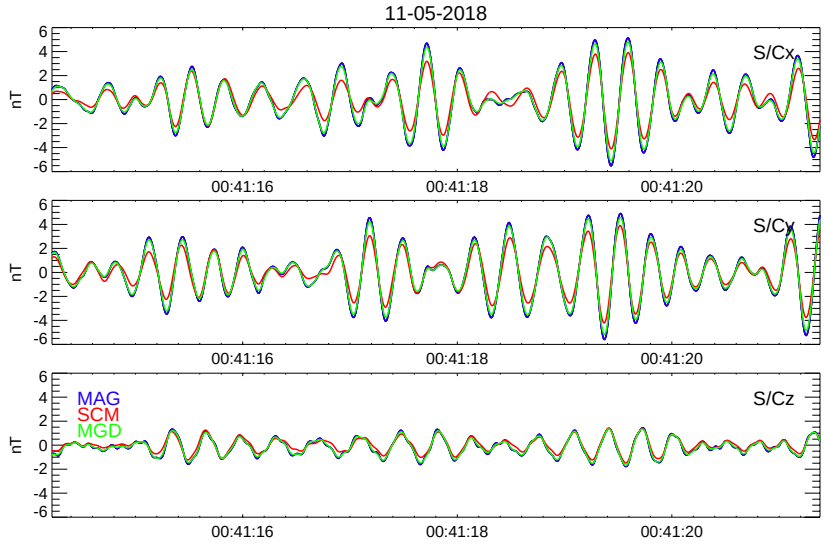

Figure 7.6: Eight second bandpass filtered waveform near the merging crossover frequency (2-12 Hz) from PSP/-FIELDS survey magnetic field data in S/C coordinates. Good phase and gain agreement is observed in the between the MAG (blue) SCM (red) and merged (SCaM, green) time series.

low pass Butterworth filter, weighted by the appropriate merging coefficients is then applied to construct the weighted MAG time series. The SCM is similarly calibrated using the instrumental response function weighted by the merge coefficients; the gain and gain phase shifts associated with digitization by the FIELDS DFB are additionally corrected (Malaspina et al., 2016). Once convolved with calibration kernels, the SCM is rotated into the outer MAG coordinate system. Time tags are corrected using spacecraft spice kernels and the weighted MAG time series is then interpolated onto the SCM time abscissae. The time series are directly summed to generate the merged data set with optimal signal to noise ratio. The SCaM data is considered at level 3 (l3) data product.

An approximate hour long interval (2^{20} samples at 293.969 Sa/sec) is highlighted to demonstrate the results of the FIELDS merging algorithm. Power spectra for each of the MAG, SCM, and SCaM time series are computed as an ensemble average of eight 2^{17} point power spectra. Figure 7.5 shows the three computed spectra with the noise-floors of either instrument. Good agreement is observed between the MGD data and spectra from either individual instrument. The in-flight observed noise-floor of the MAGo is consistent with on-ground measurements. Broadband spectral features near the crossover frequency, corresponding to coherent wave features at several Hz, are captured by both the MAG and SCM and are thus useful in analyzing the performance of the SCaM merging algorithm. Digital filters are applied to bandpass the MAG, SCM, and MGD time series to between 2 and 12 Hz in order to directly compare the time series in the crossover bandwidth, without contribution from

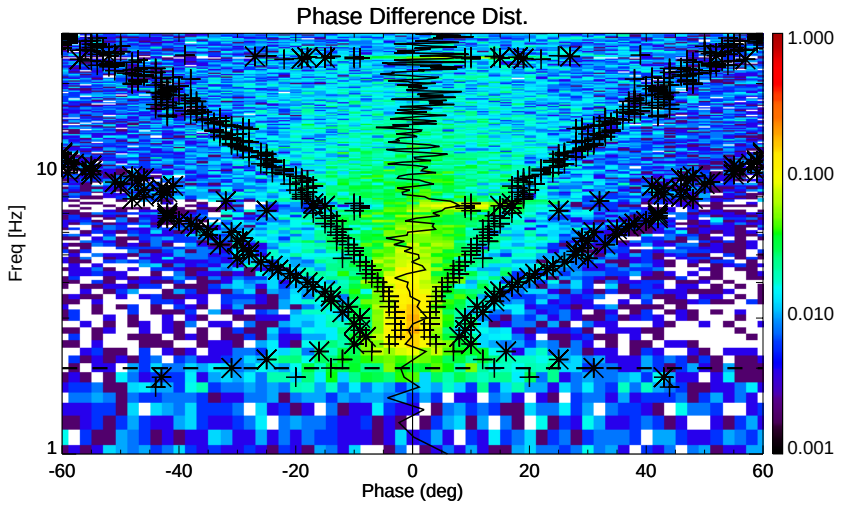

Figure 7.7: (Left) Distribution of measured phase delays between the MAG and SCM as a function of frequency. The black line shows the mean phase error at each frequency, each + and x show to the quartiles corresponding to the 50% and 75% measured phase delay.

low or high frequency signals. Figure 7.6 shows excellent qualitative agreement in phase between the three different axes.

A quantitative determination of the accuracy of calibration is performed by computing short time Fourier transform cross spectra of each of the three combinations of signals. The short time cross spectra is defined as

$$S_{xy} = \mathcal{F}\{B_1(t)\}\mathcal{F}^{\dagger}\{B_1(t)\} \tag{7.13}$$

where $\mathcal{F}$ is the Fourier transform, computed via fast fourier transform (FFT) algorithms.

The argument of the cross spectra gives the phase delay between the two signals at a given frequency $\arg(S_{xy}) = \tan^{-1}\left(\frac{\mathrm{Img}\{S_{xy}\}}{\mathrm{Re}\{S_{xy}\}}\right)$. As each sensor, and the merged data, observe the same time series, zero-phase differences should exist between each signal. However, the presence of noise in the sensor systems will cause deviations in the measured phase, which can help quantify the accuracy of the calibration. Figure 7.7 shows the measured distributions of phase delays between the MAG and SCM as a function of frequency, calculated using the ensemble provided by the short-time Fourier transform (each of the 1024 frequency bins provides has an ensemble of, 512 phase delays). The MAG and SCM are shown to be in good agreement between 2-10 Hz. At 3 Hz, where the cross over frequency occurs, roughly 50% 75% of frequency bins within ≈ 2 and 10 degrees. These values respectively correspond to time delays of ≈ 0.4 Δt and 2.7 Δt. f At 10 Hz, agreement between the sensors is degraded with approximately 50% of coefficients within 20 degrees of phase shift; corresponding to a time error of

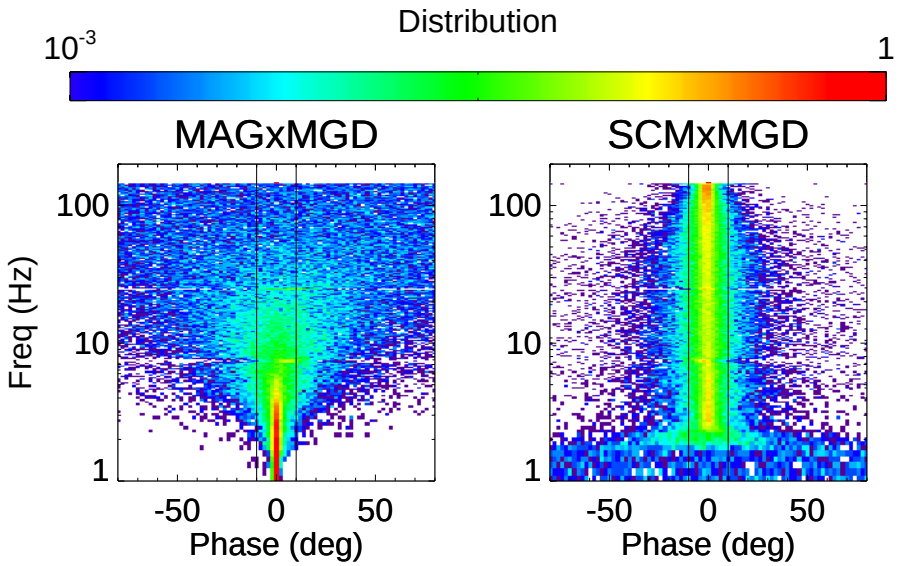

Figure 7.8: (Left) Distribution of phase delays between the MAG and MGD data product as a function of frequency. (Right) Distribution of phase delays between the SCM and MGD data product as a function of frequency

1.5Δ t. Quartile measurements were used rather than statistical variance in this analysis because the presence of large outliers leads to a leptokurtic distributions which significantly differ from Gaussian statistics. These results show that the phase alignment of the MAG and SCM is accurate to within a small phase error in the frequencies surrounding the cross-over point.

Figure 7.8 shows the distribution of phase delays between the SCaM-MAGo and SCaM-SCM short time Fourier transform coefficients. Good agreement is observed between the merged data product and the MAGo below ~10 Hz and the merged data and SCM above ~3 Hz. These results, which suggest that the MAGo time-series has large noise contribution at 10 Hz, support our choice of merging coefficient scaling outlined in Figure 7.3. The presence of large amplitude narrow band noise from spacecraft reaction wheels is evident in Figure 7.8, causing anomalous measurements of the phase error corresponding to the wheel rotation.

7.5 CONCLUSION

An algorithm to merge fluxgate and search coil magnetometer data on PSP/FIELDS is developed and implemented. The technique is similar to the effort made by Fischer et al. (2016) for MMS. Our approach to data-merging is based on previously developed techniques from radio-systems engineering for optimal signal to noise diversity combining (Kahn, 1954; Brennan, 1959). The optimal merging methods takes into account sensor design and operation in order to construct a merged data product

wit spectral composition which smoothly transitions between the MAG at low frequencies and SCM at high frequencies. The crossover point with equal spectral composition between the sensors is 3 Hz. We demonstrate that at the crossover frequency, our calibrations are accurate to within a fraction of a sample period, enabling a smooth, artifact free transition in this range.

In order to maintain the level three SCaM data product for continued public use, the FIELDS team intends to regularly update the merging algorithm using measured onboard frequency responses, temperatures, noise floors, MAG offsets etc. The SCaM data will be publicly available at sprg.ssl.berkeley.edu/data/psp/fields/l3/SCaM/

8

CONCLUDING REMARKS

Part II of this dissertation discusses the calibration of magnetic field instrumentation. Chapter 6 provides an introduction to linear filter theory and application to magnetometer calibration; though these calibrations routines and concepts are specifically discussed for spaceflight calibration of magnetometers, and in particular the PSP/FIELDS instrument suite, they are general to interdisciplinary observations of magnetic fields (Bowen et al., 2019).

The merged SCM and MAG (SCaM) data product for PSP, outlined in Chapter 7, will exist as one of the first publicly available merged magnetic field data products for the space physics community. Ongoing work to maintain the quality of the product will ensure optimal outcomes for scientific work on turbulence heating in the solar wind and corona. Currently, work is being undertaken to characterize polarization signatures of fluctuations and intermittency of the dissipative range of magnetic fluctuations in the inner heliosphere. These observations provided by the merged SCaM data promise to help define the early results of the PSP mission.

While this work has focused on the most fundamental calibration efforts of inverting instrumental transfer functions, there are a number of higher order calibration procedures which have not been discussed: removal of spacecraft noise, time varying calibrations of instrumental response and spacecraft zeros, and correlating magnetic field observations with measurements of electric field and plasma velocity. While the discussion of such concepts has only tangentially entered this dissertation, maintaining correct calibrations for the PSP magnetometers will require continued attention during the missions lifetime.

The essential research contained in this dissertation is separated into two complementary parts, each existing as the foundation for continued work on the PSP mission. Part I attempts to develop a robust understanding contemporary problems in astrophysical plasma physics, particularly those formulated within the paradigm of statistical observations easily connected to turbulence, relevant to the observational goals of PSP/FIELDS. In turn, Part II highlights the development of observational tools–via physical hardware and technical processing– which enable research into non-linear processes outlined in Part I. The two parts, together, provide a substantial research effort in preparation for continued work on the PSP mission.

Thank you for reading!

BIBLIOGRAPHY

M. H. Acuña. Space-based magnetometers. Review of Scientific Instruments, 73:3717–3736, November 2002. doi: 10.1063/1.1510570.

M. H. Acuña, D. Curtis, J. L. Scheifele, C. T. Russell, P. Schroeder, A. Szabo, and J. G. Luhmann. The STEREO/IMPACT Magnetic Field Experiment. Space Sci. Rev., 136:203–226, April 2008. doi: 10.1007/s11214-007-9259-2.

Acuña, M. MAGSAT-Vector Magnetometer Absolute Sensor Alignment Determination. NASA Technical Memorandum 79648, Sep 1981.

M. Acuna. Fluxgate magnetometers for outer planets exploration. IEEE Transactions on Magnetics, 10:519–523, Sep 1974. doi: 10.1109/TMAG.1974.1058457.

O. Alexandrova, A. Mangeney, M. Maksimovic, C. Lacombe, N. Cornilleau-Wehrlin, E. A. Lucek, P. M. E. DéCréAu, J. M. Bosqued, P. Travnicek, and A. N. Fazakerley. Cluster observations of finite amplitude Alfvén waves and small-scale magnetic filaments downstream of a quasi-perpendicular shock. Journal of Geophysical Research (Space Physics), 109:A05207, May 2004. doi: 10.1029/2003JA010056.

O. Alexandrova, C. H. K. Chen, L. Sorriso-Valvo, T. S. Horbury, and S. D. Bale. Solar Wind Turbulence and the Role of Ion Instabilities. Space Sci. Rev., 178:101–139, Oct 2013. doi: 10.1007/s11214-013-0004-8.

H. Alfvén. Existence of Electromagnetic-Hydrodynamic Waves. Nature, 150:405–406, Oct 1942. doi: 10.1038/150405d0.

H. Alfvén. On the Theory of Comet Tails. Tellus, 9(1):92–96, 1957. doi: 10.1111/j.2153-3490.1957.tb01855.x. URL https://onlinelibrary.wiley.com/doi/abs/10.1111/j.2153-3490.1957.tb01855.x.

H. Alfvén. On the theory of magnetic storms and aurorae. Tellus, 10(1):104–116, 1958. doi: 10.1111/j.2153-3490.1958.tb01991.x. URL https://onlinelibrary.wiley.com/doi/abs/10.1111/j.2153-3490.1958.tb01991.x.

V. Angelopoulos. The themis mission. Space Science Reviews, 141(1):5, Apr 2008. ISSN 1572-9672. doi: 10.1007/s11214-008-9336-1. URL https://doi.org/10.1007/s11214-008-9336-1.

J. A. Araneda, Y. Maneva, and E. Marsch. Preferential Heating and Acceleration of α Particles by Alfvén-Cyclotron Waves. Physical Review Letters, 102(17):175001, May 2009. doi: 10.1103/PhysRevLett.102.175001.

Jaime A. Araneda, Eckart Marsch, and Adolfo F.-Viñas. Proton core heating and beam formation via parametrically unstable alfvén-cyclotron waves. Phys. Rev. Lett., 100:125003, Mar 2008. doi: 10.1103/PhysRevLett.100.125003. URL https://link.aps.org/doi/10.1103/PhysRevLett.100.125003.

J. W. Armstrong and B. J. Rickett. Power spectrum of small-scale density irregularities in the interstellar medium. MNRAS, 194:623–638, Feb 1981. doi: 10.1093/mnras/194.3.623.

S. A. Balbus. Formation Interuniversitaire de Physique. 2018. URL https://www2.physics.ox.ac.uk/sites/default/files/profiles/balbus/hydrosun-42467.pdf.

S. D. Bale, P. J. Kellogg, F. S. Mozer, T. S. Horbury, and H. Reme. Measurement of the Electric Fluctuation Spectrum of Magnetohydrodynamic Turbulence. Phys. Rev. Lett., 94:215002, Jun 2005. doi: 10.1103/PhysRevLett.94.215002.

S. D. Bale, J. C. Kasper, G. G. Howes, E. Quataert, C. Salem, and D. Sundkvist. Magnetic fluctuation power near proton temperature anisotropy instability thresholds in the solar wind. Phys. Rev. Lett., 103:211101, Nov 2009. doi: 10.1103/PhysRevLett.103.211101. URL https://link.aps.org/doi/10.1103/PhysRevLett.103.211101.

S. D. Bale, K. Goetz, P. R. Harvey, P. Turin, J. W. Bonnell, T. Dudok de Wit, R. E. Ergun, R. J. MacDowall, M. Pulupa, M. Andre, M. Bolton, J. L. Bougeret, T. A. Bowen, D. Burgess, C. A. Cattell, B. D. G. Chandran, C. C. Chaston, C. H. K. Chen, M. K. Choi, J. E. Connerney, S. Cranmer, M. Diaz-Aguado, W. Donakowski, J. F. Drake, W. M. Farrell, P. Fergeau, J. Fermin, J. Fischer, N. Fox, D. Glaser, M. Goldstein, D. Gordon, E. Hanson, S. E. Harris, L. M. Hayes, J. J. Hinze, J. V. Hollweg, T. S. Horbury, R. A. Howard, V. Hoxie, G. Jannet, M. Karlsson, J. C. Kasper, P. J. Kellogg, M. Kien, J. A. Klimchuk, V. V. Krasnoselskikh, S. Krucker, J. J. Lynch, M. Maksimovic, D. M. Malaspina, S. Marker, P. Martin, J. Martinez-Oliveros, J. McCauley, D. J. McComas, T. McDonald, N. Meyer-Vernet, M. Moncuquet, S. J. Monson, F. S. Mozer, S. D. Murphy, J. Odom, R. Oliverson, J. Olson, E. N. Parker, D. Pankow, T. Phan, E. Quataert, T. Quinn, S. W. Ruplin, C. Salem, D. Seitz, D. A. Sheppard, A. Siy, K. Stevens, D. Summers, A. Szabo, M. Timofeeva, A. Vaivads, M. Velli, A. Yehle, D. Werthimer, and J. R. Wygant. The FIELDS Instrument Suite for Solar Probe Plus. Measuring the Coronal Plasma and Magnetic Field, Plasma Waves and Turbulence, and Radio Signatures of Solar Transients. Space Science Rev., 204:49–82, December 2016a. doi: 10.1007/s11214-016-0244-5.

S. D. Bale, K. Goetz, P. R. Harvey, P. Turin, J. W. Bonnell, T. Dudok de Wit, R. E. Ergun, R. J. MacDowall, M. Pulupa, M. Andre, M. Bolton, J.-L. Bougeret, T. A. Bowen, D. Burgess, C. A. Cattell,

B. D. G. Chandran, C. C. Chaston, C. H. K. Chen, M. K. Choi, J. E. Connerney, S. Cranmer, M. Diaz-Aguado, W. Donakowski, J. F. Drake, W. M. Farrell, P. Fergeau, J. Fermin, J. Fischer, N. Fox, D. Glaser, M. Goldstein, D. Gordon, E. Hanson, S. E. Harris, L. M. Hayes, J. J. Hinze, J. V. Hollweg, T. S. Horbury, R. A. Howard, V. Hoxie, G. Jannet, M. Karlsson, J. C. Kasper, P. J. Kellogg, M. Kien, J. A. Klimchuk, V. V. Krasnoselskikh, S. Krucker, J. J. Lynch, M. Maksimovic, D. M. Malaspina, S. Marker, P. Martin, J. Martinez-Oliveros, J. McCauley, D. J. McComas, T. McDonald, N. Meyer-Vernet, M. Moncuquet, S. J. Monson, F. S. Mozer, S. D. Murphy, J. Odom, R. Oliverson, J. Olson, E. N. Parker, D. Pankow, T. Phan, E. Quataert, T. Quinn, S. W. Ruplin, C. Salem, D. Seitz, D. A. Sheppard, A. Siy, K. Stevens, D. Summers, A. Szabo, M. Timofeeva, A. Vaivads, M. Velli, A. Yehle, D. Werthimer, and J. R. Wygant. The FIELDS Instrument Suite for Solar Probe Plus. Measuring the Coronal Plasma and Magnetic Field, Plasma Waves and Turbulence, and Radio Signatures of Solar Transients. Space Sci. Rev., 204: 49–82, December 2016b. doi: 10.1007/s11214-016-0244-5.

A. Balogh, C. M. Carr, M. H. Acuña, M. W. Dunlop, T. J. Beek, P. Brown, K.-H. Fornacon, E. Georgescu, K.-H. Glassmeier, J. Harris, G. Musmann, T. Oddy, and K. Schwingenschuh. The cluster magnetic field investigation: overview of in-flight performance and initial results. Annales Geophysicae, 19(10/12):1207–1217, 2001. doi: 10.5194/angeo-19-1207-2001. URL https://www.ann-geophys.net/19/1207/2001/.

A. Barnes. Collisionless Damping of Hydromagnetic Waves. Physics of Fluids, 9:1483–1495, August 1966. doi: 10.1063/1.1761882.

A. Barnes. Interplanetary Alfvénic fluctuations: A stochastic model. Journal of Geophysical Research, 86:7498–7506, Sep 1981. doi: 10.1029/JA086iA09p07498.

Aaron Barnes. Theory of magnetohydrodynamic waves: The WKB approximation revisited. Journal of Geophysical Research, 97:12105–12112, Aug 1992. doi: 10.1029/92JA00996.

G. K. Batchelor. On the Spontaneous Magnetic Field in a Conducting Liquid in Turbulent Motion. Proceedings of the Royal Society of London Series A, 201:405–416, Apr 1950. doi: 10.1098/rspa.1950.0069.

B. Bavassano and R. Bruno. On the role of interplanetary source in the evolution of low-frequency Alfvénic turbulence in the solar wind. Journal of Geophysical Research, 97:19129–19137, Dec 1992. doi: 10.1029/92JA01510.

B. Bavassano, M. Dobrowolny, G. Fanfoni, F. Mariani, and N. F. Ness. Statistical Properties of Magnetohydrodynamic Fluctuations Associated with High Speed Streams from HELIOS-2 Observations. Sol. Phys., 78:373–384, Jun 1982a. doi: 10.1007/BF00151617.

B. Bavassano, M. Dobrowolny, F. Mariani, and N. F. Ness. Radial evolution of power spectra of interplantary Alfvénic turbulence. Journal of Geophysical Research, 87:3617–3622, May 1982b. doi: 10.1029/JA087iA05p03617.

B. Bavassano, M. Dobrowolny, F. Mariani, and N. F. Ness. Radial evolution of power spectra of interplanetary alfv□nic turbulence. Journal of Geophysical Research: Space Physics, 87(A5):3617–3622, 1982. doi: 10.1029/JA087iA05p03617. URL https://agupubs.onlinelibrary.wiley.com/doi/abs/10.1029/JA087iA05p03617.

B. Bavassano, E. Pietropaolo, and R. Bruno. Cross-helicity and residual energy in solar wind turbulence - Radial evolution and latitudinal dependence in the region from 1 to 5 AU. J. Geophys. Res., 103: 6521, April 1998. doi: 10.1029/97JA03029.

J. W. Belcher. A variation of the Davis-Smith method for in-flight determination of spacecraft magnetic fields. J. Geophys. Res., 78:6480–6490, October 1973. doi: 10.1029/JA078i028p06480.

J. W. Belcher and Jr. Davis, Leverett. Large-amplitude Alfvén waves in the interplanetary medium, 2. Journal of Geophysical Research, 76:3534, Jan 1971. doi: 10.1029/JA076i016p03534.

Beau R. Bellamy, Iver H. Cairns, and C. W. Smith. Voyager spectra of density turbulence from 1 AU to the outer heliosphere. Journal of Geophysical Research (Space Physics), 110:A10104, Oct 2005. doi: 10.1029/2004JA010952.

Julius S. Bendat and Allan G. Piersol. Random Data: Analysis and Measurement Procedures. John Wiley & Sons, Inc., New York, NY, USA, 2nd edition, 1990. ISBN 0471040002.

A. Bershadskii and K. R. Sreenivasan. Intermittency and the Passive Nature of the Magnitude of the Magnetic Field. Phys. Rev. Lett., 93:064501, Aug 2004. doi: 10.1103/PhysRevLett.93.064501.

R J Bickerton. Magnetic turbulence and the transport of energy and particles in tokamaks. Plasma Physics and Controlled Fusion, 39(3):339–365, mar 1997. doi: 10.1088/0741-3335/39/3/002.

John W. Bieber, Wolfgang Wanner, and William H. Matthaeus. Dominant two-dimensional solar wind turbulence with implications for cosmic ray transport. Journal of Geophysical Research, 101:2511–2522, Feb 1996. doi: 10.1029/95JA02588.

L. Biermann. Physical Processes in Comet tails and their relation to solar activity. MPI, Göttingen, 1953.

L. Biermann. Solar corpuscular radiation and the interplanetary gas. The Observatory, 77:109–110, June 1957.

D. Biskamp. Magnetohydrodynamic Turbulence. Cambridge University Press, 2003. ISBN 9780511072673. URL https://books.google.com/books?id=JioMkAEACAAJ.

R. B. Blackman and J. W. Tukey. The measurement of power spectra from the point of view of communications engineering ? part i. Bell System Technical Journal, 37(1):185–282, 1958. doi: 10.1002/j.1538-7305.1958.tb03874.x. URL https://onlinelibrary.wiley.com/doi/abs/10.1002/j.1538-7305.1958.tb03874.x.

S. Boldyrev. Spectrum of Magnetohydrodynamic Turbulence. Physical Review Letters, 96(11):115002, March 2006. doi: 10.1103/PhysRevLett.96.115002.

S. Boldyrev, J. C. Perez, J. E. Borovsky, and J. J. Podesta. Spectral Scaling Laws in Magnetohydrodynamic Turbulence Simulations and in the Solar Wind. ApJ, 741:L19, November 2011. doi: 10.1088/2041-8205/741/1/L19.

Stanislav Boldyrev. On the Spectrum of Magnetohydrodynamic Turbulence. ApJ, 626:L37–L40, Jun 2005. doi: 10.1086/431649.

Stanislav Boldyrev and Jean Carlos Perez. SPECTRUM OF KINETIC-ALFVén TURBULENCE. The Astrophysical Journal, 758(2):L44, oct 2012. doi: 10.1088/2041-8205/758/2/l44. URL https://doi.org/10.1088%2F2041-8205%2F758%2F2%2Fl44.

Stanislav Boldyrev and Jean Carlos Perez. Spectrum of Kinetic-Alfvén Turbulence. ApJ, 758:L44, Oct 2012. doi: 10.1088/2041-8205/758/2/L44.

J. W. Bonnell, F. S. Mozer, G. T. Delory, A. J. Hull, R. E. Ergun, C. M. Cully, V. Angelopoulos, and P. R. Harvey. The Electric Field Instrument (EFI) for THEMIS, pages 303–341. Springer New York, New York, NY, 2009.

J. E. Borovsky. Flux tube texture of the solar wind: Strands of the magnetic carpet at 1 AU? Journal of Geophysical Research (Space Physics), 113:A08110, August 2008. doi: 10.1029/2007JA012684.

J. E. Borovsky. Contribution of Strong Discontinuities to the Power Spectrum of the Solar Wind. Physical Review Letters, 105(11):111102, September 2010. doi: 10.1103/PhysRevLett.105.111102.

J. E. Borovsky. The velocity and magnetic field fluctuations of the solar wind at 1 AU: Statistical analysis of Fourier spectra and correlations with plasma properties. Journal of Geophysical Research (Space Physics), 117:A05104, May 2012. doi: 10.1029/2011JA017499.

J. E. Borovsky and M. H. Denton. Solar wind turbulence and shear: A superposed-epoch analysis of corotating interaction regions at 1 AU. Journal of Geophysical Research (Space Physics), 115: A10101, October 2010. doi: 10.1029/2009JA014966.

J. L. Bougeret, M. L. Kaiser, P. J. Kellogg, R. Manning, K. Goetz, S. J. Monson, N. Monge, L. Friel, C. A. Meetre, C. Perche, L. Sitruk, and S. Hoang. Waves: The radio and plasma wave investigation on the wind spacecraft. Space Science Reviews, 71(1):231–263, Feb 1995. ISSN 1572-9672. doi: 10.1007/BF00751331. URL https://doi.org/10.1007/BF00751331.

Sofiane Bourouaine and Jean C. Perez. On the Limitations of Taylor's Hypothesis in Parker Solar Probe's Measurements near the Alfvén Critical Point. ApJ, 858:L20, May 2018. doi: 10.3847/2041-8213/aabccf.

T. A. Bowen, S. Badman, P. Hellinger, and S. D. Bale. Density Fluctuations in the Solar Wind Driven by Alfvén Wave Parametric Decay. ApJ, 854:L33, February 2018a. doi: 10.3847/2041-8213/aaabbe.

T. A. Bowen, A. Mallet, J. W. Bonnell, and S. D. Bale. Impact of Residual Energy on Solar Wind Turbulent Spectra. ApJ, 865:45, Sep 2018b. doi: 10.3847/1538-4357/aad95b.

T. A. Bowen, E. Zhivun, A. Wickenbrock, V. Dumont, S. D. Bale, C. Pankow, G. Dobler, J. S. Wurtele, and D. Budker. A network of magnetometers for multi-scale urban science and informatics. Geoscientific Instrumentation, Methods and Data Systems, 8(1):129–138, 2019. doi: 10.5194/gi-8-129-2019. URL https://www.geosci-instrum-method-data-syst.net/8/129/2019/.

D.G. Brennan. Linear Diversity Combining Techniques. Proceedings of the IRE, Proc. IRE, page 1075, 1959. ISSN 0096-8390.

G. Brunetti and A. Lazarian. Compressible turbulence in galaxy clusters: physics and stochastic particle re-acceleration. MNRAS, 378:245–275, Jun 2007. doi: 10.1111/j.1365-2966.2007.11771.x.

R. Bruno and V. Carbone. The Solar Wind as a Turbulence Laboratory. Living Reviews in Solar Physics, 10:2, May 2013a. doi: 10.12942/lrsp-2013-2.

R. Bruno and L. Trenchi. Radial Dependence of the Frequency Break between Fluid and Kinetic Scales in the Solar Wind Fluctuations. ApJ, 787:L24, Jun 2014. doi: 10.1088/2041-8205/787/2/L24.

R. Bruno, B. Bavassano, and U. Villante. Evidence for long period Alfven waves in the inner solar system. J. Geophys. Res., 90:4373–4377, May 1985. doi: 10.1029/JA090iA05p04373.

R. Bruno, V. Carbone, P. Veltri, E. Pietropaolo, and B. Bavassano. Identifying intermittency events in the solar wind. Planet. Space Sci., 49:1201–1210, October 2001. doi: 10.1016/S0032-0633(01)00061-7.

R. Bruno, V. Carbone, L. Sorriso-Valvo, and B. Bavassano. Radial evolution of solar wind intermittency in the inner heliosphere. Journal of Geophysical Research (Space Physics), 108:1130, March 2003. doi: 10.1029/2002JA009615.

R. Bruno, R. D'Amicis, B. Bavassano, V. Carbone, and L. Sorriso-Valvo. Magnetically dominated structures as an important component of the solar wind turbulence. Annales Geophysicae, 25:1913–1927, August 2007. doi: 10.5194/angeo-25-1913-2007.

R. Bruno, V. Carbone, Z. Vörös, R. D'Amicis, B. Bavassano, M. B. Cattaneo, A. Mura, A. Milillo, S. Orsini, P. Veltri, L. Sorriso-Valvo, T. Zhang, H. Biernat, H. Rucker, W. Baumjohann, D. Jankovičová, and P. Kovács. Coordinated Study on Solar Wind Turbulence During the Venus-Express, ACE and Ulysses Alignment of August 2007. Earth Moon and Planets, 104:101–104, Apr 2009. doi: 10.1007/s11038-008-9272-9.

Roberto Bruno and Vincenzo Carbone. The Solar Wind as a Turbulence Laboratory. Living Reviews in Solar Physics, 10:2, May 2013b. doi: 10.12942/lrsp-2013-2.

J. L. Burch, T. E. Moore, R. B. Torbert, and B. L. Giles. Magnetospheric multiscale overview and science objectives. Space Science Reviews, 199(1):5–21, Mar 2016. ISSN 1572-9672. doi: 10.1007/s11214-015-0164-9. URL https://doi.org/10.1007/s11214-015-0164-9.

L. F. Burlaga. Lognormal and multifractal distributions of the heliospheric magnetic field. Journal of Geophysical Research, 106:15917–15928, Aug 2001. doi: 10.1029/2000JA000107.

L. F. Burlaga and K. W. Ogilvie. Magnetic and Thermal Pressures in the Solar Wind. Sol. Phys., 15: 61–71, Nov 1970. doi: 10.1007/BF00149472.

L. F. Burlaga, K. W. Ogilvie, and D. H. Fairfield. Microscale Fluctuations in the Interplanetary Magnetic Field. ApJ, 155:L171, March 1969. doi: 10.1086/180329.

B. D. G. Chandran. Parametric Instability, Inverse Cascade, and the $1/f$ Range of Solar-Wind Turbulence. ArXiv e-prints, December 2017.

B. D. G. Chandran. Parametric instability, inverse cascade and the range of solar-wind turbulence. Journal of Plasma Physics, 84(1):905840106, February 2018. doi: 10.1017/S0022377818000016.

B. D. G. Chandran, A. A. Schekochihin, and A. Mallet. Intermittency and Alignment in Strong RMHD Turbulence. ApJ, 807:39, July 2015. doi: 10.1088/0004-637X/807/1/39.

Benjamin D. G. Chandran, Bo Li, Barrett N. Rogers, Eliot Quataert, and Kai Germaschewski. PERPENDICULAR ION HEATING BY LOW-FREQUENCY ALFVén-WAVE TURBULENCE IN THE SOLAR WIND. The Astrophysical Journal, 720(1):503–515, aug 2010. doi: 10.1088/0004-637x/720/1/503.

T. Chang, S. W. Y. Tam, and C.-C. Wu. Complexity induced anisotropic bimodal intermittent turbulence in space plasmas. Physics of Plasmas, 11:1287–1299, April 2004. doi: 10.1063/1.1667496.

S. Chapman. Theories of the aurora polaris. Annales de Geophysique, 8:205, 1952.

C. H. K. Chen. Recent progress in astrophysical plasma turbulence from solar wind observations. Journal of Plasma Physics, 82:535820602, Dec 2016. doi: 10.1017/S0022377816001124.

C. H. K. Chen, T. S. Horbury, A. A. Schekochihin, R. T. Wicks, O. Alexandrova, and J. Mitchell. Anisotropy of Solar Wind Turbulence between Ion and Electron Scales. Phys. Rev. Lett., 104:255002, Jun 2010a. doi: 10.1103/PhysRevLett.104.255002.

C. H. K. Chen, T. S. Horbury, A. A. Schekochihin, R. T. Wicks, O. Alexandrova, and J. Mitchell. Anisotropy of Solar Wind Turbulence between Ion and Electron Scales. Phys. Rev. Lett., 104:255002, Jun 2010b. doi: 10.1103/PhysRevLett.104.255002.

C. H. K. Chen, R. T. Wicks, T. S. Horbury, and A. A. Schekochihin. Interpreting Power Anisotropy Measurements in Plasma Turbulence. ApJ, 711:L79–L83, Mar 2010c. doi: 10.1088/2041-8205/711/2/L79.

C. H. K. Chen, S. D. Bale, C. Salem, and F. S. Mozer. Frame Dependence of the Electric Field Spectrum of Solar Wind Turbulence. ApJ, 737:L41, Aug 2011. doi: 10.1088/2041-8205/737/2/L41.

C. H. K. Chen, A. Mallet, A. A. Schekochihin, T. S. Horbury, R. T. Wicks, and S. D. Bale. Three-dimensional Structure of Solar Wind Turbulence. ApJ, 758:120, October 2012. doi: 10.1088/0004-637X/758/2/120.

C. H. K. Chen, S. D. Bale, C. S. Salem, and B. A. Maruca. Residual Energy Spectrum of Solar Wind Turbulence. ApJ, 770:125, June 2013. doi: 10.1088/0004-637X/770/2/125.

C. H. K. Chen, L. Leung, S. Boldyrev, B. A. Maruca, and S. D. Bale. Ion-scale spectral break of solar wind turbulence at high and low beta. Geophysical Research Letters, 41:8081–8088, Nov 2014. doi: 10.1002/2014GL062009.

C. H. K. Chen, K. G. Klein, and G. G. Howes. Evidence for electron Landau damping in space plasma turbulence. Nature Communications, 10:740, Feb 2019. doi: 10.1038/s41467-019-08435-3.

F.F. Chen. Introduction to plasma physics. Plenum Press, 1974. ISBN 9780306307553. URL https://books.google.com/books?id=u8nvAAAAMAAJ.

Ronald H. Cohen. Mode decay and evolution of the solar wind alfv□n wave spectrum. Journal of Geophysical Research (1896-1977), 80(25):3678–3680, 1975. doi: 10.1029/JA080i025p03678. URL https://agupubs.onlinelibrary.wiley.com/doi/abs/10.1029/JA080i025p03678.

P. J. Coleman, Jr. Turbulence, Viscosity, and Dissipation in the Solar-Wind Plasma. ApJ, 153:371, August 1968. doi: 10.1086/149674.

Paul J. Coleman Jr. Characteristics of the region of interaction between the interplanetary plasma and the geomagnetic field: Pioneer 5. Journal of Geophysical Research (1896-1977), 69(15):3051–3076, 1964. doi: 10.1029/JZ069i015p03051. URL https://agupubs.onlinelibrary.wiley.com/doi/abs/10.1029/JZ069i015p03051.

Paul J. Coleman Jr. Variations in the interplanetary magnetic field: Mariner 2: 1. observed properties. Journal of Geophysical Research (1896-1977), 71(23):5509–5531, 1966. doi: 10.1029/JZ071i023p05509. URL https://agupubs.onlinelibrary.wiley.com/doi/abs/10.1029/JZ071i023p05509.

J. E. P. Connerney, J. Espley, P. Lawton, S. Murphy, J. Odom, R. Oliversen, and D. Sheppard. The MAVEN Magnetic Field Investigation. Space Science Rev., 195:257–291, December 2015. doi: 10.1007/s11214-015-0169-4.

J. E. P. Connerney, M. Benn, J. B. Bjarno, T. Denver, J. Espley, J. L. Jorgensen, P. S. Jorgensen, P. Lawton, A. Malinnikova, J. M. Merayo, S. Murphy, J. Odom, R. Oliversen, R. Schnurr, D. Sheppard, and E. J. Smith. The Juno Magnetic Field Investigation. Space Science Rev., 213:39–138, November 2017. doi: 10.1007/s11214-017-0334-z.

J W Connor. Tokamak turbulence-electrostatic or magnetic? Plasma Physics and Controlled Fusion, 35(SB):B293–B305, dec 1993. doi: 10.1088/0741-3335/35/sb/024.

N. Cornilleau-Wehrlin, G. Chanteur, S. Perraut, L. Rezeau, P. Robert, A. Roux, C. de Villedary, P. Canu, M. Maksimovic, Y. de Conchy, D. Hubert, C. Lacombe, F. Lefeuvre, M. Parrot, J. L. Pinçon, P. M. E. Décréau, C. C. Harvey, Ph. Louarn, O. Santolik, H. St. C. Alleyne, M. Roth, T. Chust, O. Le Contel, and STAFF team. First results obtained by the cluster staff experiment. Annales Geophysicae, 21(2): 437–456, 2003. doi: 10.5194/angeo-21-437-2003. URL https://www.ann-geophys.net/21/437/2003/.

G. V. A. Costa. Characterizing spatiotemporal methods for taking up space and wasting time. Journal of Youth and Adolescence, 28:523–43, Jun 2008.

Steven R. Cranmer. Turbulence-driven polar winds from t tauri stars energized by magnetospheric accretion. The Astrophysical Journal, 689(1):316–334, dec 2008. doi: 10.1086/592566. URL https://doi.org/10.1086%2F592566.

Steven R. Cranmer, William H. Matthaeus, Benjamin A. Breech, and Justin C. Kasper. Empirical Constraints on Proton and Electron Heating in the Fast Solar Wind. ApJ, 702:1604–1614, Sep 2009. doi: 10.1088/0004-637X/702/2/1604.

R.E. Crochiere and L.R. Rabiner. Multirate Digital Signal Processing. Prentice-Hall Signal Processing Series: Advanced monographs. Prentice-Hall, 1983. ISBN 9780136051626. URL https://books.google.com/books?id=X_NSAAAAMAAJ.

M. Davidson. The quark-gluon plasma and the stochastic interpretation of quantum mechanics. Physica E Low-Dimensional Systems and Nanostructures, 42:317–322, January 2010. doi: 10.1016/j.physe.2009.06.076.

P. Davidson. Turbulence: An Introduction for Scientists and Engineers. Oxford University Press, 2015. ISBN 9780198722595. URL https://books.google.com/books?id=VblDCQAAQBAJ.

L. Davis and E. J. Smith. The in-flight determination of spacecraft magnetic field zeros. volume 49, page 257, 1968.

L. Davis, Jr., E. J. Smith, and D. E. Jones. Comments on paper by N. F. Ness, K. W. Behannon, R. P. Lepping, and K. H. Schatten, Use of two magnetometers for magnetic field measurements on a spacecraft. J. Geophys. Res., 78:4803–4808, August 1973. doi: 10.1029/JA078i022p04803.

L. Del Zanna. Parametric decay of oblique arc-polarized Alfvén waves. Geophys. Res. Lett., 28:2585–2588, 2001. doi: 10.1029/2001GL012911.

L. Del Zanna, M. Velli, and P. Londrillo. Parametric decay of circularly polarized Alfvén waves: Multidimensional simulations in periodic and open domains. A&A, 367:705–718, February 2001. doi: 10.1051/0004-6361:20000455.

L. Del Zanna, L. Matteini, S. Landi, A. Verdini, and M. Velli. Parametric decay of parallel and oblique Alfvén waves in the expanding solar wind. Journal of Plasma Physics, 81(1):325810102, January 2015. doi: 10.1017/S0022377814000579.

K. U. Denskat and F. M. Neubauer. Statistical properties of low-frequency magnetic field fluctuations in the solar wind from 0.29 to 1.0 AU during solar minimum conditions: HELIOS 1 and HELIOS 2. Journal of Geophysical Research, 87:2215–2223, Apr 1982. doi: 10.1029/JA087iA04p02215.

N. F. Derby, Jr. Modulational instability of finite-amplitude, circularly polarized Alfven waves. ApJ, 224:1013–1016, September 1978. doi: 10.1086/156451.

Pablo Dmitruk, W. H. Matthaeus, and N. Seenu. Test particle energization by current sheets and nonuniform fields in magnetohydrodynamic turbulence. The Astrophysical Journal, 617(1):667–679, dec 2004. doi: 10.1086/425301. URL https://doi.org/10.1086%2F425301.

M. Dobrowolny, A. Mangeney, and P. Veltri. Fully developed anisotropic hydromagnetic turbulence in interplanetary space. Phys. Rev. Lett., 45:144–147, Jul 1980. doi: 10.1103/PhysRevLett.45.144. URL https://link.aps.org/doi/10.1103/PhysRevLett.45.144.

M. Dobrowolny, A. Mangeney, and P. Veltri. Properties of magnetohydrodynamic turbulence in the solar wind. A&A, 83:26–32, Mar 1980a.

M. Dobrowolny, A. Mangeney, and P. Veltri. Fully Developed Anisotropic Hydromagnetic Turbulence in Interplanetary Space. Phys. Rev. Lett., 45:144–147, Jul 1980b. doi: 10.1103/PhysRevLett.45.144.

Marino Dobrowolny. Kelvin helmholtz instability in a high β collisionless plasma. The Physics of Fluids, 15(12):2263–2270, 1972. doi: 10.1063/1.1693866. URL https://aip.scitation.org/doi/abs/10.1063/1.1693866.

Donadio, M. P. CIC Filter Introduction. http://dspguru.com/sites/dspguru/files/cic.pdf, 2000.

S. Dorfman and T. A. Carter. Observation of an Alfvén Wave Parametric Instability in a Laboratory Plasma. Phys. Rev. Lett., 116:195002, May 2016. doi: 10.1103/PhysRevLett.116.195002.

T. Dudok de Wit. Can high-order moments be meaningfully estimated from experimental turbulence measurements? Phys. Rev. E, 70:055302, Nov 2004. doi: 10.1103/PhysRevE.70.055302.

T. Dudok de Wit, O. Alexandrova, I. Furno, L. Sorriso-Valvo, and G. Zimbardo. Methods for Characterising Microphysical Processes in Plasmas. Space Sci. Rev., 178:665–693, Oct 2013. doi: 10.1007/s11214-013-9974-9.

Walter M. Elsasser. The hydromagnetic equations. Phys. Rev., 79:183–183, Jul 1950. doi: 10.1103/PhysRev.79.183. URL https://link.aps.org/doi/10.1103/PhysRev.79.183.

R. E. Ergun, S. Tucker, J. Westfall, K. A. Goodrich, D. M. Malaspina, D. Summers, J. Wallace, M. Karlsson, J. Mack, N. Brennan, B. Pyke, P. Withnell, R. Torbert, J. Macri, D. Rau, I. Dors, J. Needell, P.-A. Lindqvist, G. Olsson, and C. M. Cully. The axial double probe and fields signal processing for the mms mission. Space Science Reviews, 199(1):167–188, Mar 2016. ISSN 1572-9672. doi: 10.1007/s11214-014-0115-x. URL https://doi.org/10.1007/s11214-014-0115-x.

C.P. Escoubet, R. Schmidt, and M.L. Goldstein. Cluster – science and mission overview. Space Science Reviews, 79(1):11–32, Jan 1997. ISSN 1572-9672. doi: 10.1023/A:1004923124586. URL https://doi.org/10.1023/A:1004923124586.

M. Farge. Wavelet transforms and their applications to turbulence. Annual Review of Fluid Mechanics, 24(1):395–458, 1992. doi: 10.1146/annurev.fl.24.010192.002143. URL http://dx.doi.org/10.1146/annurev.fl.24.010192.002143.

W. M. Farrell, R. F. Thompson, R. P. Lepping, and J. B. Byrnes. A method of calibrating magnetometers on a spinning spacecraft. IEEE Transactions on Magnetics, 31:966–972, March 1995. doi: 10.1109/20.364770.

David Fischer, Werner Magnes, Christian Hagen, Ivan Dors, Mark W. Chutter, Jerry Needell, Roy B. Torbert, Olivier Le Contel, Robert J. Strangeway, Gernot Kubin, Aris Valavanoglou, Ferdinand Plaschke, Rumi Nakamura, Laurent Mirioni, Christopher T. Russell, Hannes K. Leinweber, Kenneth R. Bromund, Guan Le, Lawrence Kepko, Brian J. Anderson, James A. Slavin, and Wolfgang Baumjohann. Optimized merging of search coil and fluxgate data for MMS. Geoscientific Instrumentation, Methods and Data Systems, 5:521–530, Nov 2016. doi: 10.5194/gi-5-521-2016.

R. Fitzpatrick. Plasma Physics: An Introduction. Taylor & Francis, 2014. ISBN 9781466594265. URL https://books.google.com/books?id=0RwbBAAAQBAJ.

Miriam A. Forman, Robert T. Wicks, and Timothy S. Horbury. Detailed Fit of "Critical Balance" Theory to Solar Wind Turbulence Measurements. ApJ, 733:76, Jun 2011. doi: 10.1088/0004-637X/733/2/76.

N. J. Fox, M. C. Velli, S. D. Bale, R. Decker, A. Driesman, R. A. Howard, J. C. Kasper, J. Kinnison, M. Kusterer, D. Lario, M. K. Lockwood, D. J. McComas, N. E. Raouafi, and A. Szabo. The solar probe plus mission: Humanity's first visit to our star. Space Science Reviews, 204(1):7–48, Dec 2016. ISSN 1572-9672. doi: 10.1007/s11214-015-0211-6. URL https://doi.org/10.1007/s11214-015-0211-6.

R. W. Fredricks and F. V. Coroniti. Ambiguities in the deduction of rest frame fluctuation spectrums from spectrums computed in moving frames. Journal of Geophysical Research, 81:5591–5595, Nov 1976. doi: 10.1029/JA081i031p05591.

M. Frerking. Digital Signal Processing in Communications Systems. Springer US, 1994. ISBN 9780442016166. URL https://books.google.com/books?id=_WEwIH3B120C.

U. Frisch. Turbulence: The Legacy of A. N. Kolmogorov. Cambridge University Press, 1995. ISBN 9780521457132. URL https://books.google.com/books?id=K-Pf7RuYkf0C.

A. A. Galeev and V. N. Oraevskii. The Stability of Alfvén Waves. Soviet Physics Doklady, 7:988, May 1963.

Sebastien Galtier. Wave turbulence in incompressible hall magnetohydrodynamics. Journal of Plasma Physics, 72(5):721?769, 2006. doi: 10.1017/S0022377806004521.

S. Peter Gary and Martin A. Lee. The ion cyclotron anisotropy instability and the inverse correlation between proton anisotropy and proton beta. Journal of Geophysical Research: Space Physics, 99 (A6):11297–11301, 1994. doi: 10.1029/94JA00253. URL https://agupubs.onlinelibrary.wiley.com/doi/abs/10.1029/94JA00253.

S. Peter Gary and Charles W. Smith. Short-wavelength turbulence in the solar wind: Linear theory of whistler and kinetic alfv□n fluctuations. Journal of Geophysical Research: Space Physics, 114 (A12), 2009. doi: 10.1029/2009JA014525. URL https://agupubs.onlinelibrary.wiley.com/doi/abs/10.1029/2009JA014525.

G. Gogoberidze, S. C. Chapman, and B. Hnat. Generation of residual energy in the turbulent solar wind. Physics of Plasmas, 19(10):102310, October 2012a. doi: 10.1063/1.4764469.

G. Gogoberidze, S. C. Chapman, B. Hnat, and M. W. Dunlop. Impact of measurement uncertainties on universal scaling of MHD turbulence. MNRAS, 426:951–955, October 2012b. doi: 10.1111/j.1365-2966.2012.21775.x.

P. Goldreich and S. Sridhar. Toward a theory of interstellar turbulence. 2: Strong alfvenic turbulence. ApJ, 438:763–775, January 1995. doi: 10.1086/175121.

P. Goldreich and S. Sridhar. Magnetohydrodynamic Turbulence Revisited. ApJ, 485:680–688, Aug 1997. doi: 10.1086/304442.

M. L. Goldstein. An instability of finite amplitude circularly polarized Alfven waves. ApJ, 219:700–704, January 1978. doi: 10.1086/155829.

M. L. Goldstein, D. A. Roberts, and W. H. Matthaeus. Magnetohydrodynamic Turbulence In The Solar Wind. Annual Review of Astronomy and Astrophysics, 33:283–326, Jan 1995. doi: 10.1146/annurev.aa.33.090195.001435.

G .H. Golub and C. Reinsch. Singular Value Decomposition and Least Squares Solutions. Numer. Math., 14(5):403–420, 1970.

R. Grappin, U. Frisch, A. Pouquet, and J. Leorat. Alfvenic fluctuations as asymptotic states of MHD turbulence. A&A, 105:6–14, Jan 1982.

R. Grappin, J. Leorat, and A. Pouquet. Dependence of MHD turbulence spectra on the velocity field-magnetic field correlation. A&A, 126:51–58, September 1983.

F. J. Harris. On the use of windows for harmonic analysis with the discrete fourier transform. Proceedings of the IEEE, 66(1):51–83, Jan 1978. ISSN 0018-9219. doi: 10.1109/PROC.1978.10837.

M.H. Hayes. Statistical digital signal processing and modeling. John Wiley & Sons, 1996. ISBN 9780471594314. URL https://books.google.com/books?id=N_VSAAAAMAAJ.

Jiansen He, Chuanyi Tu, Eckart Marsch, and Shuo Yao. Do Oblique Alfvén/Ion-cyclotron or Fast-mode/Whistler Waves Dominate the Dissipation of Solar Wind Turbulence near the Proton Inertial Length? ApJ, 745:L8, Jan 2012. doi: 10.1088/2041-8205/745/1/L8.

P. Hellinger and H. Matsumoto. Nonlinear competition between the whistler and Alfvén fire hoses. Journal of Geophysical Research, 106:13215–13218, Jul 2001. doi: 10.1029/2001JA900026.

Petr Hellinger. Comment on the linear mirror instability near the threshold. Physics of Plasmas, 14: 082105, Aug 2007. doi: 10.1063/1.2768318.

Petr Hellinger, Pavel Trávníček, Justin C. Kasper, and Alan J. Lazarus. Solar wind proton temperature anisotropy: Linear theory and WIND/SWE observations. Geophysical Research Letters, 33:L09101, May 2006. doi: 10.1029/2006GL025925.

J. C. Higdon. Density fluctuations in the interstellar medium: Evidence for anisotropic magnetogasdynamic turbulence. I - Model and astrophysical sites. ApJ, 285:109–123, Oct 1984. doi: 10.1086/162481.

Bogdan Hnat, Sandra C. Chapman, and George Rowlands. Intermittency, scaling, and the Fokker-Planck approach to fluctuations of the solar wind bulk plasma parameters as seen by the WIND spacecraft. Phys. Rev. E, 67:056404, May 2003. doi: 10.1103/PhysRevE.67.056404.

Bogdan Hnat, Sandra C. Chapman, and George Rowlands. Compressibility in Solar Wind Plasma Turbulence. Phys. Rev. Lett., 94:204502, May 2005. doi: 10.1103/PhysRevLett.94.204502.

E. Hogenauer. An economical class of digital filters for decimation and interpolation. IEEE Transactions on Acoustics, Speech, and Signal Processing, 29(2):155–162, Apr 1981. ISSN 0096-3518. doi: 10.1109/TASSP.1981.1163535.

J. V. Hollweg. Beat, modulational, and decay instabilities of a circularly polarized Alfven wave. J. Geophys. Res., 99:23, December 1994. doi: 10.1029/94JA02185.

Joseph V. Hollweg. Waves and instabilities in the solar wind. Reviews of Geophysics, 13(1):263–289, 1975. doi: 10.1029/RG013i001p00263. URL https://agupubs.onlinelibrary.wiley.com/doi/abs/10.1029/RG013i001p00263.

Joseph V. Hollweg and Philip A. Isenberg. Generation of the fast solar wind: A review with emphasis on the resonant cyclotron interaction. Journal of Geophysical Research (Space Physics), 107:1147, Jul 2002. doi: 10.1029/2001JA000270.

T. S. Horbury and A. Balogh. Structure function measurements of the intermittent MHD turbulent cascade. Nonlinear Processes in Geophysics, 4:185–199, Jan 1997.

T. S. Horbury, R. T. Wicks, and C. H. K. Chen. Anisotropy in Space Plasma Turbulence: Solar Wind Observations. Space Sci. Rev., 172:325–342, Nov 2012. doi: 10.1007/s11214-011-9821-9.

Timothy S. Horbury, Miriam Forman, and Sean Oughton. Anisotropic Scaling of Magnetohydrodynamic Turbulence. Phys. Rev. Lett., 101:175005, Oct 2008. doi: 10.1103/PhysRevLett.101.175005.

G. G. Howes, J. M. TenBarge, W. Dorland, E. Quataert, A. A. Schekochihin, R. Numata, and T. Tatsuno. Gyrokinetic simulations of solar wind turbulence from ion to electron scales. Phys. Rev. Lett., 107: 035004, Jul 2011. doi: 10.1103/PhysRevLett.107.035004. URL https://link.aps.org/doi/10.1103/PhysRevLett.107.035004.

G. G. Howes, S. D. Bale, K. G. Klein, C. H. K. Chen, C. S. Salem, and J. M. TenBarge. The Slow-mode Nature of Compressible Wave Power in Solar Wind Turbulence. ApJ, 753:L19, July 2012. doi: 10.1088/2041-8205/753/1/L19.

P. S. Iroshnikov. Turbulence of a Conducting Fluid in a Strong Magnetic Field. AZh, 40:742, Jan 1963.

K. Issautier, M. Moncuquet, N. Meyer-Vernet, S. Hoang, and R. Manning. Quasi-thermal noise diagnostics in space plasmas. Astrophysics and Space Science, 277(1):309–311, Jun 2001. ISSN 1572-946X. doi: 10.1023/A:1012281730151. URL https://doi.org/10.1023/A:1012281730151.

K. Issautier, A. Mangeney, and O. Alexandrova. Spectrum of the electron density fluctuations: preliminary results from Ulysses observations. In M. Maksimovic, K. Issautier, N. Meyer-Vernet, M. Moncuquet, and F. Pantellini, editors, Twelfth International Solar Wind Conference, volume 1216 of American Institute of Physics Conference Series, pages 148–151, Mar 2010. doi: 10.1063/1.3395822.

Jannet, G., and Martin, P. and Dudok de Wit, T. SPP-SCM-TEC-10000-SP-0079-LPC2E SPP FIELDS SCM Technical Specification, 2013.

V. Jayanti and J. V. Hollweg. Parametric instabilities of parallel-propagating Alfven waves: Some analytical results. J. Geophys. Res., 98:19, November 1993. doi: 10.1029/93JA02208.

J. R. Jokipii. Modulation of low-rigidity cosmic rays and the power spectrum of the interplanetary magnetic field in 1962 and 1965. Canadian Journal of Physics, 46(10):S950–S953, 1968. doi: 10.1139/p68-391. URL https://doi.org/10.1139/p68-391.

J. R. Jokipii and L. Davis, Jr. Long-Wavelength Turbulence and the Heating of the Solar Wind. ApJ, 156: 1101, June 1969. doi: 10.1086/150037.

L.R. Kahn. Radio Squarer. Proceedings of the IRE, Proc. IRE, page 1704, Nov 1954. ISSN 0096-8390.

Justin C. Kasper, Alan J. Lazarus, and S. Peter Gary. Wind/SWE observations of firehose constraint on solar wind proton temperature anisotropy. Geophysical Research Letters, 29:1839, Sep 2002. doi: 10.1029/2002GL015128.

Justin C. Kasper, Robert Abiad, Gerry Austin, Marianne Balat-Pichelin, Stuart D. Bale, John W. Belcher, Peter Berg, Henry Bergner, Matthieu Berthomier, Jay Bookbinder, Etienne Brodu, David Caldwell, Anthony W. Case, Benjamin D. G. Chandran, Peter Cheimets, Jonathan W. Cirtain, Steven R. Cranmer, David W. Curtis, Peter Daigneau, Greg Dalton, Brahmananda Dasgupta, David DeTomaso, Millan Diaz-Aguado, Blagoje Djordjevic, Bill Donaskowski, Michael Effinger, Vladimir Florinski, Nichola Fox, Mark Freeman, Dennis Gallagher, S. Peter Gary, Tom Gauron, Richard Gates, Melvin Goldstein, Leon Golub, Dorothy A. Gordon, Reid Gurnee, Giora Guth, Jasper Halekas, Ken Hatch, Jacob Heerikuisen, George Ho, Qiang Hu, Greg Johnson, Steven P. Jordan, Kelly E. Korreck, Davin Larson, Alan J. Lazarus, Gang Li, Roberto Livi, Michael Ludlam, Milan Maksimovic, James P. McFadden, William Marchant, Bennet A. Maruca, David J. McComas, Luciana Messina, Tony Mercer, Sang Park, Andrew M. Peddie, Nikolai Pogorelov, Matthew J. Reinhart, John D. Richardson, Miles Robinson, Irene Rosen, Ruth M. Skoug, Amanda Slagle, John T. Steinberg, Michael L. Stevens, Adam Szabo, Ellen R. Taylor, Chris Tiu, Paul Turin, Marco Velli, Gary Webb, Phyllis Whittlesey, Ken Wright, S. T. Wu, and Gary Zank. Solar wind electrons alphas and protons (sweap) investigation: Design of the solar wind and coronal plasma instrument suite for solar probe plus. Space Science Reviews, 204(1):131–186, Dec 2016. ISSN 1572-9672. doi: 10.1007/s11214-015-0206-3. URL https://doi.org/10.1007/s11214-015-0206-3.

K. Kauffmann and J. A. Araneda. Parametric instabilities of Alfvén waves in a multispecies plasma: Kinetic effects. Physics of Plasmas, 15(6):062106, June 2008. doi: 10.1063/1.2932113.

P. J. Kellogg and T. S. Horbury. Rapid density fluctuations in the solar wind. Annales Geophysicae, 23(12):3765–3773, 2005. doi: 10.5194/angeo-23-3765-2005. URL https://www.ann-geophys.net/23/3765/2005/.

K. G. Klein, G. G. Howes, J. M. TenBarge, S. D. Bale, C. H. K. Chen, and C. S. Salem. Using Synthetic Spacecraft Data to Interpret Compressible Fluctuations in Solar Wind Turbulence. ApJ, 755:159, August 2012. doi: 10.1088/0004-637X/755/2/159.

Kristopher G. Klein, Jean C. Perez, Daniel Verscharen, Alfred Mallet, and Benjamin D. G. Chandran. A Modified Version of Taylor's Hypothesis for Solar Probe Plus Observations. ApJ, 801:L18, Mar 2015. doi: 10.1088/2041-8205/801/1/L18.

C. A. Kletzing, W. S. Kurth, M. Acuna, R. J. MacDowall, R. B. Torbert, T. Averkamp, D. Bodet, S. R. Bounds, M. Chutter, J. Connerney, D. Crawford, J. S. Dolan, R. Dvorsky, G. B. Hospodarsky, J. Howard, V. Jordanova, R. A. Johnson, D. L. Kirchner, B. Mokrzycki, G. Needell, J. Odom, D. Mark, R. Pfaff, J. R. Phillips, C. W. Piker, S. L. Remington, D. Rowland , O. Santolik, R. Schnurr, D. Sheppard, C. W. Smith, R. M. Thorne, and J. Tyler. The Electric and Magnetic Field Instrument Suite and Integrated Science (EMFISIS) on RBSP. Space Sci. Rev., 179:127–181, Nov 2013. doi: 10.1007/s11214-013-9993-6.

A. Kolmogorov. The Local Structure of Turbulence in Incompressible Viscous Fluid for Very Large Reynolds' Numbers. Akademiia Nauk SSSR Doklady, 30:301–305, Jan 1941.

N.P. Korzhov, V.V. Mishin, and V.M. Tomozov. On the role of plasma parameters and the kelvin-helmholtz instability in a viscous interaction of solar wind streams. Planetary and Space Science, 32(9):1169 – 1178, 1984. ISSN 0032-0633. doi: https://doi.org/10.1016/0032-0633(84)90142-9. URL http://www.sciencedirect.com/science/article/pii/0032063384901429.

Robert H. Kraichnan. Inertial-Range Spectrum of Hydromagnetic Turbulence. Physics of Fluids, 8: 1385–1387, Jul 1965. doi: 10.1063/1.1761412.

D. Krauss-Varban, N. Omidi, and K. B. Quest. Mode properties of low-frequency waves: Kinetic theory versus Hall-MHD. Journal of Geophysical Research, 99:5987–6010, Apr 1994. doi: 10.1029/93JA03202.

S. Lang. Linear Algebra. Springer Undergraduate Texts in Mathematics and Technology. Springer, 1987. ISBN 9780387964126. URL https://books.google.com/books?id=0DUXym7QWfYC.

Davin Larson. Private Communication, 2018-2019.

O. Le Contel, A. Roux, P. Robert, C. Coillot, A. Bouabdellah, B. de la Porte, D. Alison, S. Ruocco, V. Angelopoulos, K. Bromund, C. C. Chaston, C. Cully, H. U. Auster, K. H. Glassmeier, W. Baumjohann, C. W. Carlson, J. P. McFadden, and D. Larson. First results of the themis search coil magnetometers. Space Science Reviews, 141(1):509–534, Dec 2008. ISSN 1572-9672. doi: 10.1007/s11214-008-9371-y. URL https://doi.org/10.1007/s11214-008-9371-y.

Robert J. Leamon, Charles W. Smith, Norman F. Ness, William H. Matthaeus, and Hung K. Wong. Observational constraints on the dynamics of the interplanetary magnetic field dissipation range. Journal of Geophysical Research, 103:4775–4788, Mar 1998. doi: 10.1029/97JA03394.

H. K. Leinweber, C. T. Russell, K. Torkar, T. L. Zhang, and V. Angelopoulos. An advanced approach to finding magnetometer zero levels in the interplanetary magnetic field. Measurement Science and Technology, 19(5):055104, May 2008. doi: 10.1088/0957-0233/19/5/055104.

R. P. Lepping, M. H. Acũna, L. F. Burlaga, W. M. Farrell, J. A. Slavin, K. H. Schatten, F. Mariani, N. F. Ness, F. M. Neubauer, Y. C. Whang, J. B. Byrnes, R. S. Kennon, P. V. Panetta, J. Scheifele, and E. M. Worley. The Wind Magnetic Field Investigation. Space Sci. Rev., 71:207–229, February 1995b. doi: 10.1007/BF00751330.

R. P. Lepping, M. H. Acũna, L. F. Burlaga, W. M. Farrell, J. A. Slavin, K. H. Schatten, F. Mariani, N. F. Ness, F. M. Neubauer, Y. C. Whang, J. B. Byrnes, R. S. Kennon, P. V. Panetta, J. Scheifele, and E. M. Worley. The Wind Magnetic Field Investigation. Space Sci. Rev., 71:207–229, February 1995a. doi: 10.1007/BF00751330.

E. C. Levy. Complex-curve fitting. IRE Transactions on Automatic Control, AC-4:37–43, 1959.

O. Le Contel, P. Leroy, A. Roux, C. Coillot, D. Alison, A. Bouabdellah, L. Mirioni, L. Meslier, A. Galic, M. C. Vassal, R. B. Torbert, J. Needell, D. Rau, I. Dors, R. E. Ergun, J. Westfall, D. Summers, J. Wallace, W. Magnes, A. Valavanoglou, G. Olsson, M. Chutter, J. Macri, S. Myers, S. Turco, J. Nolin, D. Bodet, K. Rowe, M. Tanguy, and B. de la Porte. The search-coil magnetometer for mms. Space Science Reviews, 199(1):257–282, Mar 2016. ISSN 1572-9672. doi: 10.1007/s11214-014-0096-9. URL https://doi.org/10.1007/s11214-014-0096-9.

G. Li, B. Miao, Q. Hu, and G. Qin. Effect of Current Sheets on the Solar Wind Magnetic Field Power Spectrum from the Ulysses Observation: From Kraichnan to Kolmogorov Scaling. Physical Review Letters, 106(12):125001, March 2011. doi: 10.1103/PhysRevLett.106.125001.

R. P. Lin, K. A. Anderson, S. Ashford, C. Carlson, D. Curtis, R. Ergun, D. Larson, J. McFadden, M. McCarthy, G. K. Parks, H. Rème, J. M. Bosqued, J. Coutelier, F. Cotin, C. D'Uston, K.-P. Wenzel, T. R. Sanderson, J. Henrion, J. C. Ronnet, and G. Paschmann. A Three-Dimensional Plasma and Energetic Particle Investigation for the Wind Spacecraft. Space Sci. Rev., 71:125–153, February 1995. doi: 10.1007/BF00751328.

Y. Lithwick, P. Goldreich, and S. Sridhar. Imbalanced Strong MHD Turbulence. ApJ, 655:269–274, Jan 2007. doi: 10.1086/509884.

Yoram Lithwick and Peter Goldreich. Compressible Magnetohydrodynamic Turbulence in Interstellar Plasmas. ApJ, 562:279–296, Nov 2001. doi: 10.1086/323470.

S. MacIntyre. A portable low noise low frequency three-axis search coil magnetometer. IEEE Transactions on Magnetics, 16:761–763, September 1980. doi: 10.1109/TMAG.1980.1060818.

F. Malara, L. Primavera, and P. Veltri. Nonlinear evolution of the parametric instability: numerical predictions versus observations in the heliosphere. Nonlinear Processes in Geophysics, 8:159–166, 2001.

David M. Malaspina, Robert E. Ergun, Mary Bolton, Mark Kien, David Summers, Ken Stevens, Alan Yehle, Magnus Karlsson, Vaughn C. Hoxie, Stuart D. Bale, and Keith Goetz. The Digital Fields Board for the FIELDS instrument suite on the Solar Probe Plus mission: Analog and digital signal processing. Journal of Geophysical Research (Space Physics), 121:5088–5096, June 2016. doi: 10.1002/2016JA022344.

A. Mallet and A. A. Schekochihin. A statistical model of three-dimensional anisotropy and intermittency in strong Alfvénic turbulence. MNRAS, 466:3918–3927, April 2017. doi: 10.1093/mnras/stw3251.

A. Mallet, A. A. Schekochihin, B. D. G. Chandran, C. H. K. Chen, T. S. Horbury, R. T. Wicks, and C. C. Greenan. Measures of three-dimensional anisotropy and intermittency in strong Alfvénic turbulence. MNRAS, 459:2130–2139, June 2016. doi: 10.1093/mnras/stw802.

A. Mallet, A. A. Schekochihin, and B. D. G. Chandran. Disruption of sheet-like structures in Alfvénic turbulence by magnetic reconnection. MNRAS, 468:4862–4871, July 2017. doi: 10.1093/mnras/stx670.

Alfred Mallet, Alexander A. Schekochihin, and Benjamin D. G. Chandran. Disruption of alfv□nic turbulence by magnetic reconnection in a collisionless plasma. Journal of Plasma Physics, 83(6): 905830609, 2017. doi: 10.1017/S0022377817000812.

Alfred Mallet, Kristopher G. Klein, Benjamin D. G. Chand ran, Daniel Groselj, Ian W. Hoppock, Trevor A. Bowen, Chadi S. Salem, and Stuart D. Bale. Interplay between intermittency and dissipation in collisionless plasma turbulence. arXiv e-prints, art. arXiv:1807.09301, Jul 2018.

A. Mangeney. Intermittency in the Solar Wind Turbulence and the Haar Wavelet Transform. In B. Warmbein, editor, Sheffield Space Plasma Meeting: Multipoint Measurements versus Theory, volume 492 of ESA Special Publication, page 53, January 2001.

F. Mariani, B. Bavassano, U. Villante, and N. F. Ness. Variations of the occurrence rate of discontinuities in the interplanetary magnetic field. J. Geophys. Res., 78:8011, 1973. doi: 10.1029/JA078i034p08011.

C. B. Markwardt. Non-linear Least-squares Fitting in IDL with MPFIT. In D. A. Bohlender, D. Durand, and P. Dowler, editors, Astronomical Data Analysis Software and Systems XVIII, volume 411 of Astronomical Society of the Pacific Conference Series, page 251, September 2009.

Jason Maron and Peter Goldreich. Simulations of Incompressible Magnetohydrodynamic Turbulence. ApJ, 554:1175–1196, June 2001. doi: 10.1086/321413.

E. Marsch and C. Y. Tu. On the radial evolution of MHD turbulence in the Inner heliosphere. Journal of Geophysical Research, 95:8211–8229, Jun 1990a. doi: 10.1029/JA095iA06p08211.

E. Marsch and C. Y. Tu. Spectral and spatial evolution of compressible turbulence in the inner solar wind. Journal of Geophysical Research, 95:11945–11956, Aug 1990b. doi: 10.1029/JA095iA08p11945.

Eckart Marsch. Kinetic Physics of the Solar Corona and Solar Wind. Living Reviews in Solar Physics, 3:1, Jul 2006. doi: 10.12942/lrsp-2006-1.

L. Matteini, S. Landi, L. Del Zanna, M. Velli, and P. Hellinger. Parametric decay of linearly polarized shear Alfvén waves in oblique propagation: One and two-dimensional hybrid simulations. Geophys. Res. Lett., 37:L20101, October 2010a. doi: 10.1029/2010GL044806.

L. Matteini, D. Stansby, T. S. Horbury, and C. H. K. Chen. On the 1/f Spectrum in the Solar Wind and Its Connection with Magnetic Compressibility. ApJ, 869(2):L32, Dec 2018. doi: 10.3847/2041-8213/aaf573.

Lorenzo Matteini, Simone Landi, Marco Velli, and Petr Hellinger. Kinetics of parametric instabilities of Alfvén waves: Evolution of ion distribution functions. Journal of Geophysical Research (Space Physics), 115:A09106, Sep 2010b. doi: 10.1029/2009JA014987.

W. H. Matthaeus and M. L. Goldstein. Measurement of the rugged invariants of magnetohydrodynamic turbulence in the solar wind. Journal of Geophysical Research, 87:6011–6028, Aug 1982a. doi: 10.1029/JA087iA08p06011.

W. H. Matthaeus and M. L. Goldstein. Stationarity of magnetohydrodynamic fluctuations in the solar wind. Journal of Geophysical Research, 87:10347–10354, Dec 1982b. doi: 10.1029/JA087iA12p10347.

W. H. Matthaeus and M. L. Goldstein. Low-frequency 1/f noise in the interplanetary magnetic field. Phys. Rev. Lett., 57:495–498, Jul 1986. doi: 10.1103/PhysRevLett.57.495.

W. H. Matthaeus, M. L. Goldstein, and J. H. King. An interplanetary magnetic field ensemble at 1 au. Journal of Geophysical Research: Space Physics, 91(A1):59–69, 1986. doi: 10.1029/JA091iA01p00059. URL https://agupubs.onlinelibrary.wiley.com/doi/abs/10.1029/JA091iA01p00059.

W. H. Matthaeus, B. Breech, P. Dmitruk, A. Bemporad, G. Poletto, M. Velli, and M. Romoli. Density and Magnetic Field Signatures of Interplanetary 1/f Noise. ApJ, 657:L121–L124, Mar 2007. doi: 10.1086/513075.

W. H. Matthaeus, M. Wan, S. Servidio, A. Greco, K. T. Osman, S. Oughton, and P. Dmitruk. Intermittency, nonlinear dynamics and dissipation in the solar wind and astrophysical plasmas. Philosophical Transactions of the Royal Society of London Series A, 373:20140154–20140154, April 2015. doi: 10.1098/rsta.2014.0154.

William H. Matthaeus, Melvyn L. Goldstein, and D. Aaron Roberts. Evidence for the presence of quasi-two-dimensional nearly incompressible fluctuations in the solar wind. Journal of Geophysical Research, 95:20673–20683, Dec 1990. doi: 10.1029/JA095iA12p20673.

William H. Matthaeus, Larry W. Klein, Sanjoy Ghosh, and Michael R. Brown. Nearly incompressible magnetohydrodynamics, pseudosound, and solar wind fluctuations. Journal of Geophysical Research, 96:5421–5435, Apr 1991. doi: 10.1029/90JA02609.

J. H. McClellan and T. W. Parks. A personal history of the Parks-McClellan algorithm. IEEE Signal Processing Magazine, 22:82–86, March 2005. doi: 10.1109/MSP.2005.1406492.

D. J. McComas, N. Alexander, N. Angold, S. Bale, C. Beebe, B. Birdwell, M. Boyle, J. M. Burgum, J. A. Burnham, E. R. Christian, W. R. Cook, S. A. Cooper, A. C. Cummings, A. J. Davis, M. I. Desai, J. Dickinson, G. Dirks, D. H. Do, N. Fox, J. Giacalone, R. E. Gold, R. S. Gurnee, J. R. Hayes, M. E. Hill, J. C. Kasper, B. Kecman, J. Klemic, S. M. Krimigis, A. W. Labrador, R. S. Layman, R. A. Leske, S. Livi, W. H. Matthaeus, R. L. McNutt, R. A. Mewaldt, D. G. Mitchell, K. S. Nelson, C. Parker, J. S. Rankin, E. C. Roelof, N. A. Schwadron, H. Seifert, S. Shuman, M. R. Stokes, E. C. Stone, J. D. Vandegriff, M. Velli, T. T. von Rosenvinge, S. E. Weidner, M. E. Wiedenbeck, and P. Wilson. Integrated science investigation of the sun (isis): Design of the energetic particle investigation. Space Science Reviews, 204(1):187–256, Dec 2016. ISSN 1572-9672. doi: 10.1007/s11214-014-0059-1. URL https://doi.org/10.1007/s11214-014-0059-1.

Nicole Meyer-Vernet and Claude Perche. Tool kit for antennae and thermal noise near the plasma frequency. Journal of Geophysical Research: Space Physics, 94(A3):2405–2415, 1989. doi: 10.1029/JA094iA03p02405. URL https://agupubs.onlinelibrary.wiley.com/doi/abs/10.1029/JA094iA03p02405.

Romain Meyrand, Anjor Kanekar, William Dorland, and Alexander A. Schekochihin. Fluidization of collisionless plasma turbulence. Proceedings of the National Academy of Sciences, 116(4):1185–1194, 2019. ISSN 0027-8424. doi: 10.1073/pnas.1813913116. URL https://www.pnas.org/content/116/4/1185.

P. D. Mininni and A. Pouquet. Finite dissipation and intermittency in magnetohydrodynamics. Phys. Rev. E, 80(2):025401, August 2009. doi: 10.1103/PhysRevE.80.025401.

D. Montgomery. Major disruptions, inverse cascades, and the Strauss equations. Physica Scripta Volume T, 2:83–88, January 1982. doi: 10.1088/0031-8949/1982/T2A/009.

D. Montgomery, M. R. Brown, and W. H. Matthaeus. Density fluctuation spectra in magnetohydrodynamic turbulence. Journal of Geophysical Research, 92:282–284, Jan 1987. doi: 10.1029/JA092iA01p00282.

W.-C. Müller and R. Grappin. Spectral Energy Dynamics in Magnetohydrodynamic Turbulence. Physical Review Letters, 95(11):114502, September 2005. doi: 10.1103/PhysRevLett.95.114502.

Günter Musmann. Problems with magnetic field measurements on spacecrafts. Deutsche Hydrografische Zeitschrift, 41(3):265–276, May 1988. ISSN 1616-7228. doi: 10.1007/BF02225935. URL https://doi.org/10.1007/BF02225935.

Y. Narita and E. Marsch. Kinetic Slow Mode in the Solar Wind and Its Possible Role in Turbulence Dissipation and Ion Heating. ApJ, 805:24, May 2015. doi: 10.1088/0004-637X/805/1/24.

N. F. Ness. Magnetometers for Space Research. Space Sci. Rev., 11:459–554, November 1970. doi: 10.1007/BF00183028.

N. F. Ness. A note on signal enhancement for dual magnetometer systems. J. Geophys. Res., 78:1709–1710, April 1973. doi: 10.1029/JA078i010p01709.

N. F. Ness, K. W. Behannon, R. P. Lepping, and K. H. Schatten. Use of two magnetometers for magnetic field measurements on a spacecraft. J. Geophys. Res., 76:3564, 1971. doi: 10.1029/JA076i016p03564.

Norman F. Ness, Clell S. Scearce, and Joseph B. Seek. Initial results of the imp 1 magnetic field experiment. Journal of Geophysical Research (1896-1977), 69(17):3531–3569, 1964. doi: 10.1029/JZ069i017p03531. URL https://agupubs.onlinelibrary.wiley.com/doi/abs/10.1029/JZ069i017p03531.

M. Neugebauer and C. W. Snyder. Solar Plasma Experiment. Science, 138:1095–1097, December 1962. doi: 10.1126/science.138.3545.1095-a.

D.R. Nicholson. Introduction to plasma theory. Wiley series in plasma physics. Wiley, 1983. ISBN 9780471090458. URL https://books.google.com/books?id=fyRRAAAAMAAJ.

R. M. Nicol, S. C. Chapman, and R. O. Dendy. Quantifying the Anisotropy and Solar Cycle Dependence of "1/f" Solar Wind Fluctuations Observed by Advanced Composition Explorer. ApJ, 703:2138–2151, Oct 2009. doi: 10.1088/0004-637X/703/2/2138.

K. W. Ogilvie, D. J. Chornay, R. J. Fritzenreiter, F. Hunsaker, J. Keller, J. Lobell, G. Miller, J. D. Scudder, E. C. Sittler, Jr., R. B. Torbert, D. Bodet, G. Needell, A. J. Lazarus, J. T. Steinberg, J. H. Tappan, A. Mavretic, and E. Gergin. SWE, A Comprehensive Plasma Instrument for the Wind Spacecraft. Space Sci. Rev., 71:55–77, February 1995. doi: 10.1007/BF00751326.

N. Olsen, L. Tøffner-Clausen, T. J. Sabaka, P. Brauer, J. M. G. Merayo, J. L. Jörgensen, J. M. Léger, O. V. Nielsen, F. Primdahl, and T. Risbo. Calibration of the Ørsted vector magnetometer. Earth, Planets, and Space, 55:11–18, Jan 2003.

Alan V. Oppenheim and R.W. Schafer. Digital Signal Processing. MIT video course. Prentice-Hall, 1975. ISBN 9780132146357. URL https://books.google.com/books?id=vfdSAAAAMAAJ.

K. T. Osman, W. H. Matthaeus, A. Greco, and S. Servidio. EVIDENCE FOR INHOMOGENEOUS HEATING IN THE SOLAR WIND. The Astrophysical Journal, 727(1):L11, dec 2010. doi: 10.1088/2041-8205/727/1/l11. URL https://doi.org/10.1088%2F2041-8205%2F727%2F1%2Fl11.

E. N. Parker. Dynamics of the Interplanetary Gas and Magnetic Fields. ApJ, 128:664, November 1958. doi: 10.1086/146579.

E. N. Parker. The Hydrodynamic Theory of Solar Corpuscular Radiation and Stellar Winds. ApJ, 132: 821, November 1960. doi: 10.1086/146985.

J. C. Perez and S. Boldyrev. Role of Cross-Helicity in Magnetohydrodynamic Turbulence. Physical Review Letters, 102(2):025003, January 2009. doi: 10.1103/PhysRevLett.102.025003.

T. D. Phan, J. P. Eastwood, M. A. Shay, J. F. Drake, B. U. Ö. Sonnerup, M. Fujimoto, P. A. Cassak, M. Øieroset, J. L. Burch, R. B. Torbert, A. C. Rager, J. C. Dorelli, D. J. Gershman, C. Pollock, P. S. Pyakurel, C. C. Haggerty, Y. Khotyaintsev, B. Lavraud, Y. Saito, M. Oka, R. E. Ergun, A. Retino, O. Le Contel, M. R. Argall, B. L. Giles, T. E. Moore, F. D. Wilder, R. J. Strangeway, C. T. Russell, P. A. Lindqvist, and W. Magnes. Electron magnetic reconnection without ion coupling in Earth's turbulent magnetosheath. Nature, 557:202–206, May 2018. doi: 10.1038/s41586-018-0091-5.

F. Plaschke, R. Nakamura, H. K. Leinweber, M. Chutter, H. Vaith, W. Baumjohann, M. Steller, and W. Magnes. Flux-gate magnetometer spin axis offset calibration using the electron drift instrument. Measurement Science and Technology, 25(10):105008, October 2014. doi: 10.1088/0957-0233/25/10/105008.

J. J. Podesta. Spectra that behave like power-laws are not necessarily power-laws. Advances in Space Research, 57:1127–1132, February 2016. doi: 10.1016/j.asr.2015.12.020.

J. J. Podesta and J. E. Borovsky. Scale invariance of normalized cross-helicity throughout the inertial range of solar wind turbulence. Physics of Plasmas, 17(11):112905, November 2010. doi: 10.1063/1.3505092.

J. J. Podesta and V. Roytershteyn. The most intense electrical currents in the solar wind: Comparisons between single-spacecraft measurements and plasma turbulence simulations. Journal of Geophysical Research (Space Physics), 122:6991–7004, July 2017. doi: 10.1002/2017JA024074.

J. J. Podesta, D. A. Roberts, and M. L. Goldstein. Power spectrum of small-scale turbulent velocity fluctuations in the solar wind. Journal of Geophysical Research (Space Physics), 111:A10109, Oct 2006. doi: 10.1029/2006JA011834.

J. J. Podesta, D. A. Roberts, and M. L. Goldstein. Spectral Exponents of Kinetic and Magnetic Energy Spectra in Solar Wind Turbulence. ApJ, 664:543–548, July 2007. doi: 10.1086/519211.

J. J. Podesta, B. D. G. Chandran, A. Bhattacharjee, D. A. Roberts, and M. L. Goldstein. Scale-dependent angle of alignment between velocity and magnetic field fluctuations in solar wind turbulence. Journal of Geophysical Research (Space Physics), 114:A01107, Jan 2009. doi: 10.1029/2008JA013504.

R. J. Prance, T. D. Clark, and H. Prance. Compact room-temperature induction magnetometer with superconducting quantum interference device level field sensitivity. Review of Scientific Instruments, 74:3735–3739, August 2003. doi: 10.1063/1.1590745.

William H. Press, Saul A. Teukolsky, William T. Vetterling, and Brian P. Flannery. Numerical Recipes in C (2Nd Ed.): The Art of Scientific Computing. Cambridge University Press, New York, NY, USA, 1992a. ISBN 0-521-43108-5.

William H. Press, Saul A. Teukolsky, William T. Vetterling, and Brian P. Flannery. Numerical Recipes in C (2Nd Ed.): The Art of Scientific Computing. Cambridge University Press, New York, NY, USA, 1992b. ISBN 0-521-43108-5.

F. Primdahl. The fluxgate magnetometer. Journal of Physics E Scientific Instruments, 12:241–253, April 1979. doi: 10.1088/0022-3735/12/4/001.

Fritz Primdahl, Torben Risbo, José M. G. Merayo, Peter Brauer, and Lars Tøffner-Clausen. In-flight spacecraft magnetic field monitoring using scalar/vector gradiometry. Measurement Science and Technology, 17:1563–1569, Jun 2006. doi: 10.1088/0957-0233/17/6/038.

M. Pulupa, S. D. Bale, J. W. Bonnell, T. A. Bowen, N. Carruth, K. Goetz, D. Gordon, P. R. Harvey, M. Maksimovic, J. C. Martínez-Oliveros, M. Moncuquet, P. Saint-Hilaire, D. Seitz, and D. Sundkvist. The Solar Probe Plus Radio Frequency Spectrometer: Measurement requirements, analog design, and digital signal processing. Journal of Geophysical Research (Space Physics), 122:2836–2854, March 2017. doi: 10.1002/2016JA023345.

M. P. Pulupa, S. D. Bale, C. Salem, and K. Horaites. Spin-modulated spacecraft floating potential: Observations and effects on electron moments. Journal of Geophysical Research: Space Physics, 119 (2):647–657, 2014. ISSN 2169-9402. doi: 10.1002/2013JA019359. URL http://dx.doi.org/10.1002/2013JA019359.

L.F. Richardson. Weather prediction by numerical process. University Press, 1922. URL https://books.google.com/books?id=cWXWhffnUokC.

A. Rigby, F. Cruz, B. Albertazzi, R. Bamford, A. R. Bell, J. E. Cross, F. Fraschetti, P. Graham, Y. Hara, P. M. Kozlowski, Y. Kuramitsu, D. Q. Lamb, S. Lebedev, J. R. Marques, F. Miniati, T. Morita, M. Oliver, B. Reville, Y. Sakawa, S. Sarkar, C. Spindloe, R. Trines, P. Tzeferacos, L. O. Silva,

R. Bingham, M. Koenig, and G. Gregori. Electron acceleration by wave turbulence in a magnetized plasma. Nature Physics, 14(5):475–479, 2018. doi: 10.1038/s41567-018-0059-2. URL https://doi.org/10.1038/s41567-018-0059-2.

Torben Risbo, Peter Brauer, Jose M. G. Merayo, Otto V. Nielsen, Jan R. Petersen, Fritz Primdahl, and Ingo Richter. Ørsted pre-flight magnetometer calibration mission. Measurement Science and Technology, 14:674–688, May 2003.

P. Robert, N. Cornilleau-Wehrlin, R. Piberne, Y. de Conchy, C. Lacombe, V. Bouzid, B. Grison, D. Alison, and P. Canu. Cluster-staff search coil magnetometer calibration - comparisons with fgm. Geoscientific Instrumentation, Methods and Data Systems, 3(2):153–177, 2014. doi: 10.5194/gi-3-153-2014. URL https://www.geosci-instrum-method-data-syst.net/3/153/2014/.

D. A. Roberts. Heliocentric distance and temporal dependence of the interplanetary density-magnetic field magnitude correlation. Journal of Geophysical Research, 95:1087–1090, Feb 1990. doi: 10.1029/JA095iA02p01087.

D. A. Roberts and M. L. Goldstein. Spectral signatures of jumps and turbulence in interplanetary speed and magnetic field data. J. Geophys. Res., 92:10, September 1987. doi: 10.1029/JA092iA09p10105.

D. A. Roberts, M. L. Goldstein, L. W. Klein, and W. H. Matthaeus. Origin and evolution of fluctuations in the solar wind: Helios observations and Helios-Voyager comparisons. Journal of Geophysical Research, 92:12023–12035, Nov 1987a. doi: 10.1029/JA092iA11p12023.

D. A. Roberts, L. W. Klein, M. L. Goldstein, and W. H. Matthaeus. The nature and evolution of magnetohydrodynamic fluctuations in the solar wind - Voyager observations. J. Geophys. Res., 92:11021–11040, October 1987b. doi: 10.1029/JA092iA10p11021.

D. A. Roberts, L. W. Klein, M. L. Goldstein, and W. H. Matthaeus. The nature and evolution of magnetohydrodynamic fluctuations in the solar wind: Voyager observations. Journal of Geophysical Research, 92:11021–11040, Oct 1987c. doi: 10.1029/JA092iA10p11021.

A. Roux, O. Le Contel, C. Coillot, A. Bouabdellah, B. de la Porte, D. Alison, S. Ruocco, and M. C. Vassal. The search coil magnetometer for themis. Space Science Reviews, 141(1):265–275, Dec 2008. ISSN 1572-9672. doi: 10.1007/s11214-008-9455-8. URL https://doi.org/10.1007/s11214-008-9455-8.

C. T. Russell, B. J. Anderson, W. Baumjohann, K. R. Bromund, D. Dearborn, D. Fischer, G. Le, H. K. Leinweber, D. Leneman, W. Magnes, J. D. Means, M. B. Moldwin, R. Nakamura, D. Pierce,

F. Plaschke, K. M. Rowe, J. A. Slavin, R. J. Strangeway, R. Torbert, C. Hagen, I. Jernej, A. Valavanoglou, and I. Richter. The magnetospheric multiscale magnetometers. Space Science Reviews, 199(1):189–256, Mar 2016. ISSN 1572-9672. doi: 10.1007/s11214-014-0057-3. URL https://doi.org/10.1007/s11214-014-0057-3.

Christopher T. Russell. Comments on the Measurement of Power Spectra of the Interplanetary Magnetic Field, page 365. National Aeronautics and Space Administration, 1972.

R.Z. Sagdeev and A.A. Galeev. Nonlinear Plasma Theory. Frontiers in physics. W.A. Benjamin, 1969. URL https://books.google.com/books?id=5gRlNwAACAAJ.

C. Salem, A. Mangeney, S. D. Bale, and P. Veltri. Solar Wind Magnetohydrodynamics Turbulence: Anomalous Scaling and Role of Intermittency. ApJ, 702:537–553, September 2009. doi: 10.1088/0004-637X/702/1/537.

C. S. Salem, G. G. Howes, D. Sundkvist, S. D. Bale, C. C. Chaston, C. H. K. Chen, and F. S. Mozer. IDENTIFICATION OF KINETIC ALFVén WAVE TURBULENCE IN THE SOLAR WIND. The Astrophysical Journal, 745(1):L9, jan 2012. doi: 10.1088/2041-8205/745/1/l9. URL https://doi.org/10.1088%2F2041-8205%2F745%2F1%2Fl9.

A. A. Schekochihin, S. C. Cowley, W. Dorland, G. W. Hammett, G. G. Howes, E. Quataert, and T. Tatsuno. Astrophysical Gyrokinetics: Kinetic and Fluid Turbulent Cascades in Magnetized Weakly Collisional Plasmas. ApJS, 182:310–377, May 2009. doi: 10.1088/0067-0049/182/1/310.

A. A. Schekochihin, J. T. Parker, E. G. Highcock, P. J. Dellar, W. Dorland, and G. W. Hammett. Phase mixing versus nonlinear advection in drift-kinetic plasma turbulence. Journal of Plasma Physics, 82:905820212, Apr 2016. doi: 10.1017/S0022377816000374.

Alexander A. Schekochihin and Steven C. Cowley. Turbulence and Magnetic Fields in Astrophysical Plasmas, page 85. Springer, Dordrecht, The Netherlands, 2007, p.85, 2007.

Henning Schepker and Simon Doclo. Least-squares estimation of the common pole-zero filter of acoustic feedback paths in hearing aids. IEEE/ACM Trans. Audio, Speech and Lang. Proc., 24(8):1334–1347, August 2016. ISSN 2329-9290. doi: 10.1109/TASLP.2016.2554288. URL https://doi.org/10.1109/TASLP.2016.2554288.

E. O. Schulz-DuBois and I. Rehberg. Structure function in lieu of correlation function. Applied physics, 24(4):323–329, Apr 1981. ISSN 1432-0630. doi: 10.1007/BF00899730. URL https://doi.org/10.1007/BF00899730.

R. Schwenn and E. Marsch. Physics of the inner heliosphere. Number v. 20 in Physics and chemistry in space. Springer-Verlag, 1991. ISBN 9783540520818. URL https://books.google.com/books?id=oLAuAQAAIAAJ.

H. C. Séran and P. Fergeau. An optimized low-frequency three-axis search coil magnetometer for space research. Review of Scientific Instruments, 76(4):044502-044502-10, April 2005. doi: 10.1063/1.1884026.

J. V. Shebalin, W. H. Matthaeus, and D. Montgomery. Anisotropy in MHD turbulence due to a mean magnetic field. Journal of Plasma Physics, 29:525–547, Jun 1983. doi: 10.1017/S0022377800000933.

Sheppard, D. FM-1 and FM-2 Fluxgate Magnetometer Calibration Report LWS-MAG-RPT-0011, 2017.

M. Shi, H. Li, C. Xiao, and X. Wang. The Parametric Decay Instability of Alfvén Waves in Turbulent Plasmas and the Applications in the Solar Wind. ApJ, 842:63, June 2017. doi: 10.3847/1538-4357/aa71b6.

B. K. Shivamoggi. Modulational instability of finite-amplitude Alfven waves. Ap&SS, 103:391–393, August 1984. doi: 10.1007/BF00653754.

Julius O. Smith. Introduction to digital filters with audio applications. http://ccrma.stanford.edu/~jos/filters, accessed 2019. online book.

B. U. O. Sonnerup and L. J. Cahill, Jr. Magnetopause Structure and Attitude from Explorer 12 Observations. J. Geophys. Res., 72:171, January 1967. doi: 10.1029/JZ072i001p00171.

Sorkine-Hornung,O., and Rabinovich, M. Least-Squares Rigid Motion Using SVD. http://www.igl.ethz.ch/projects/ARAP/svd_rot.pdf, 2017.

J. Squire, E. Quataert, and A. A. Schekochihin. A Stringent Limit on the Amplitude of Alfvénic Perturbations in High-beta Low-collisionality Plasmas. ApJ, 830:L25, Oct 2016. doi: 10.3847/2041-8205/830/2/L25.

J. Squire, M. W. Kunz, E. Quataert, and A. A. Schekochihin. Kinetic Simulations of the Interruption of Large-Amplitude Shear-Alfvén Waves in a High-β Plasma. Phys. Rev. Lett., 119:155101, Oct 2017. doi: 10.1103/PhysRevLett.119.155101.

P. Stoica and R.L. Moses. Spectral Analysis of Signals. Pearson Prentice Hall, 2005. ISBN 9780131139565. URL https://books.google.com/books?id=h78ZAQAAIAAJ.

H. R. Strauss. Nonlinear, three-dimensional magnetohydrodynamics of noncircular tokamaks. Physics of Fluids, 19:134–140, January 1976. doi: 10.1063/1.861310.

G. I. Taylor. The Spectrum of Turbulence. Proceedings of the Royal Society of London Series A, 164:476–490, Feb 1938. doi: 10.1098/rspa.1938.0032.

A. Tenerani and M. Velli. Parametric decay of radial Alfvén waves in the expanding accelerating solar wind. Journal of Geophysical Research (Space Physics), 118:7507–7516, December 2013. doi: 10.1002/2013JA019293.

Anna Tenerani, Marco Velli, and Petr Hellinger. The Parametric Instability of Alfvén Waves: Effects of Temperature Anisotropy. ApJ, 851:99, Dec 2017. doi: 10.3847/1538-4357/aa9bef.

Jeffrey A. Tessein, Charles W. Smith, Benjamin T. MacBride, William H. Matthaeus, Miriam A. Forman, and Joseph E. Borovsky. Spectral Indices for Multi-Dimensional Interplanetary Turbulence at 1 AU. ApJ, 692:684–693, Feb 2009. doi: 10.1088/0004-637X/692/1/684.

Yuguang Tong, Ivan Y. Vasko, Marc Pulupa, Forrest S. Mozer, Stuart D. Bale, Anton V. Artemyev, and Vladimir Krasnoselskikh. Whistler Wave Generation by Halo Electrons in the Solar Wind. ApJ, 870: L6, Jan 2019. doi: 10.3847/2041-8213/aaf734.

R. B. Torbert, C. T. Russell, W. Magnes, R. E. Ergun, P. A. Lindqvist, O. Le Contel, H. Vaith, J. Macri, S. Myers, D. Rau, J. Needell, B. King, M. Granoff, M. Chutter, I. Dors, G. Olsson, Y. V. Khotyaintsev, A. Eriksson, C. A. Kletzing, S. Bounds, B. Anderson, W. Baumjohann, M. Steller, K. Bromund, Guan Le, R. Nakamura, R. J. Strangeway, H. K. Leinweber, S. Tucker, J. Westfall, D. Fischer, F. Plaschke, J. Porter, and K. Lappalainen. The FIELDS Instrument Suite on MMS: Scientific Objectives, Measurements, and Data Products. Space Sci. Rev., 199:105–135, Mar 2016. doi: 10.1007/s11214-014-0109-8.

Christopher Torrence and Gilbert P. Compo. A Practical Guide to Wavelet Analysis. Bulletin of the American Meteorological Society, 79:61–78, January 1998. doi: 10.1175/1520-0477(1998)079<0061:APGTWA>2.0.CO;2.

R. A. Treumann and W. Baumjohann. Advanced space plasma physics. Imperial College Press, 1997. doi: 10.1142/p020.

C. Y. Tu and E. Marsch. A case study of very low cross-helicity fluctuations in the solar wind. Annales Geophysicae, 9:319–332, May 1991.

C.-Y. Tu and E. Marsch. A model of solar wind fluctuations with two components - Alfven waves and convective structures. J. Geophys. Res., 98:1257–1276, February 1993. doi: 10.1029/92JA01947.

C. Y. Tu and E. Marsch. On the nature of compressive fluctuations in the solar wind. Journal of Geophysical Research: Space Physics, 99(A11):21481–21509, 1994. ISSN 2156-2202. doi: 10.1029/94JA00843. URL http://dx.doi.org/10.1029/94JA00843.

C. Y. Tu and E. Marsch. Magnetohydrodynamic Structures Waves and Turbulence in the Solar Wind - Observations and Theories. Space Sci. Rev., 73:1–210, Jul 1995. doi: 10.1007/BF00748891.

C. Y. Tu, Z. Y. Pu, and F. S. Wei. The power spectrum of interplanetary Alfvénic fluctuations: Derivation of the governing equation and its solution. Journal of Geophysical Research, 89:9695–9702, Nov 1984. doi: 10.1029/JA089iA11p09695.

C. Y. Tu, E. Marsch, and K. M. Thieme. Basic properties of solar wind MHD turbulence near 0.3 AU analyzed by means of Elsässer variables. Journal of Geophysical Research, 94:11739–11759, Sep 1989. doi: 10.1029/JA094iA09p11739.

I. Y. Vasko, V. Krasnoselskikh, Y. Tong, S. D. Bale, J. W. Bonnell, and F. S. Mozer. Whistler Fan Instability Driven by Strahl Electrons in the Solar Wind. ApJ, 871:L29, Feb 2019. doi: 10.3847/2041-8213/ab01bd.

Bernard J. Vasquez, Charles W. Smith, Kathleen Hamilton, Benjamin T. MacBride, and Robert J. Leamon. Evaluation of the turbulent energy cascade rates from the upper inertial range in the solar wind at 1 AU. Journal of Geophysical Research (Space Physics), 112:A07101, Jul 2007. doi: 10.1029/2007JA012305.

Daniel Vech, Alfred Mallet, Kristopher G. Klein, and Justin C. Kasper. Magnetic Reconnection May Control the Ion-scale Spectral Break of Solar Wind Turbulence. ApJ, 855:L27, Mar 2018. doi: 10.3847/2041-8213/aab351.

Marco Velli, Roland Grappin, and Andre Mangeney. Turbulent cascade of incompressible unidirectional Alfvén waves in the interplanetary medium. Phys. Rev. Lett., 63:1807–1810, Oct 1989. doi: 10.1103/PhysRevLett.63.1807.

P. Veltri and A. Mangeney. Scaling laws and intermittent structures in solar wind MHD turbulence. In S. R. Habbal, R. Esser, J. V. Hollweg, and P. A. Isenberg, editors, American Institute of Physics Conference Series, volume 471 of American Institute of Physics Conference Series, pages 543–546, June 1999. doi: 10.1063/1.58809.

Andrea Verdini, Roland Grappin, Rui Pinto, and Marco Velli. On the Origin of the 1/f Spectrum in the Solar Wind Magnetic Field. ApJ, 750:L33, May 2012. doi: 10.1088/2041-8205/750/2/L33.

D. Verscharen, C. H. K. Chen, and R. T. Wicks. On Kinetic Slow Modes, Fluid Slow Modes, and Pressure-balanced Structures in the Solar Wind. ApJ, 840:106, May 2017. doi: 10.3847/1538-4357/aa6a56.

Daniel Verscharen, Sofiane Bourouaine, and Benjamin D. G. Chand ran. Instabilities Driven by the Drift and Temperature Anisotropy of Alpha Particles in the Solar Wind. ApJ, 773:163, Aug 2013. doi: 10.1088/0004-637X/773/2/163.

Angelos Vourlidas, Russell A. Howard, Simon P. Plunkett, Clarence M. Korendyke, Arnaud F. R. Thernisien, Dennis Wang, Nathan Rich, Michael T. Carter, Damien H. Chua, Dennis G. Socker, Mark G. Linton, Jeff S. Morrill, Sean Lynch, Adam Thurn, Peter Van Duyne, Robert Hagood, Greg Clifford, Phares J. Grey, Marco Velli, Paulett C. Liewer, Jeffrey R. Hall, Eric M. DeJong, Zoran Mikic, Pierre Rochus, Emanuel Mazy, Volker Bothmer, and Jens Rodmann. The wide-field imager for solar probe plus (wispr). Space Science Reviews, 204(1):83–130, Dec 2016. ISSN 1572-9672. doi: 10.1007/s11214-014-0114-y. URL https://doi.org/10.1007/s11214-014-0114-y.

R. T. Wicks, T. S. Horbury, C. H. K. Chen, and A. A. Schekochihin. Power and spectral index anisotropy of the entire inertial range of turbulence in the fast solar wind. MNRAS, 407:L31–L35, Sep 2010. doi: 10.1111/j.1745-3933.2010.00898.x.

R. T. Wicks, A. Mallet, T. S. Horbury, C. H. K. Chen, A. A. Schekochihin, and J. J. Mitchell. Alignment and Scaling of Large-Scale Fluctuations in the Solar Wind. Physical Review Letters, 110(2):025003, January 2013a. doi: 10.1103/PhysRevLett.110.025003.

R. T. Wicks, D. A. Roberts, A. Mallet, A. A. Schekochihin, T. S. Horbury, and C. H. K. Chen. Correlations at Large Scales and the Onset of Turbulence in the Fast Solar Wind. ApJ, 778:177, December 2013b. doi: 10.1088/0004-637X/778/2/177.

III Wilson, Lynn B., Michael L. Stevens, Justin C. Kasper, Kristopher G. Klein, Bennett A. Maruca, Stuart D. Bale, Trevor A. Bowen, Marc P. Pulupa, and Chadi S. Salem. The Statistical Properties of Solar Wind Temperature Parameters Near 1 au. The Astrophysical Journal Supplement Series, 236: 41, Jun 2018. doi: 10.3847/1538-4365/aab71c.

M. Wüest, D. S. Evans, and R. von Steiger. Calibration of Particle Instruments in Space Physics. ESA Communications, Noordwijk, The Netherlands, December 2007.

S. Yao, J.-S. He, E. Marsch, C.-Y. Tu, A. Pedersen, H. Rème, and J. G. Trotignon. Multi-scale Anticorrelation Between Electron Density and Magnetic Field Strength in the Solar Wind. ApJ, 728:146, February 2011. doi: 10.1088/0004-637X/728/2/146.

S. Yao, J.-S. He, C.-Y. Tu, L.-H. Wang, and E. Marsch. Small-scale Pressure-balanced Structures Driven by Mirror-mode Waves in the Solar Wind. ApJ, 776:94, October 2013a. doi: 10.1088/0004-637X/776/2/94.

S. Yao, J.-S. He, C.-Y. Tu, L.-H. Wang, and E. Marsch. Small-scale Pressure-balanced Structures Driven by Oblique Slow Mode Waves Measured in the Solar Wind. ApJ, 774:59, September 2013b. doi: 10.1088/0004-637X/774/1/59.

G. P. Zank and W. H. Matthaeus. Nearly incompressible fluids. II: Magnetohydrodynamics, turbulence, and waves. Physics of Fluids A, 5:257–273, Jan 1993. doi: 10.1063/1.858780.

Gaetano Zimbardo. Magnetic turbulence in space plasmas: in and around the earth's magnetosphere. Plasma Physics and Controlled Fusion, 48(12B):B295–B302, nov 2006. doi: 10.1088/0741-3335/48/12b/s28.

PART III

APPENDIX

A

SINGULAR VALUE DECOMPOSITION

A.1 LEAST SQUARES FITTING THROUGH SVD

The solution to an overdetermined system of equations, given in matrix form as $\mathbf{Ax} = \mathbf{y}$, is typically taken as that which minimizes the sum of the magnitude of squares, also known the the Euclidian or Frebonius vector norm, of the residual vector $\|\breve{}\| = \sum_i |\lambda_i|^2$, in accordance with $\|\mathbf{Ax} - \mathbf{y}\| = \|\breve{}\|$ (Lang, 1987; Press et al., 1992b). A common numerical tool to obtain the least square error solution is the singular value decomposition (SVD) (Press et al., 1992b; Golub and Reinsch, 1970). Any $m \times n$matrix $\mathbf{A}$ can be written as the composition

$$\mathbf{A} = \mathbf{UWV}^\dagger, \tag{A.1}$$

where $\mathbf{U}$ and $\mathbf{V}$ are orthonormal eigenvectors of square matrices $\mathbf{AA}^\dagger$ and $\mathbf{A}^\dagger\mathbf{A}$. The matrix $\mathbf{W}$ is a diagonal matrix with entries referred to as singular values (Lang, 1987; Press et al., 1992b). A matrix with p such non-zero singular values has rank equal to p.

Using the SVD of $\mathbf{A}$ a pseudo-inverse to matrix $\mathbf{A}$ is constructed using the orthonormal properties of $\mathbf{U}$ and $\mathbf{V}$

$$\mathbf{A}^\dagger = (\mathbf{UWV}^\dagger)^\dagger = \mathbf{VWU}^\dagger. \tag{A.2}$$

Consider $\mathbf{A}^\dagger\mathbf{A}$ and the fact that $\mathbf{V}$ and $\mathbf{U}$ are orthonormal, then

$$\mathbf{A}^\dagger\mathbf{A} = \mathbf{VWU}^\dagger\mathbf{UWV}^\dagger = \mathbf{VW^2V}^\dagger \tag{A.3}$$

From which it is easily shown both that $\mathbf{V}$ is an eigenvector of $\mathbf{A}^\dagger\mathbf{A}$ with eigenvalues $\mathbf{W}^2$ and the pseudo-inverse of $\mathbf{A}$ is given as

$$\mathbf{A^{-1}} = \mathbf{A}^\dagger/\mathbf{W^2} = \mathbf{VW^{-1}U}^\dagger,$$

where $\mathbf{W^{-1}}$ is a diagonal matrix consisting of the reciprocal non-zero values of $\mathbf{W}$. It is then evident that $\mathbf{A^{-1}A}$=$\mathbf{I}$. Where $\mathbf{I}$ is the identity matrix.

Returning to the matrix equation $\mathbf{Ax} = \mathbf{y}$ where the least squares solution is obtained through minimizing the residual

$$\|\mathbf{Ax} - \mathbf{y}\| = \|\lambda\|,$$

the SVD allows for the residual to be written as $\|\mathbf{UWV}^{\dagger}\mathbf{x} - \mathbf{y}\| = \|\lambda\|$. The orthogonality of $\mathbf{U}$ and $\mathbf{V}$, which states that the matrix operators do not change the magnitude of the vector, allows for

$$\|\mathbf{U}^{\dagger}(\mathbf{UWV}^{\dagger}\mathbf{x} - \mathbf{y})\| = \|\mathbf{WV}^{\dagger}\mathbf{x} - \mathbf{U}^{\dagger}\mathbf{y}\|.$$

For he diagonal matrix $\mathbf{W}$ composed of the singular values W_i such that it is clear that the residual is minimized when $\mathbf{V}^{\dagger}x_i = \mathbf{U}^{\dagger}y_i/W_i$ or $x_i = \mathbf{VU}^{\dagger}y_i/W_i$ subject to the constraint of finite, non-zero, singular values. It is clear that this operation is identical to the multiplication of $\mathbf{y}$ by the pseudo-inverse $\mathbf{A}^{-1} = \mathbf{A}^{\dagger}/\mathbf{W^2}$:

$$\|\mathbf{A^{-1}Ax} - \mathbf{A^{-1}y}\| = min(\sum_i \lambda_i^2) = \|\mathbf{x} - (\mathbf{VWU})^{\dagger}\mathbf{y}/\mathbf{W}^2\|.$$

The least square value solution for x is then observed to be $\hat{\mathbf{x}} = \mathbf{A}^{-1}\mathbf{y}$, (Golub and Reinsch, 1970; Press et al., 1992b).

A.2 ORTHOGONALIZATION AND PRINCIPAL COMPONENTS WITH SVD

The square $n \times n$ matrix $\mathbf{A}$ is diagonalizable if $\mathbf{V}^{\dagger}\mathbf{AV}$=$\mathbf{D}$ where $\mathbf{D}$ is an $n \times n$ square matrix with non-zero entries only on the diagonal. This condition is easily expressed as an eigenvalue equation

$$\mathbf{Av} = \alpha\mathbf{v}$$

such that $\mathbf{V}$ is an $n \times n$ orthogonal matrix composed of the $n \times 1$ eigenvectors $\mathbf{v}$ and the matrix $\mathbf{D}$ has diagonal entries composed of the set of eigenvalues $\{\alpha\}$ of $\mathbf{A}$.

For two $n \times 1$ vectors,$\mathbf{x}$ and $\mathbf{y}$, the variance is a scalar computed as

$$\sigma_x^2 = E[(\mathbf{x} - \bar{x})^2] = (1/N)\mathbf{x'}^{\dagger}\mathbf{x'},$$

where $\mathbf{x'} = \mathbf{x} - \bar{x}$, is the centered, i.e. mean removed, vector. The variance is easily generalized to the covariance between two $n \times m$ vectors

$$\text{cov}(\mathbf{x}, \mathbf{y}) = (1/N)\mathbf{x'}^{\dagger}\mathbf{y'}$$

which is an $m \times m$ matrix with entries $x_i^{\dagger}y_j$. The covariance of an $n \times m$ vector with itself

$$\mathbf{X} = \text{cov}(\mathbf{x}, \mathbf{x}) = (1/N)\mathbf{x'}^{\dagger}\mathbf{x'}$$

is a symmetric matrix with diagonal entries X_{ii} given by the variance of each dimension m. Because $\mathbf{X}$ is symmetric, i.e $X_{ij} = X_{ji}$ it follows that $\mathbf{X}$ is diagonalizable. The m eigenvalues of $\mathbf{Xv}_i = \alpha_i\mathbf{v}_i$ are commonly known as the principal components of x with the eigenvectors v_i known as the principal

directions or axes. The rotation $\mathbf{x}_{pca} = \mathbf{V}^{\dagger} x^{\dagger}$, where $\mathbf{V}$ is a matrix consisting of the m, eigenvectors is a commonly used numerical technique to rotate data into the principal component coordinate system.

In the most general case of a matrix, $\mathbf{Z} = (\mathbf{x}^{\dagger}, \mathbf{y})$ where $\mathbf{x} \neq \mathbf{y}$ is not a symmetric matrix, i.e. $Z_{ij} = x_i^{\dagger} y_j$ and $Z_{ij} \neq Z_{ji}$ the matrix $\mathbf{Z}$ may not be exactly diagonalizable, such that multiplication by orthogonal rotation matrices can achieve a diagonal matrix. However, two approaches exist for finding an approximate principal component basis.

For approximately symmetric matrices, the anti-symmetric component is a small perturbation such that the dominant symmetric matrix may be diagonalized to approximate the PCA basis. Any matrix may be written as the sum of a symmetric matrix $\mathbf{S}$ and anti-symmetric matrix $\mathbf{T}$:

$$\mathbf{S} = \frac{\mathbf{Z} + \mathbf{Z}^{\dagger}}{2} \mathbf{T} = \frac{\mathbf{Z} - \mathbf{Z}^{\dagger}}{2} \tag{A.4}$$

Additionally, if non-orthogonal rotation are allowed, it is then possible to use SVD to determine the linear map between two vectors $\mathbf{A}\mathbf{x} = \mathbf{y}$ and rotate into an approximate PCA coordinate system for

$$\hat{\mathbf{Z}} = \mathrm{cov}(\mathbf{A}\mathbf{x}, \mathbf{y})$$

where the linear map is determined using SVD methods Sorkine-Hornung,O., and Rabinovich, M. (2017). The linear map $\mathbf{A}$ scales the vector $\mathbf{x}$ such that an orthogonal rotation can, with respect to least square error, diagonalize the covariance matrix.